Braking Forces in Highway Bridge Substructures

by

Anna J. Quinn

A thesis submitted to the Graduate Faculty of
Auburn University
in partial fulfillment of the
requirements for the Degree of
Master of Science

Auburn, Alabama
August 3, 2019

Keywords: braking; bridges; deceleration; dynamic analysis; finite-element modeling; live load

Approved by

Robert W. Barnes, Ph.D., P.E., Chair, Associate Professor of Civil Engineering
J. Brian Anderson, Ph.D., P.E., Associate Professor of Civil Engineering
Justin D. Marshall, Ph.D., P.E., Associate Professor of Civil Engineering

ABSTRACT

Under the Load-and-Resistance Factor Design Specification, the longitudinal braking force that must be designed for was increased when compared to a bridge designed according to the previous code, the Standard Specification. The Standard Specification required 5 percent of the live load be designed for, whereas, the LRFD Specification increased this value to 25 percent. For short to medium span bridges, this was a signification increase, as much as 400 percent in some cases. This increase in live load also increases the demand on the bridge bents and other substructure elements. This change in the code raises questions about the path the load is taking and ultimately the intensity of the load going into the supporting substructure.

The primary focus of this study was to investigate the amount of shear force in the piles of a short-span bridge typical of Alabama Department of Transportation construction. This was accomplished through static pull tests and dynamic braking tests on the Macon County Road 9 bridge. The static pull tests involved positioning the load truck on individual spans and pulling on it with a tow truck that was connected with a cable and outfitted with a load cell. The load cell allowed for correspondence between bent and girder displacements and longitudinal force imparted on the bridge deck. The cable was tensioned until approximately 20 kips was achieved or the truck began to slide. The dynamic braking tests involved the load truck accelerating to approximately 12-15 mph before getting on the bridge and once entirely within the span being tested the brakes were applied and the truck came to a stop within the same span. Using the results from the field tests, an analytical model was created and calibrated to be able to obtain the forces that are not well understood.

From this model, it was determined that the total braking force can be distributed among all components of the substructure and the amount of which varies depending on the location on the bridge that the vehicle was braking. Furthermore, it was established that the code provision of 25 percent of the design truck axle weight is generally not over conservative. From the field tests conducted, potentially 35 percent of the vehicle weight can be imparted into the bridge substructure components in sum.

ACKNOWLEDGMENTS

To truly acknowledge and thank everyone who has supported me throughout my time in school would be an impossible task. As someone who never really gave that much effort to education until later in my academic career, achieving a Master's degree is something I would have never planned or envisioned for myself. But, here we are and it's pretty awesome!

To my parents who always supported me in whatever crazy dream I had, thank you. From traveling all over the country for sports, to coming to my college volleyball games at Montevallo, to supporting me when I decided I wanted to work in rural Appalachia for four summers, to transferring to Auburn to finish my undergraduate studies and then on to graduate school, I can't thank you enough for your support. You both taught me the value of hard work and not giving up on something once you start (no matter how many times I really wanted to quit school especially). You both are steadfast in your support of whatever crazy dream I have and I truly appreciate it.

To my friends, thank you for always being there. There are far too many to name because Auburn has given me some of my greatest and most valued friendships and I know that I can always count on any of you to be there for me and to always put up with me. To Rob, Christian and Grant, you better not find a replacement for the Monday Hamilton's lunch bunch.

This thesis would not be possible without the guidance and support of my Committee Chair, Dr. Barnes and the rest of my advising committee, Drs. Anderson and Marshall. Thank you Dr. B for everything! Finally, this project would not have been possible without the Highway Research Center and the Alabama Department of Transportation. Their funding of this research afforded me with an opportunity to have a Graduate Assistantship and make my graduate studies possible.

Last but certainly not least, War Damn Eagle!

TABLE OF CONTENTS

LIST OF TABLES

LIST OF FIGURES

CHAPTER 1: INTRODUCTION

1.1 BACKGROUND

In Alabama, one of the most common bridge types is the multi-span bridge with prestressed concrete girders, cast-in-place concrete bent caps and driven steel HP pile bents. To prevent section loss of the HP pile bents, if in the path of a flowing channel, the bents can be encased with non-structural concrete for 3 ft above the mudline, or they can be galvanized. Additionally, if the top of the encasement is more than 14 ft below the bent cap, welded sway bracing is added to provide lateral stiffness and strength. Figure 1-1 and Figure 1-2 are from a typical multi-span bridge of ALDOT construction, located in Macon County, Alabama.

Figure 1-1 – Side View of a Typical ALDOT Multi-Span Bridge

Figure 1-2 – HP Pile Bents Typical of Alabama Bridges

In these bridges, the primary horizontal force in the longitudinal direction is the vehicular braking force. Upon the transition from the Standard Specification (AASHTO 2002) to the LRFD Specification (AASHTO 2017), the design braking force increased significantly. In the Standard Specification, 5 percent of the live load was required to be designed for whereas in the LRFD Specification, either 25 percent of the live load or 5 percent of the lane load plus live load, whichever is greater, must be designed for. In bridges with less than 450 ft between deck expansion joints, 25 percent of the live load will control.

The increase in force can have a significant influence on the required strength of the substructure elements, such as the foundations and piers. With the state having various standardized bridges, this poses the question of what is the load path and intensity of substructure forces resulting from braking. Moreover, it raises the question of whether the provisions in the LRFD Specification are adequate and is there a way to aid designers when making decisions on how this force should be distributed. Previous research into this topic is lacking, but this information could affect future bridge design and repair of older structures.

1.2 RESEARCH OBJECTIVES

This project was conducted to gain insight about the path and distribution of the longitudinal braking force in short- to medium-span highway bridges. How the load is transferred from superstructure to substructure is vital to accurately estimating what force is being transferred and ultimately has to be resisted by the structure.

This thesis outlines the processing of the data from the field tests, the creation of an analytical model and the calibration of said model to the field data. The primary objectives of this study include

- Comparison of code requirements to determine if the LRFD Specification is overly conservative or not adequate in regards to the braking force provision
- Identify load path of longitudinal braking force
- Identify distribution of horizontal shear forces in bents from the braking force
- Provide recommendations of how to distribute the braking force in short-span bridge bents
- Provide recommendations of how to appropriately model a braking maneuver to produce reliable shear forces in the piles of the bents

1.3 RESEARCH SCOPE

The scope of this project was to create an analytical model that was calibrated to results obtained during field testing. From this model, determining the path and distribution of the shear forces going into the bents was the overall goal.

Static pull tests were conducted on each span of the bridge and during these tests the load and displacements of the girders and bents were recorded. The dynamic braking tests occurred on spans 2, 3, and 5 in the center of the spans as well as on the right side of the spans. The goal with the dynamic tests on the right side of the bridge deck was to determine if any twist would occur at the bents. During the dynamic tests, bent and girder accelerations and displacements were recorded. In addition to this data, the truck was instrumented with an inertial measurement unit to obtain a braking profile and be able to use that information in the model. All of the field data was processed and used to calibrate the analytical model. Once the displacements under static loading and accelerations under dynamic loading correlated well between the field data and model results, it was assumed that the recorded shear forces were accurate.

Beyond the scope of this thesis but of importance to future research, the information obtained will be applied to other short- to medium-span bridges to understand how modifying variables of the bridge geometry will affect the braking force distribution but this is beyond the scope of this thesis.

1.4 ORGANIZATION OF THESIS

Chapter 2 outlines many topics that were pertinent to understanding the behavior of a bridge experiencing a braking force. It also includes information on truck braking characteristics that directly relate to how much force is transferred into a bridge deck and ultimately the supporting substructure elements. This chapter contains modeling information that is relevant to properly exciting the bridge model to achieve conditions similar to the forces imparted on the bridge during field tests.

The modeling procedure developed during this project is outlined in Chapter 3. This includes the definitions of materials and frame sections and construction of the initial model in CSiBridge and the subsequent steps that followed once it was exported to SAP2000 for refinement and analysis. Details of the static loading and dynamic loading of the model are presented in this chapter along with an overview of the field testing procedures to understand what the model is to be calibrated to.

Chapter 4 of this thesis presents the results and an analysis of the displacements, accelerations and shear forces reported by the calibrated analytical model. Included in this chapter is a graphical representation of the correlation between the model and the field tests to support the graphs of the shear forces generated.

Chapter 5 presents a discussion of the model results and compares them to the code provisions for longitudinal braking force. General conclusions from this research are presented in Chapter 5 also. Finally, recommendations for future work are proposed.

CHAPTER 2: LITERATURE REVIEW

2.1 INTRODUCTION

This chapter covers background information related to bridge design codes, truck braking, and modeling considerations. A review of literature on the following topics was conducted: design codes and philosophies, longitudinal braking, road-tire friction, bearing pads, and different analysis methods for modeling of the bridge. Overall, previous work related to this project is limited, which lead to a wide-ranging review of topics to achieve a thorough understanding of how to complete this research project.

2.2 TRANSITION FROM STANDARD SPECIFICATION TO LOAD-AND-RESISTANCE FACTOR DESIGN SPECIFICATION

Prior to 2007, the AASHTO Standard Specification was the most widely used code for bridge design in the United States. With the first edition published in 1931, it was updated periodically, and by 1949, was regularly updated every 4 years until the publication of the 17th edition. As design capabilities progressed and alternative design philosophies were adopted, the Federal Highway Administration and the States established that load-and-resistance factor design (LRFD) shall be the standard used in all bridge design by 2007 (AASHTO 2002). This transition came about due to a request by the Subcommittee on Bridges and Structures for the review of foreign design specifications and codes to understand their philosophies compared to the underlying design philosophies of the Standard Specification. It was discerned that the Standard Specification had inconsistences, conflicts, and gaps in its methodology as well as no incorporation of the newly developed LRFD philosophy that was quickly becoming popular among structural engineers in Canada and Europe (AASHTO 2017).

The underlying design philosophy on which the Standard Specification is built is working stress design (WSD). Within WSD, an allowable stress is determined as a fraction of the material's load carrying capacity, this capacity shall not be exceeded by the design stresses. It was not until the early 1970's that WSD incorporated the variability of certain loads such as

wind or vehicular. To account for this variable predictability, design factors were computed and a shift to the design philosophy known as load factor design (LFD) was created. LFD still failed to consider the variability of properties of the structural elements, themselves, though. For these reasons, LRFD became the predominant design method because it incorporates the variability of structural elements explicitly (AASHTO 2017). Additionally, LRFD relies on factors derived from statistical methods and presents them in an easy to use manner.

2.3 LONGITUDINAL BRAKING FORCE

Upon the switch between design methodologies, the design amount of longitudinal braking force increased significantly. This is especially true for common short- to medium-span bridges. In the Standard Specification, the equation for braking force is

$$BR_{Standard\ Spec} = 0.05 \times (LL + Concentrated\ Load) \times N_{Lanes} \quad \text{Equation 2-1}$$

Where

$$LL = lane\ load$$

$$N_{Lanes} = Number\ of\ Lanes\ Carrying\ Traffic\ in\ the\ Same\ Direction$$

The lane load plus the concentrated load for moment is specified in Article 3.7 of the Standard Specification. The lane load is 0.64 klf and the concentrated load is 72 kips, as prescribed in the HS20-44 loading. Application of the reduction for multiple-loaded lanes as directed in Article 3.12 (2002) must also be included. The reduction in live load intensity shall be applied prior to computing the breaking force using Equation 2-2. Reducing the live load incorporates the "improbability of the coincident maximum loading" as stated in the Standard Specification (2002).

In the LRFD Specification, braking force is computed as follows

$$BR_{LRFD} = maximum\begin{Bmatrix} 0.25 \times axle\ weight \\ 0.05 \times (axle\ weight + LL) \end{Bmatrix} \times N_{Lanes} \times MPF \quad \text{Equation 2-2}$$

Where,

$$axle\ weight = 72\ kips$$

$$LL = 0.64\ k/ft$$

$$N_{Lanes} = Number\ of\ Lanes\ Carrying\ Traffic\ in\ the\ Same\ Direction$$

$$MPF = Multiple\ Presence\ Factor$$

Additionally, in the Commentary to the LRFD Specifications it explicitly states that for short- and medium-span bridges, the braking force used in design can be significantly greater than the Standard Specification braking force. This is due to the data being used to determine the braking force having not been modified since at least the early 1940's, and it does not account for the improved baking capacity of trucks in today's era (AASHTO 2017). Published in the Commentary to the LRFD Specifications are Figures 2-1 through Figures 2-4 that illustrate how insufficient the Standard Specification has become in accounting for braking force and how it trailed Canada in their respective design codes.

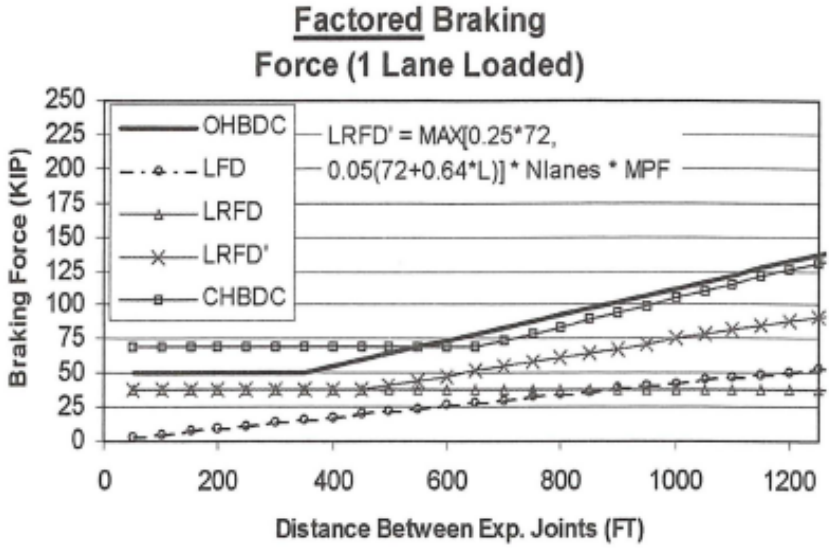

Figure 2-1 – Factored Braking Force Comparisons for 1 Lane Loaded (AASHTO 2017)

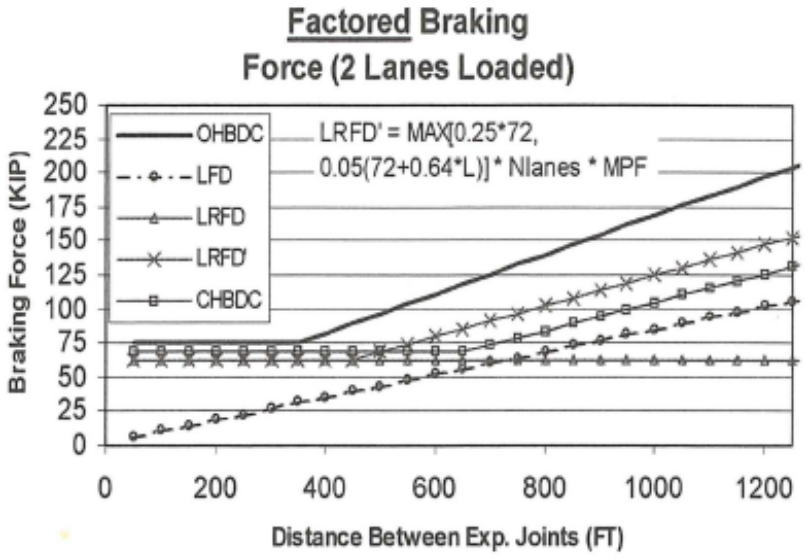

Figure 2-2 – Factored Braking Force Comparisons for 2 Lanes Loaded (AASHTO 2017)

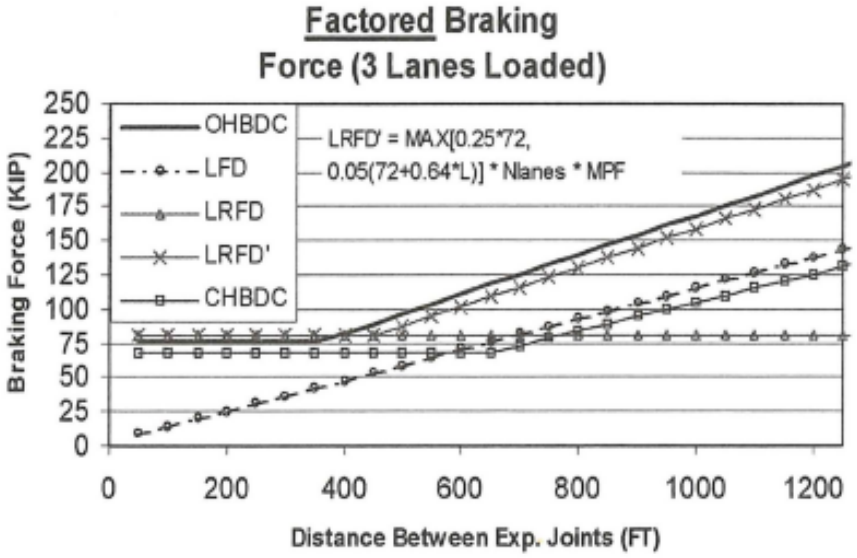

Figure 2-3 – Factored Braking Force Comparisons for 3 Lanes Loaded (AASHTO 2017)

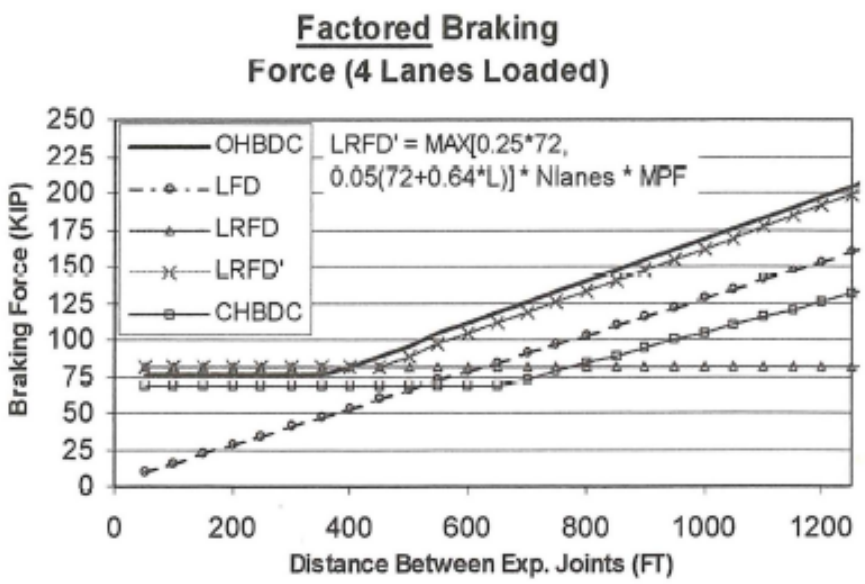

Figure 2-4 – Factored Braking Force Comparisons for 4 Lanes Loaded (AASHTO 2017)

In all of the figures, OHBDC is Ontario Highway Bridge Design Code, LFD is the factored braking force as specified in the Standard Specification, LRFD is the originally specified braking force (up to the 2001 Interim edition), LRFD' is the current specified braking force, and CHBDC is the braking force specified by the Canadian Highway Bridge Design Code. It is not known where the data used to create these graphs originated, but it illustrates how the increase in braking force could pose issues with rehabilitation projects where the bridge was designed according to the Standard Specification but is now governed by LRFD Specifications. Furthermore, it shows how design of new structures could require larger structural components and foundations to satisfy design requirements.

With the lane load appearing in both equations, its significance cannot be neglected. For both codes, the lane load is 0.64 kips per linear foot. Its purpose is to "emulate a caravan of vehicles" and was introduced in 1944 (Chen and Duan 1999).

2.4 FRICTION

The amount of longitudinal force that gets transmitted into the superstructure from the braking vehicle is dependent upon the friction between the tire and road interface. The 25 percent as specified in the LRFD Specification could be interpreted as the estimated maximum coefficent of friction expected between the tires and roadway. For a non-skewed bridge without elevation

change, the friction force is directly related to the coefficient of friction for the bridge deck surface and the normal force of the vehicle undergoing the braking maneuver. The friction coefficient is also dependent on many factors such as: amount of moisture on the pavement, temperature, whether the vehicle has locked its brakes during the maneuver and the type of surface.

Locked-wheel braking occurs when the brakes grip too tightly to the wheel, causing the vehicle to slide. During this type of braking sliding friction is used, and is less than the peak achievable friction value (Torbic, et al. 2003). For all of the tests conducted in this research, the goal was to complete the braking maneuver within the span of interest without inducing locking of the brakes. Since it is extremely difficult to know precisely the coefficient of friction for a bridge deck, data from the Federal Motor Vehicle Safety Standard (FMVSS) 121 was used to compute approximate values for the coefficient of friction for various truck configurations, vehicle speeds, and braking distances over those speeds. These values aided in the formulation of expected deceleration rates and coefficients of friction during testing. In order to calculate these values from the FMVSS 121 (2008), the standard constant-acceleration kinematic equation presented in Equation 2-3 was rearranged and used to obtain a deceleration rate.

$$v_f^2 = v_o^2 + 2a(\Delta x) \qquad \text{Equation 2-3}$$

Where,

$$v_f = final\ velocity$$

$$v_o = initial\ velocity$$

$$a = deceleration$$

$$\Delta x = change\ in\ displacement$$

The deceleration rate was divided by gravity (32.2 ft/s^2) to arrive at an acceleration value in terms of gravity. These values ranged between 0.34g to 0.39g for trucks that were loaded, unloaded, and loaded with an unbraked trailer. The following table is the maximum likely deceleration rates resulting from the calculations using the FMVSS 121 data (2008).

Table 2-1 – Vehicle Speed and Braking Distance and the Resulting Deceleration Rates

		Truck Braking Distance (ft)			Truck Deceleration Rate (g)		
Vehicle Speed (mph)	Vehicle Speed (ft/s)	Loaded single-unit truck (1)	Unloaded truck tractors and single-unit trucks (2)	Loaded truck tractors with an unbraked control trailer (3)	(1)	(2)	(3)
20	29.33	35	38	40	0.382	0.352	0.334
25	36.67	54	59	62	0.387	0.354	0.337
30	44.00	78	84	89	0.385	0.358	0.338
35	51.33	106	114	121	0.386	0.359	0.338
40	58.67	138	149	158	0.387	0.359	0.338
45	66.00	175	189	200	0.387	0.358	0.338
50	73.33	216	233	247	0.387	0.358	0.338
55	80.67	261	281	299	0.387	0.360	0.338
60	88.00	310	335	355	0.388	0.359	0.339

In order to accurately model the dynamic tests, using a reasonable value for the achievable braking deceleration is vital to ensuring the proper amount of force is being transmitted longitudinally.

2.5 TRUCK BRAKING CAPACITY

Trucks in today's modern era use compressed air to deliver air to each individual wheel's brake. Due to this, there is a slight delay in response as a result of the compressibility of the air. As the pedal is released, air is released from the system into the atmosphere and replaced by air from the compressor. For this reason, pumping of the brakes must be avoided so as not to deplete the compressed air too quickly (Torbic, et al. 2003). Additionally, when the air becomes depleted, the compressibility of the brakes decreases, and they are less capable of providing braking ability to the vehicle. If there is no air, the brakes cannot effectively engage.

2.6 BEARING PADS

Within the bridge design specifications for the state of Alabama, there are numerous types of bearing pads that could be used in design. Bearing pads play an integral role in transferring the forces in the superstructure to the substructure. From shape to thickness, material, reinforcement, and composition of the bearing pad, all of these factors have an effect. In this bridge, Type 2,

Mark B1 elastomeric bearing pads were used. The pads were 14.5 in long by 9 in wide by 0.75 in thick. The thickness was composed of two layers of elastomer with one 12-gauge steel shim in between. Figure 2-5 is the standard detail for these bearing pads.

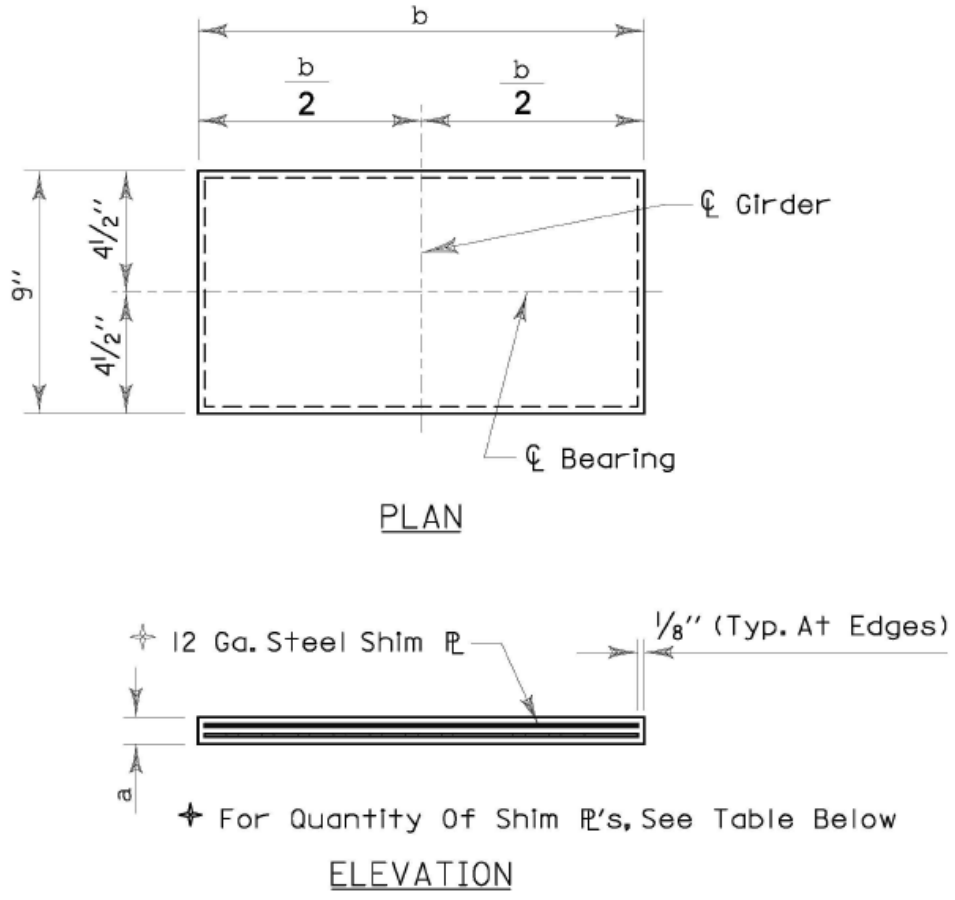

ELASTOMERIC BEARING PAD DETAIL
(FOR BEARING MARK "B" & "VB")

Figure 2-5 – Standard Detail for ALDOT Elastomeric Bearing Pad Detail (ALDOT 2013)

Elastomeric bearing pads are designed to be able to support and transfer the vertical forces from the girders of the bridge to the bents. They allow for horizontal movements and rotations of the girders as a result of thermal expansion or contraction, beam end rotations, traffic loads, elastic shortening, and time-dependent changes in the concrete such as creep and shrinkage.

When designing the bearing pad, the most important material property is the shear modulus, according to AASHTO section C14.7.5.2. The elastomer must have a specified shear modulus between 0.080 ksi and 0.175 ksi. Going beyond the upper limit for the shear modulus is not allowed due to the elastomer having more creep at this stiffness then a softer bearing and because these bearings generally break at a smaller elongation then its softer counterparts. These undesirable qualities can be a result of more filler being present in the elastomer in order to reach the higher shear modulus value (AASHTO 2017).

Typically, under service loads the bearing pads deflect horizontally and vertically as well as providing some damping of vibration to the superstructure. In order to compute the stiffnesses of a bearing pad, six equations can be derived from beam theory principles and are presented in "The Effect of Bearing Pads on Precast Prestressed Concrete Bridges" presented by Cai, Eddy, and Yazdani (2000) as follows:

$$k_x = \frac{EA_x}{H} \qquad \text{Equation 2-4}$$

$$k_y = \frac{GA_y}{H} \qquad \text{Equation 2-5}$$

$$k_z = \frac{GA_z}{H} \qquad \text{Equation 2-6}$$

$$k_{Rx} = \frac{GI_x}{H} \qquad \text{Equation 2-7}$$

$$k_{Ry} = \frac{EI_y}{H} \qquad \text{Equation 2-8}$$

$$k_{Rz} = \frac{EI_z}{H} \qquad \text{Equation 2-9}$$

Where

$$E = Modulus\ of\ Elasticity$$

$$A = Cross - Sectional\ Area\ Corresponding\ to\ each\ Axis$$

$$H = total\ thickness\ of\ the\ bearing\ pad\ excluding\ rigid\ plates$$

$$I = Moment\ of\ Inertia\ Corresponding\ to\ each\ Axis$$

$$G = Shear\ Modulus$$

The value for the modulus of elasticity is assumed to be 30 ksi since there is no pad-specific test data as per 14.7.6.3.3 in the LRFD Specification (2017), and the shear modulus was

assumed to be 0.135 ksi based off values presented in the Caltrans design memo (1994). The cross-sectional properties, area and moment of inertia, can be calculated with the geometry of the bearing pad as detailed in the ALDOT Standard Details Drawing No. I-131 (2013).

2.7 MODELING SOFTWARE

Throughout the duration of this project, three modeling software applications' were used. Two were structural analysis and design softwares, CSiBridge v15.2.0 and SAP2000 v20.2.0, referred to as CSI and SAP, respectively, throughout the remainder of this thesis. Both of these are finite element programs capable of linear and nonlinear analyses and were used due to their ability to accurately model the bridge and the capability to perform static and dynamic analyses efficiently and accurately.

The third software utilized was FB-MultiPier, referred to as FBMP. This finite element geotechnical software is capable of modeling various structural elements as well as an entire bridge through linear or nonlinear analysis. The user inputs soil profiles and element geometry, then FBMP generates results for soil and structure behavior.

The ability to generate p-y curves was utilized for this project to transfer the lateral pile resistance capabilities into SAP by creating soil springs that replicate the effect of the below grade conditions on the pile bents. A p-y curve represents the soil resistance at a given depth, defined in terms of the soil's resistance per unit length versus deflection (Reese and Wang 1993). With the software automatically dividing the pier into numerous elements for analysis, the results output for each node in terms of p (lbs/in) versus y (in). By taking the slope of the linear portion of the curve, resulting in lbs/in/in units, and multiplying this value by the tributary length of that node, a stiffness in terms of lbs per inch was obtained and this was used as the stiffness of a spring added to the corresponding joint in SAP. A more thorough explanation of this procedure is outlined in Chapter 3.6.1.

2.8 BRIDGE MODEL EXCITATION – DYNAMIC ANALYSIS PROCEDURES

Two methods of excitation for the model of the bridge were researched. The goal was to investigate which method would impart the dynamic force on the bridge in the most similar method as in the field. In SAP2000 there is an option for a time history analysis or a response spectrum analysis.

2.8.1 Time-History Analysis

A time-history analysis provides for linear or nonlinear evaluation of a dynamic structures' response under loading. This loading may vary according to the function that is specified over the given time duration. In this method, the dynamic equilibrium equation given in Equation 2-10 is solved by either direct integration or modal response history analysis (Chopra 2017).

$$m\ddot{u} + c\dot{u} + ku = \rho(t) \qquad \text{Equation 2-10}$$

Where,

$$m = mass$$
$$\ddot{u} = acceleration$$
$$c = damping$$
$$\dot{u} = velocity$$
$$k = stiffness$$
$$u = displacement$$
$$\rho(t) = forcing\ function$$

A time-history analysis was selected instead of a response spectrum analysis due to the response spectrum being a plot of the peak response quantity as a function of the natural period of the entire system.

2.8.2 Analysis Procedure

A linear analysis using a modal integration solution type was selected. Modal analysis superimposes the various mode shapes of a structure to characterize the displacements of each element in each individual mode shape. Then, all of the mode contributions are combined to determine the total response (Chopra 2017).

Mode shapes are representations of how the structure will naturally want to displace. Typically, the lower mode shapes provide the largest contribution to the overall structural response and are easier to accurately predict their behavior. When deciding how many modes is enough to consider, the modal mass participation ratio is the driving factor. To determine a sufficient number of modes, a minimum of 90 percent of the total mass should be involved in the analysis. This can benefit computational time, because once a sufficient number of modes is

achieved, then the overall number of modes can be truncated if there is no benefit to including higher order modes (Computers and Structures, Inc. 2018).

Modal integration is also desirable when compared to direct integration because it does not have to integrate the fully coupled equations of motion for each time step under which the structure is loaded. Whereas in modal integration, each mode shape is integrated independently of one another and is normalized so that it can be superimposed with the other modes to obtain the overall response. This significantly reduces computational effort and time (Computers and Structures, Inc. 2018).

2.9 RAMP FUNCTIONS FOR VEHICLE DECELERATION PROFILES

An important aspect to load the model similarly to how the bridge was loaded during braking in the field was a critical aspect in the dynamic analyses. In order to replicate the loading of the bridge during dynamic testing in the model, representing the vehicle deceleration profiles had potential to capture this time-dependent event. To do this, defining a ramp function based on vehicular longitudinal deceleration data is a way to incorporate the truck braking characteristics and apply a load to the model over time. Information from the National Highway Traffic Safety Administration's (NHTSA) report on Experimental Measurement of the Stopping Performance of a Tractor-Semitrailer from Multiple Speeds (Garrott, Heitz and Bean 2011) provided foundational information to support this method of modeling the braking of the truck.
In this report, creating a ramp function based on the deceleration rise time, the time it takes for the vehicle to reach constant deceleration; steady-state deceleration time, and the decrease of steady state deceleration to final stopping of the vehicle was evaluated. The aim of this paper was to investigate the stopping distance of a vehicle from varying initial speeds in order to create a single governing equation for maximum permitted stopping distance that could incorporate the various decelerations and initial speeds.

During the stopping tests in the NHTSA report, the longitudinal deceleration was recorded. From that data, a time history trace of the deceleration versus time was created as shown in Figure 2-6.

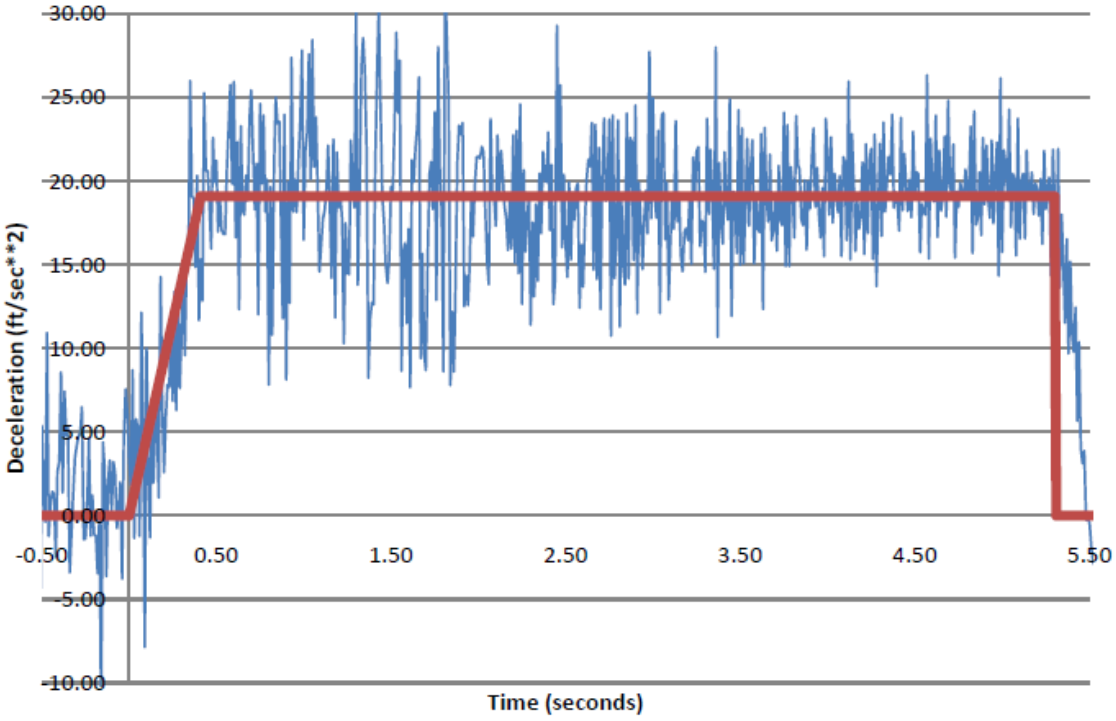

Figure 2-6 – Measured and Idealized Deceleration for a Typical 60 mph Stop (Garrott, Heitz and Bean 2011)

In each test, the deceleration rise time and the magnitude of the steady state deceleration were the most important values affecting the braking distance. For each test, the analyst determined the rise time in seconds based on their clearest indication of how long it took to reach the steady state deceleration. Doing this for each test provided results that where within the margin of compliance for the data set and indicated that this method of analyzing the deceleration profiles could produce accurate results when used determine other unmeasured values.

CHAPTER 3: FIELD TESTS AND ANALYTICAL MODELING

3.1 INTRODUCTION

This chapter provides information on the bridge that was used for field testing, reviews the procedures for the static and dynamic tests, outlines the steps in the data analysis, and reviews the modeling procedures used.

3.2 MACON COUNTY ROAD 9 BRIDGE DESCRIPTION

The Macon County Road 9 bridge was constructed in 2014 and crosses over Old Town Creek in Shorter, Alabama. Figure 3-1 and Figure 3-2 are the plan and elevation views of the final design. The bridge has no horizontal curve or slope, features six 40 ft spans, four prestressed concrete girders per span, cast-in-place concrete bent caps, and five bents each with four piles. The exterior piles are battered at a 1.5/12 slope. The piles of bents 2, 5, and 6 are steel HP 14x89 piles encased in non-structural concrete and the piles of bents 3 and 4 are non-encased, but rather are galvanized. The piles of bents 3 and 4 are in the channel of Old Town Creek. Additionally, the spans in this bridge are discontinuous and there are expansion joints between the girders and bridge deck at each bent.

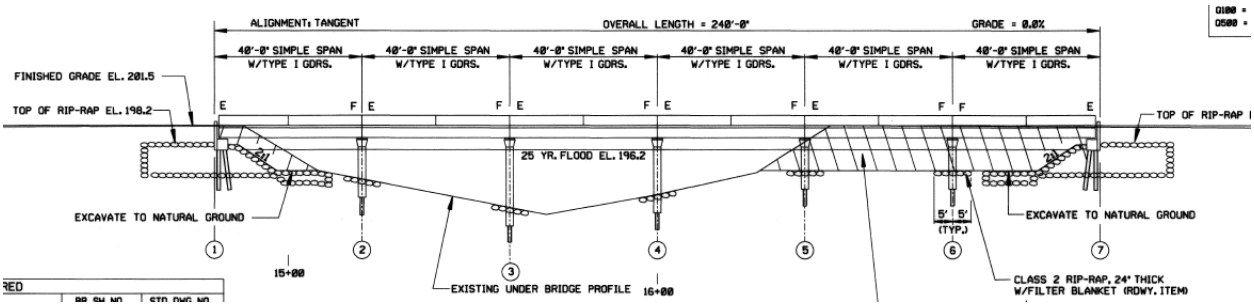

Figure 3-1 – Bridge over Old Town Creek Elevation View (ALDOT 2013)

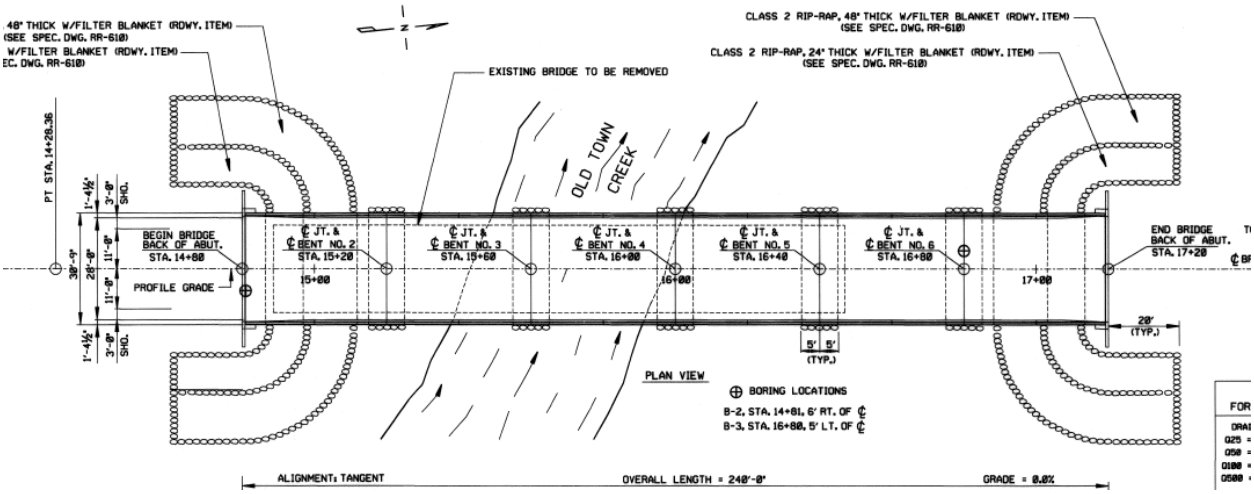

Figure 3-2 – Bridge over Old Town Creek Plan View (ALDOT 2013)

On the elevation view of the bridge plans, there is an “F” or an “E” at the end of each span. This is a designation for fixed or expansion, referring to the fixity of the girder ends. It is important to note that the designation “fixed” is ALDOT terminology meaning the longitudinal translation is restrained but rotation is not, acting more like a pinned connection rather than truly fixed. Figure 3-3 is an expansion connection at abutment 1 where the clip has a slit, allowing for translation of the girder end. Figure 3-4 is a typical fixed connection where translation is not permitted.

Figure 3-3 – Expansion Joint Connection

Figure 3-4 – Fixed Joint Connection

3.3 TESTING PROCEDURE

The field testing consisted of static pull tests and dynamic braking tests on the Macon County Road 9 bridge. The static pull tests were conducted on each span with the load truck positioned in the center of the span, and a tow truck was used to pull the load truck while the truck remained stationary. The goal was to achieve either 20 kips of tension in the cable, measured by a load cell, or sliding of the truck due to the brakes not holding, whichever came first. Figure 3-5 illustrates how a typical span was tested.

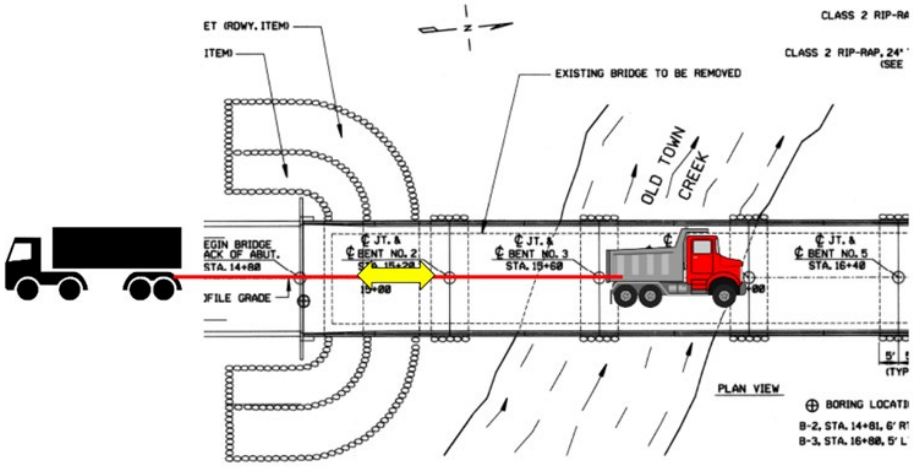

Figure 3-5 – Static Pull Test Setup

For the dynamic braking tests, spans 2, 3 and 5 were tested with braking occurring in the center and the right side of each of these spans. For each test, the truck approached the bridge at approximately 12-15 mph and the goal was to stop the truck as rapidly as possible without lock the brakes or skidding. The initial speed was selected to ensure that the stopping maneuver was restricted entirely to the span of interest. In addition to the instrumentation of the bridge, an inertial measurement unit (IMU) was mounted on the vehicle to record its acceleration, velocity and position. By knowing the deceleration rate at which the truck was braking and the weight of the truck, the amount of braking force could be obtained.

In order to impart enough longitudinal force to excite the bridge, and to use a truck with a weight similar to the design truck in the LRFD Specifications, the use of the ALDOT Load truck was required. The load truck was configured in Load Combination 2, the set-up of which is shown in Figure 3-6 and totals 70.2 kips distributed among the three axles.

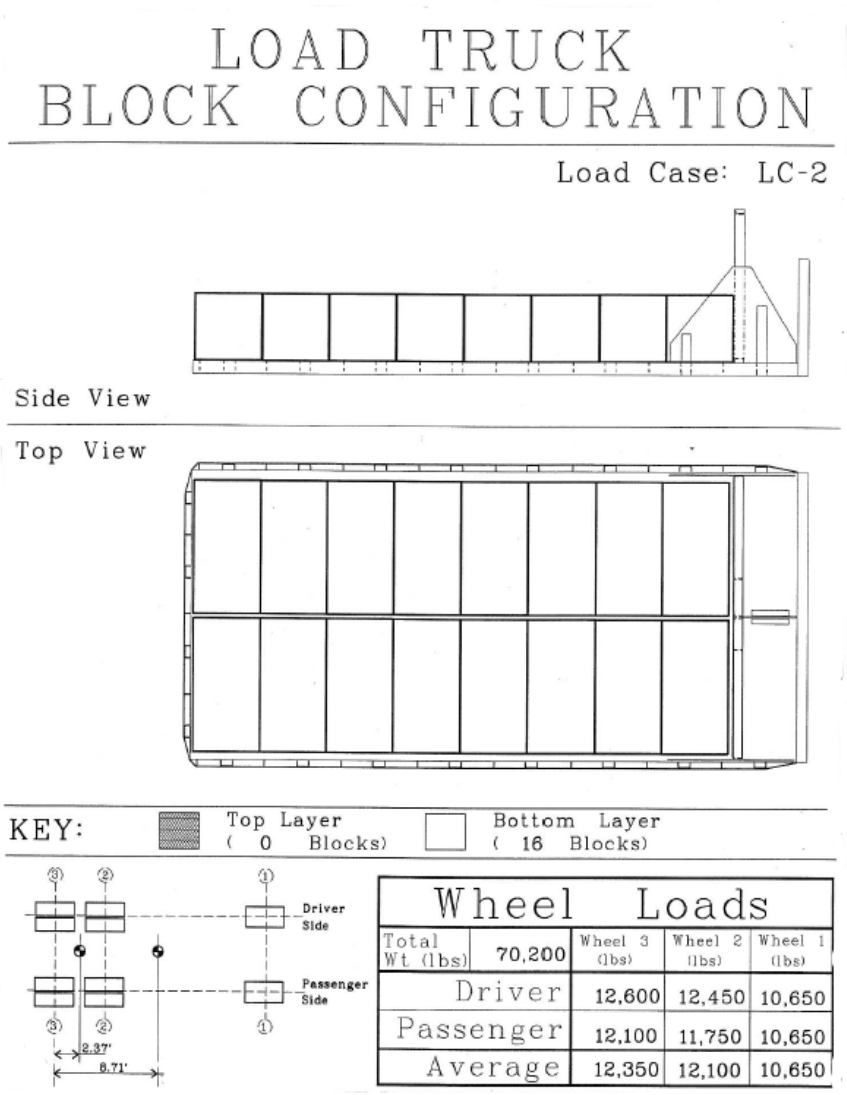

Figure 3-6 – ALDOT Load Combination Configuration for Load Combination 2 (2018)

While performing the static tests, the tension force applied to the load truck was recorded via the load cell and the corresponding displacements of the bents and girders were recorded. In the dynamic tests, the IMU data for the truck was recorded as well as displacements and accelerations of the bents and girders of the bridge. For a more detailed explanation of the testing procedure and the instrumentation of the bridge, refer to Matthew Barr's thesis "Experimental Determination of Braking Force Distribution in Steel Pile Bent Bridges" (2019).

3.4 DATA REDUCTION

To obtain useful information from the load tests, the files required downsampling to get the data to an appropriate size for functionality without sacrificing accuracy. The process of downsampling can be done at random or periodic intervals. For this project, periodic was chosen. For the static tests, in order to know what rate to downsample at, the frequency at which the data acquisition software sampled at was estimated in order to avoid decimating points that would leave only local maxima and minima, but rather, would result in median values remaining and give an accurate representation of the data set but with fewer values. For these tests, that resulted in an interval of 45. For the dynamic tests, the downsampling was at a rate that produced the same time step interval as the inertial measurement unit that was mounted to the truck. To accomplish this, the period downsampled at was 10.

3.5 MODELING PROCEDURE

The steps in creating the model can be generalized into two phases: the CSiBridge phase and the SAP2000 phase. Construction of the bridge model began in CSiBridge v. 15.2.0. This program, produced by Computers and Structures, Inc., is a structural analysis software specifically for bridges and had advantages for building the initial, unrefined version of the model before transferring to SAP2000 for calibration and analysis. The advantage was the predefined bridge elements that made construction of the model significantly quicker and more realistic to the geometry of the real bridge. CSI provided a step-by-step process to build the superstructure and substructure and connected them appropriately.

3.5.1 Constructing the Analytical Model in CSiBridge

To begin, a layout line of 240 ft with a 0.0 percent grade was inserted with a 12 ft wide lane on either side of the layout line. From the components tab, the appropriate materials and section properties were defined to correspond to this bridge. The modeled elements included were

- Bridge deck
- Precast prestressed Type I AASHTO concrete girders
- Bearing pads
- Bent Caps
- Galvanized HP14x89 piles

- Encased HP14x89 piles
- Abutments

With these elements properly defined, the deck cross section was created. The software creates the deck as shell elements and the girders as frame elements. For the deck, CSI subdivides the end spans into thirty-two shell elements and interior spans into forty-eight shell elements. Figure 3-7 is a wire-frame view illustrating how the interior spans have more shell elements then end spans. This is due to the girder lines being discontinuous from the superstructure. This definition results in two connections, one on either side of the centerline of the bent cap to the two girder ends, requiring more joints to be able to connect to.

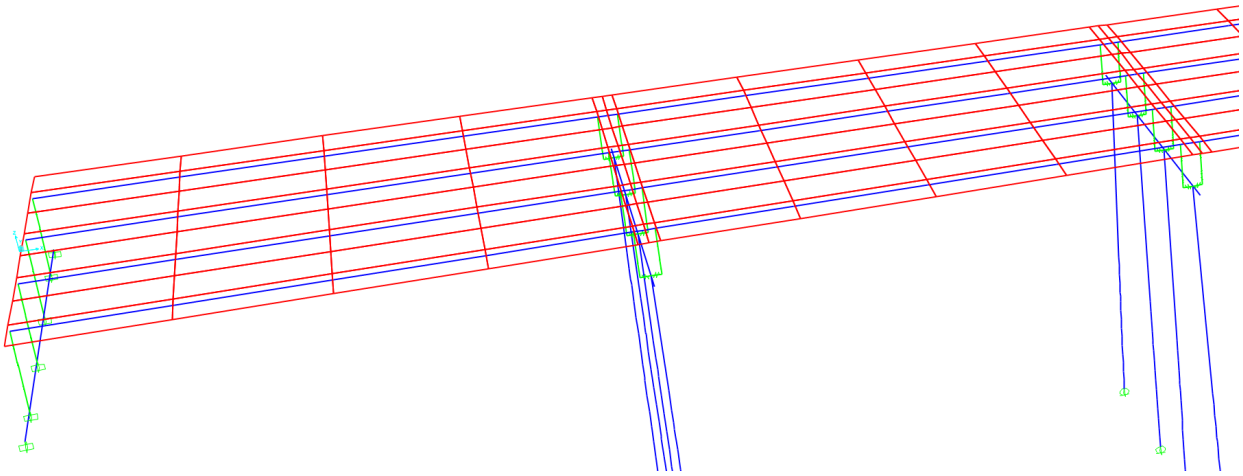

Figure 3-7 – Bridge Modeler Shell Element Discretization for Interior and Exterior Spans

The girder frame elements are automatically discretized into lengths that are the same as the shell elements above them. This results in four 117.75 in long elements and one 9 in long element for end spans and four 115.5 in long elements and two 9 in long elements for interior spans. The girders are connected to the deck via rigid links automatically defined by CSI. Figure 3-8 displays the input used in CSI to generate the superstructure. The remaining inputs not shown in this figure are: Right Overhang Data, Live Load Curb Locations, and Insertion Point Location.

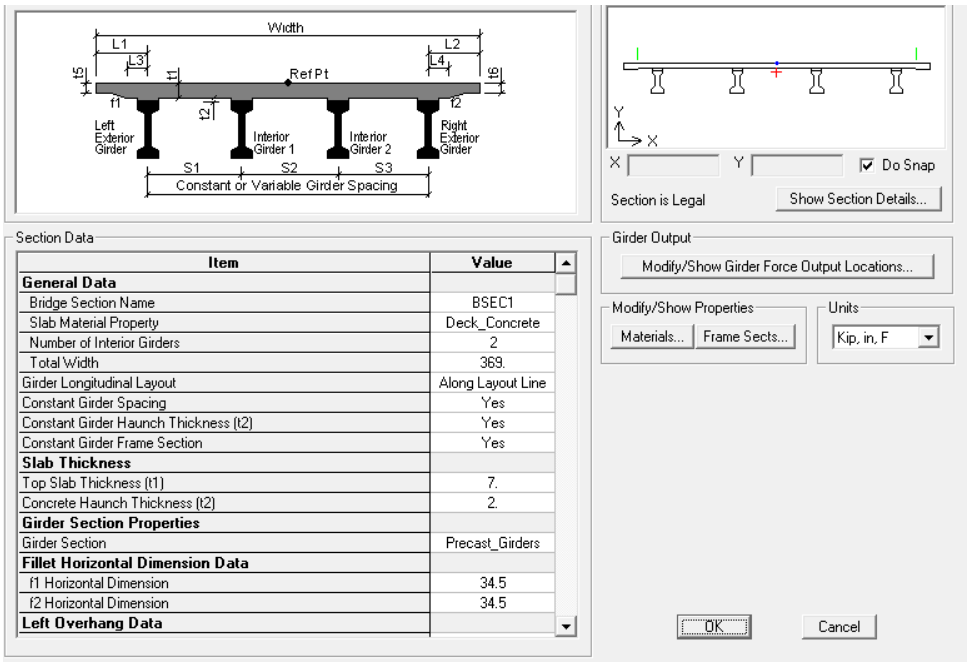

Figure 3-8 – CSiBridge Superstructure Input Dialog Box (2010)

After the superstructure was defined, the substructure components were generated using their respective input fields. The substructure includes the bearing pads, abutments and bents.

3.5.1.1 Bents

To model the bents, a frame element was created for the bent caps and frame elements were generated for the piles. The girders connecting to the bent cap were all defined as discontinuous from the superstructure. The column heights were appropriately defined based off the elevations in the plans and were fixed at ground level. In the plans for the bridge, the elevation was recorded for the top of each pile as well as the elevation for the ground line so it was known how long to define each pile.

For the encased piles, the section designer was required to achieve the proper geometry, as this section type is not a predefined frame section. Creating the piles in this manner required a verification of the cross section behavior to ensure it was behaving as intended. To accomplish this, a beam was created with the same geometry and material properties in SAP. It was fixed at one end and free at the other. A load of 1 kip was applied to the free end of the beam, and the resulting displacement is shown in Figure 3-9.

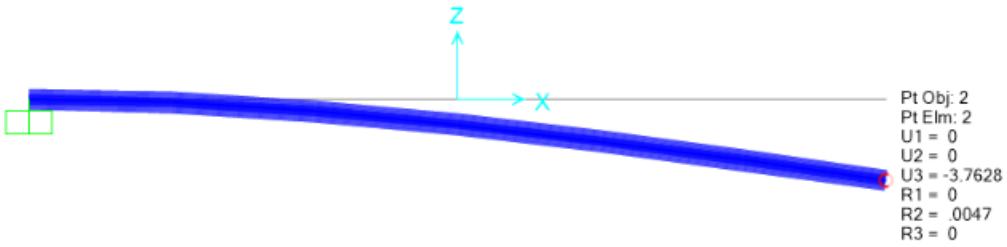

Figure 3-9 – SAP2000 Validation of Cross-Sectional Geometry of Pile

The deflection computed by SAP at the free end was 3.76 inches and the deflection computed by hand, considering flexural only deformations, was 3.71 inches. When computing by hand, the deflection equation used was

$$\Delta = \frac{PL^3}{3E_{concrete}I_{transformed}} \qquad \text{Equation 3-1}$$

Where

$$P = 1\ kip$$

$$L = 1200\ inches$$

$$E_{concrete} = 3320\ ksi$$

$$I_{transformed} = 46722\ in^4$$

Since the deflection reported by SAP was less than 1.5 percent greater than the flexure-only calculation, this method of defining the encased piles in CSI was deemed acceptable. The piles of bents 3 and 4 did not have to be verified since they were predefined sections in the software.

3.5.1.2 Abutments

The next substructure items defined were the abutments. These were frame elements that match the geometry of the abutment grade beam. The wall behind this beam was neglected in the model as were the piles since it was assumed the abutment was completely fixed. The connection to the girders was defined as "Connect to Girder Bottom Only." The bottom of this beam was defined as fixed.

3.5.1.3 Bearing Pads

The stiffness of the bearing pads were instrumental in how the load would be transferred from the superstructure to the substructure. Therefore, much effort was placed in defining this properly in the model and later calibrating to match the field results. In this bridge, elastomeric

bearing pads, type 2, mark B1 with a total thickness of 0.75 in, length of 14.5 in and width of 9.0 in were used. There are two individual layers of elastomer and one 12-gauge steel shim plate between the layers. To model the properties of the bearing pad and represent the girder end fixities defined in the plans, three types of bearings were created in CSI. The fixities that had to be accounted for were

1. Expansion with no bolts to resist transverse movement, no direction fully restrained in this setup. Used on interior girders on ends designated expansion in the plans.
2. Expansion with bolts that provided transverse resistance, restraining only transverse translation. Used on exterior girders on ends designated expansion in the plans.
3. Fixed, restraining transverse and longitudinal translation. Used on interior and exterior girders as designated in the plans.

Using the equations defined in Chapter 2.6 for the pads and the bolt stiffness equation discussed below, the stiffness values were computed. For these equations, two characteristics of the bearing pad had to be assumed. The shear modulus of the elastomer was assumed to be 0.135 ksi and the modulus of elasticity was assumed to be 30 ksi as discussed in Chapter 2.6. The stiffness calculation for the girder ends that contained bolts included the shear and flexural resistance from the bolt in addition to the pad. The two components of the bolt stiffness act in series and Equation 3-2 is how the stiffness for a single bolt was calculated.

$$\frac{1}{k_{bolt}} = \frac{1}{k_{flexure}} + \frac{1}{k_{shear}} \qquad \text{Equation 3-2}$$

Where

$$k_{flexure} = \frac{3EI}{L^3} \qquad \text{Equation 3-3}$$

$$E = 29000\ ksi$$

$$I = 0.049\ in^4$$

$$L = 0.75\ in$$

$$k_{shear} = \frac{9}{10} * \frac{GA}{L} \qquad \text{Equation 3-4}$$

$$G = 11600\ ksi$$

$$A = 0.785\ in^2$$

$$L = 0.75\ in$$

With there being a bolt on each side of the girder acting in parallel with the bearing pad, the bolt stiffness value was doubled and added to the stiffness of the pad alone. A summary of the stiffnesses used are presented in Table 3-1.

Table 3-1 – Bearing Pad Stiffness Definitions for Girder End Fixities

Girder End Condition	Stiffness values (k/in)			Stiffness (k-in/rad)
	Longitudinal Direction	Transverse Direction	Vertical Direction	Rotation about Transverse Axis
Expansion with bolts	23.5	10000	5220	35240
Expansion, no bolts	23.5	23.5	5220	35240
Fixed	10000	10000	5220	35240

With the bearing pads defined properly, at this phase Figure 3-10 depicts the model upon completion of the preliminary stages of modeling utilizing the advantages of CSI. From here, this model was exported to SAP for refinement and to begin analysis.

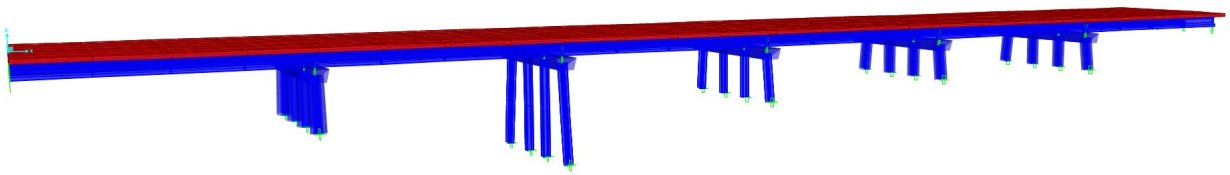

Figure 3-10 – Initial Analytical Model as Constructed in CSI

3.6 REFINEMENT OF MODEL IN SAP2000

It was determined that the entire length of the pile should be included and the influence from the soil along the pile modeled as well. After increasing the length of the piles to reflect their full length, the pile fixity was changed from completely fixed to restrained in the transverse and vertical directions and a spring added at the tip for partial fixity in the longitudinal direction. In addition, springs were added along the length of the pile to provide longitudinal stiffness, the amount of springs will be discussed in Chapter 3.6.1. To generate the soil springs, FB-MultiPier was utilized to obtain P-y curves and create equivalent springs from this information. This procedure is presented in Chapter 3.6.1. Furthermore, in CSI the correct batter would not stay applied to the outer piles, so the appropriate slope of 1.5/12 was applied. Another modification was applied to the pile heights of bent 4, these were altered to better match the field conditions as

they varied from the plans. It was observed in the field that the ground level was no longer uniform at each pile. To obtain a more accurate ground level elevation for current conditions, the 1 ft increments that were marked on the piles while being driven were used. The 1 ft increments indicated how many feet from that line to the tip of the pile. Since the tip elevation is indicated in the plans, the amount of the pile below the ground line could be obtained based on what markings were visible in the field. The final major change in the model in SAP was in the bearing pads and their stiffnesses.

3.6.1 FB-MultiPier P-y Curve Generation for Soil Springs

For each bent, a model was created in FBMP. The boring log provided in the plans (ALDOT 2013) contained the information to create an accurate soil profile. The piles were discretized into 8 nodes along the free length and 16 nodes along the embedded length. Figure 3-11 and Figure 3-12 are representative of all 6 bents. All models can be found in Appendix A as well as the inputs for the soil properties.

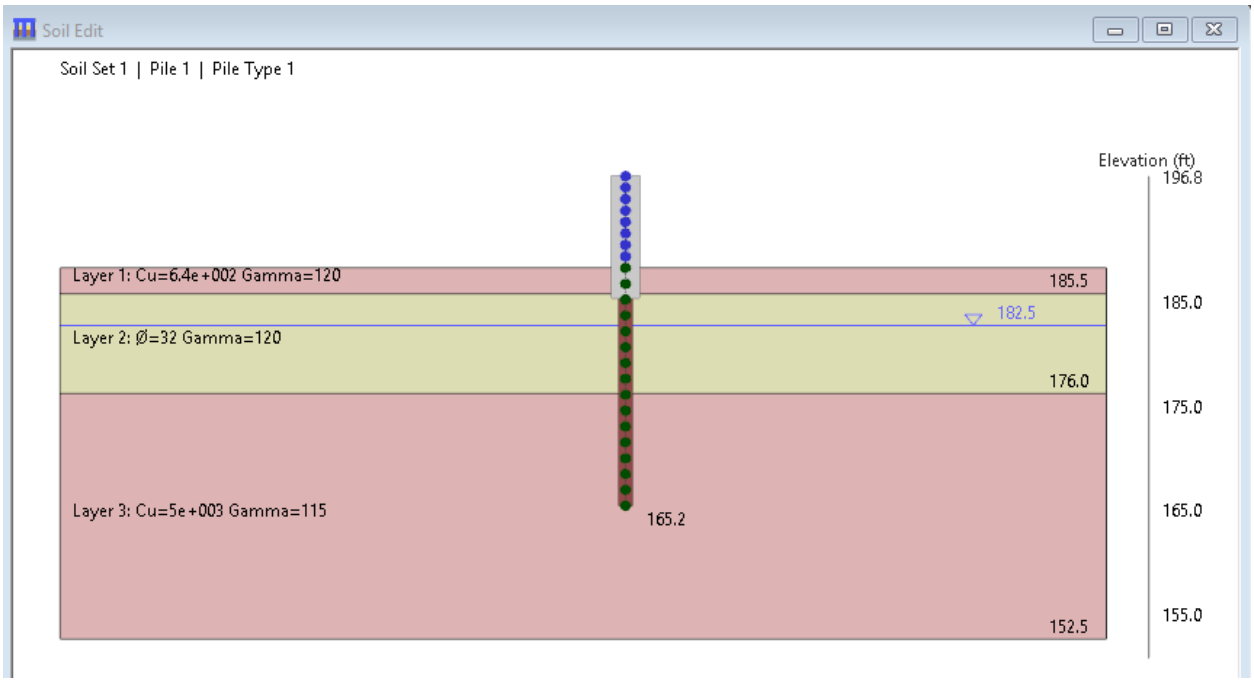

Figure 3-11 – Soil Profile and Elevations for Bent 2

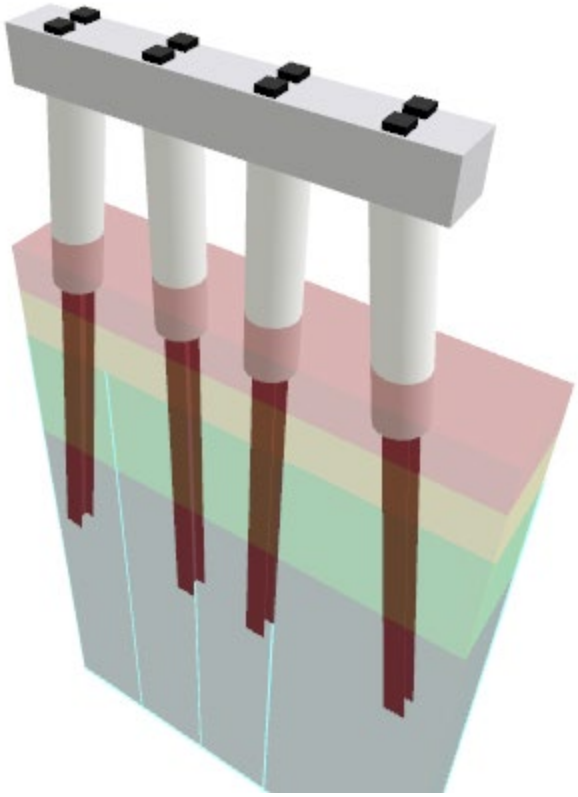

Figure 3-12 – 3-D View of Bent 2 in FB-MultiPier

Once the bent geometry and soil properties were input, FBMP automatically generates soil resistance plots for each layer and pile segment. Figure 3-13 is an example of the output for a P-y curve. For every pile, every soil layer, and both pile segments if evaluating the encased piles, a P-y curve was generated.

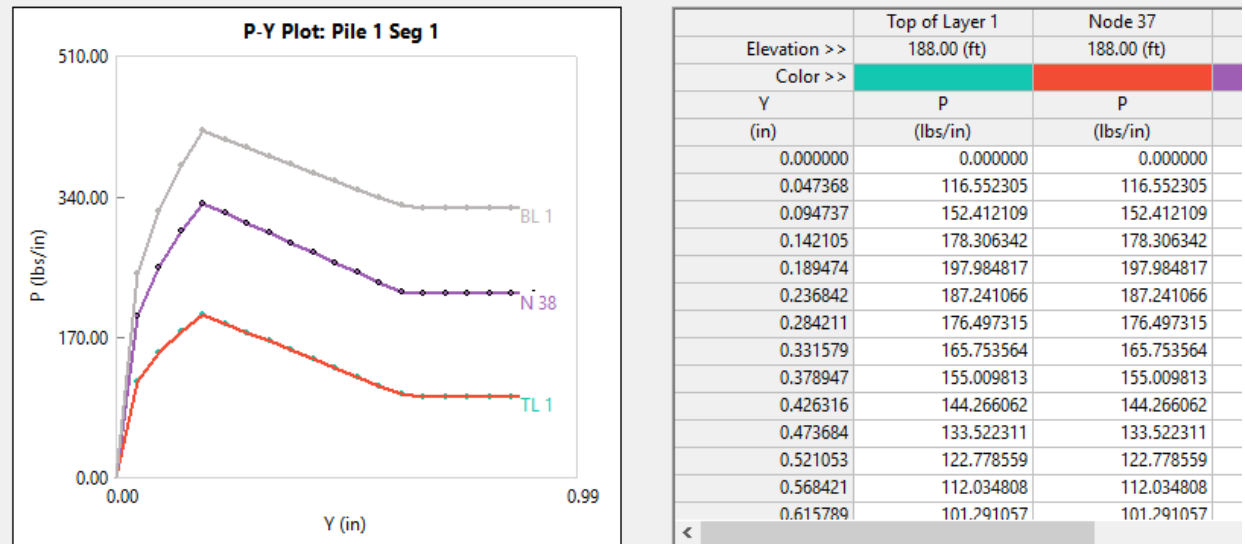

	Top of Layer 1	Node 37
Elevation >>	188.00 (ft)	188.00 (ft)
Color >>		
Y	P	P
(in)	(lbs/in)	(lbs/in)
0.000000	0.000000	0.000000
0.047368	116.552305	116.552305
0.094737	152.412109	152.412109
0.142105	178.306342	178.306342
0.189474	197.984817	197.984817
0.236842	187.241066	187.241066
0.284211	176.497315	176.497315
0.331579	165.753564	165.753564
0.378947	155.009813	155.009813
0.426316	144.266062	144.266062
0.473684	133.522311	133.522311
0.521053	122.778559	122.778559
0.568421	112.034808	112.034808
0.615789	101.291057	101.291057

Figure 3-13 – P-y Curve for the Nodes along the Encased Portion of the Pile within Layer 1

It was assumed that the soil-structure response remained linear under vehicular braking forces; therefore, to compute the spring stiffness all that was required was the slope of the linear portion of the P-y curve and the tributary length pile for each node. Table 3-2 gives an example of how the curve data was used to generate the springs. This procedure was followed for every bent, then the piles in the SAP model were discretized so that the elevations of the springs corresponded in both models and the springs defined accordingly.

Table 3-2 – Soil Layer 1 Spring Stiffness Computed from P-y Curve Data

Soil Layer 1 (Encased)									
	Top of Layer 1	Trib. Length (ft)	Elastic Region Slope for TL1	Node 38	Trib. Length (ft)	Elastic Region Slope for N38	Bottom of Layer 1	Trib. Length (ft)	Elastic Region Slope for BL1
Elevation	188.00 (ft)	0.765		186.47 (ft)	1.25		185.50 (ft)	0.485	
Y	P	P*TL		P	P*TL		P	P*TL	
(in)	(lbs/in)	(lbs)	(lbs/in)	(lbs/in)	(lbs)	(lbs/in)	(lbs/in)	(lbs)	(lbs/in)
0.047368	116.552305	1069.95	22588	196.493178	2947.40	62223	246.890714	1436.90	30335

To confirm the accuracy of these calculations, a static analysis was performed in FBMP. A load of 10 kips was applied to the center of the bent cap in the y-direction and lateral pile displacement results were generated. Figure 3-14 shows the discretized wire-frame version of bent 2 with the load applied and Figure 3-15 is a representation of the lateral deflection results obtained.

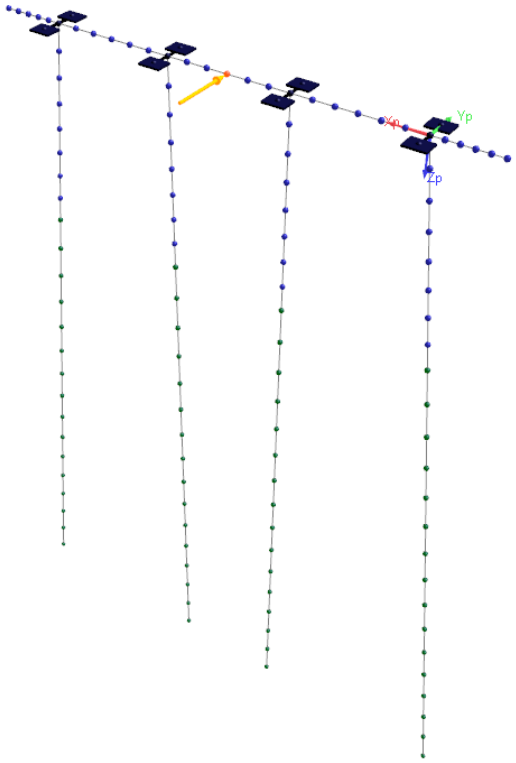

Figure 3-14 – FBMP Model of Bent 2 with 10 kips Applied to the Bent Cap

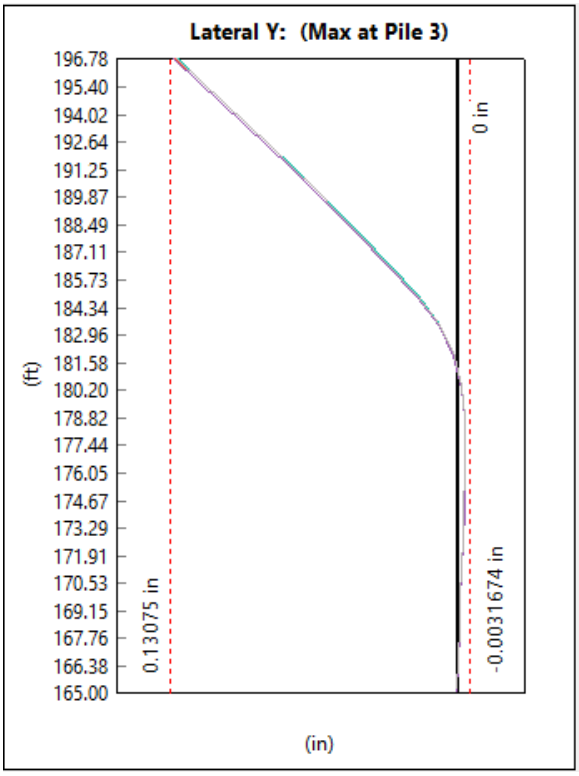

Figure 3-15 – Lateral Pile Displacements for all Piles in Bent 2

After this was completed in FBMP, the behavior of the springs needed to be checked in SAP. Each bent was isolated from the rest of the bridge in its own model and 10 kips was applied to the center of bent cap, in the same position as in FBMP. The displacement results from both models were graphed on the same plot to determine correlation. Figure 3-16 is bent 2 with the springs added along the pile length and the 10 kip load applied to the bent cap. Figure 3-17 shows the displacements along the length of the left-most pile for both models and how well they match one another.

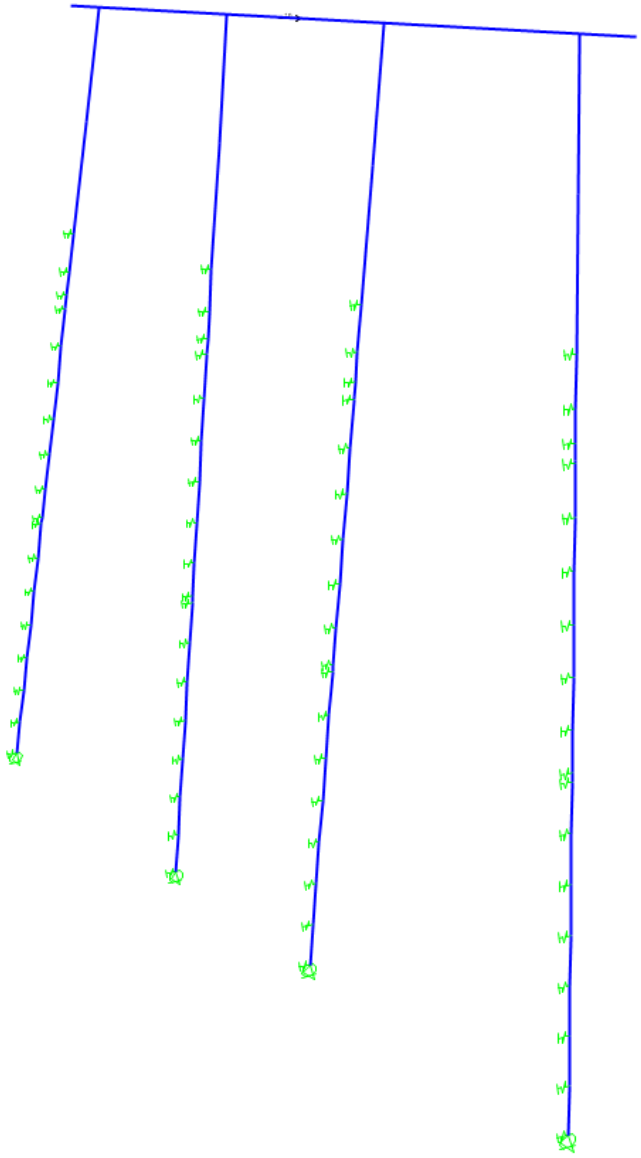

Figure 3-16 – Individual Model of Bent 2 for Static Loading Deflection Analysis

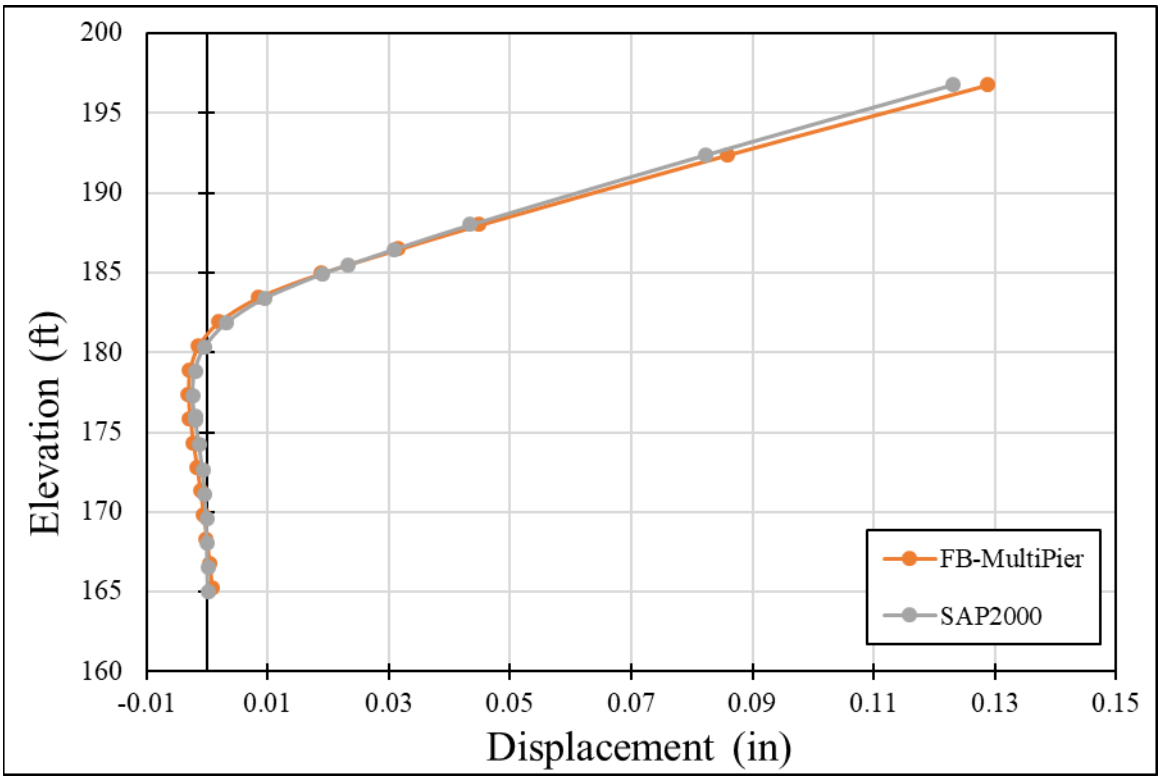

Figure 3-17 – Deflection Comparisons for Pile 1 of Bent 2

This verification was done for all 4 piles in all 5 bents, the results of which can be found in Appendix A. Pile 1 refers to the outer left pile, pile 2 is the middle-left pile, pile 3 is the right-middle pile, and pile 4 is the outer right pile.

3.6.2 Calibration of the Bearing Pad Stiffnesses

After comparing initial results from the static tests in the model, the stiffnesses of the bearing pads required adjustment to better represent what was happening in the field tests. When comparing joint displacements to field data, it was shown that the actual fixity of all the girders was closer to a version of expansion definitions 1 and 2, depending on interior or exterior girders, as defined in Chapter 3.5.1.3 for all joints rather than some being fixed and some being expansion as designated in the plans. The displacements of the girders relative to the bent caps were not matching expected values, and this was improved when all joints were changed to the appropriate expansion stiffness. This is a better representation of what was observed in the field. While in the field for testing it was realized that the nuts on the bolts were not tightened at either the fixed or expansion ends of any of the spans. Without engaging the bolt through a snug tight nut, movement of the clip and ultimately the girder is permitted.

To determine the appropriate longitudinal stiffness to define all of the bearing pads, a series of different versions of the model where only the pad stiffness was changed were run so that the errors could be analyzed and reduced. By running models that varied the longitudinal stiffness from 23.5 k/in to 50 k/in, it was determined that 45 k/in produces the least sum of the squared error (SSE) value for span displacements. Varying the stiffness from 23.5 k/in to 50 k/in was done after 50 k/in was chosen to see how displacements compared to 23.5 k/in. A boundary needed to be created within which a reasonable amount of stiffnesses could be modeled to reduce error but be too arduous of a process to obtain a stiffness value for all the bearing pads. Table 3-3 includes the SSE for each stiffness value and span. Figure 3-18 illustrates how the SSE was relatively insensitive to pad stiffness for values between approximately 42 k/in and 50 k/in. Therefore, any value in this range is acceptable and should not alter the displacement or acceleration results significantly.

Table 3-3 – Longitudinal Stiffnesses and the Corresponding Sum of the Error Squared

Stiffness	**23.5 k/in**	**30 k/in**	**35 k/in**	**38 k/in**	**40 k/in**	**42 k/in**	**45 k/in**	**50 k/in**
SSE	0.01300	0.00681	0.00495	0.00439	0.00416	0.00402	0.00392	0.00397

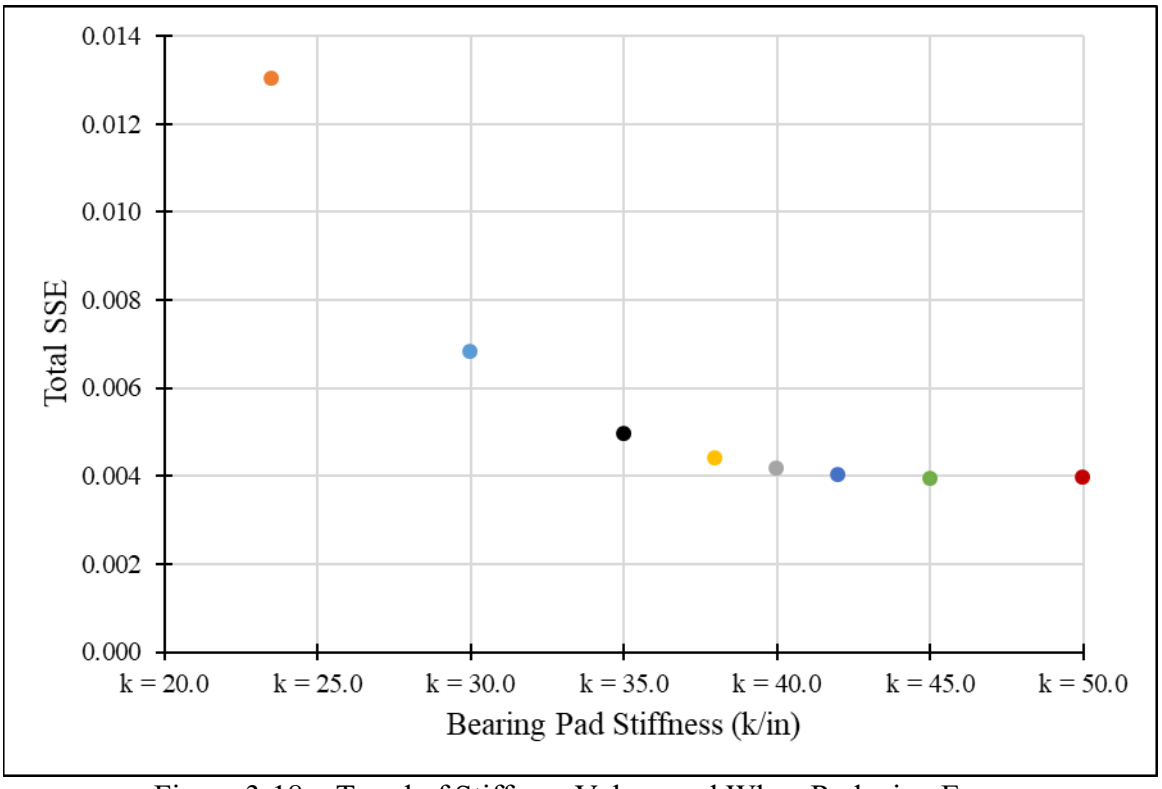

Figure 3-18 – Trend of Stiffness Values and When Reducing Error

After these adjustments were made, the final image of the model is as shown in Figure 3-19. The elements protruding from spans 2, 3 and 5 are weightless, rigid elements only intended to provide the necessary vertical offset for the mass of the truck when applied to the bridge for the dynamic analyses. They are 6 ft tall, an approximation of the height of the center of gravity of the truck and the height to offset the truck center of gravity in the LRFD Specification Section 3.5 (AASHTO 2017).

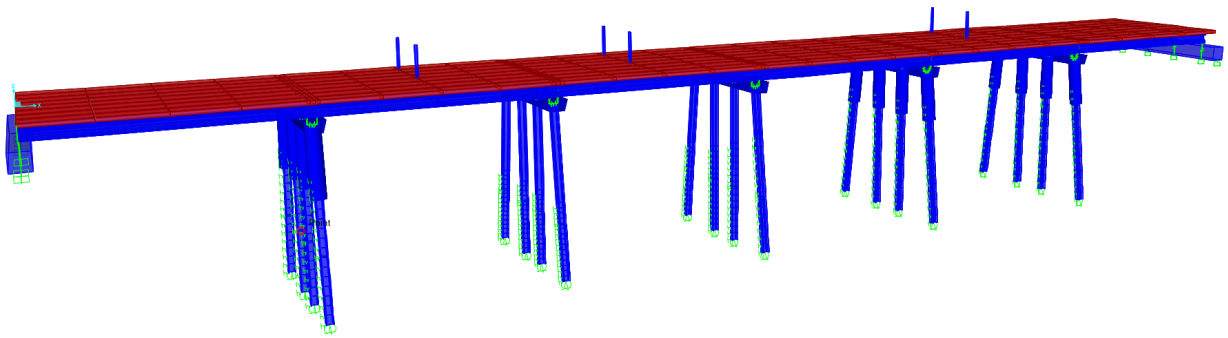

Figure 3-19 – Analytical Model After Imported to SAP and Modified

3.6.3 Static Analysis

After the field data was processed by Matt Barr (2019), it still required downsampling as discussed in Chapter 3.4. From the downsampled data, two graphs were produced for each span's test as shown in Figure 3-20 and Figure 3-21. Similar graphs for spans 2-6 can be found in Appendix B. In Figure 3-20, the black line is the force recorded in the load cell over time. The colored lines are the displacement of the girder end relative to the bent cap, this is what extension or contraction was measured by the wire potentiometer over the same time period as the load cell. The labeling of components in the legend for both graphs are as follows

- AB-1 – Abutment 1
- B-2SB – South Side of Bent 2
- B-2NB – North Side of Bent 2
- B-3SB – South Side of Bent 3
- B-3NB – North Side of Bent 3
- B-4SB – South Side of Bent 4
- B-4NB – North Side of Bent 4
- B-5SB – South Side of Bent 5

- B-5NB – North Side of Bent 5
- B-6SB – South Side of Bent 6
- B-6NB –North Side of Bent 6
- AB-7 – Abutment 7

Figure 3-21 illustrates how the bridge components displaced during loading, increasing tension in the cable connected to the load truck, and during unloading, relieving of the tension in the cable. Both loading and unloading result in linear displacements, but the slope of the two differ. For every static test, the bents or abutment supporting the span that was loaded always displaced the most.

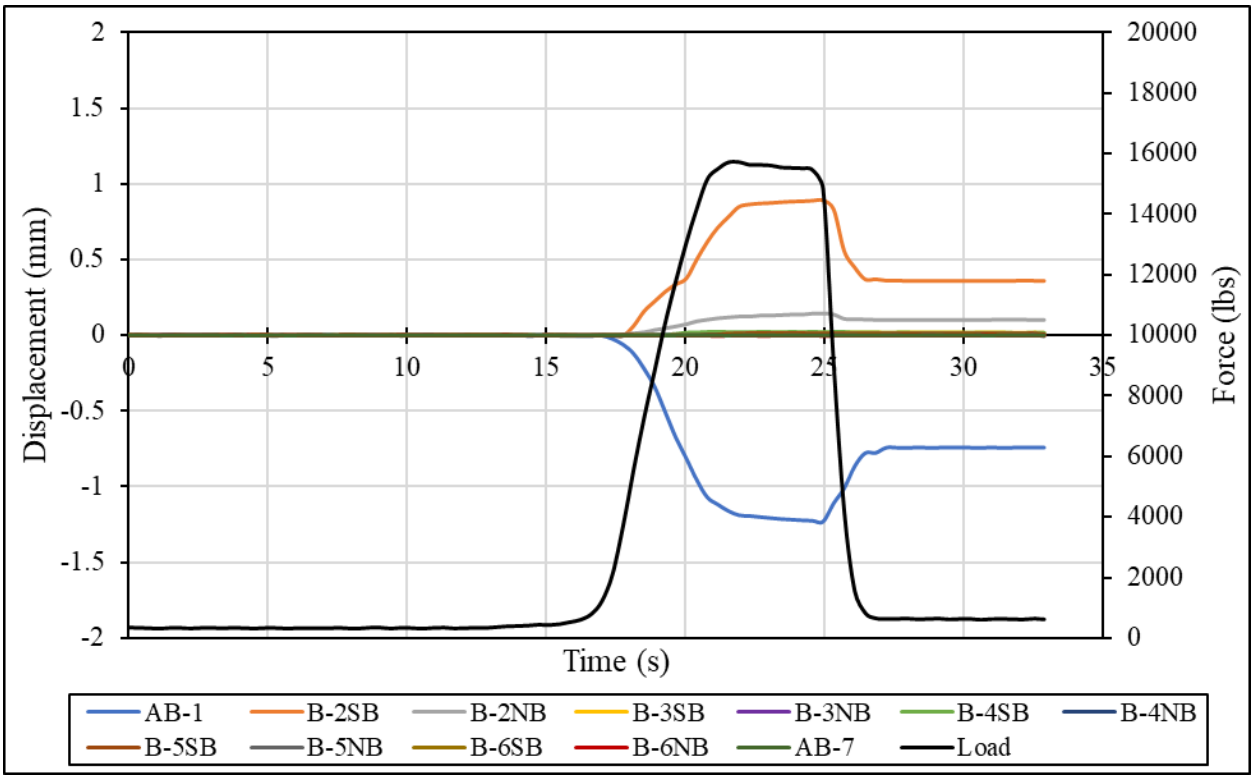

Figure 3-20 – Span 1 Displacement and Load vs Time for Static Pull Test

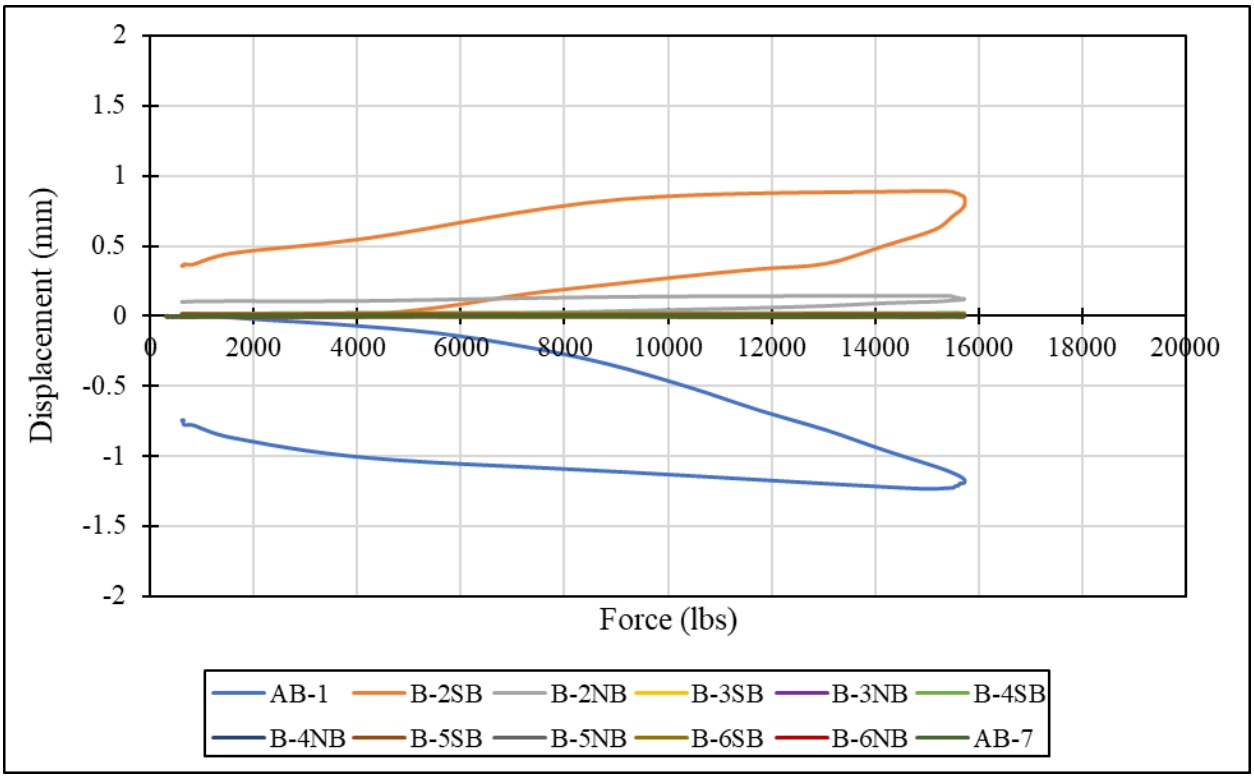

Figure 3-21 – Span 1 Displacements vs Applied Load

After reviewing the graphs, every test achieved at least 10 kips of tension with clear displacement results, based off this it was decided this would be a reasonable load to apply to the analytical model for comparisons.

Table 3-4 is the displacement data for span 1 at the measured value closest to 10 kips and this data was compared to the model displacements under 10 kips of force. The data for spans 2-5 can also be found in Appendix B. The change in force is listed also because the wire potentiometers were zeroed out between every test but the load cell was not. To account for this, the initial force recorded in the load cell was subtracted from all of the force values to get a change in force.

Table 3-4 – Wire Pot Readings and Displacements Relative to Abutment 1 for Span 1

At 10400 lbs (ΔF = 10054 lbs) applied to Span 1			
Data From Field Tests			
	Displacement of Girder End Relative to Cap (in)	Displacement Relative to AB1 (in)	
A1	-0.0199	delta_S1	-0.0199
B2S1	0.0113	delta_B2	-0.0086
B2S2	0.0019	delta_S2	-0.0068
B3S2	0.0000	delta_B3	-0.0068
B3S3	0.0001	delta_S3	-0.0067
B4S3	0.0002	delta_B4	-0.0065
B4S4	0.0000	delta_S4	-0.0065
B5S4	0.0000	delta_B5	-0.0066
B5S5	0.0000	delta_S5	-0.0066
B6S5	0.0000	delta_B6	-0.0066
B6S6	0.0000	delta_S6	-0.0067
A7	0.0000	delta_AB7	-0.0067

The wire potentiometers and accelerometers were along the left-center girder, so in the model the displacements recorded were from along the same girder-line. Additionally, the wire potentiometers were connected to an angle on the bottom of the girder and extended to a hook attached to the pedestal as shown in Figure 3-22, this had to be considered when evaluating results in the SAP model.

Figure 3-22 – Standard Wire Pot Set-Up

To account for this in the SAP model, the difference between the displacement at the top of the bearing pad link and the bottom of the bearing pad link was taken to replicate the field conditions. It was assumed there was no significant expansion or contraction of the girders when obtaining these displacement results from the model. The length of the link defined as the bearing pad was 0.75” to create the same displacement measurements in the model. Table 3-5 is representative of how the results were recorded and processed to produce values that were comparable to what was measured.

Table 3-5 – Span 1 SAP Results Processed to be Comparable to the Field Data

At 10 kips Statically Applied to Center of Span 1 in SAP Model									
Results from SAP2000 Along Girder Line 2 - All Bearing Pads 0.75"									
	Location	Joint	Global Displacement (in)	Global Rotation (rad)	Displacement between girder & support (in)	Displacement Relative to AB1 (in)		Location of Measurement	Total Displacement Relative to
AB1 (E)	Girder	135	-0.0399	-0.000014	-0.0399	delta_S1	-0.0399	$\Delta S1_a$	-0.0399
	Support	29	0.0000	0.000000				-	-
B2 SP1 (F)	Girder	151	-0.0403	0.000001	0.0158	delta_B2	-0.0241	$\Delta S1_b$	-0.0403
	Support	49	-0.0245	-0.000143				$\Delta B2_a$	-0.0245
B2 SP2 (E)	Girder	153	-0.0197	0.000006	0.0048	delta_S2	-0.0193	$\Delta S2_a$	-0.0197
	Support	48	-0.0245	-0.000143				$\Delta B2_b$	-0.0245
B3 SP2 (F)	Girder	191	-0.0195	0.000000	0.0049	delta_B3	-0.0144	$\Delta S2_b$	-0.0195
	Support	254	-0.0147	-0.000063				$\Delta B3_a$	-0.0147
B3 SP3 (E)	Girder	193	-0.0113	0.000004	0.0034	delta_S3	-0.0110	$\Delta S3_a$	-0.0113
	Support	56	-0.0147	-0.000063				$\Delta B3_b$	-0.0147
B4 SP3 (F)	Girder	211	-0.0111	-0.000001	0.0034	delta_B4	-0.0076	$\Delta S3_b$	-0.0111
	Support	260	-0.0077	-0.000039				$\Delta B4_a$	-0.0077
B4 SP4 (E)	Girder	217	-0.0054	0.000002	0.0023	delta_S4	-0.0053	$\Delta S4_a$	-0.0054
	Support	259	-0.0077	-0.000039				$\Delta B4_b$	-0.0077
B5 SP4 (F)	Girder	235	-0.0053	-0.000001	0.0023	delta_B5	-0.0031	$\Delta S4_b$	-0.0053
	Support	273	-0.0031	-0.000019				$\Delta B5_a$	-0.0031
B5 SP5 (E)	Girder	241	-0.0021	0.000001	0.0010	delta_S5	-0.0021	$\Delta S5_a$	-0.0021
	Support	299	-0.0031	-0.000019				$\Delta B5_b$	-0.0031
B6 SP5 (F)	Girder	235-1	-0.0020	0.000000	0.0010	delta_B6	-0.0011	$\Delta S5_b$	-0.0020
	Support	334	-0.0011	-0.000007				$\Delta B6_a$	-0.0011
B6 SP6 (F)	Girder	241-1	-0.0005	0.000000	0.0005	delta_S6	-0.0006	$\Delta S6_a$	-0.0005
	Support	332	-0.0011	-0.000007				$\Delta B6_b$	-0.0011
AB7 (E)	Girder	143	-0.0005	0.000000	0.0005	delta_AB7	-0.0001	$\Delta S6_b$	-0.0005
	Support	17	0.0000	0.000000				$\Delta AB7_a$	0.0000

The 10 kip load was applied in the center of the span, pointing in the same direction as the truck was being pulled as shown in Figure 3-23, where 10 kips is applied to span 1. A static load case for each span was created so that 10 kips could be applied to each span and analyzed in the model.

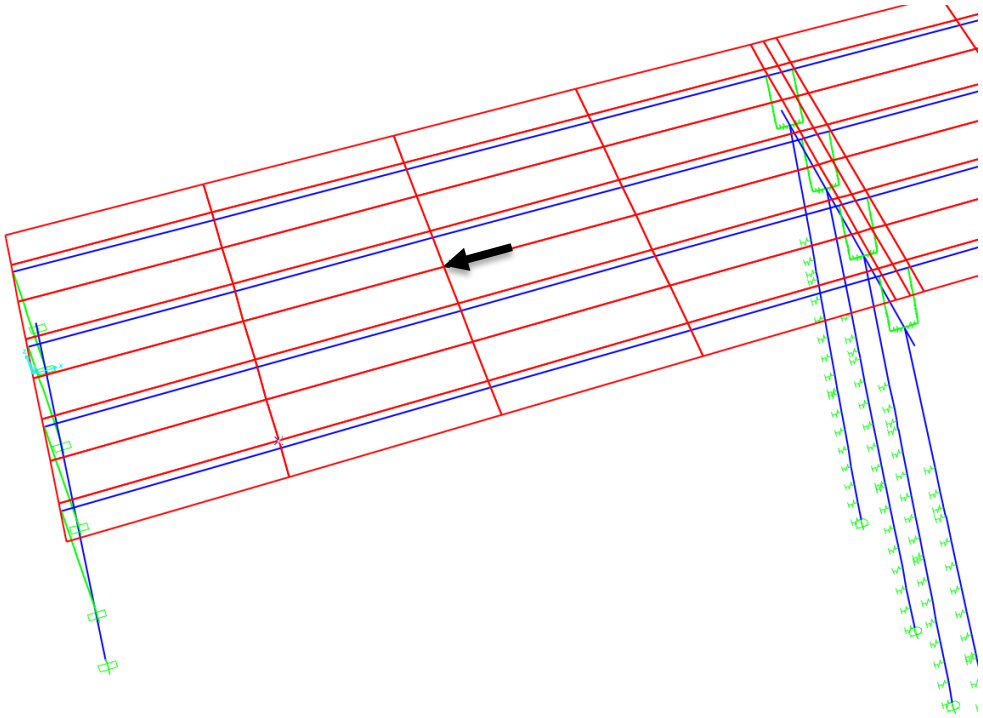

Figure 3-23 – SAP Model with 10 kip Static Load Applied to Span 1

3.6.4 Dynamic Analysis

To model the dynamic tests, the acceleration data from the field was most important. For each test, the acceleration in the longitudinal direction from the inertial measurement unit was used to obtain the braking maneuver profile. Figure 3-24 shows the IMU data from the tests that were deemed best. The designation of best was qualitative and meant: the truck approached the bridge at a constant speed and maintained this speed until reaching the span being tested, once fully in the span, the brakes were applied and a controlled stop was completed within the same span. For modeling purposes, each test was evaluated and its own braking force function defined to best match its IMU data. Figure 3-24 shows how similar the braking maneuvers were from test to test, but minor changes in intensity, build up, constant deceleration duration, and decline to zero acceleration impacted the results significantly so a single function could not be defined. In this graph, time zero is the instant that the brakes were applied so that this could be defined as a time-history analysis ramp function in SAP. On the graph, the C or R designates center or right of the span, the first number is the span stopped on and the second number is the trial number on that span.

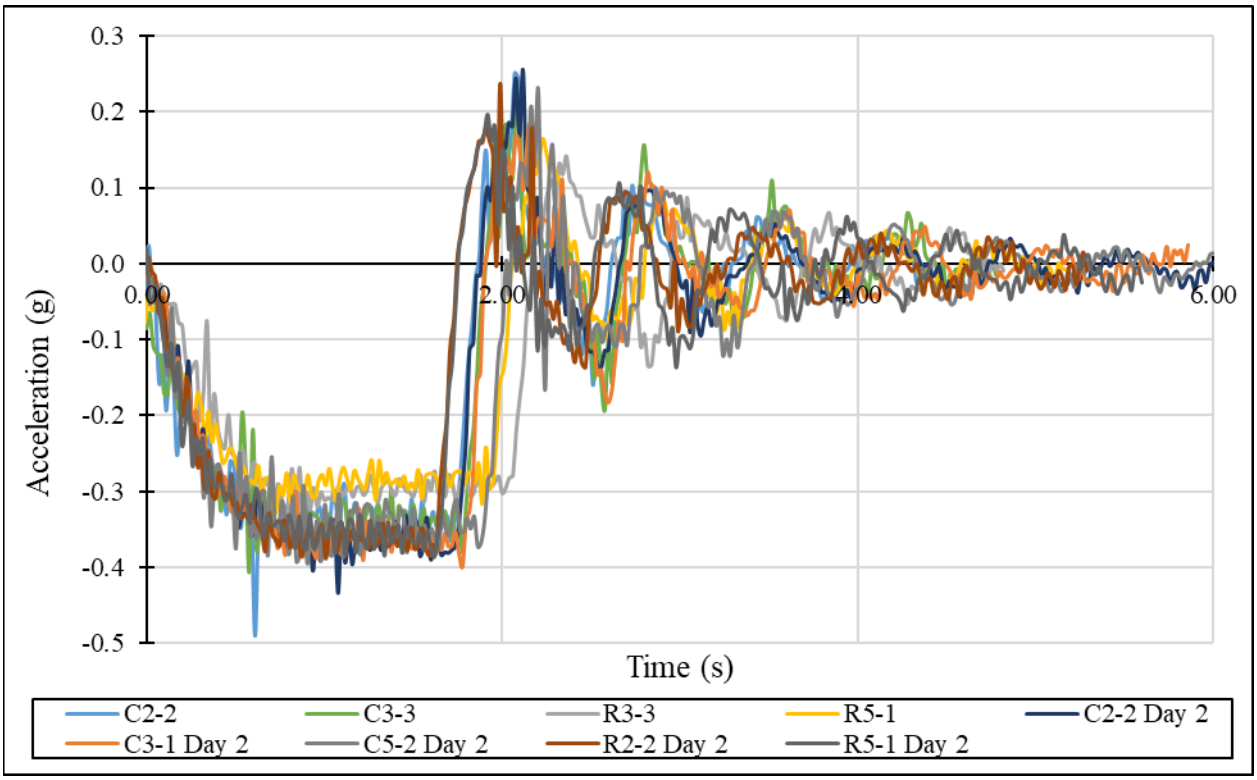

Figure 3-24 – IMU Acceleration Data for the Longitudinal Direction of the Load Truck

When comparing the measured values to the decelerations rates presented in Chapter 2.4, the correlation is good. Loaded single-unit trucks averaged 0.39g, unloaded truck tractors and single-unit trucks averaged 0.36g, and loaded truck tractors with an unbraked control trailer averaged 0.34g. The average deceleration rate for the center braking tests was 0.35g and the right-side braking tests averaged 0.30g. With the data matching the information in the literature reviewed well, this reinforced the foundational idea of this thesis that the amount of longitudinal force getting transmitted into the substructure during a braking force is dependent upon the friction between the road and tire interface. This frictional limitation results, ultimately, in the percentage of the truck weight that gets imparted on the bridge. With the data and reviewed literature greater than 0.25g, the LRFD Specification code provision would appear to be an underestimation at this point.

Figure 3-25 is a representation of how the different IMU data was defined in SAP. The test data and corresponding SAP ramp functions for every test can be found in Appendix C.

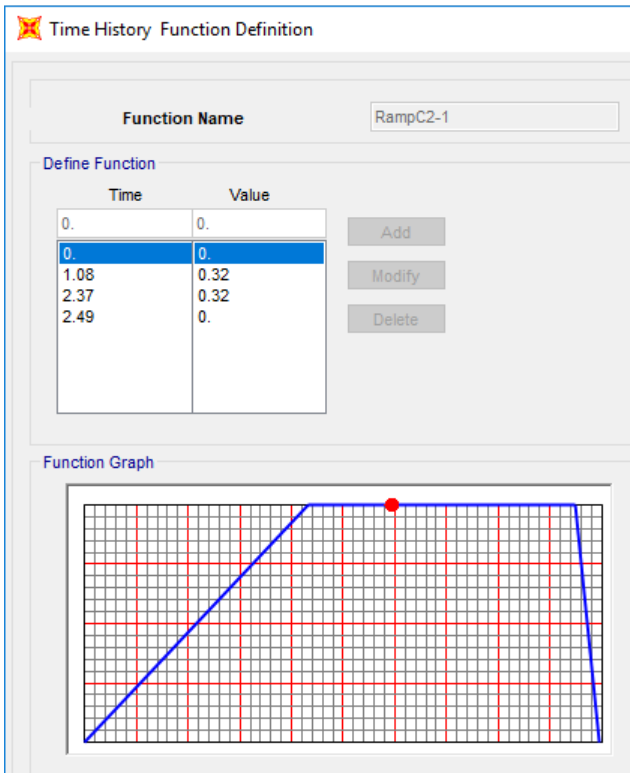

Figure 3-25 – SAP Ramp Function Defined for the Center of Span 2, Trial 1

After the ramp function was defined, it was added to the proper load case. Figure 3-26 shows the definition of the load case for the center of span 2 loading condition. Minor adjustments in rise time of the ramp resulted in changes in the results of the SAP acceleration data. This is expected based off of the findings in Chapter 2.9. By extending the ramp, there was more time before the oscillations began in the output data. Furthermore, modifying the maximum steady state deceleration resulted in changes to the magnitude of acceleration reported by the model.

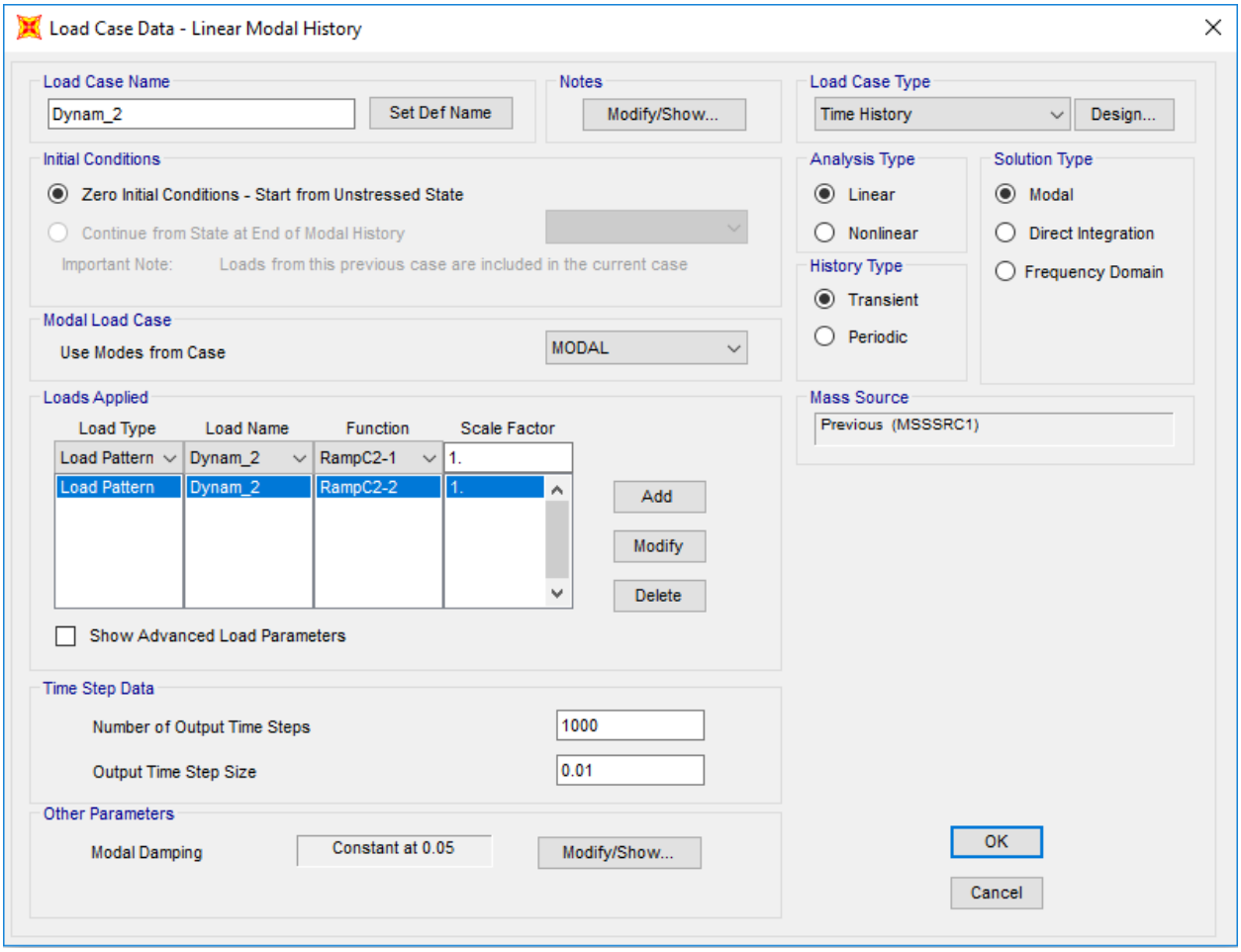

Figure 3-26 – Load Case Input for Span 2 Center Test

Every test condition had a load case defined like this, the only change was what ramp function was used and where the load was applied on the bridge deck. For the cases where the truck stopped in the center of the span, 70.2 kips was applied in the center of the deck, the same location as the static load. When the truck stopped on the right side of the deck, the 70.2 kip force was positioned on the right side of the bridge, right above the exterior girder line. During the field testing, when the truck was braking on the right side the outside wheel was kept along the stripe painted on the bridge deck which was directly above the girder line.

In a dynamic analysis, mass has to be defined properly. The barriers on both sides of the bridge deck were not modeled, but their mass could not be neglected. From the geometry of the traffic barriers and the unit weight of reinforced concrete being 150 pounds per cubic foot, it was determined that the barriers weighed 305 lbs/ft each. This was discretized into point loads that were applied to joints in the model, in units of kips, in all three directions and SAP automatically converted these weights to masses with units of k-s^2/in. The weight of the truck was applied to

the rigid elements in terms of weight in all three directions as well. The truck weight was only applied to the span that was being tested and on the center or right side depending on the test. The rigid vertical element was required to elevate the mass to 6 ft off the bridge deck, 6 ft being an approximation of the center of the mass of the truck. Figure 3-27 displays the bridge with the point masses applied along both edges for the barrier rail mass and the mass of the truck applied to a single rigid element.

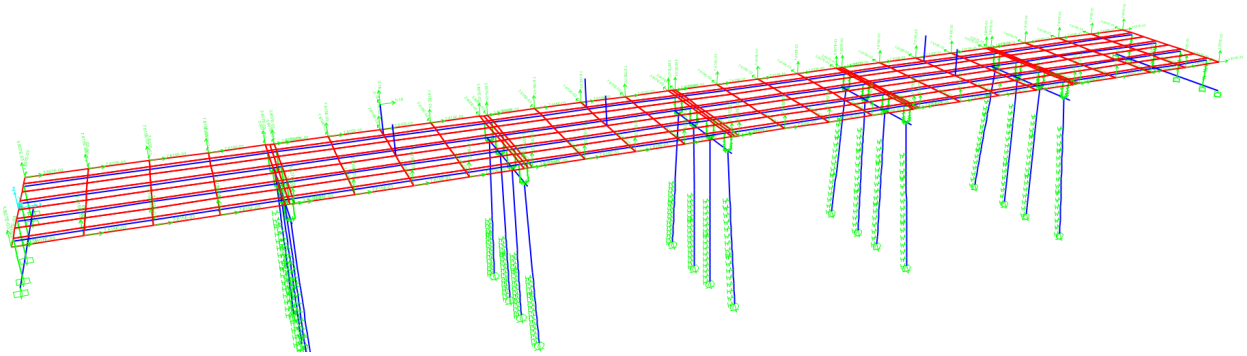

Figure 3-27 – Barrier Mass Applied along Full Length of Bridge and Truck Mass Applied to One Rigid Element

To ensure that enough of the modal mass was being included in the model, 20 modes were used. By using 20 modes, the total mass being captured in the X-direction was 93 percent. Beyond 20 modes, there was no significant increase in modal mass captured, therefore, no additional benefit to accuracy but an increase in computational duration. Throughout these 20 modes, 5 percent viscous damping was held constant. Additionally, due to limitations in the modeling software, certain time-dependent variables could not be modeled nor could they be measured in the field. Such variables include forms of hysteretic damping (friction, drag, material characteristics, etc.) instead of pure viscous damping like what is defined in SAP.

CHAPTER 4: PRESENTATION AND ANALYSIS OF RESULTS

4.1 INTRODUCTION

The analytical model results for the static and dynamic analyses are presented in this chapter. Results are presented beginning with the static model, followed by results of the dynamic testing. The main goal for the static tests was to provide a foundation for calibrating the model behavior before adding the dynamic aspects. The correlations between the model results and the field results are then evaluated. After the correlation between results are evaluated, the amount of shear force present in the bents is presented. With the ultimate goal of this project being determining the load path and intensity of the force going into the bents, observations on how the braking force is distributed are discussed.

4.2 STATIC TEST RESULTS

4.2.1 Bridge Displacements Due to Static Loading

The results presented in this section illustrate the model displacements under 10 kips statically applied to each span compared to the displacements of the real bridge. This type of comparison allowed for the bearing pad stiffness to be refined as discussed in Chapter 3.6.2. The stiffnesses played a major role in the displacement magnitudes, so with the error minimized yielding 45 k/in as the optimum value of pad stiffness, the following results are satisfactory for this analysis given the amount of unknowns and assumptions behind the creation of the model. The benefit of the static tests was to aid in the calibration of the model. By removing the dynamic variables, it is easier to isolate components that need attention and modifications to improve behavior.

Figure 4-1 through Figure 4-6 present the relative displacements of the girder ends to the bent caps versus the displacements reported by SAP, processed as discussed in Chapter 3.6.3. Only the second trial from testing on span 5 was included in these results because it yielded more realistic data than the first test. The designations for the locations in the following figures are:

- A1 – relative displacement of Span 1 girder away from top of Abutment 1
- B2S1 – relative displacement of Span 1 girder away from top of Bent 2

- B2S2 – relative displacement of Span 2 girder away from top of Bent 2
- B3S2 – relative displacement of Span 2 girder away from top of Bent 3
- B3S3 – relative displacement of Span 3 girder away from top of Bent 3
- B4S3 – relative displacement of Span 3 girder away from top of Bent 4
- B4S4 – relative displacement of Span 4 girder away from top of Bent 4
- B5S4 – relative displacement of Span 4 girder away from top of Bent 5
- B5S5 – relative displacement of Span 5 girder away from top of Bent 5
- B6S5 – relative displacement of Span 5 girder away from top of Bent 6
- B6S6 – relative displacement of Span 6 girder away from top of Bent 6
- A7 – relative displacement of Span 6 girder away from top of Abutment 7

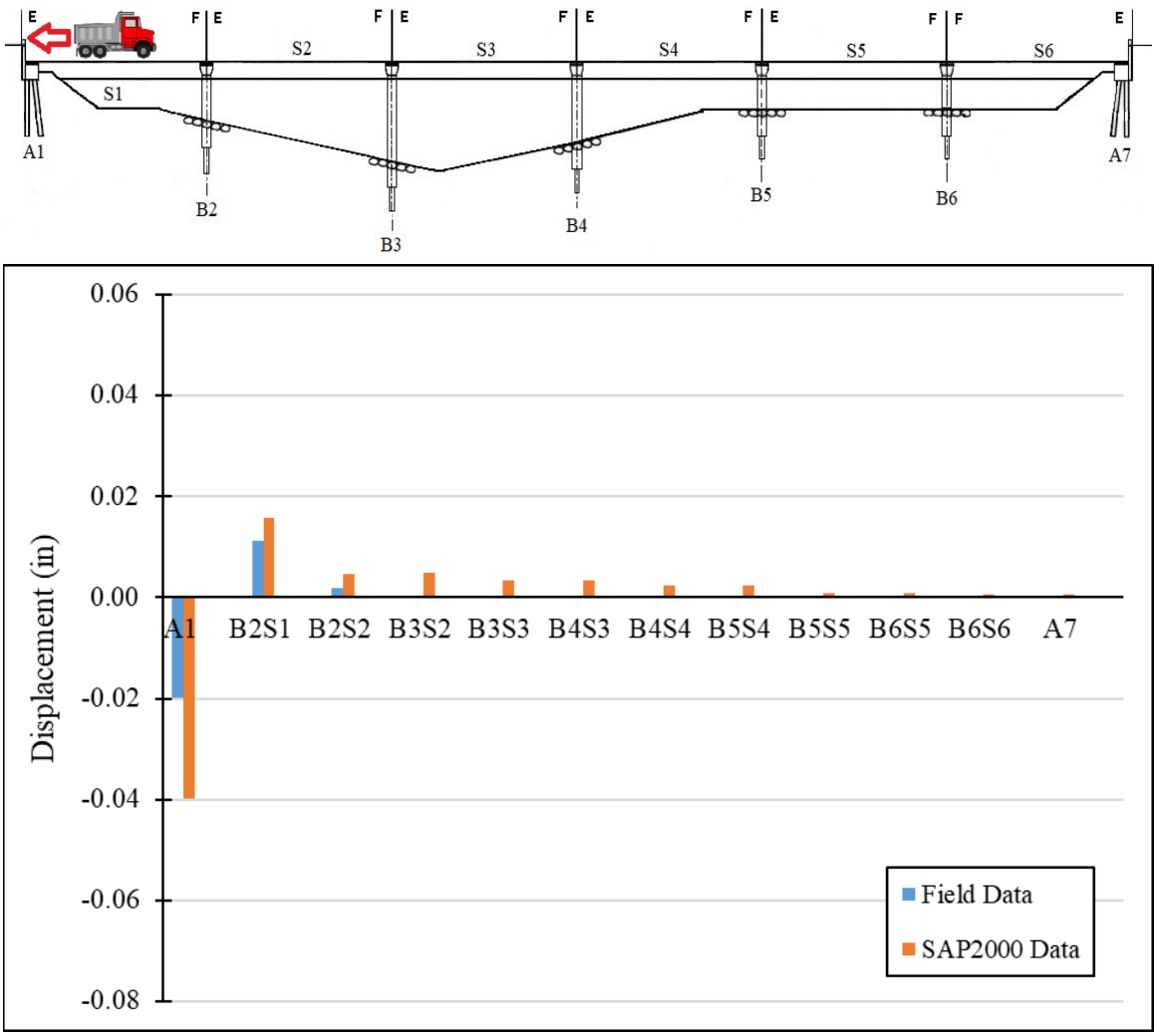

Figure 4-1 – Measured versus Model Displacements for Span 1 Static Loading

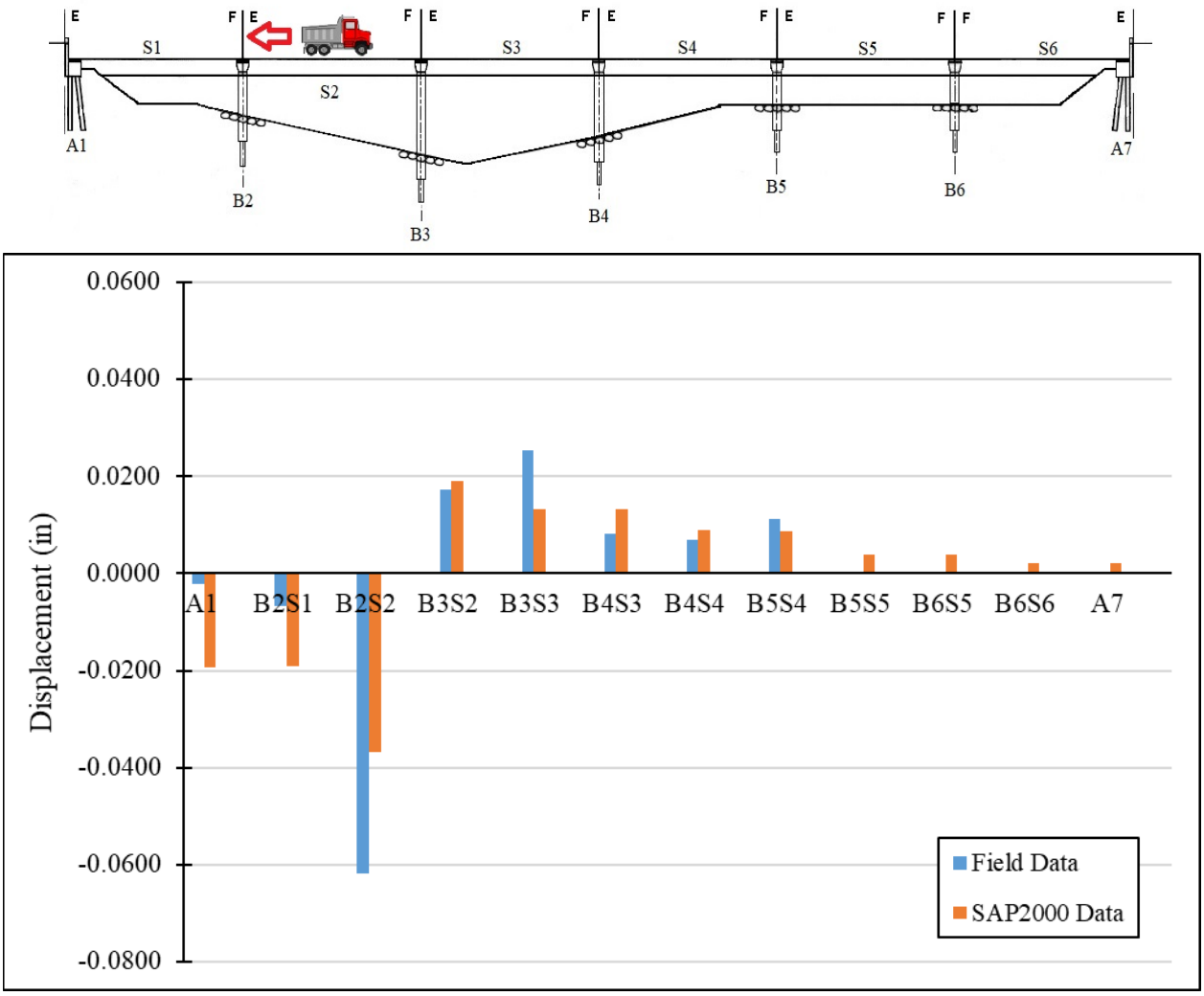

Figure 4-2 – Measured versus Model Displacements for Span 2 Static Loading

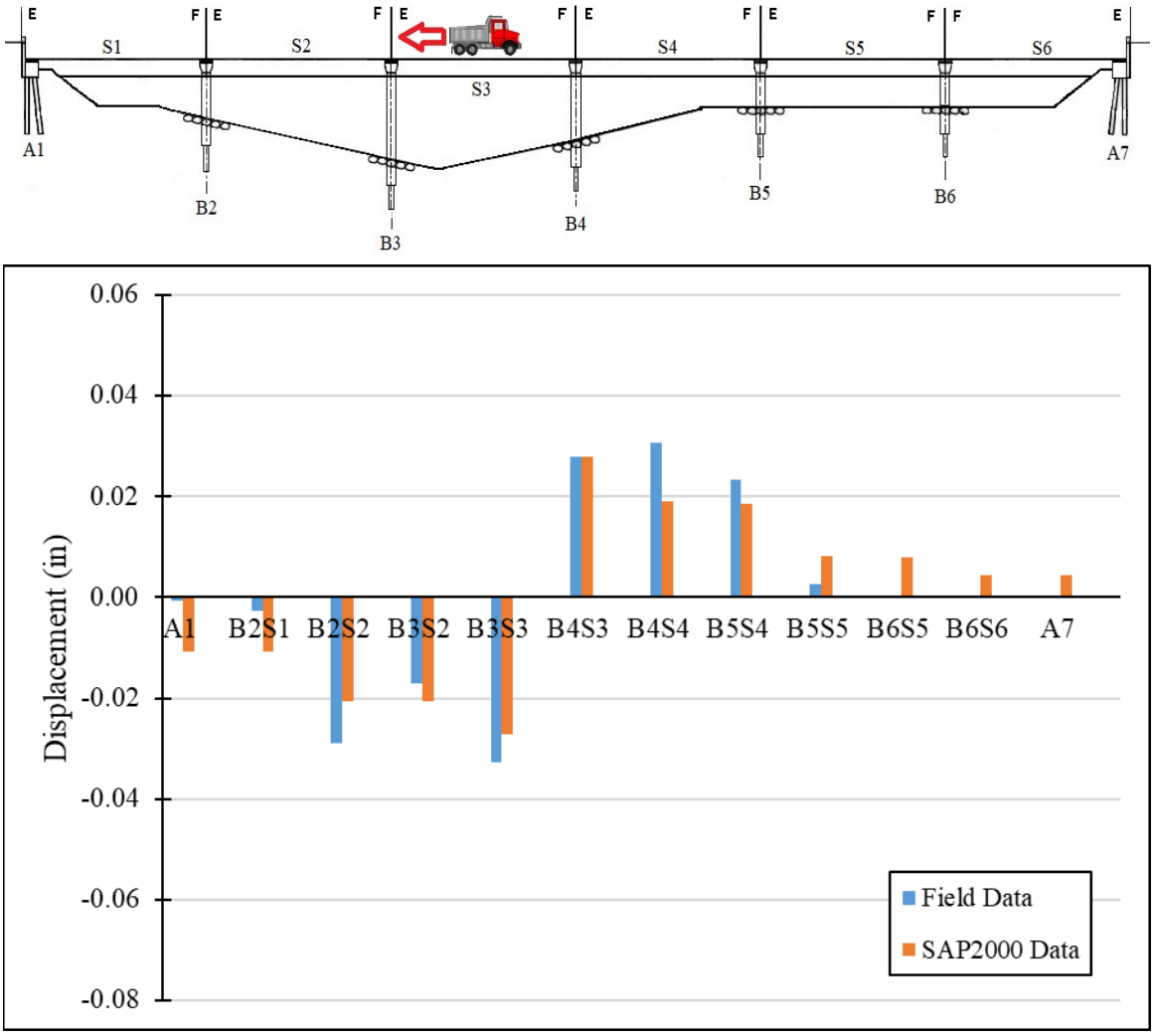

Figure 4-3 – Measured versus Model Displacements for Span 3 Static Loading

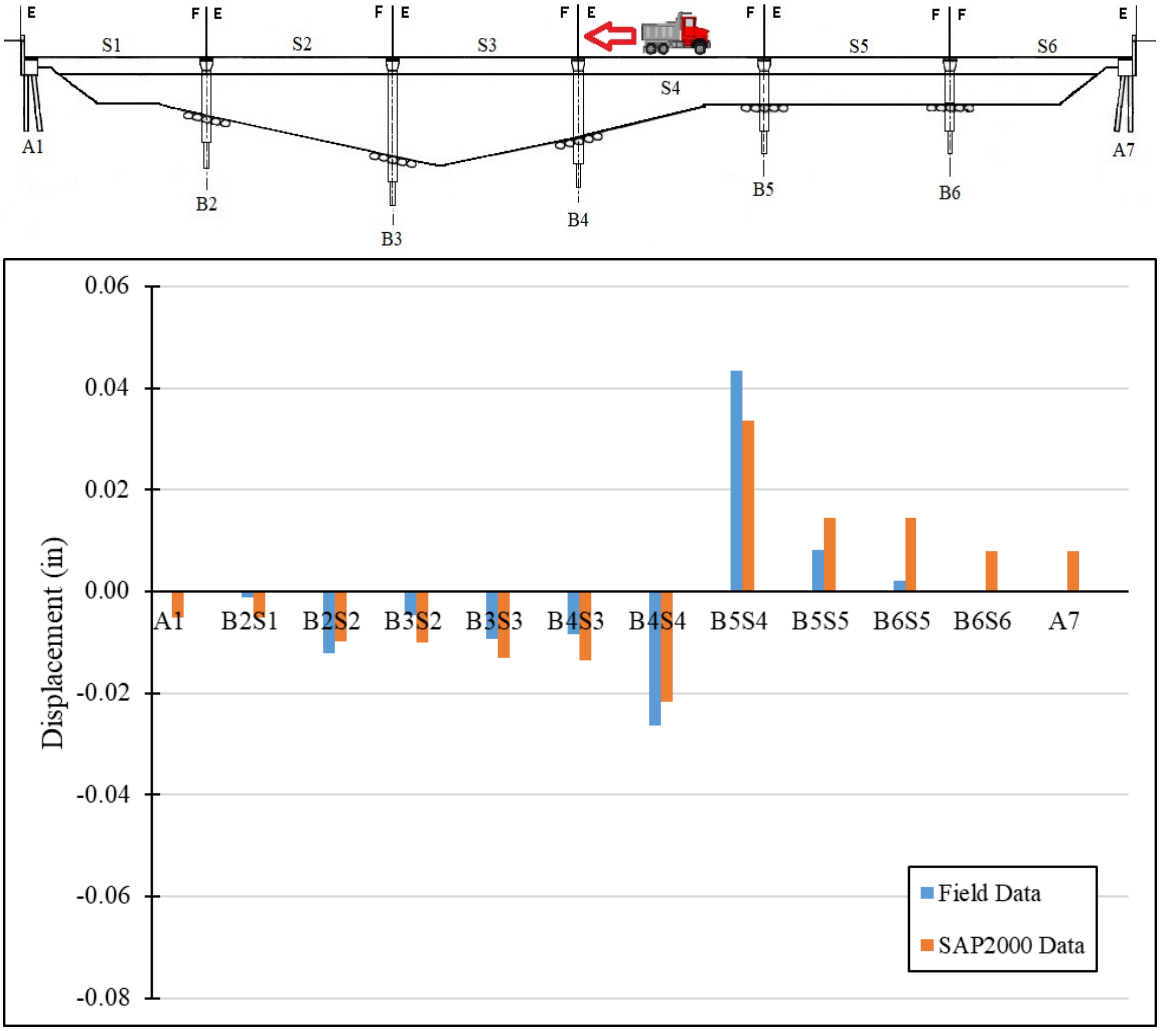

Figure 4-4 – Measured versus Model Displacements for Span 4 Static Loading

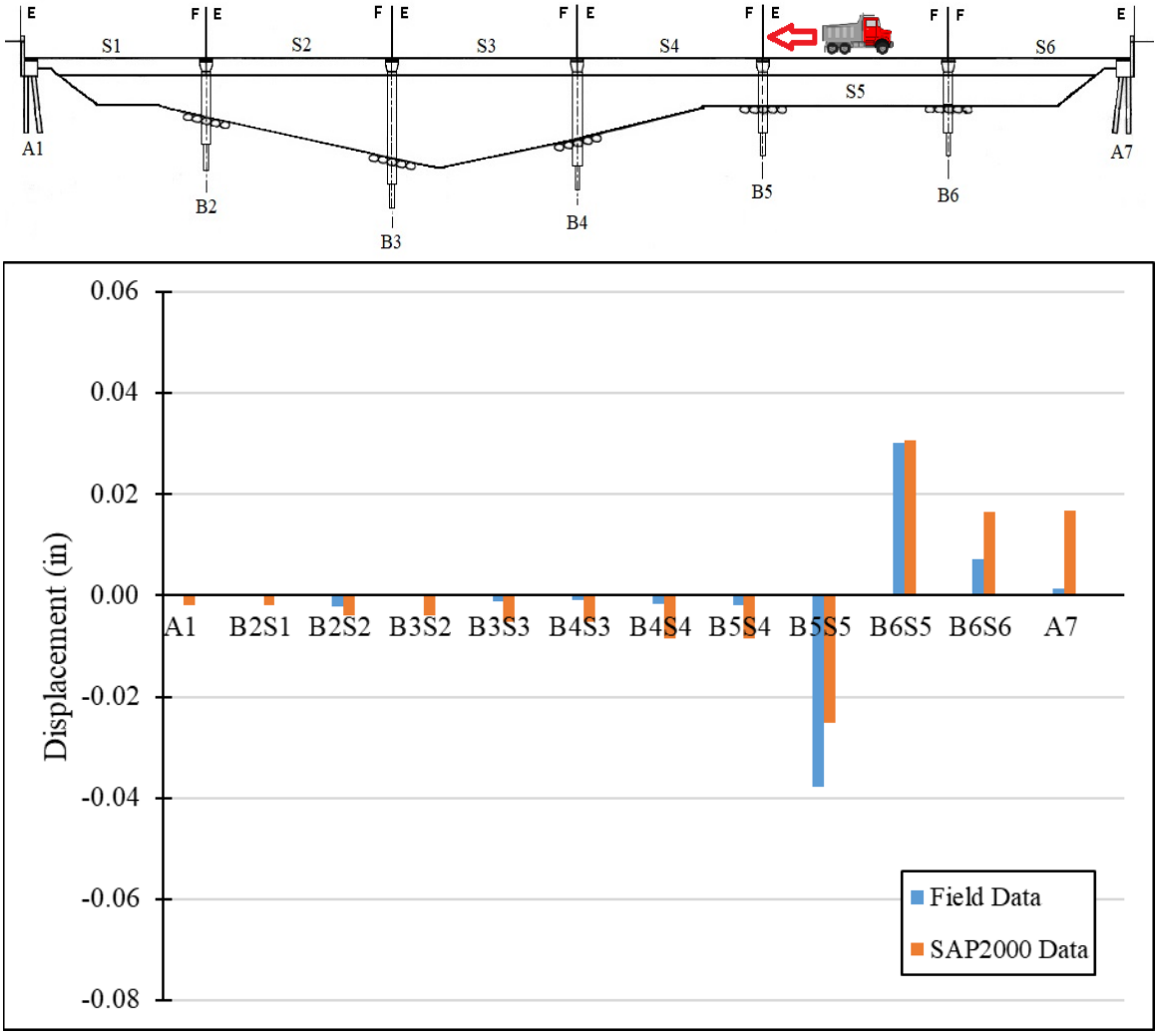

Figure 4-5 – Measured versus Model Displacements for Span 5 Static Loading

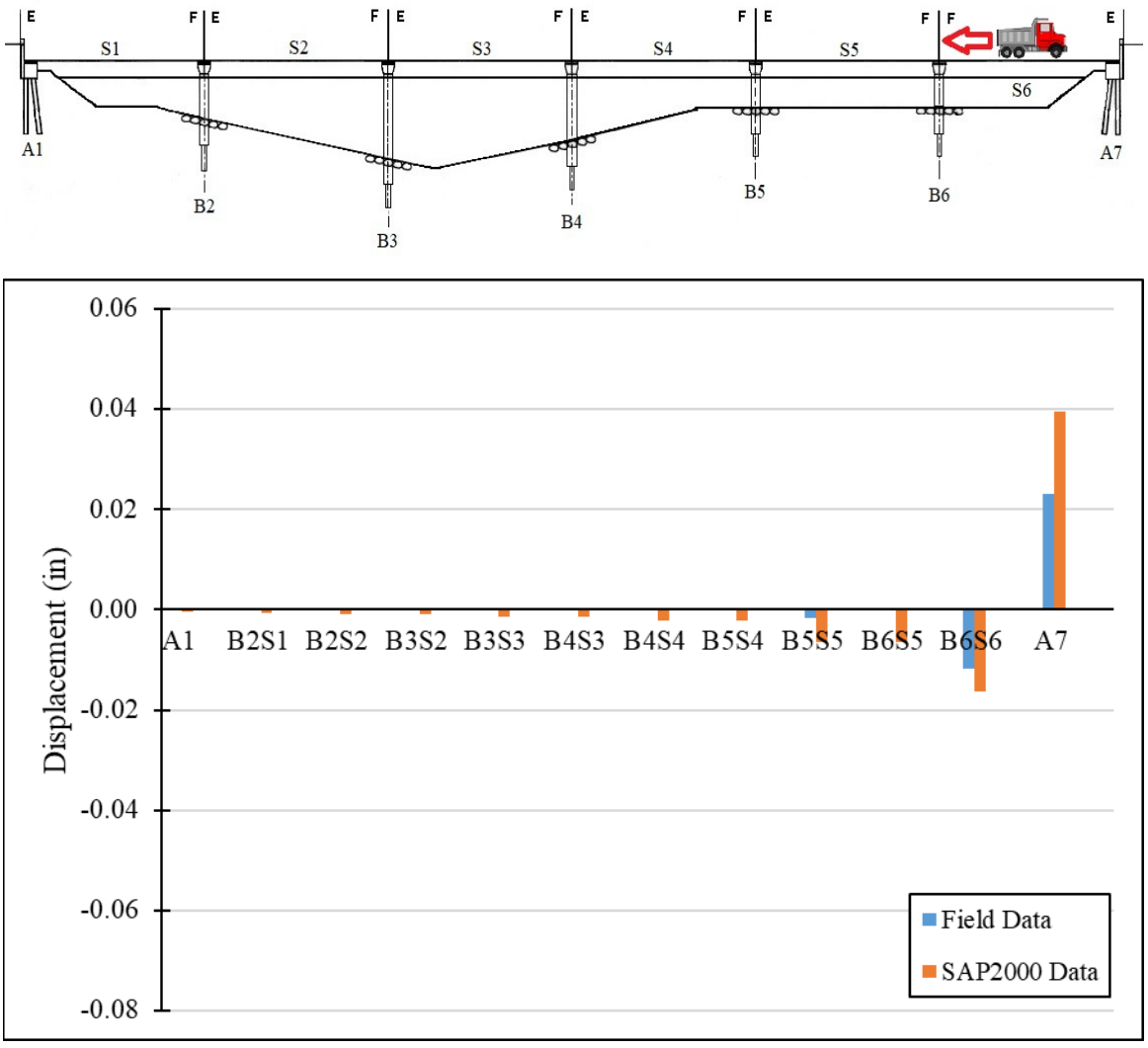

Figure 4-6 – Measured versus Model Displacements for Span 6 Static Loading

For every test case, the loaded span displaced the most. When the truck is positioned on spans 3 and 4, the adjacent spans displace more than when the truck is on other spans. Bents 3 and 4 are the tallest and are the two bents that are not encased in concrete, making them less stiff relative to the other bents. For these reasons, more displacement of adjacent spans is expected when spans 3 and 4 were tested.

Matching the displacements at the abutments proved difficult as well. At abutments 1 and 7 the model reported more displacement then was recorded in the field. But, during other span loadings away from the ends of the bridge, many bents in the model reported smaller displacements then the field data. Therefore, a general determination of the bearings being

uniformly too stiff or too flexible is not able to be determined. This is another reason for attempting to reduce the error in the displacement values mathematically since there is significant variability in the results where some locations are too flexible and some are too stiff.

4.2.2 Resulting Shear Force in Bridge Bents

Among the four piles within each bent, the shear force was fairly uniformly distributed in the model. This uniformity is an indication of the relative stiffness of the superstructure and the bent cap. Bent 4 was the only exception to this, but the pile heights within this bent varied due to the changing ground level in the field so this was expected as well. All other piles had uniform ground elevation for all four piles, preventing this variability in force distribution.

Since this uniformity in force among piles in a bent was occurring, only the percentage of shear force going into each substructure assembly (abutment or bent) are reported in Figures 4-7 through 4-12.

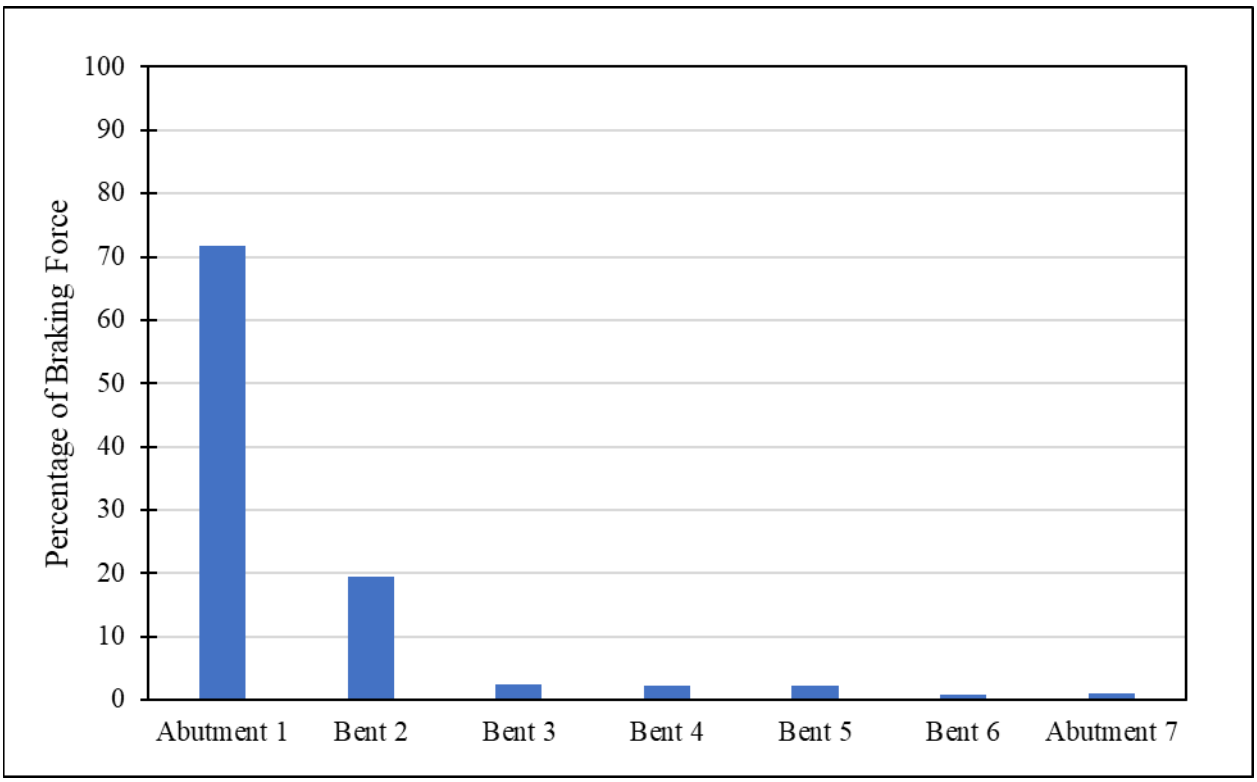

Figure 4-7 – Force Distribution in Substructure from Span 1 Loading

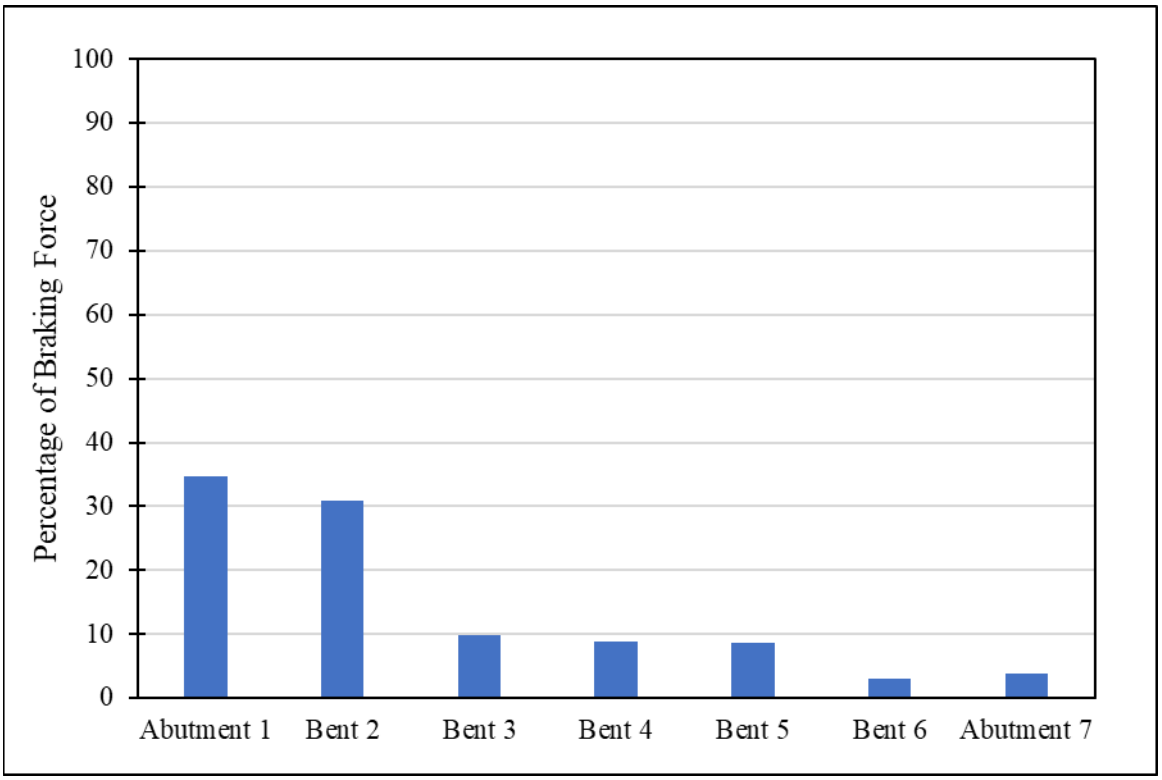

Figure 4-8 – Force Distribution in Substructure from Span 2 Loading

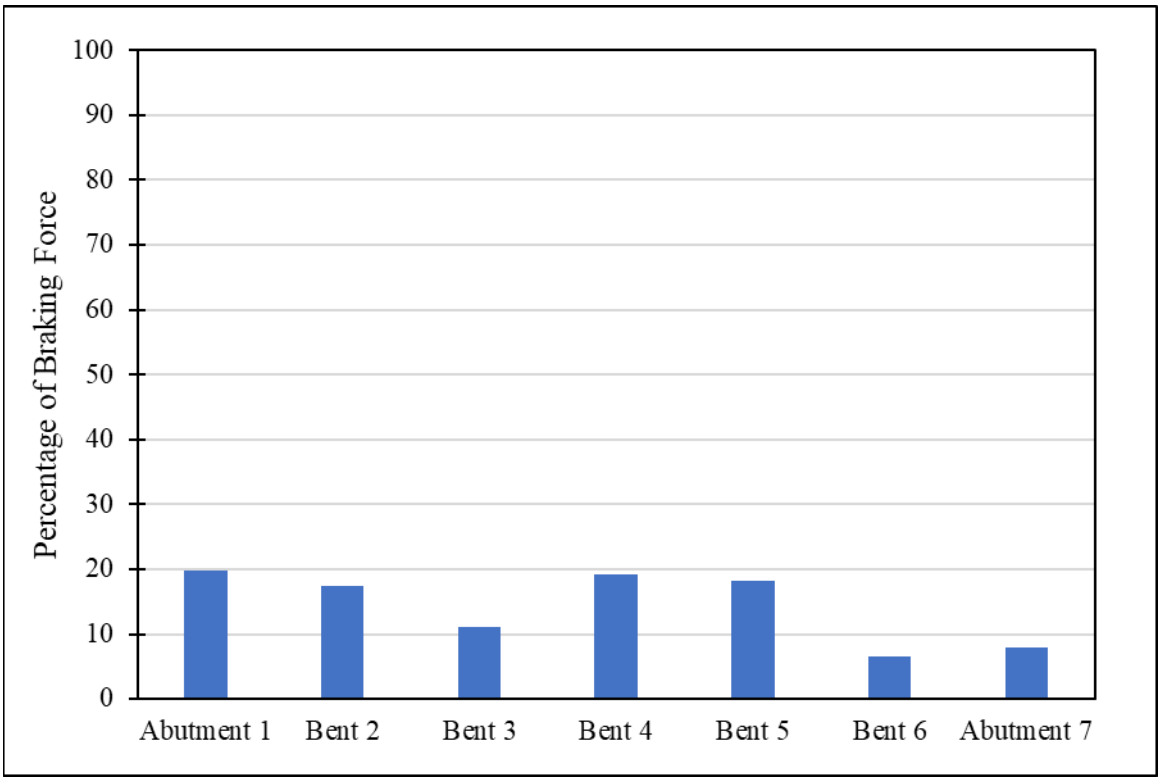

Figure 4-9 – Force Distribution in Substructure from Span 3 Loading

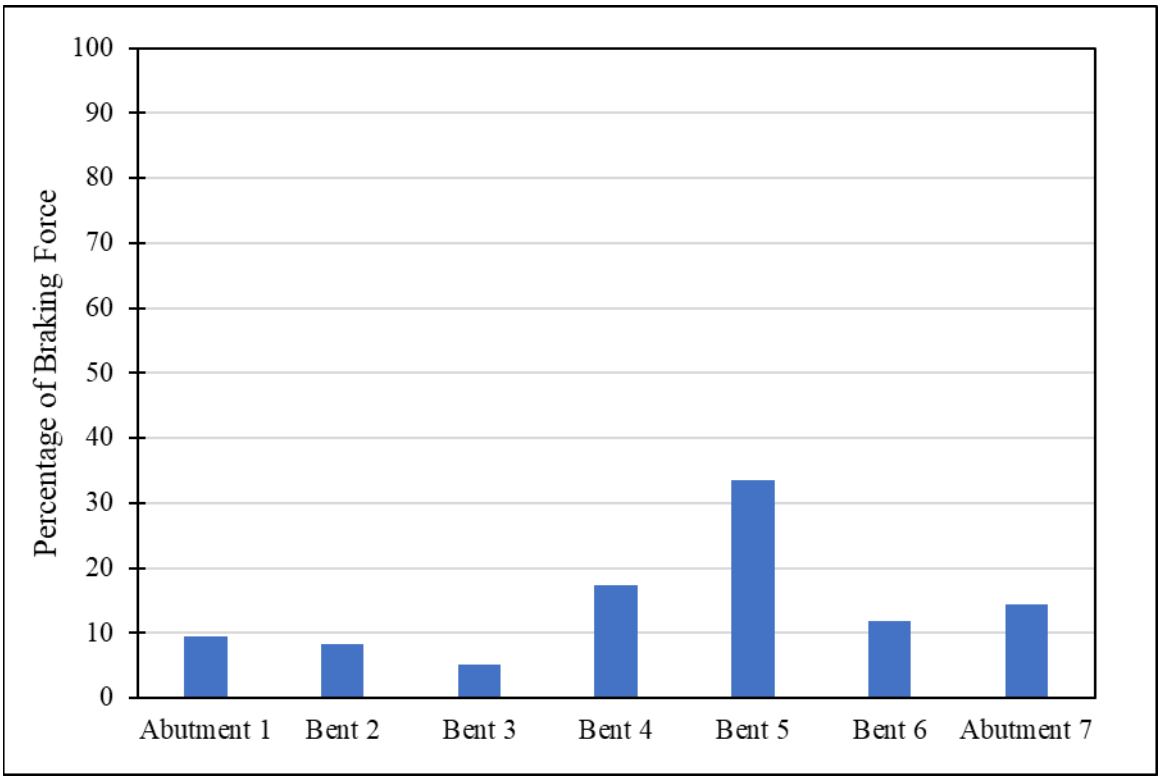

Figure 4-10 – Force Distribution in Substructure from Span 4 Loading

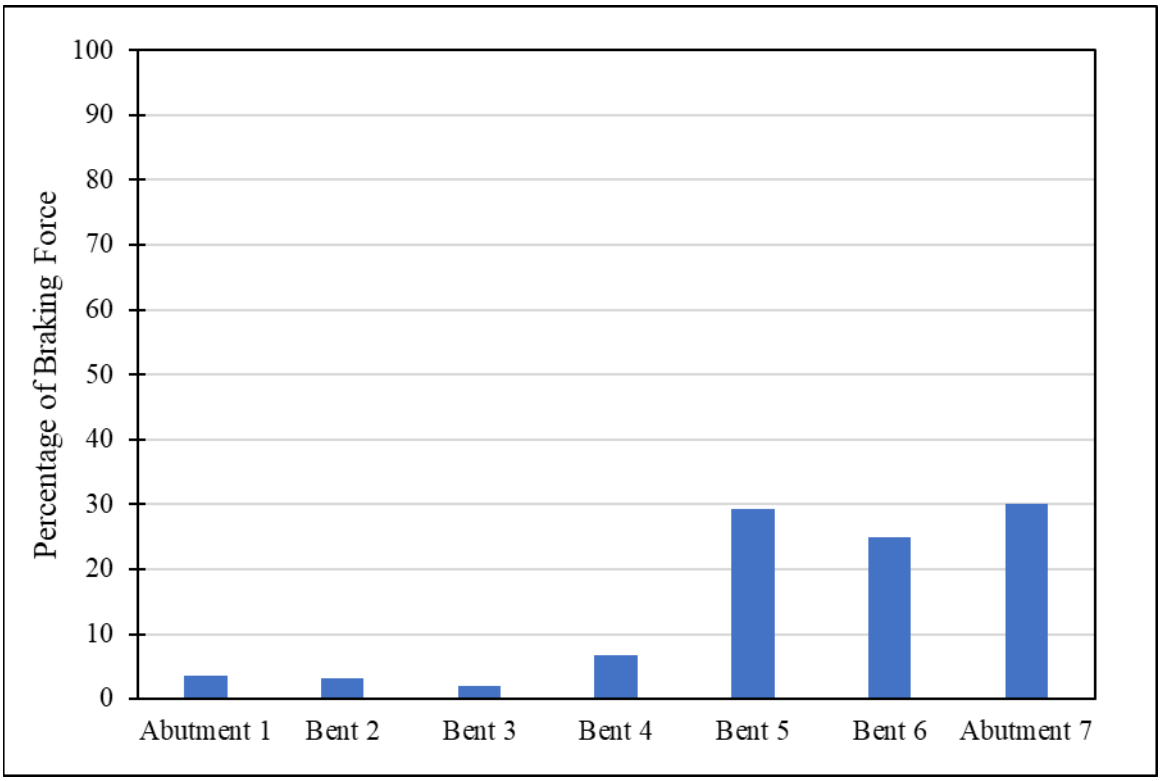

Figure 4-11 – Force Distribution in Substructure from Span 5 Loading

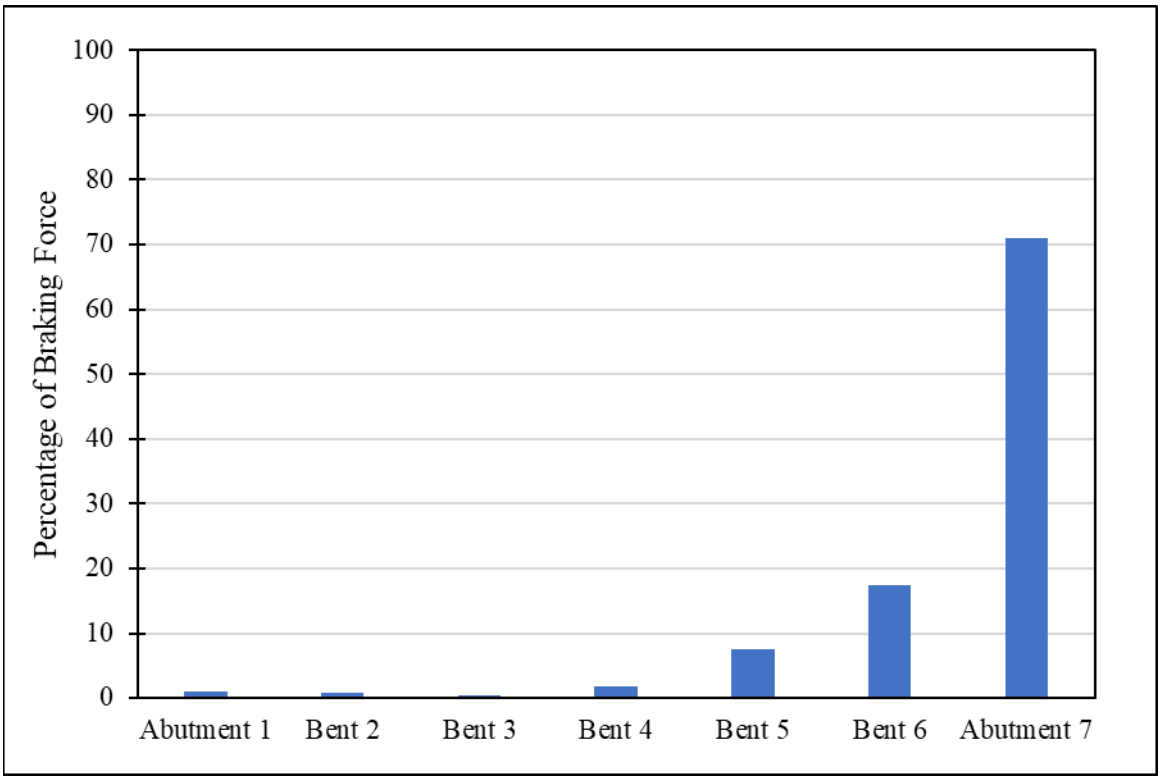

Figure 4-12 – Force Distribution in Substructure from Span 6 Loading

4.2.3 Analysis of Static Force Distribution

In every test, the total magnitude of the braking force on the bridge in the longitudinal direction is distributed among all of the supporting substructure in various amounts depending on the location, but it sums to equal the initial force.

As the static horizontal braking forces moves away from the abutment, the force becomes more evenly distributed among the other bents, especially in the middle spans of the bridge. As the force gets closer to the other abutment, the distribution of the total force becomes less throughout all bents again and the majority goes into the nearest abutment. The abutments draw large portions of the force due to their relative stiffness being so much greater than the bents.

When the load was applied to spans 1 or 6, slightly over 70 percent of the entire force went into the abutments. For spans 2, 3, 4, and 5, each substructure component resisted less than 40 percent of the entire force. When spans 3 and 5 were loaded, the substructure components resisted less than 30 percent. Therefore, as the load is applied further and further away from the ends of the bridge, the more distributed the total applied force is to the substructure, reducing the component force that must be resisted by all elements.

During the loading of spans 3 and 4, the bent at the end of the span where the front of the truck was positioned experienced a greater amount of shear force than the other bent supporting that span. For these tests, these were also the bents that displaced the most. For every test, if it was not an abutment that experienced the greatest amount of force, the bent that displaced the most was also the bent that experienced the most shear force. Moreover, it was always one of the bents supporting the loaded span.

4.3 DYNAMIC TEST RESULTS

4.3.1 Bridge Accelerations Due to Dynamic Loading

When comparing the dynamic model to the field data, the accelerations of each were evaluated. Figure 4-13 through Figure 4-23 are the measured accelerations compared to the model accelerations. In order to alleviate the amount of data displayed on each graph and to provide clarity for comparisons, the only accelerations included were from the span that was tested, the two adjacent spans and the bents supporting the test span. The accelerometers were located at each end of the girder that was designated fixed on the plans and the accelerometers on the bents were centered on the top of the bent cap. The only exception to this was accelerometer B-3a, it was placed on the outer face of bent cap of bent 3. The side it was placed on was also the same side the right side tests were conducted on. In the figures, Field Sp-1, Field B-2, etc. is the naming convention for field accelerometer on span 1, bent 2, etc. and the same naming convention is used for SAP. For each test, the diagram above the acceleration graph shows the location of the truck, peak deceleration rate and the truck weight. Additionally, where the braking of the truck began and the time when the truck was completely stopped are called out on the figures. For the exact times used, the time history functions for each test case are located in Appendix C.

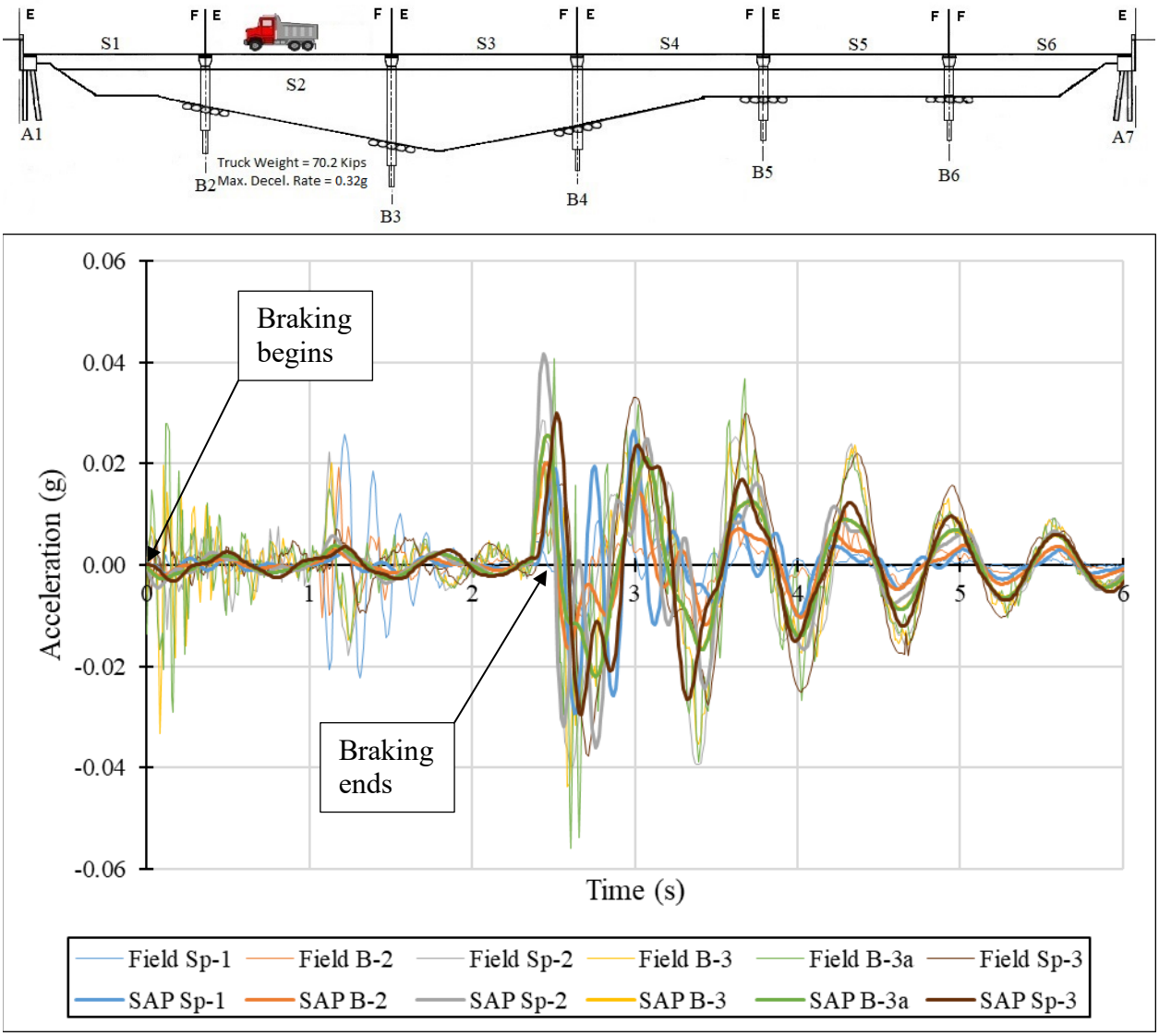

Figure 4-13 – Field and Model Accelerations for Test 1 on Center of Span 2

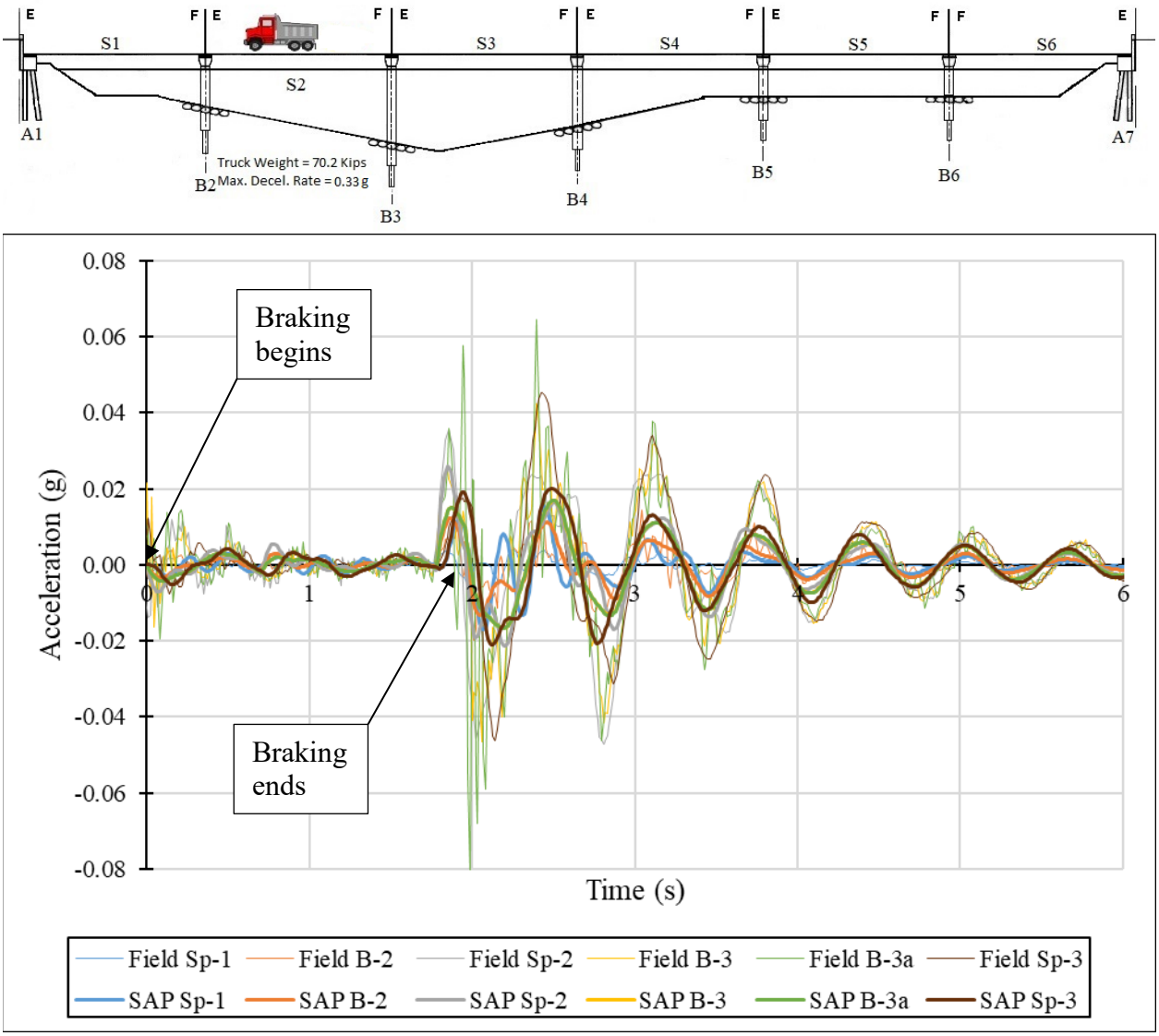

Figure 4-14 – Field and Model Accelerations for Test 2 on Center of Span 2

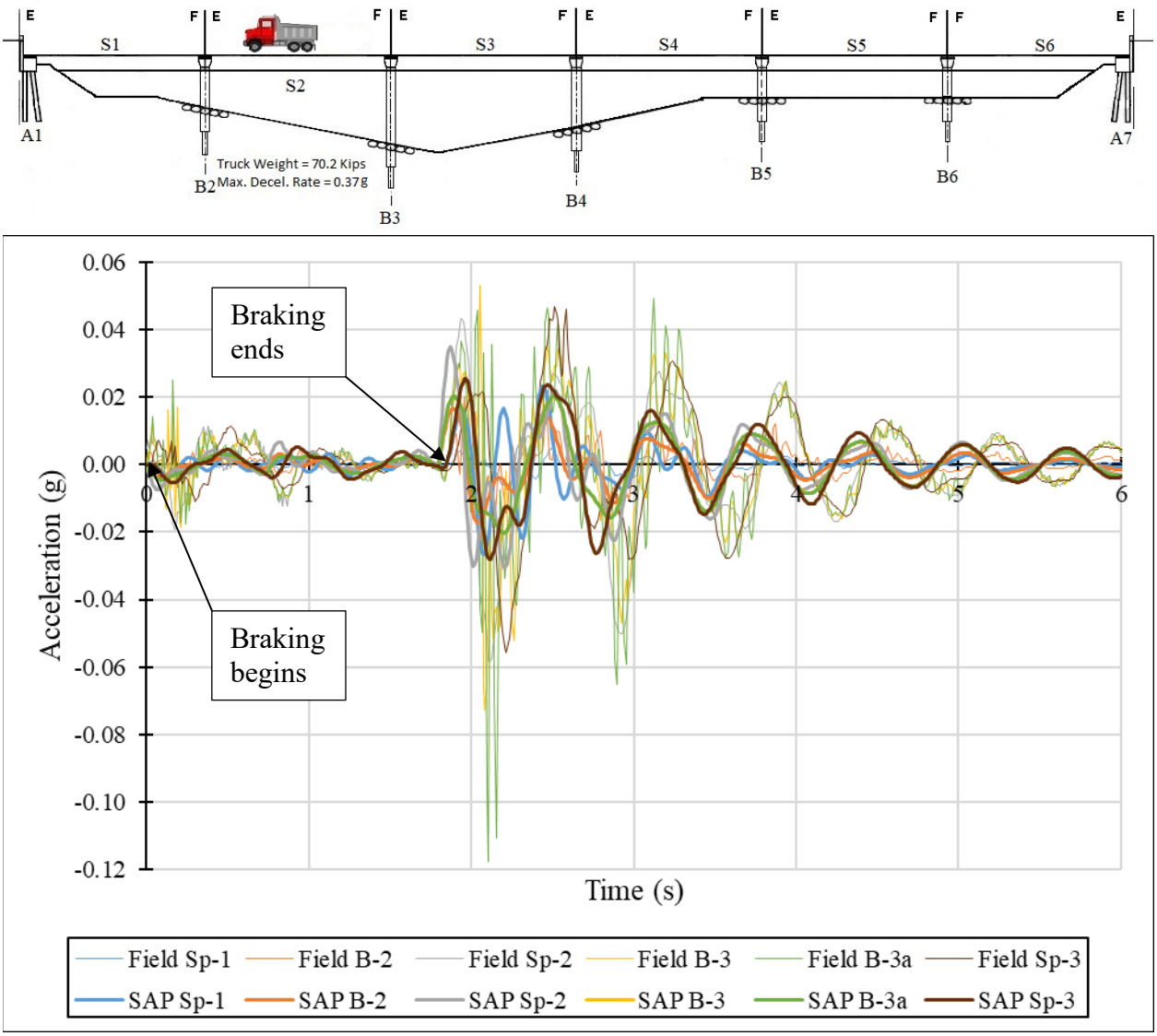

Figure 4-15 – Field and Model Accelerations for Test 3 on Center of Span 2

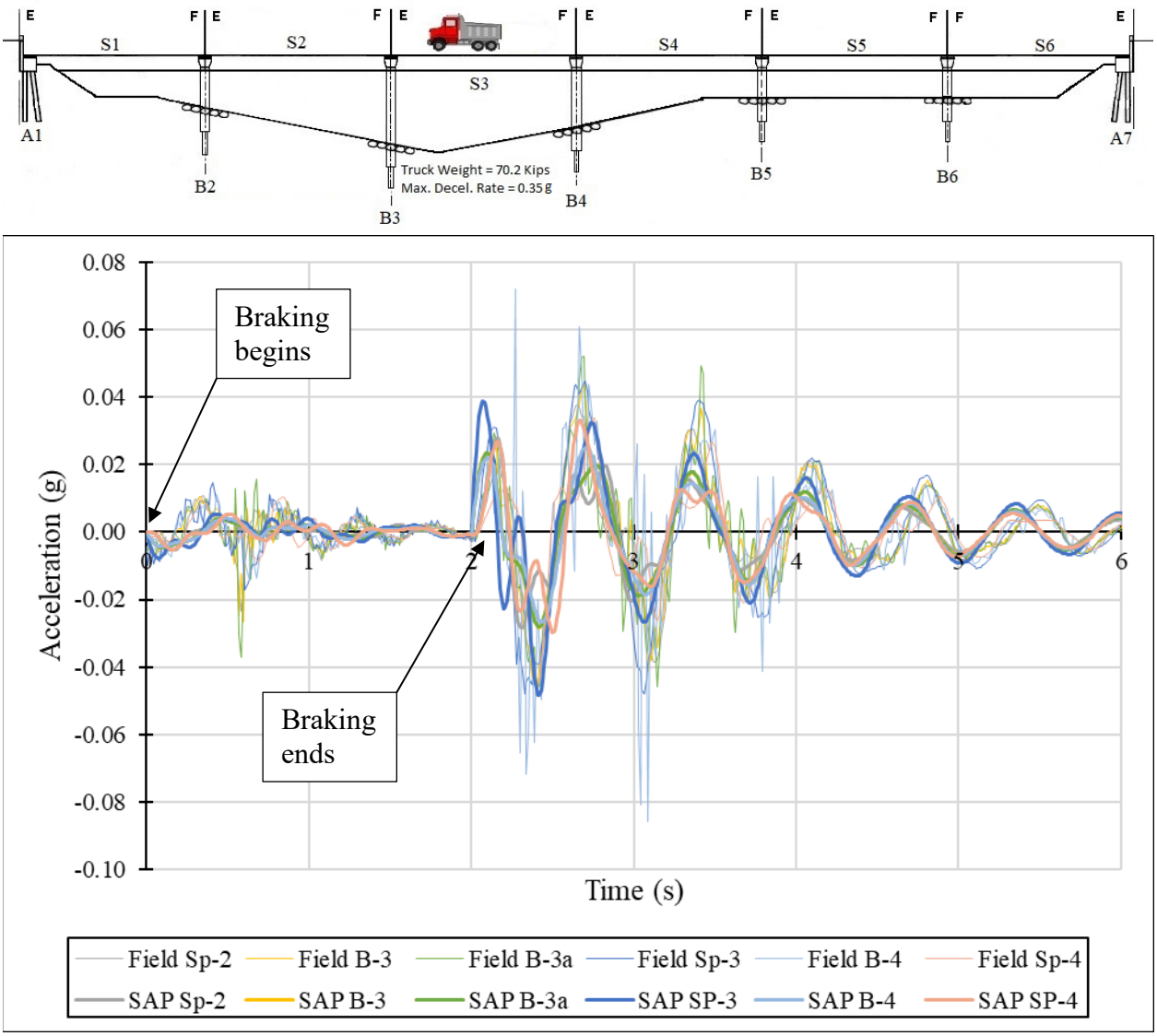

Figure 4-16 – Field and Model Accelerations for Test 1 on Center of Span 3

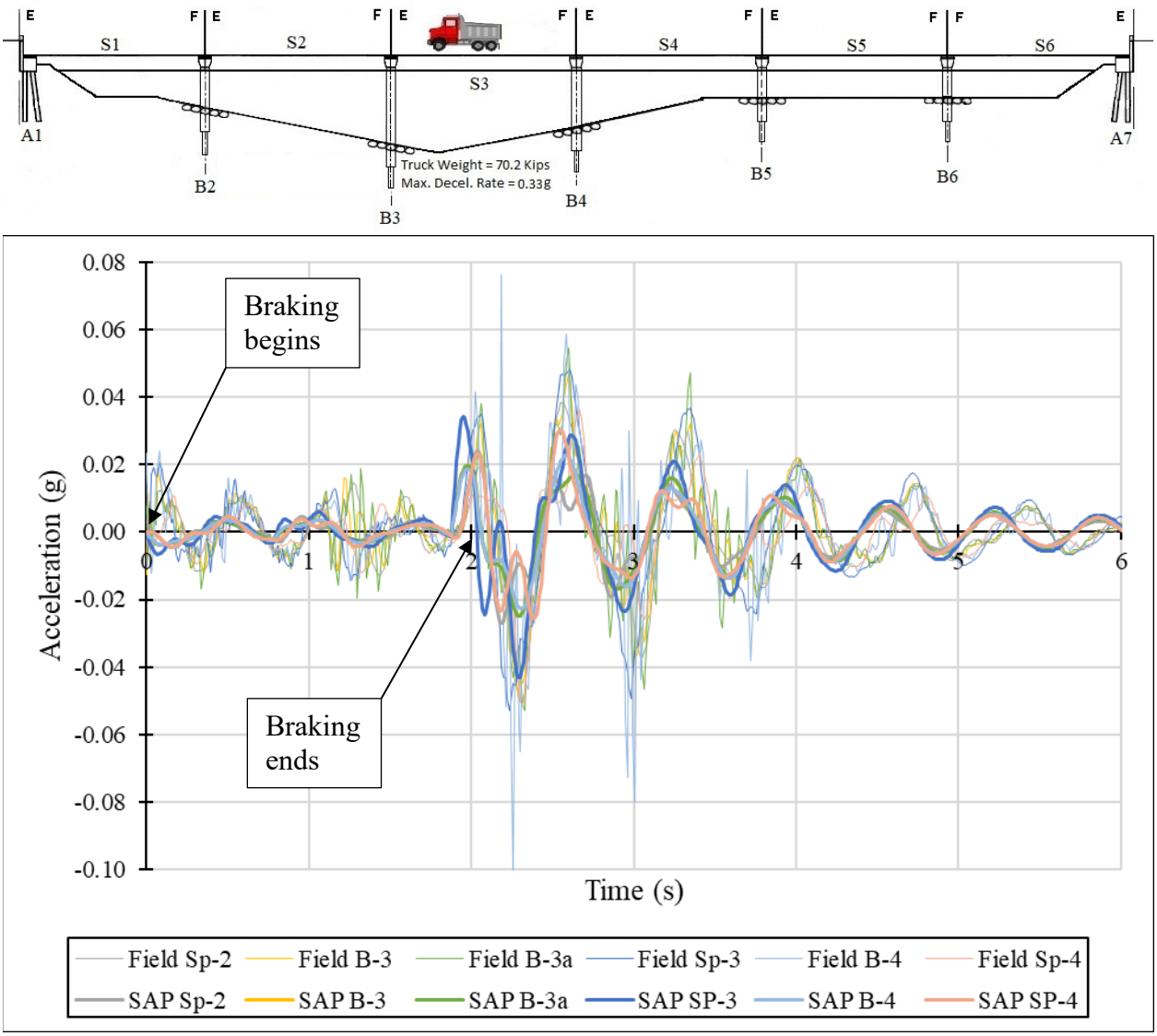

Figure 4-17 – Field and Model Accelerations for Test 3 on Center of Span 3

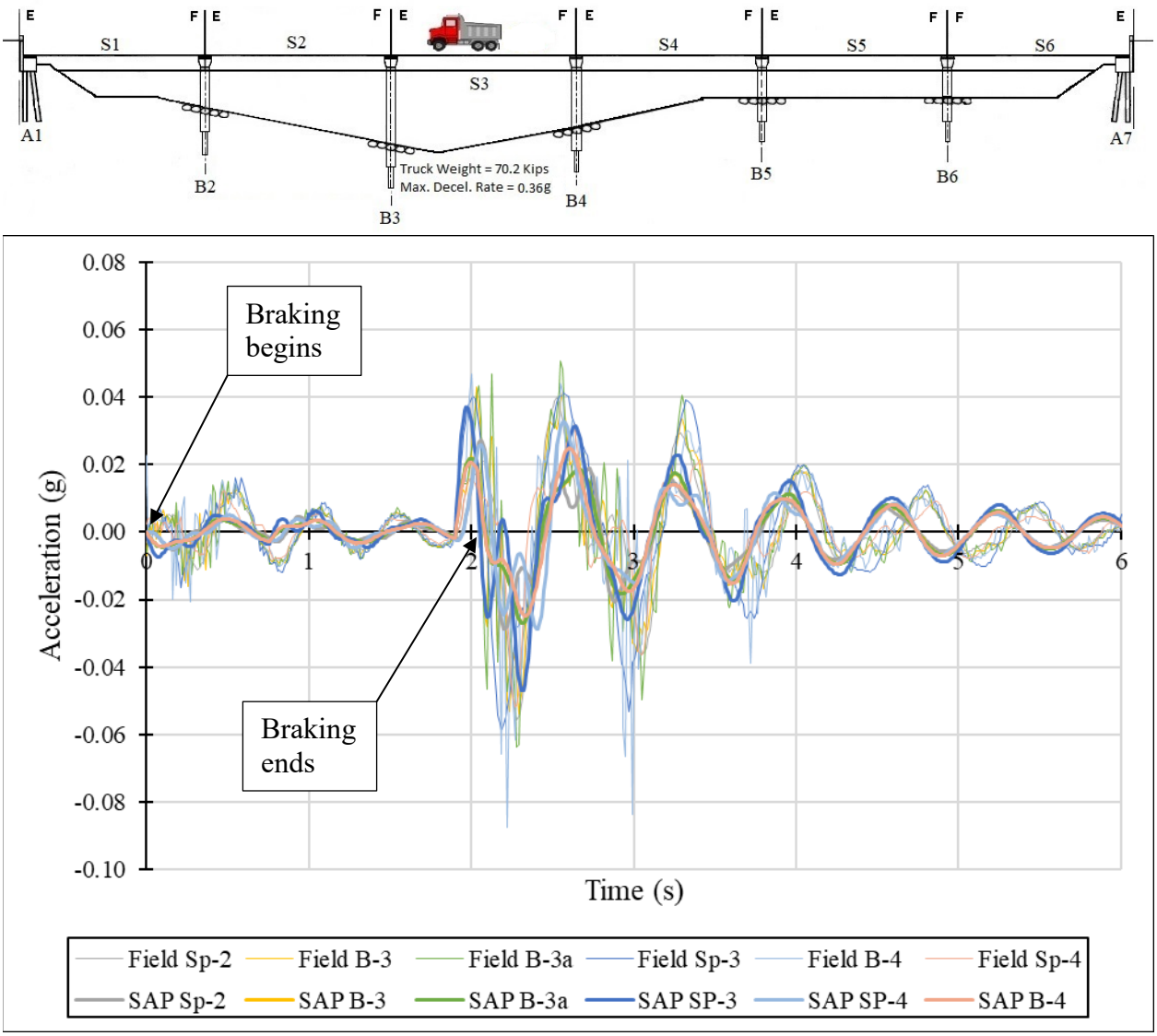

Figure 4-18 – Field and Model Accelerations for Test 4 on Center of Span 3

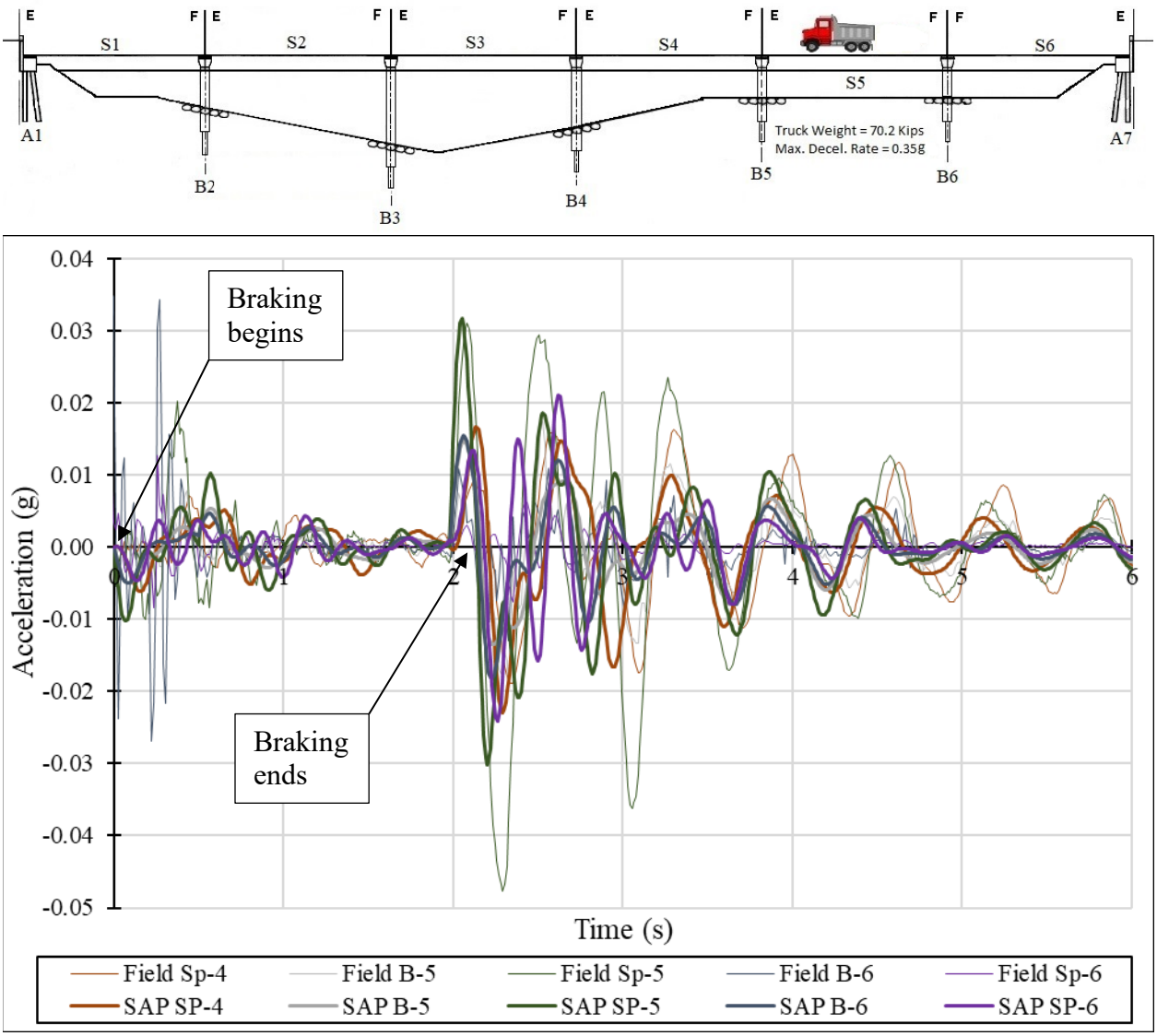

Figure 4-19 – Field and Model Accelerations for Test 2 on Center of Span 5

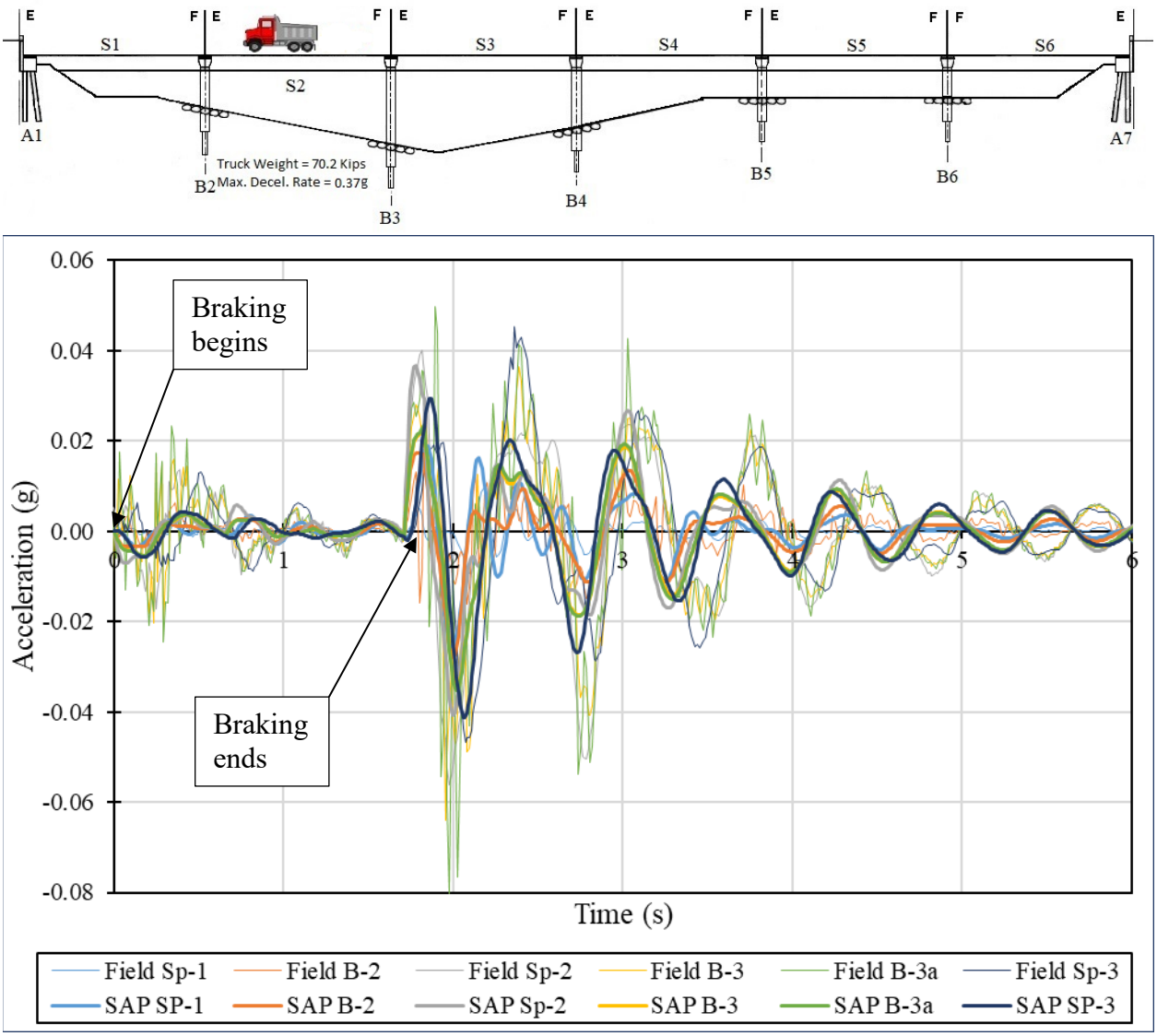

Figure 4-20 – Field and Model Accelerations for Test 2 on the Right Side of Span 2

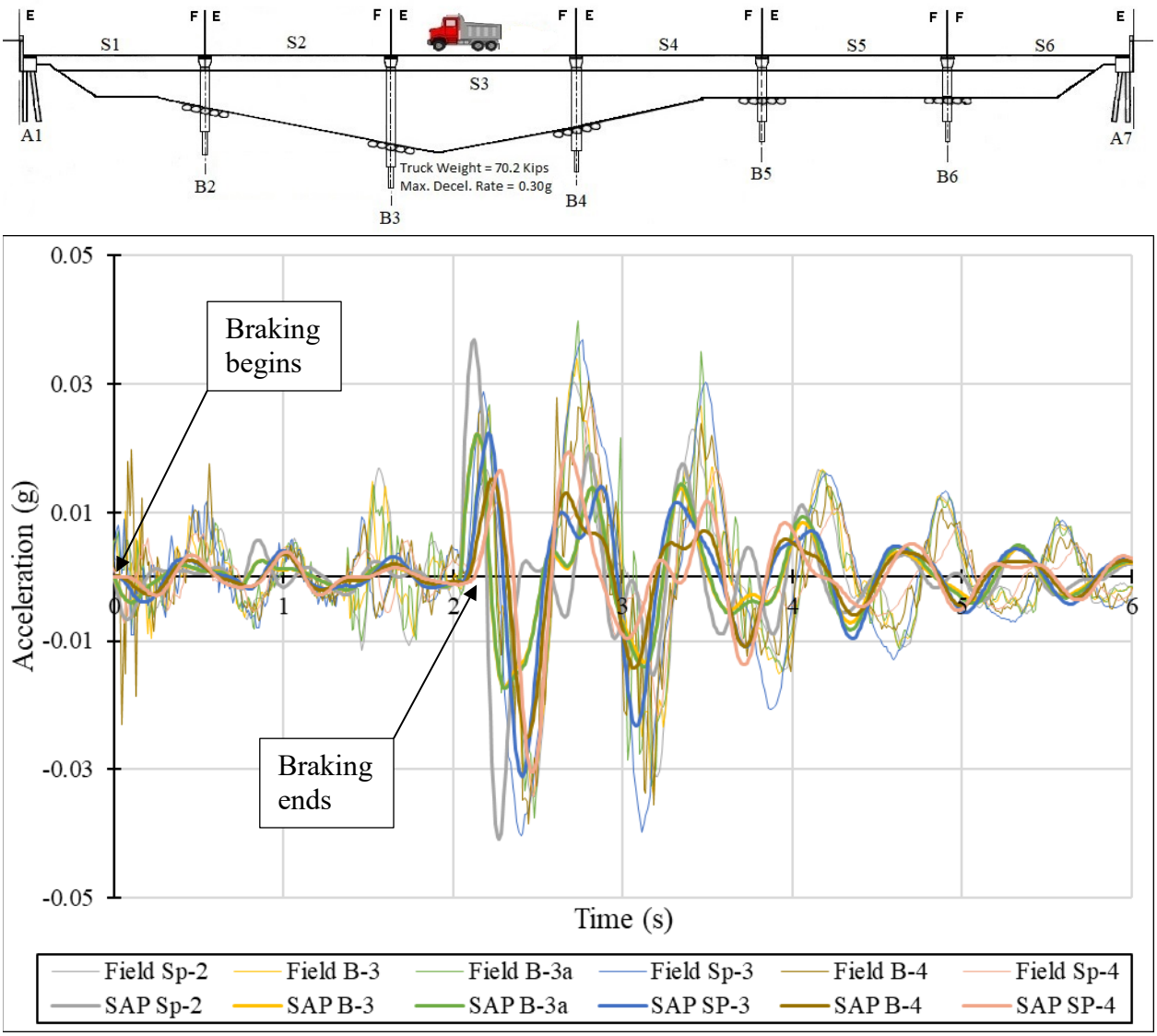

Figure 4-21 – Field and Model Accelerations for Test 3 on the Right Side of Span 3

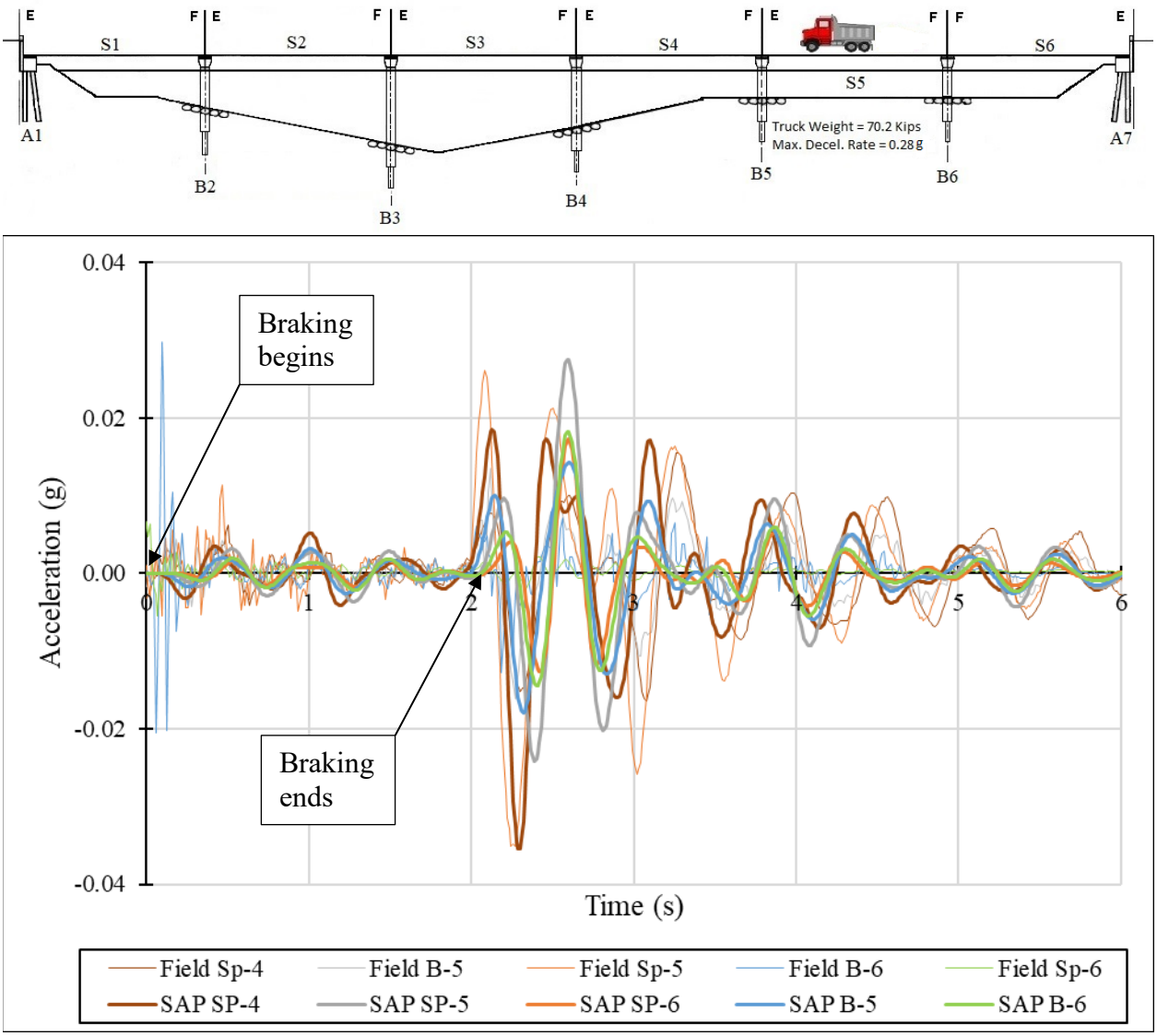

Figure 4-22 – Field and Model Accelerations for Test 1 on the Right Side of Span 5

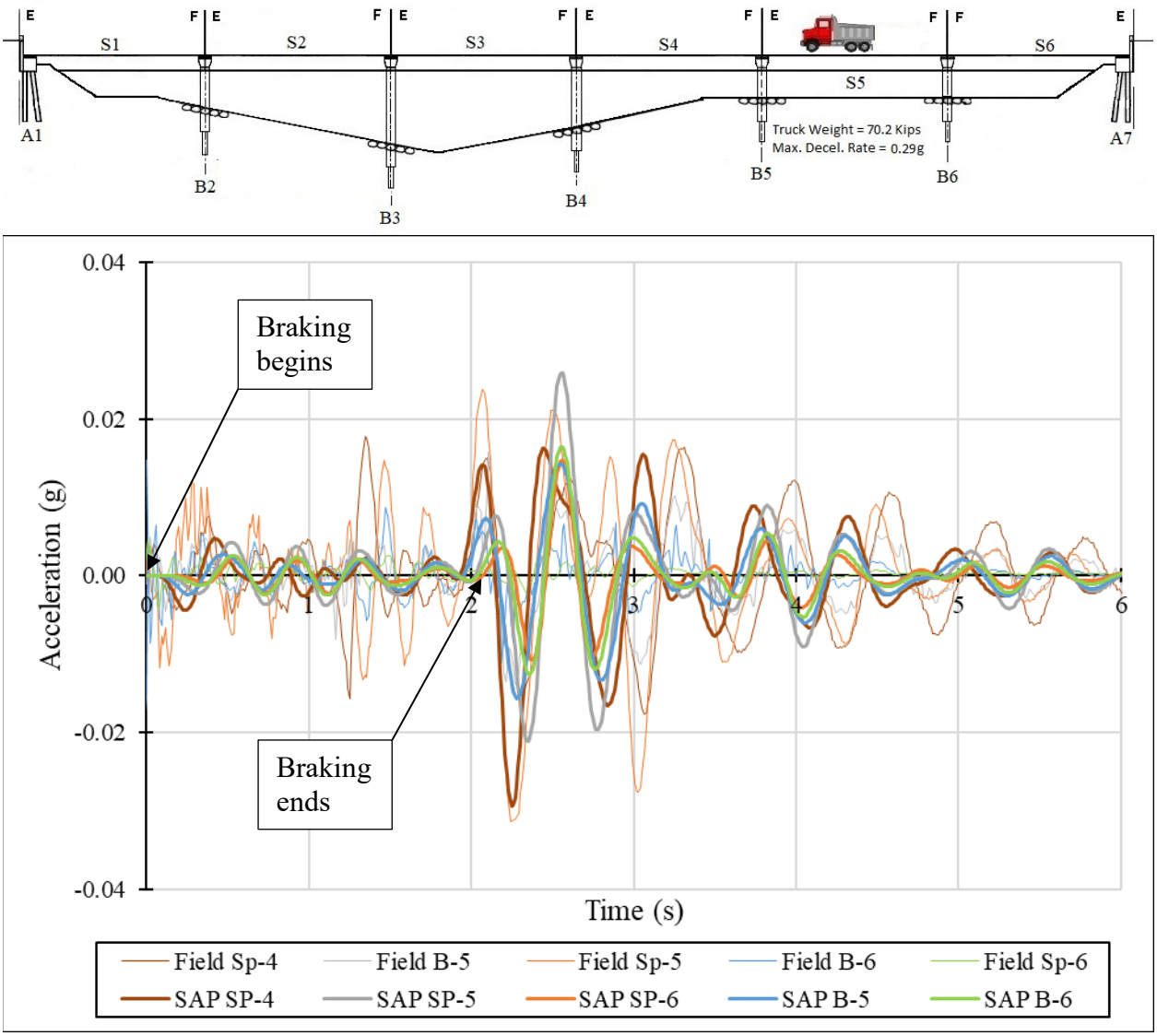

Figure 4-23 – Field and Model Accelerations for Test 3 on the Right Side of Span 5

With each of these tests, after the initial free response phase the peaks and troughs appear to become out of phase between the field data and the SAP data. But, the period and frequency of vibration between both remained similar. These response properties are more telling of the correlation despite them being slightly out of phase of one another.

4.3.2 Analysis of Bridge Substructure Accelerations

To understand the maximum amount the bridge substructure elements were accelerating in relation to the maximum truck deceleration, Figures 4-24 through 4-29 were produced. Despite there being negative accelerations on the figures above, the absolute values were taken to find the highest magnitude of acceleration for a bent or abutment.

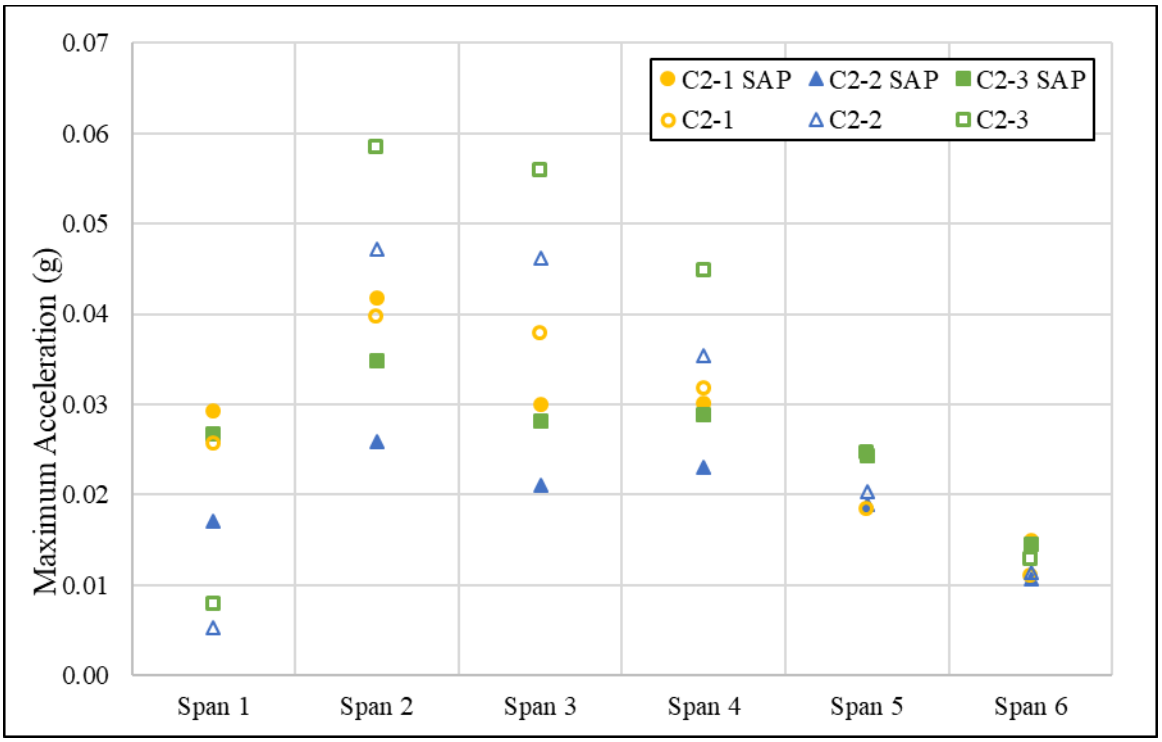

Figure 4-24 – Maximum Acceleration per Span from Field Test & Model for Span 2 Center Braking

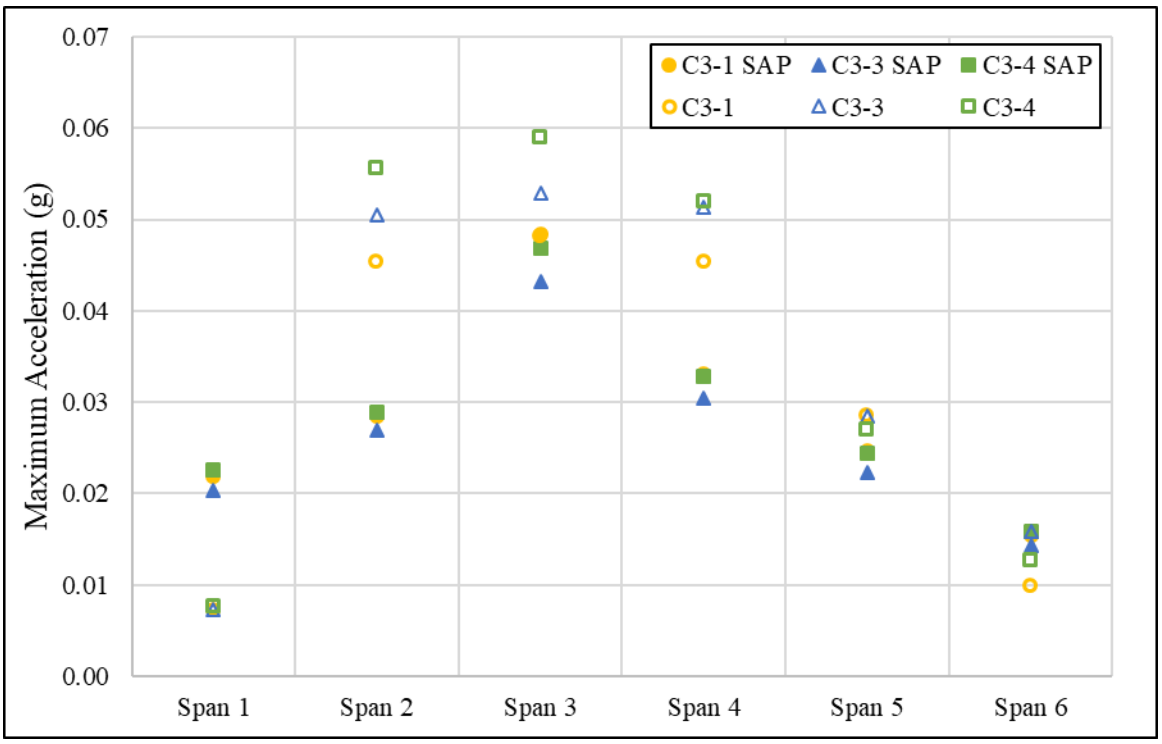

Figure 4-25 – Maximum Acceleration per Span from Field Test & Model for Span 3 Center Braking

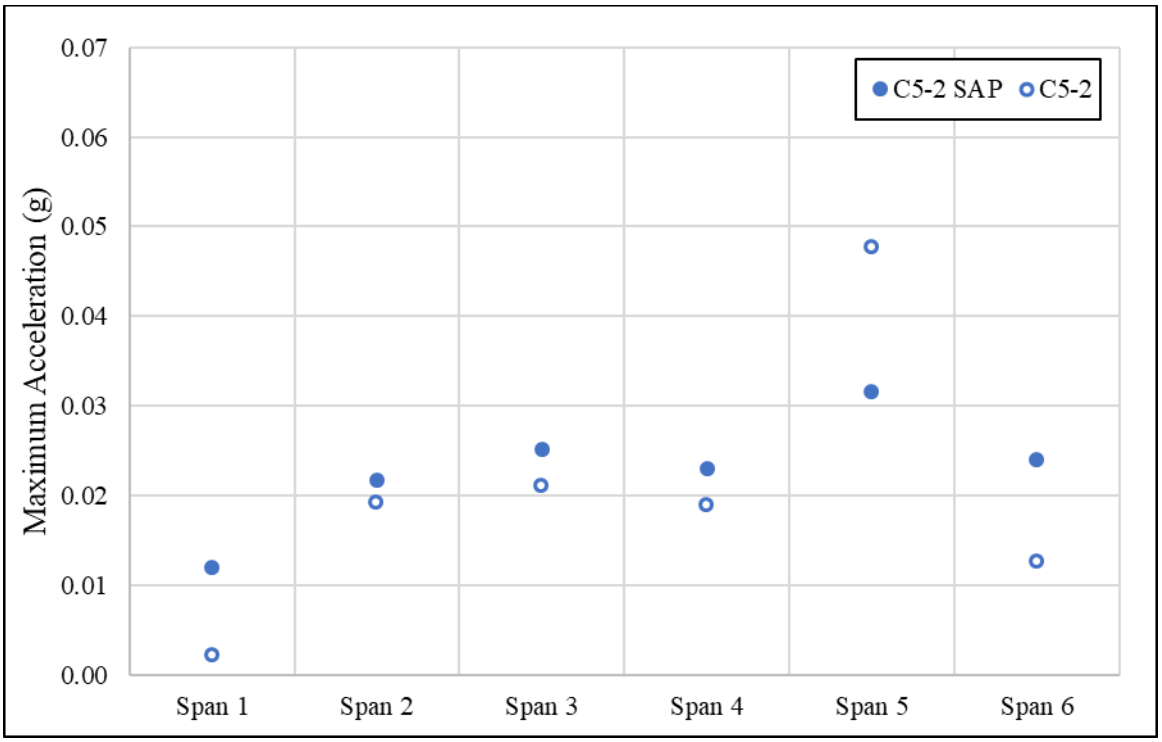

Figure 4-26 – Maximum Acceleration per Span from Field Test & Model for Span 5 Center Braking

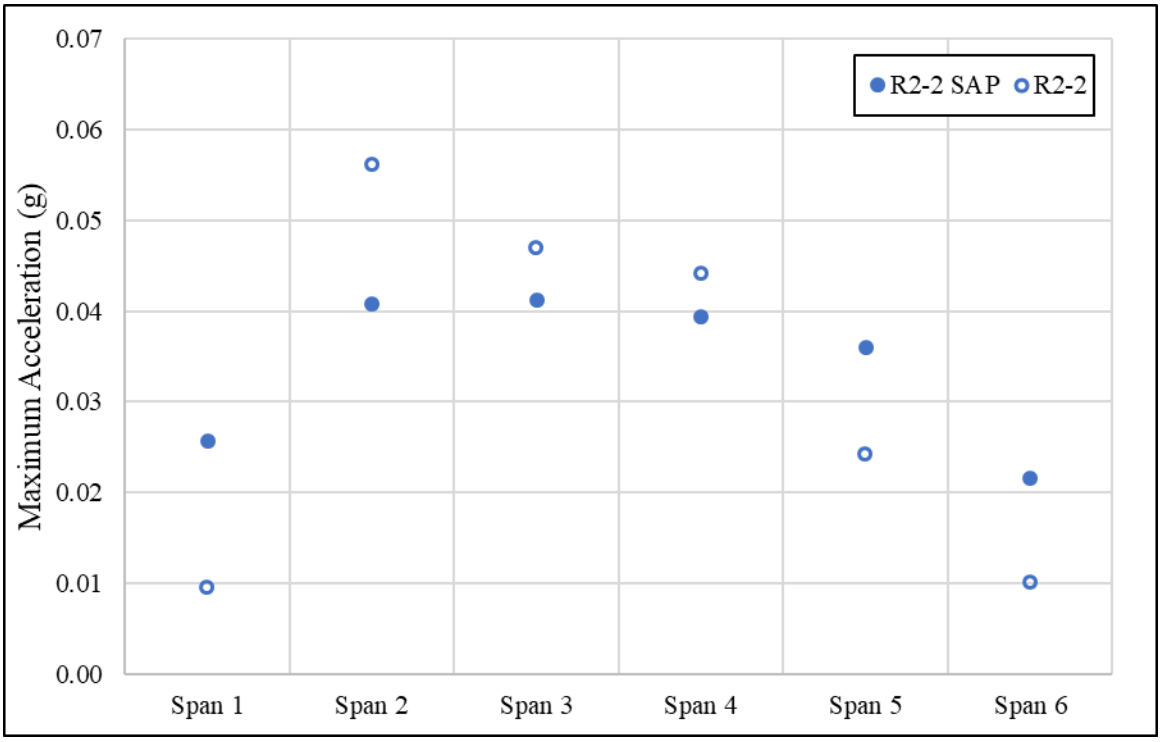

Figure 4-27 – Maximum Acceleration per Span from Field Test & Model for Span 2 Right Side Braking

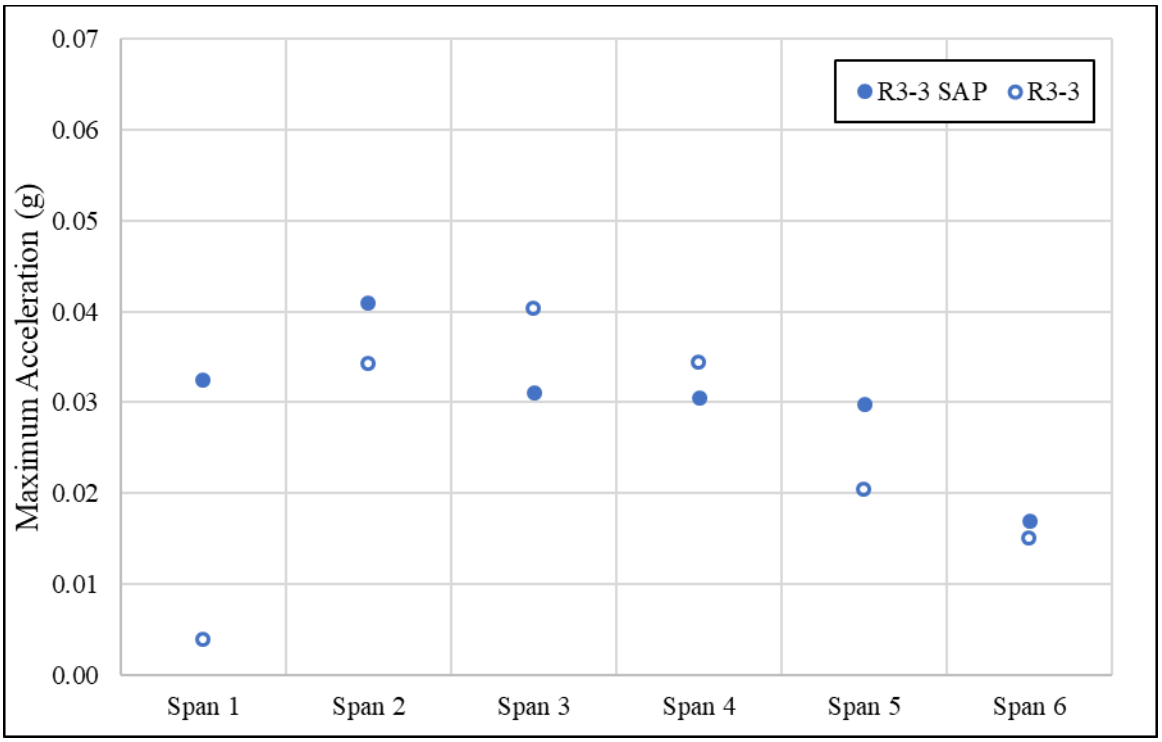

Figure 4-28 – Maximum Acceleration per Span from Field Test & Model for Span 3 Right Side Braking

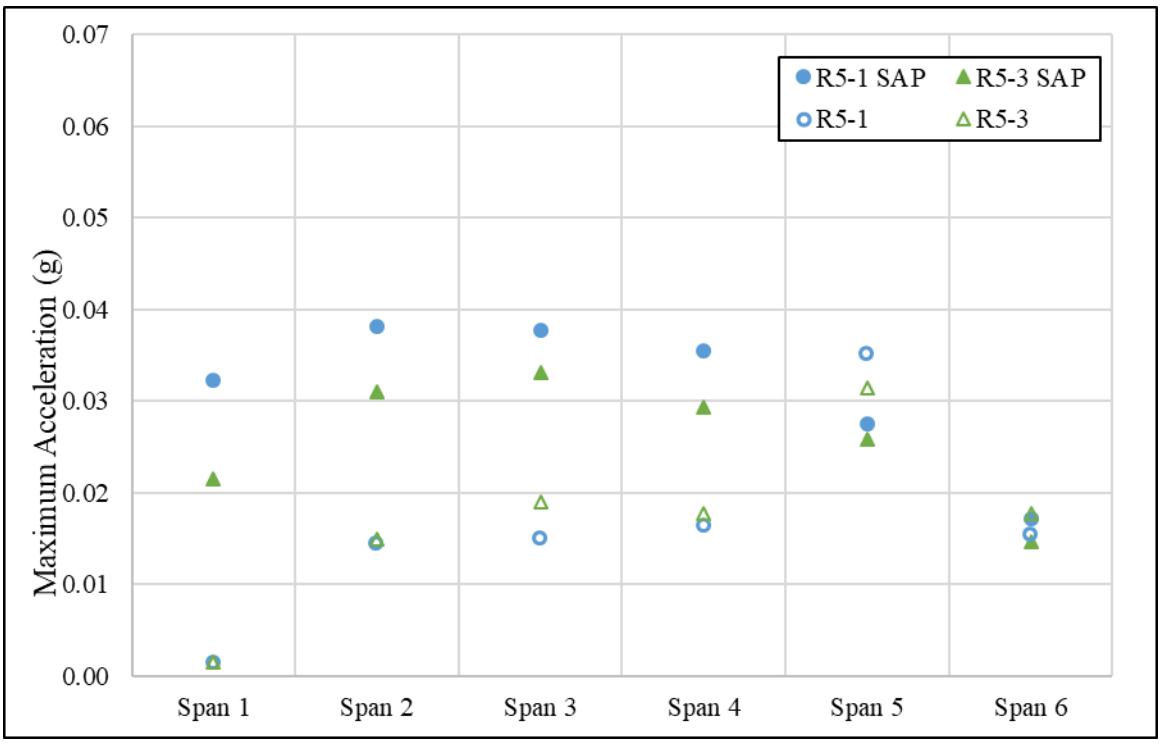

Figure 4-29 – Maximum Acceleration per Span from Field Test & Model for Span 5 Right Side Braking

In every test but span 3 when braking occurred on the right side, the span that the truck stopped on experienced the greatest acceleration.

4.3.3 Shear Forces in Bents from Dynamic Braking Tests

For each model loading condition presented in Chapter 4.3.1, Figures 4-30 through 4-40 illustrate the total shear force over time that the entire bridge substructure (bents and abutments) experienced. The maximum total horizontal force is developed during the length of time that the brakes are applied (the first few seconds). The magnitude of this force is approximately equal to the maximum deceleration rate times the mass of the truck. For example, Figure 4-30 shows the total shear force in the substructure from braking on the center of span 2, test 1. In that test, the maximum deceleration rate was 0.32g and the truck mass was 70.2 kips, therefore, the approximate maximum total horizontal force is assumed to be 22.5 kips as a result the deceleration. This simple calculation does not account for any dynamic amplification or the inertia of the bridge, but is an estimation of the maximum that is expected in a static braking force. The calculation for the approximate maximum horizontal force is included on each test's figure. It is also important to note that the total shear force in the substructure does not ever get above the total shear force during the braking event. As soon as the braking maneuver is completed, the bridge acceleration is already damping out during free response and the forces are dissipating.

Unlike the static tests where the amount of force for each component was presented, only the total shear force for each test is included since these tests were time dependent and are not easily combined in one figure.

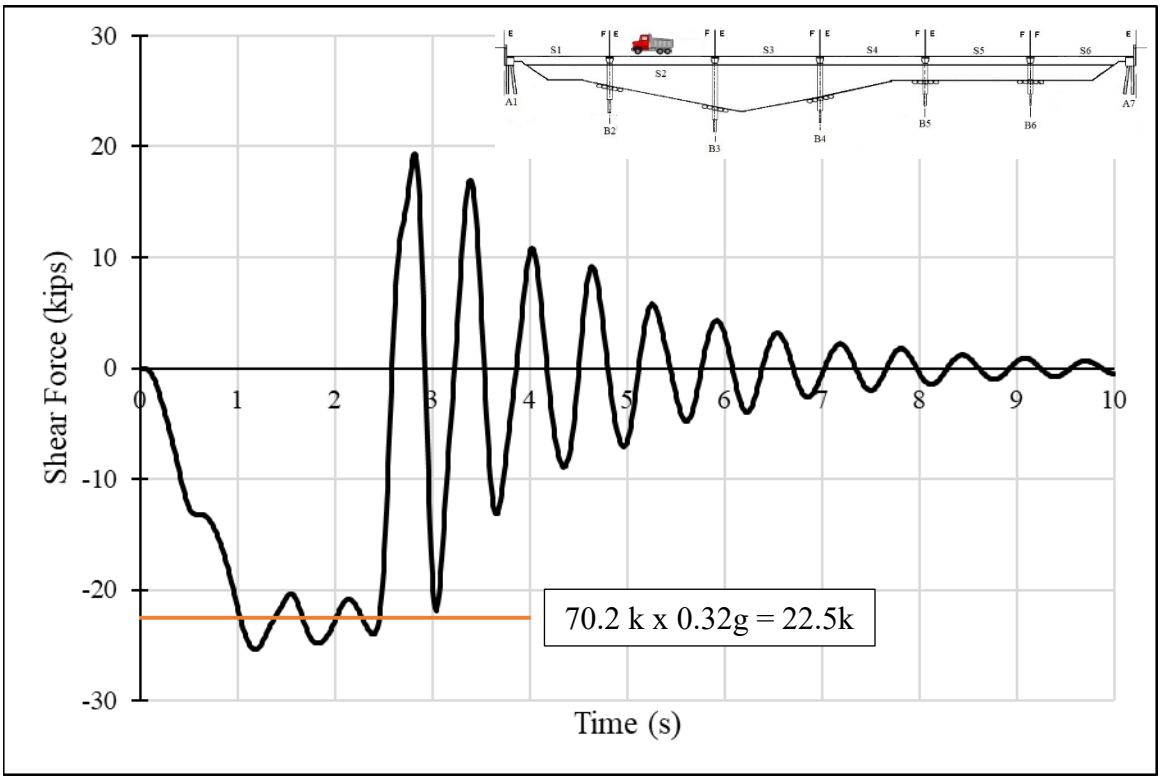

Figure 4-30 – Shear Force in Substructure from Center of Span 2 Braking Test 1

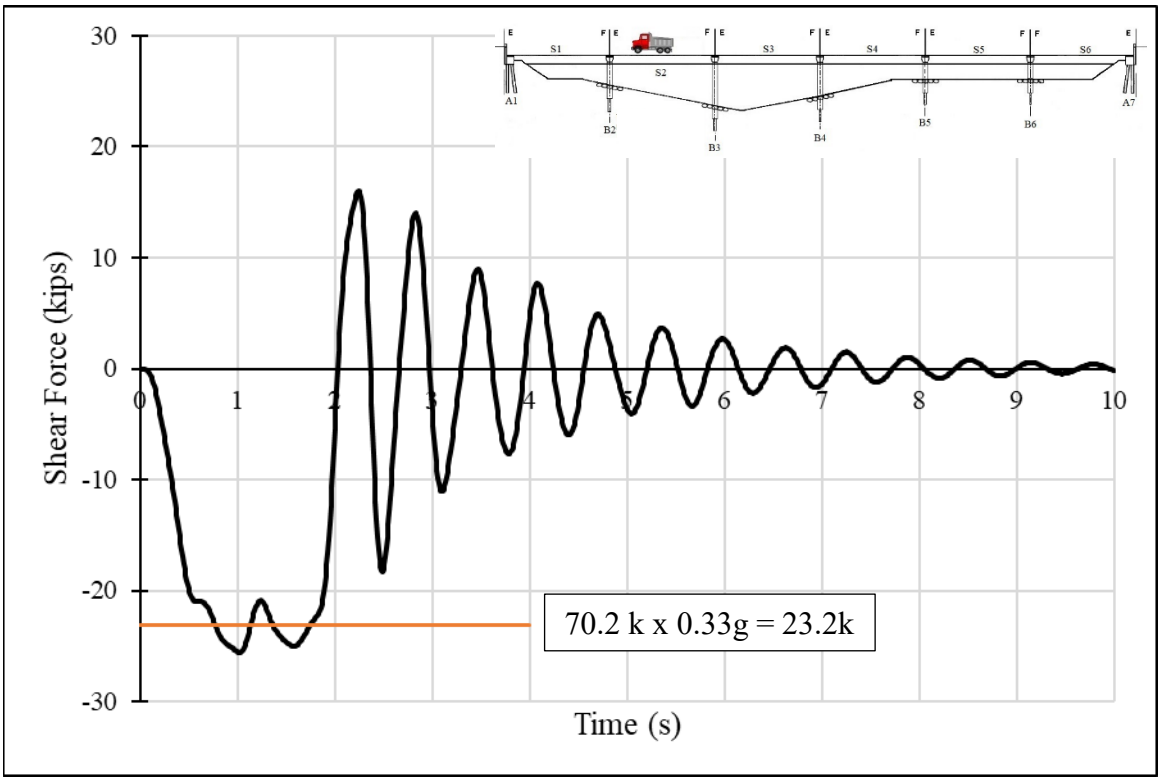

Figure 4-31 – Shear Force in Substructure from Center of Span 2 Braking Test 2

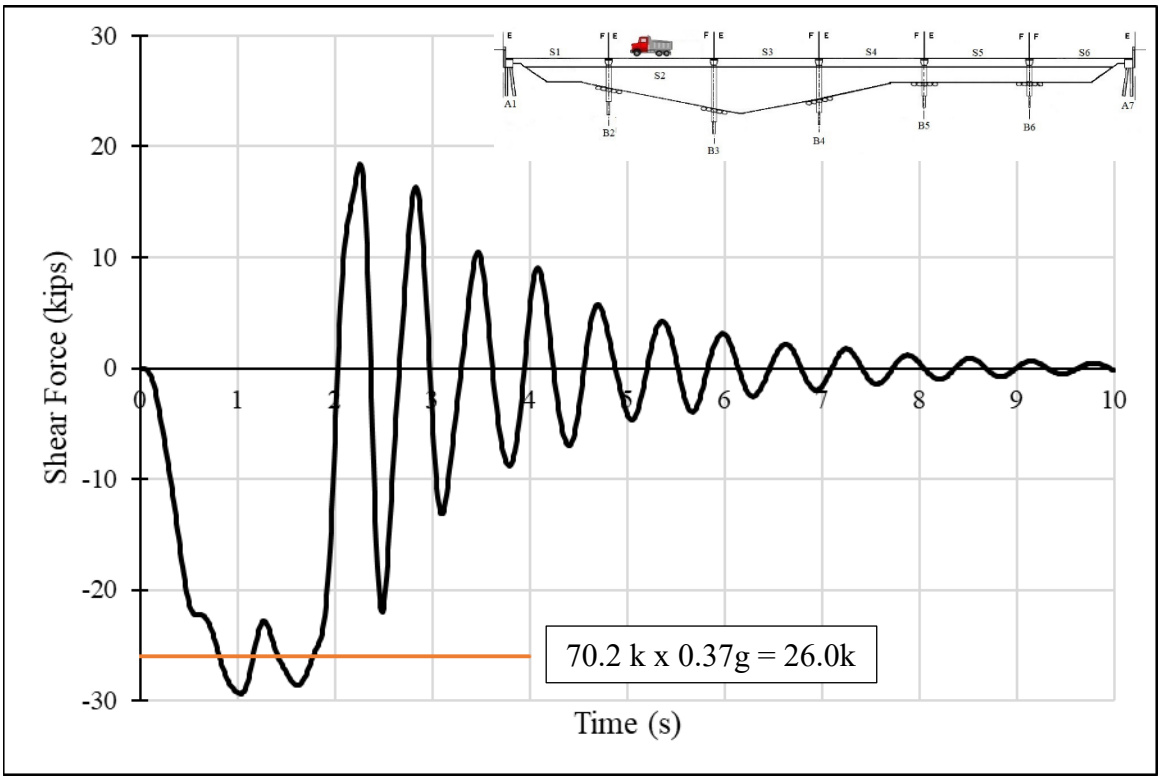

Figure 4-32 – Shear Force in Substructure from Center of Span 2 Braking Test 3

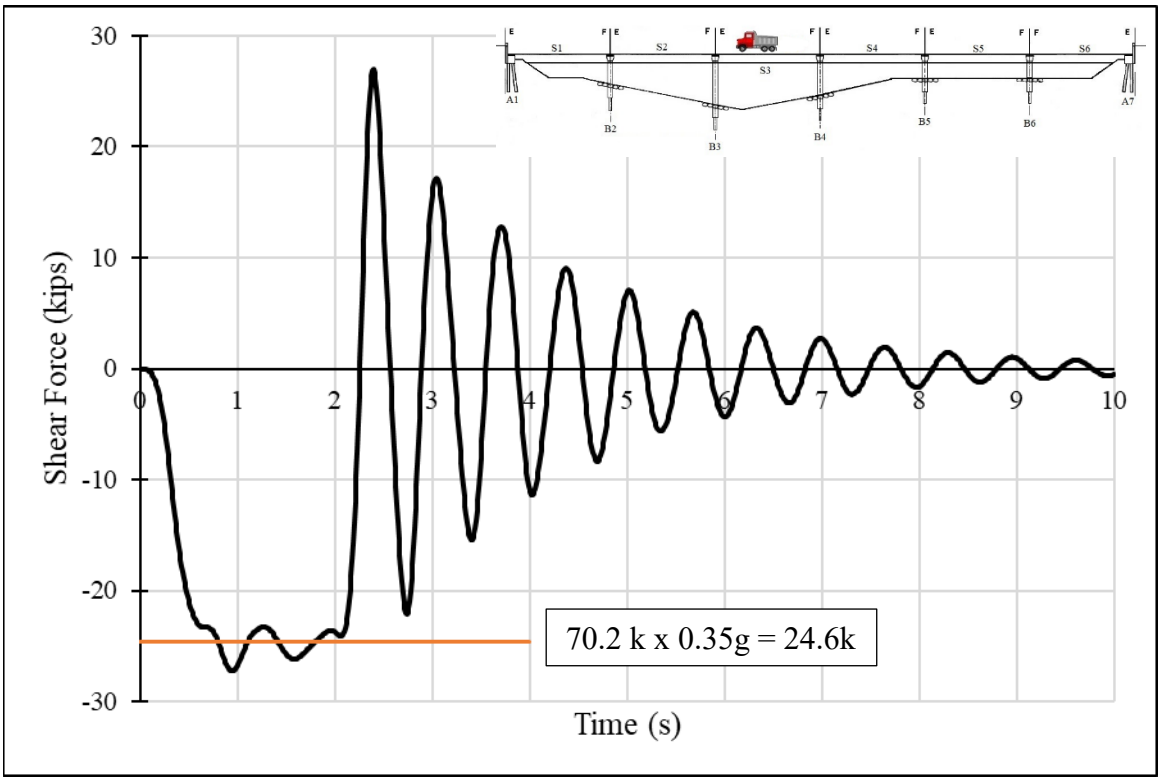

Figure 4-33 – Shear Force in Substructure from Center of Span 3 Braking Test 1

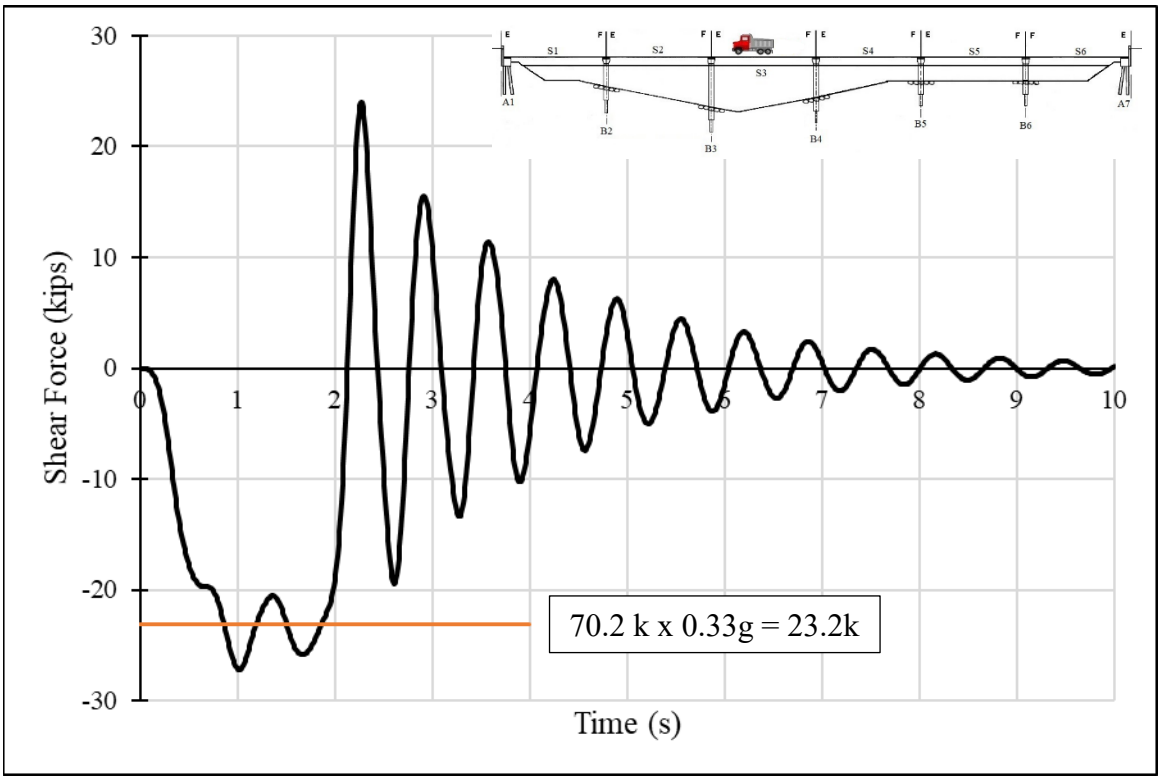

Figure 4-34 – Shear Force in Substructure from Center of Span 3 Braking Test 3

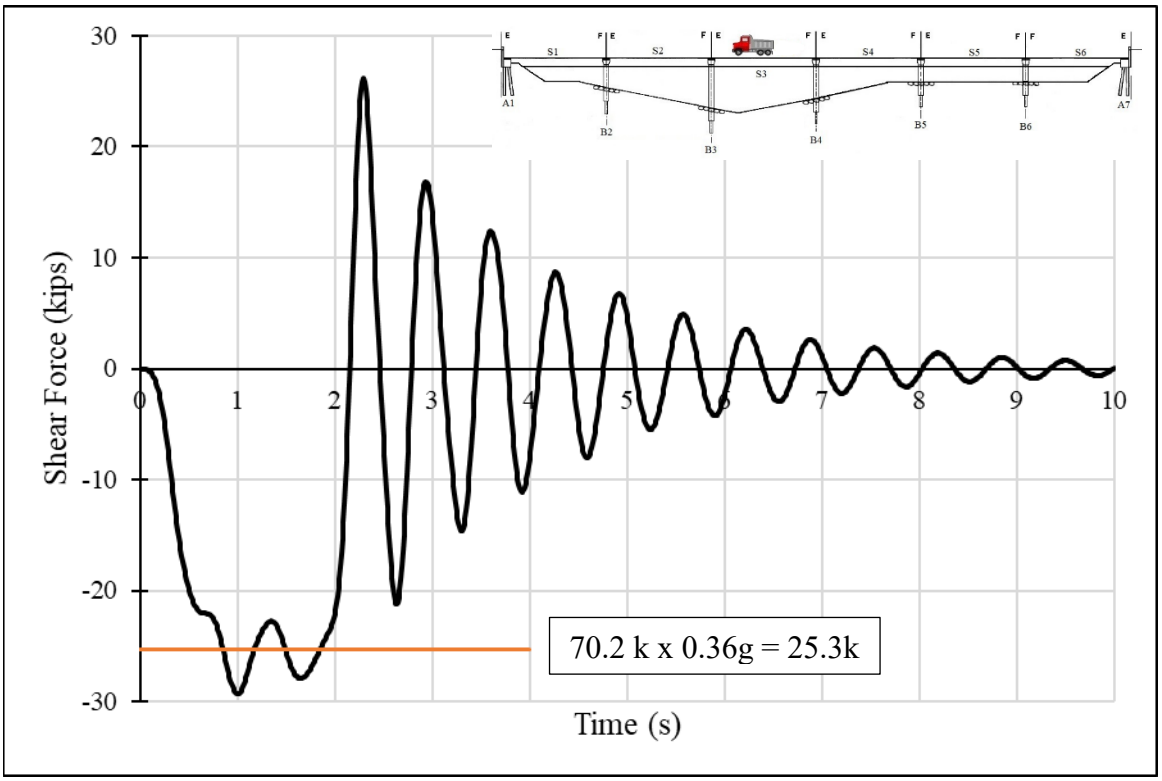

Figure 4-35 – Shear Force in Substructure from Center of Span 3 Braking Test 4

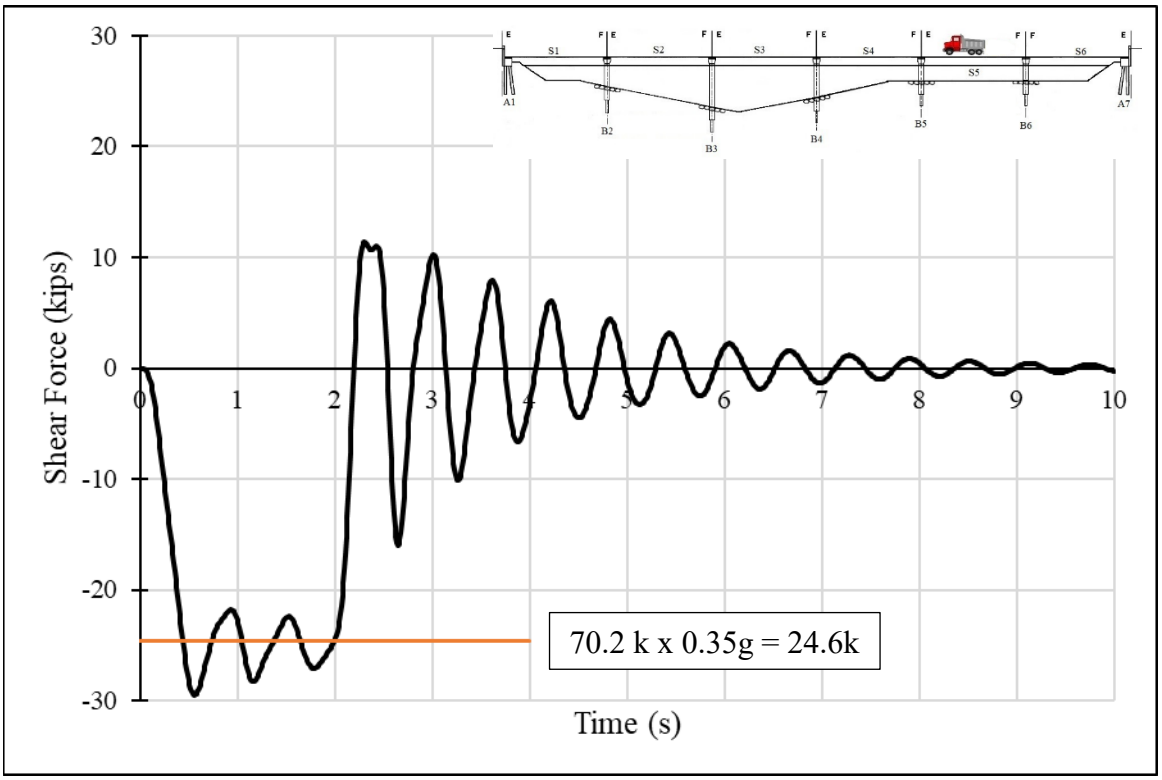

Figure 4-36 – Shear Force in Substructure from Center of Span 5 Braking Test 2

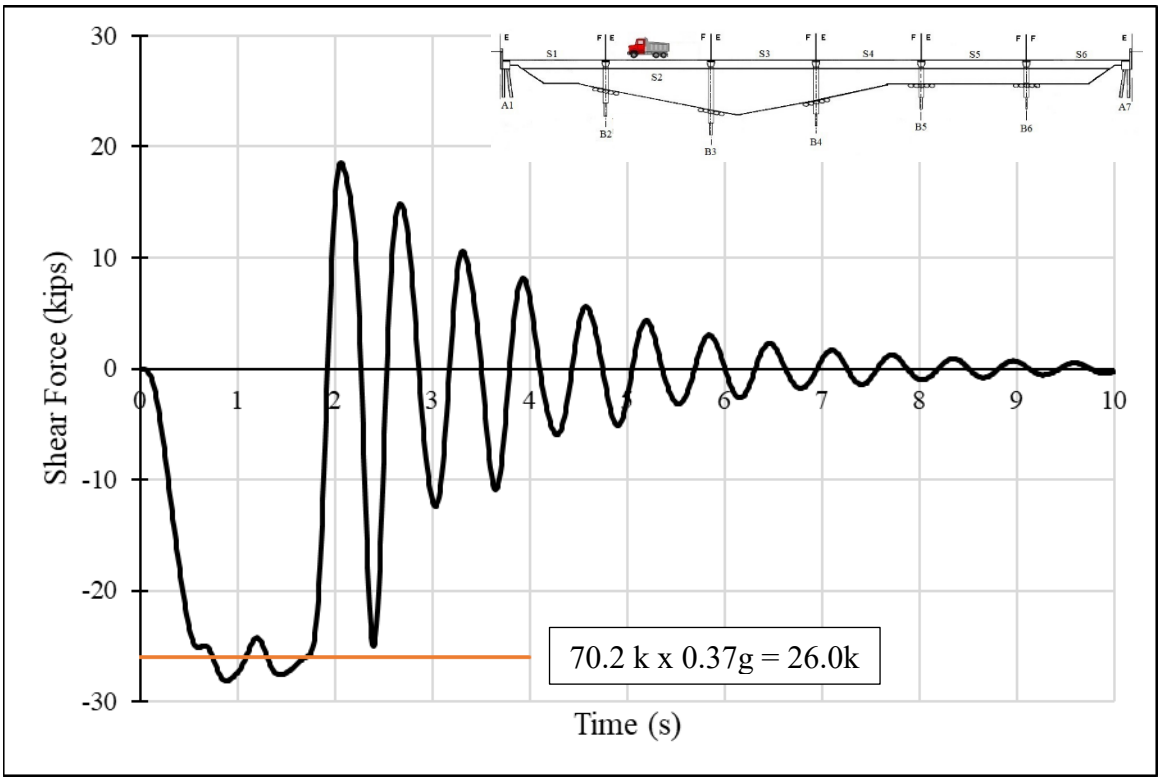

Figure 4-37 – Shear Force in Substructure from the Right Side of Span 2 Braking Test 2

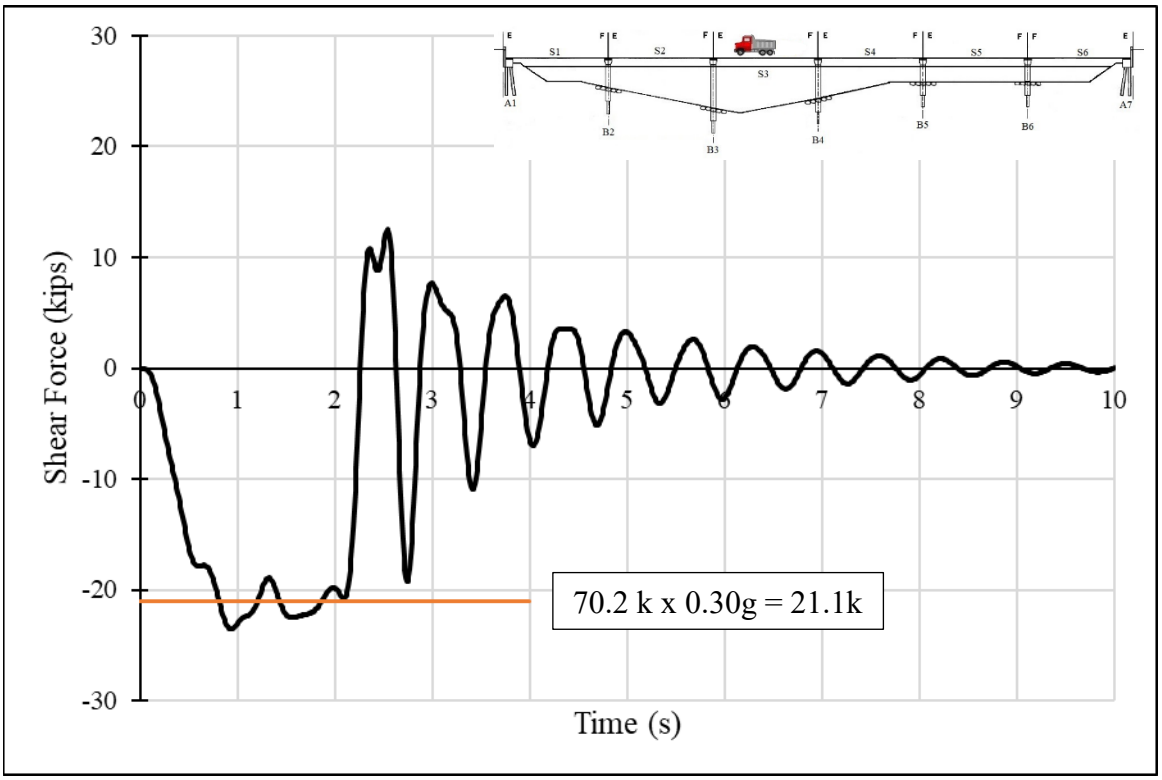

Figure 4-38 – Shear Force in Substructure from the Right Side of Span 3 Braking Test 3

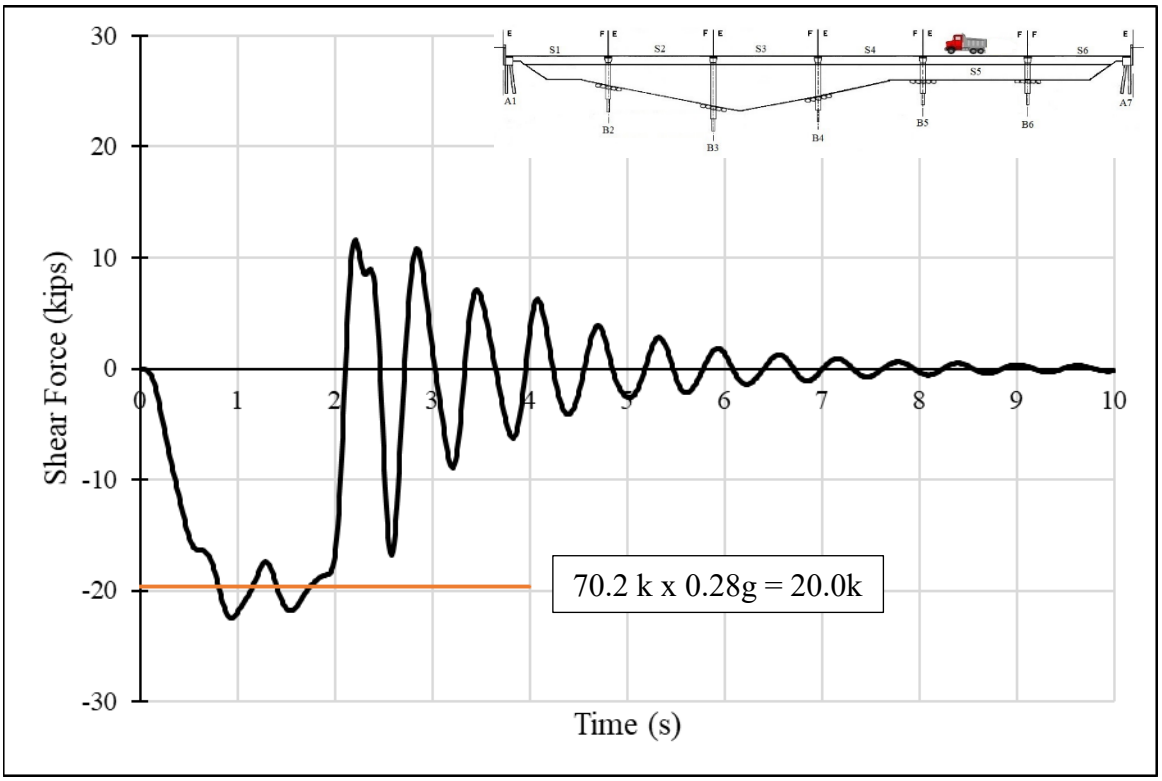

Figure 4-39 – Shear Force in Substructure from the Right Side of Span 5 Braking Test 1

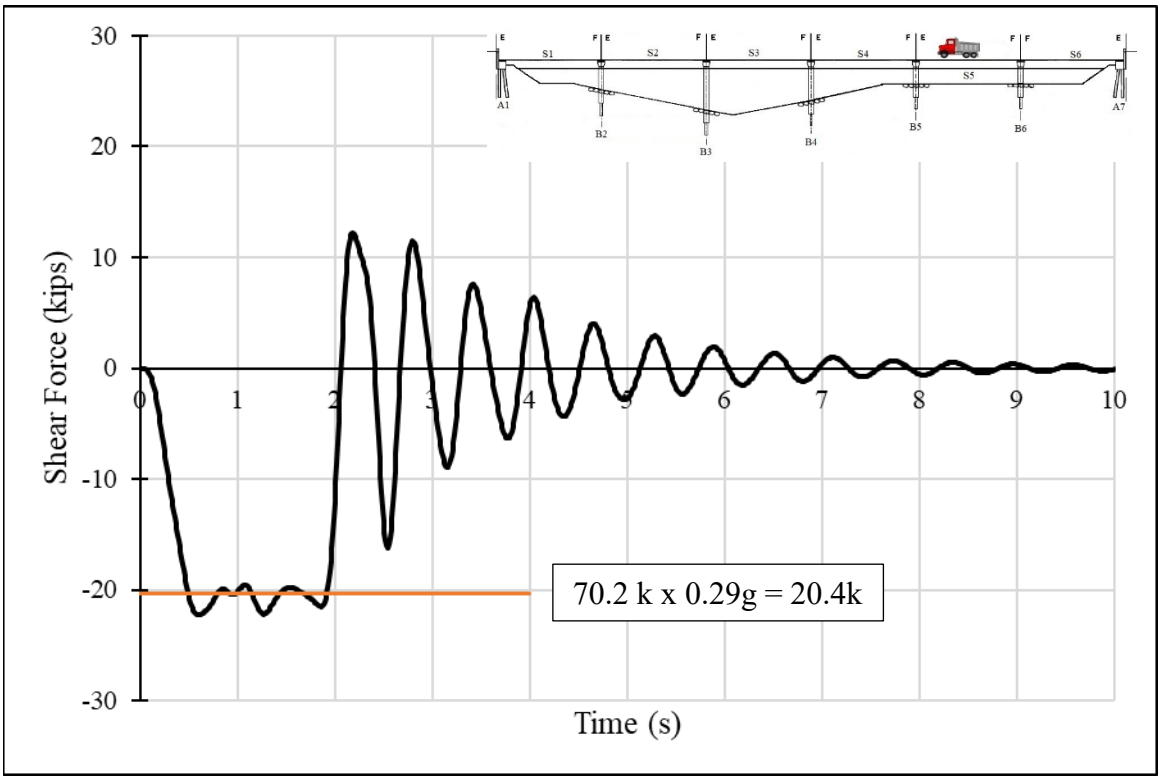

Figure 4-40 – Shear Force in Substructure from the Right Side of Span 5 Braking Test 3

4.3.1 Analysis of Dynamic Force Distribution

When analyzing each test's shear force, the peak value is approximately equal to the static horizontal braking force. The distribution of the total force among the components is more difficult to track in a dynamic situation. The figures in Chapter 4.3.1.1 through Chapter 4.3.1.6 (Figures 4-41 through 4-82) are the shear forces of each abutment or bent compared to the total shear force experienced by the entire substructure for the test deemed best from every span loading condition. The jumps in percentages and occasional steep drop offs in the percentage of force felt by the member results from the total amount of force in the entire substructure being very small, therefore, that component at that time step could be responsible for almost the entire force even though it is experiencing a small shear force itself.

The best test was selected by which model corresponded best to the field data, and in the situation where only one trial was conducted for a given loading condition this was because only the best test from the field data was processed and available for comparisons. The test that were determined best were: center of span 2 test 1, center of span 3 test 4, center of span 5 test 2, the right side of span 2 test 2, the right side of span 3 test 3, and the right side of span 5 test 1.

4.3.1.1 Horizontal Substructure Forces Resulting from Braking at Center of Span 2

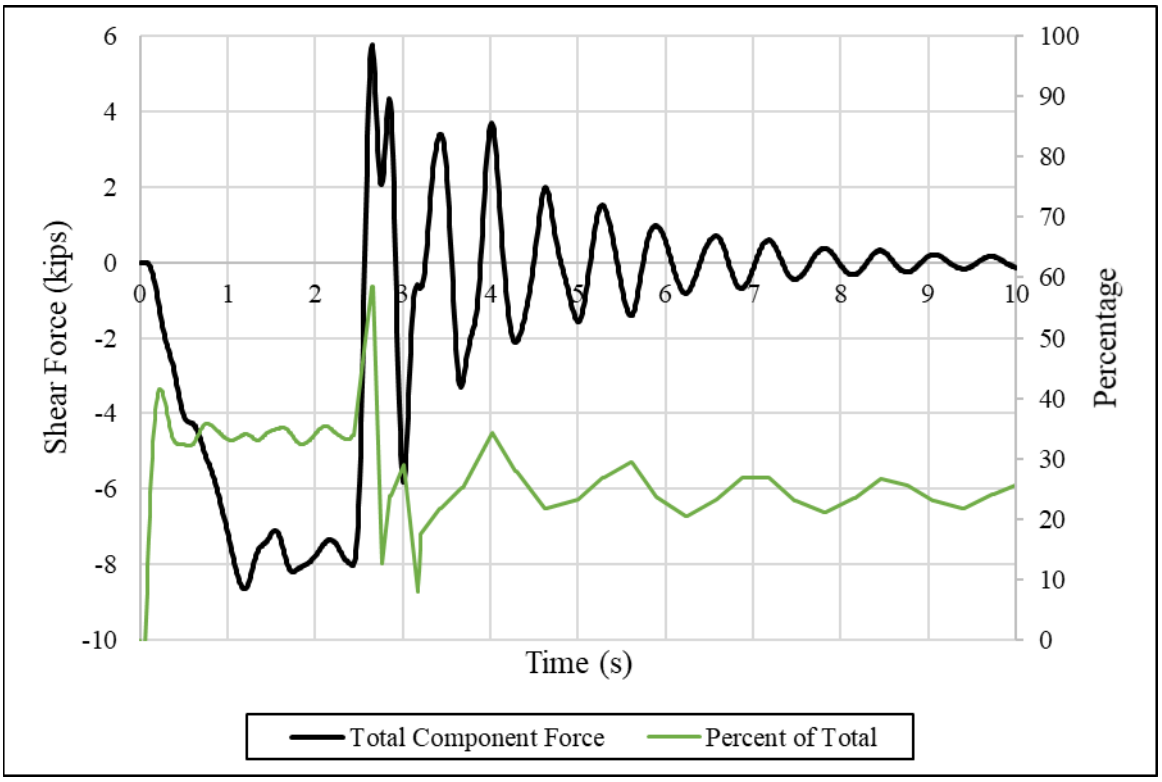

Figure 4-41 – Abutment 1 Horizontal Force due to Braking at Center of Span 2

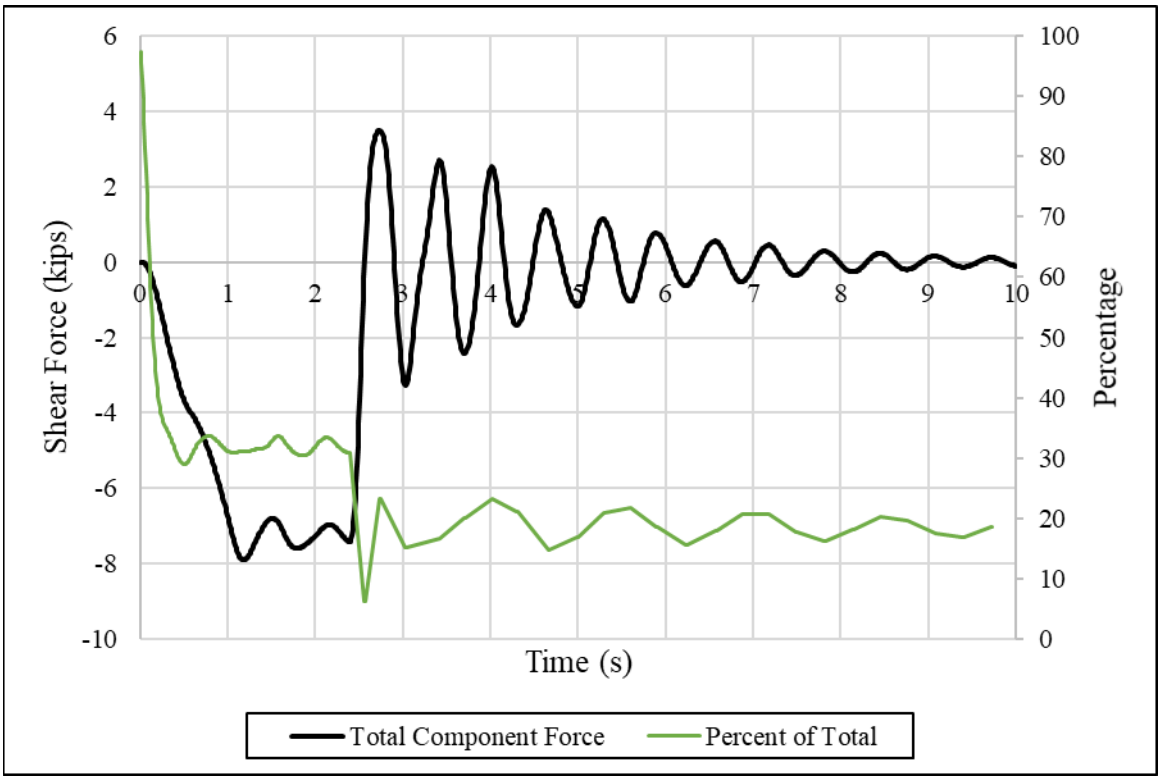

Figure 4-42 – Bent 2 Horizontal Force due to Braking at Center of Span 2

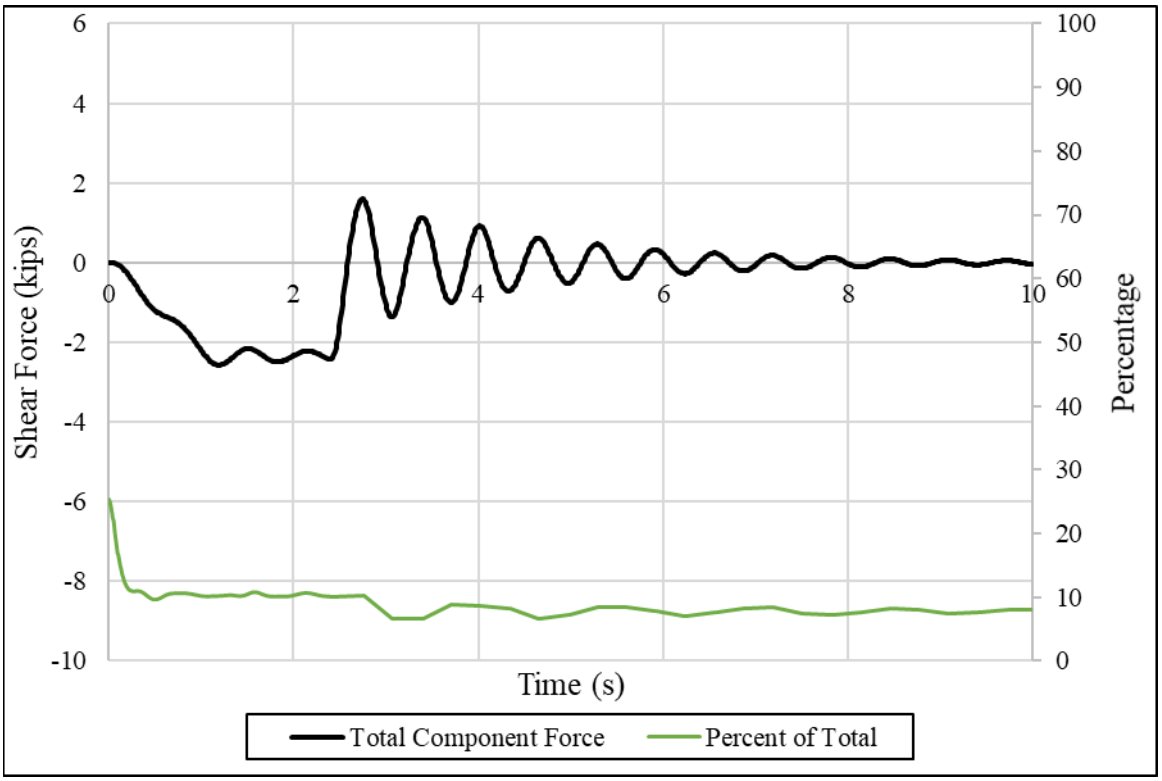

Figure 4-43 – Bent 3 Horizontal Force due to Braking at Center of Span 2

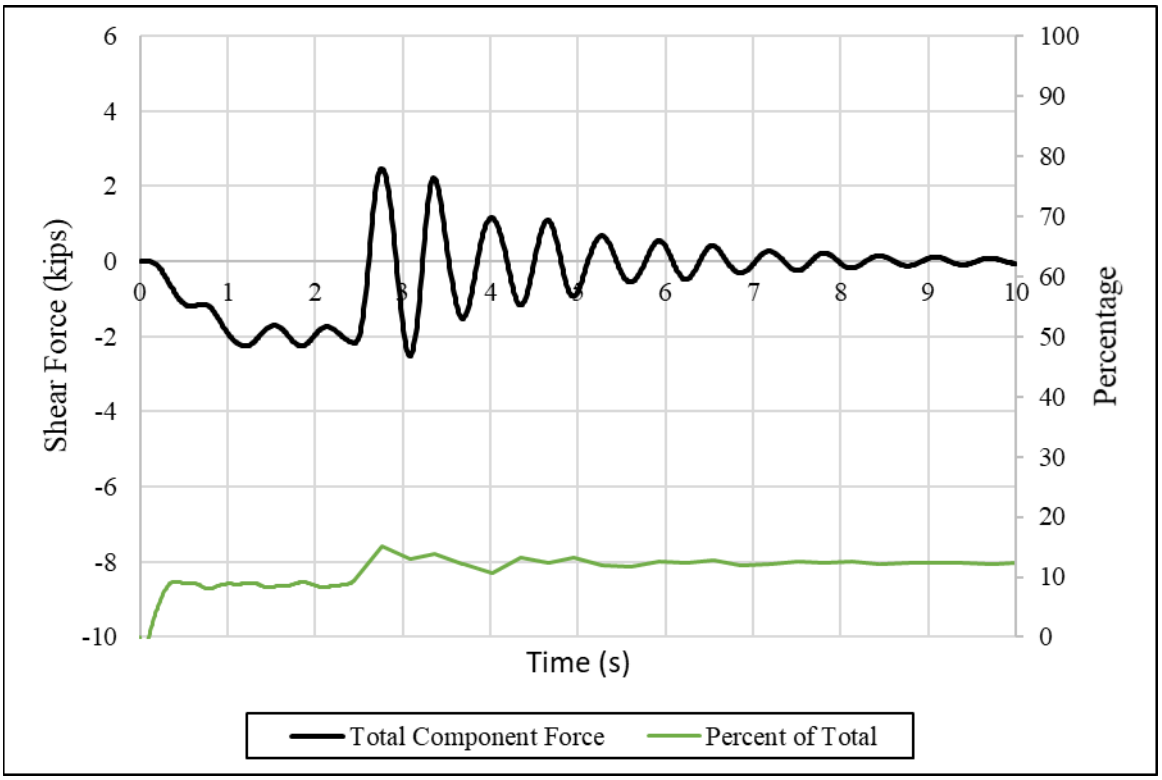

Figure 4-44 – Bent 4 Horizontal Force due to Braking at Center of Span 2

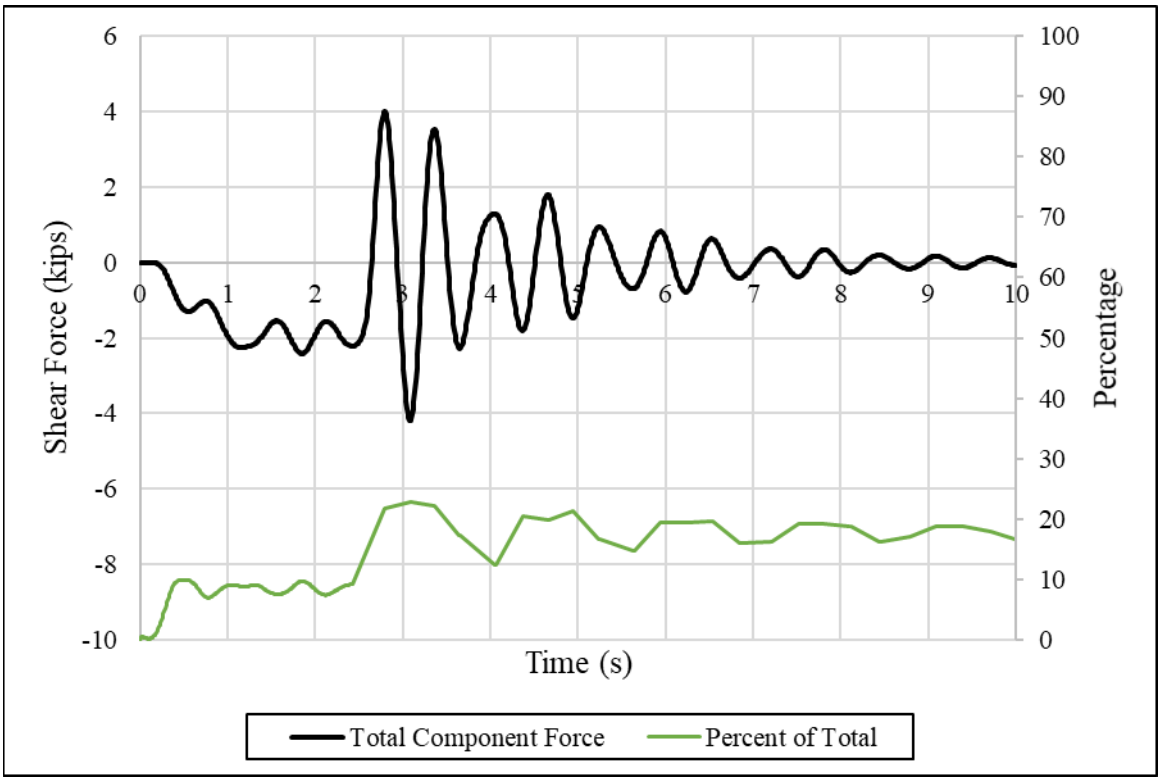

Figure 4-45 – Bent 5 Horizontal Force due to Braking at Center of Span 2

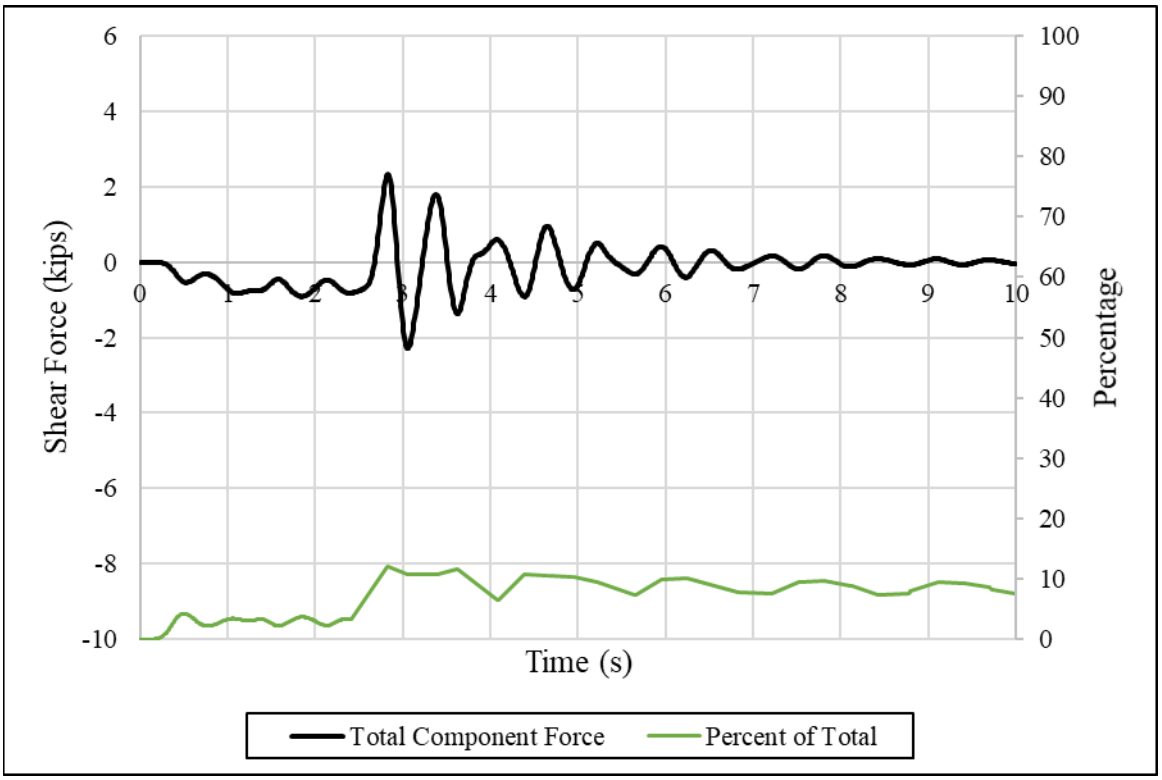

Figure 4-46 – Bent 6 Horizontal Force due to Braking at Center of Span 2

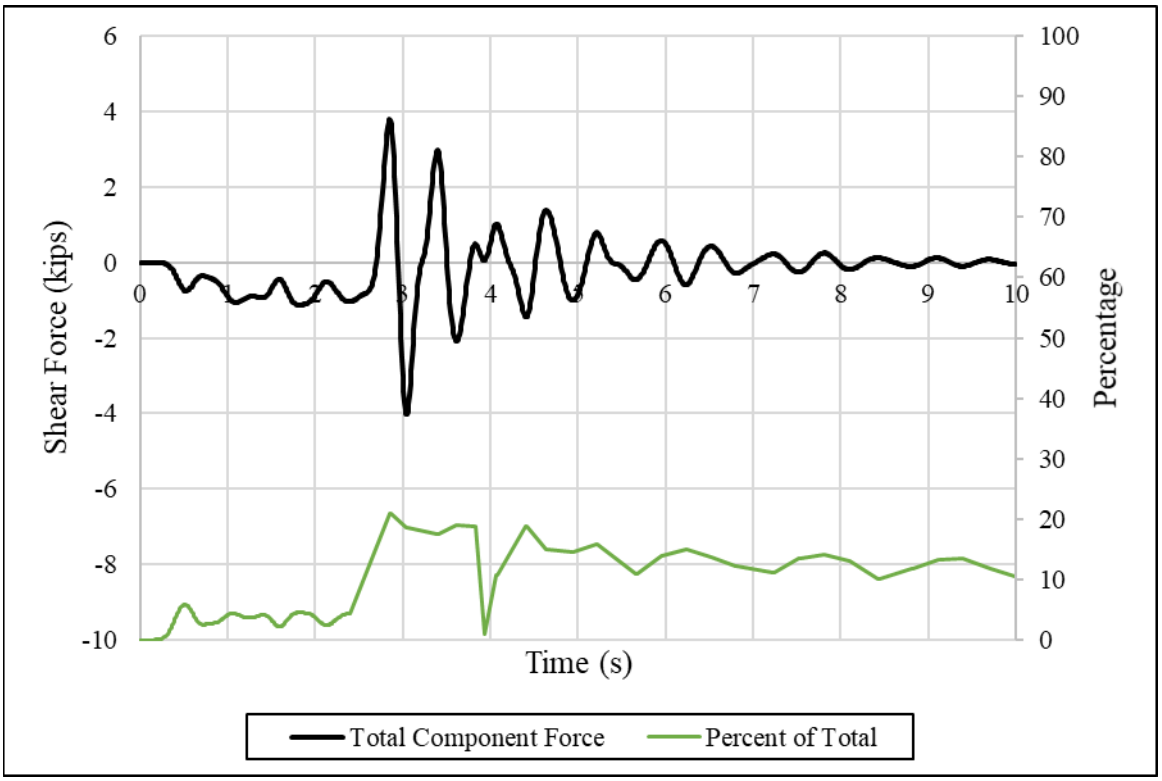

Figure 4-47 – Abutment 7 Horizontal Force due to Braking at Center of Span 2

For this test, the maximum total horizontal shear force from the truck braking from the entire substructure was approximately 23 kips. When broken down by component, abutment 1 and bent 2 carried the greatest portion of the applied force. Abutment 1 peaked at approximately 31 percent, 7.9 kips, and bent 2 peaked at approximately 31 percent of the total, 7.5 kips. This is similar to the static test where abutment 1 felt the greatest shear force, closely followed by the amount of force in bent 2. Beyond the span that the braking occurred on, the amount of individual bent or abutment shear force remained relatively low, at or below 20 percent of the entire force in the whole substructure.

4.3.1.2 Horizontal Substructure Forces Resulting from Braking at Center of Span 3

From the three tests conducted on span 3, the third provided the best data. Figure 4-48 through Figure 4-54 presents the horizontal shear force in each bent or abutment compared to the total horizontal shear force experienced by the entire substructure for this test.

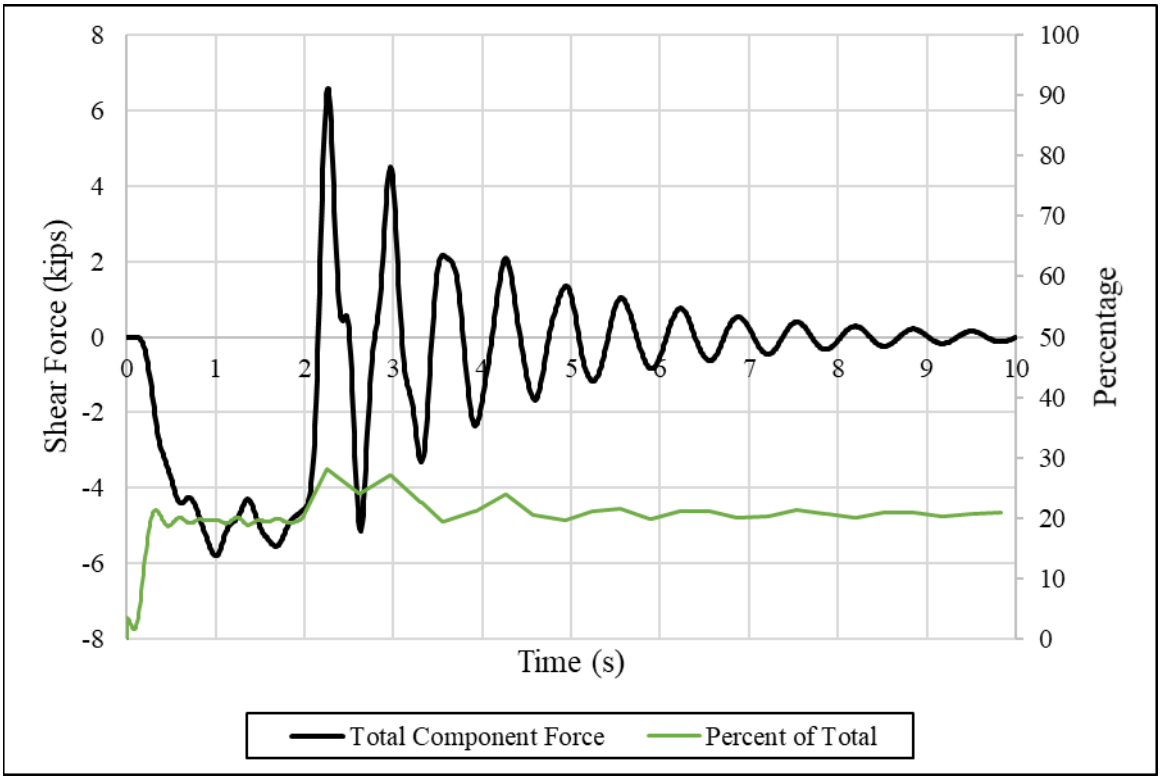

Figure 4-48 – Abutment 1 Horizontal Force due to Braking at Center of Span 3

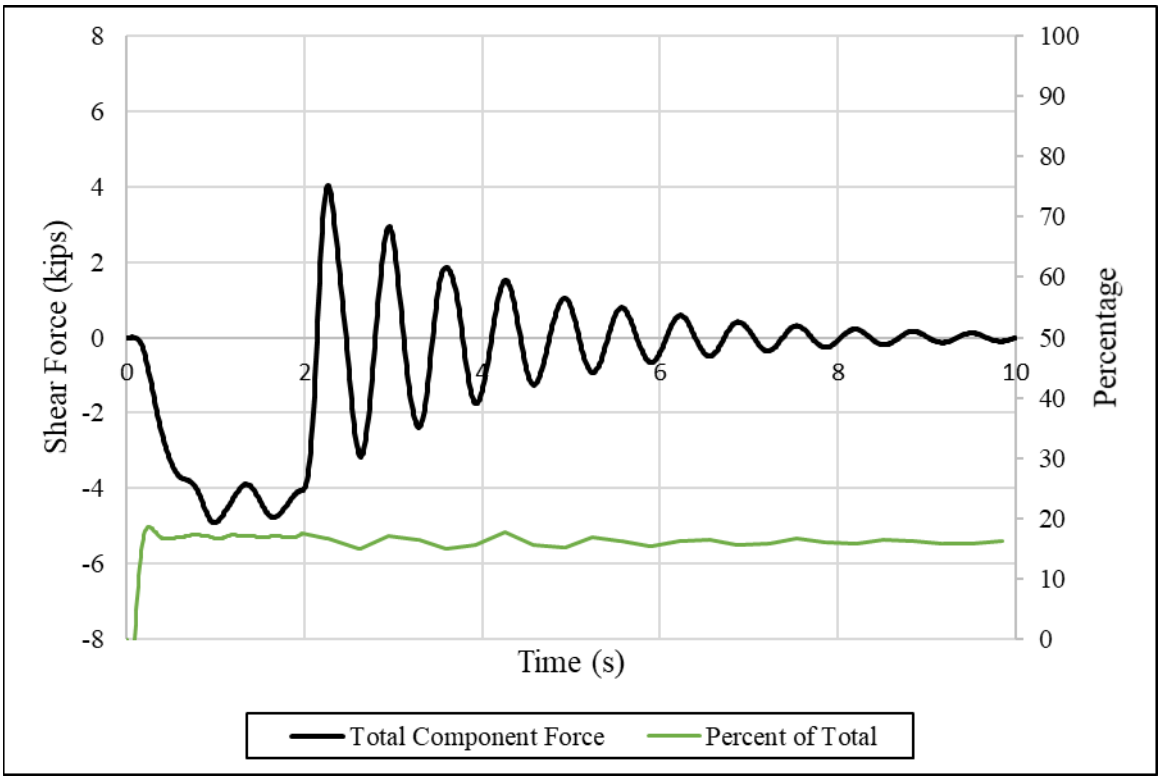

Figure 4-49 – Bent 2 Horizontal Force due to Braking at Center of Span 3

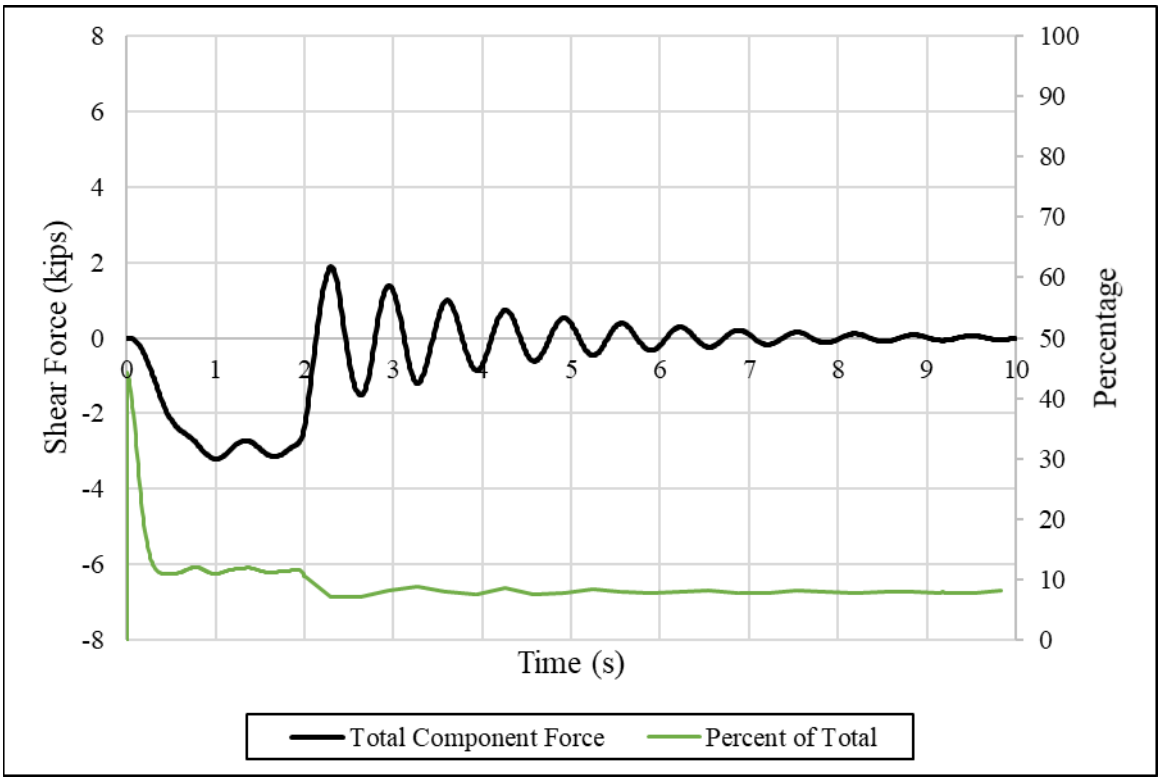

Figure 4-50 – Bent 3 Horizontal Force due to Braking at Center of Span 3

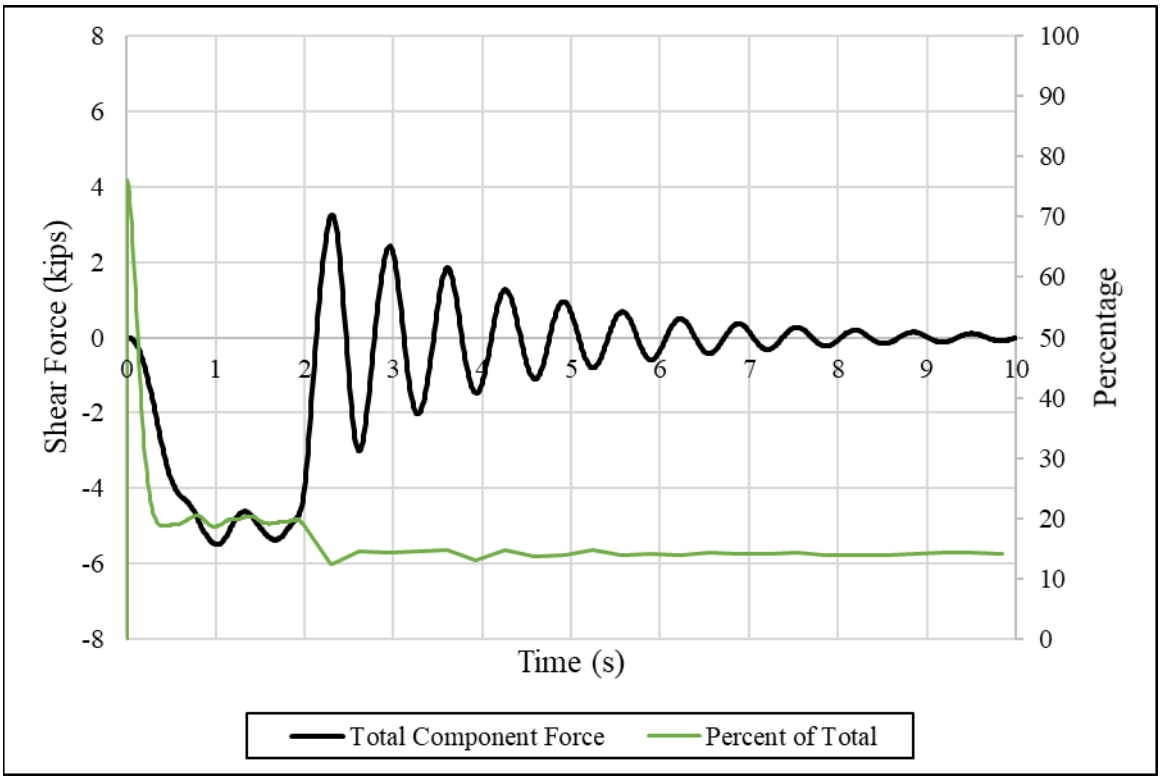

Figure 4-51 – Bent 4 Horizontal Force due to Braking at Center of Span 3

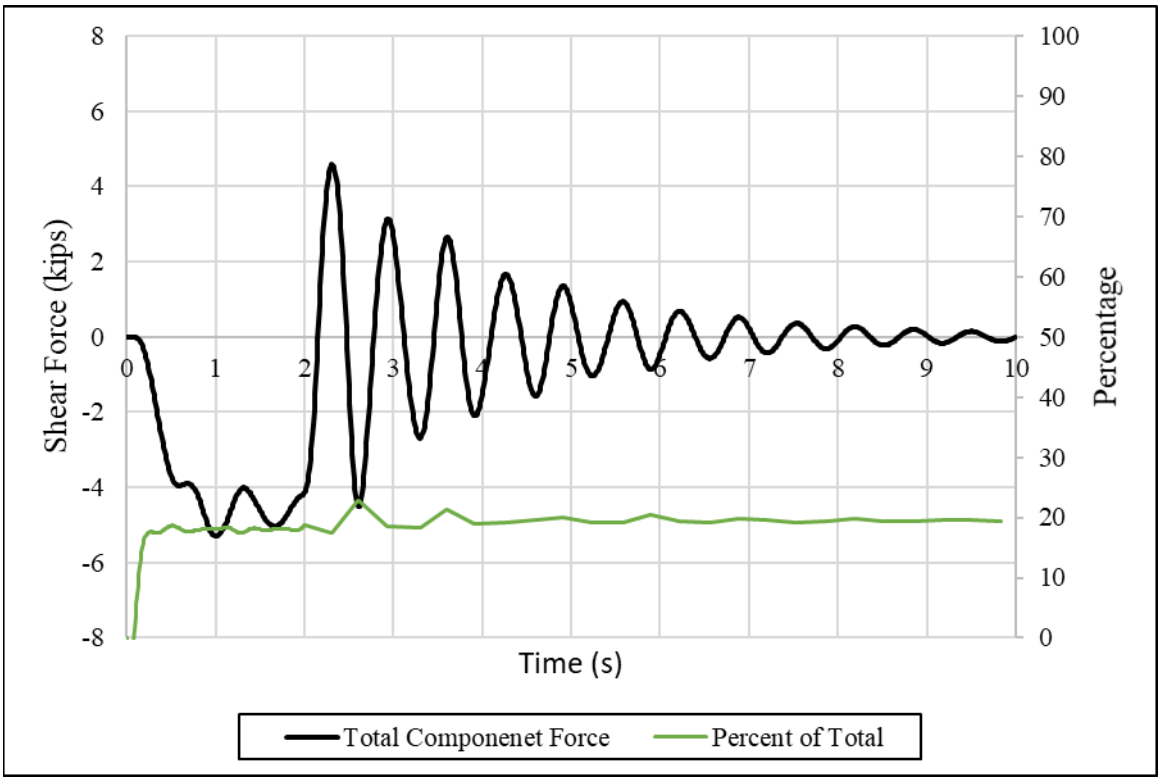

Figure 4-52 – Bent 5 Horizontal Force due to Braking at Center of Span 3

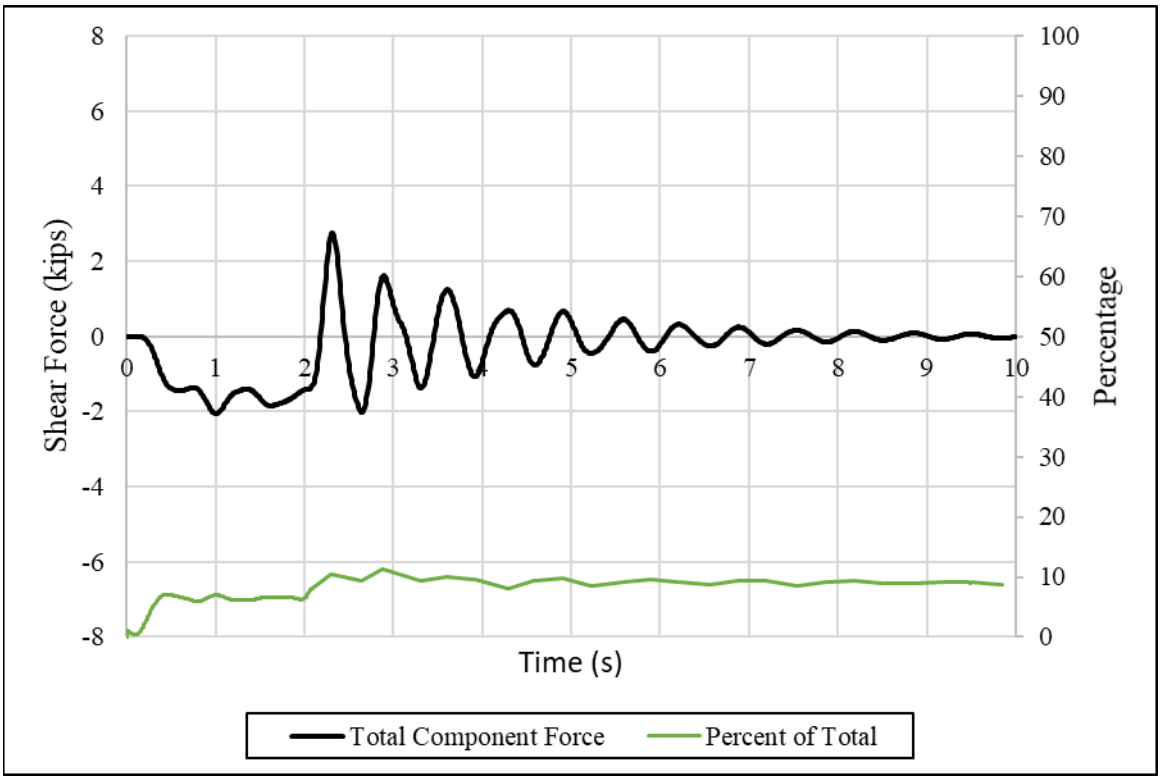

Figure 4-53 – Bent 6 Horizontal Force due to Braking at Center of Span 3

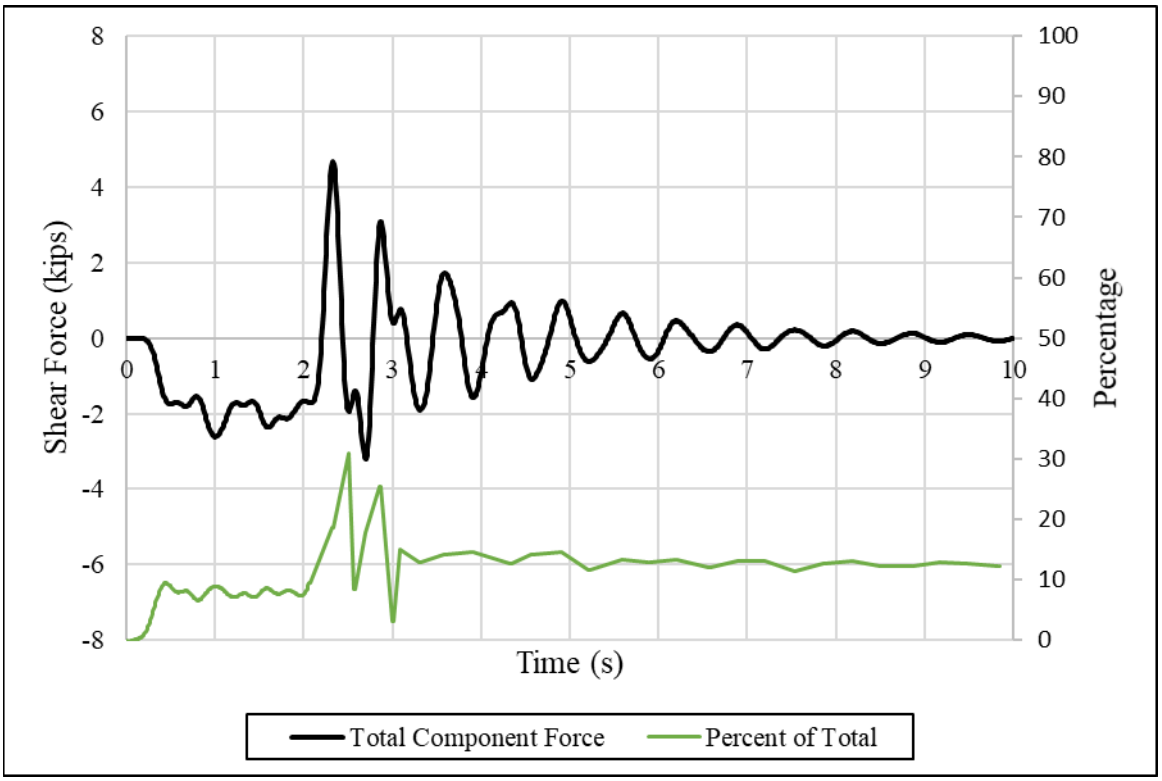

Figure 4-54 – Abutment 7 Horizontal Force due to Braking at Center of Span 3

On test 4 of the center of span 3, abutment 1 and bent 4 were the components that experienced the highest horizontal shear force. Abutment 1 experienced 6.6 kips, approximately 24 percent, and bent 4 felt approximately 20 percent of the total force, resulting in about 5 kips in each member. The maximum total horizontal force experienced during this test was approximately 25 kips. During the free response phase, all of components remained at or below 20 percent shear force distributed to them. This, again, corresponds to the static tests where one of the bents supporting the span that was loaded experienced a larger amount of force then other members.

4.3.1.3 Horizontal Substructure Forces Resulting from Braking at Center of Span 5

From the tests conducted on span 5, the second provided the best data. Figure 4-55 through Figure 4-61 presents the horizontal shear force in each bent or abutment compared to the total horizontal shear force experienced by the entire substructure for this test.

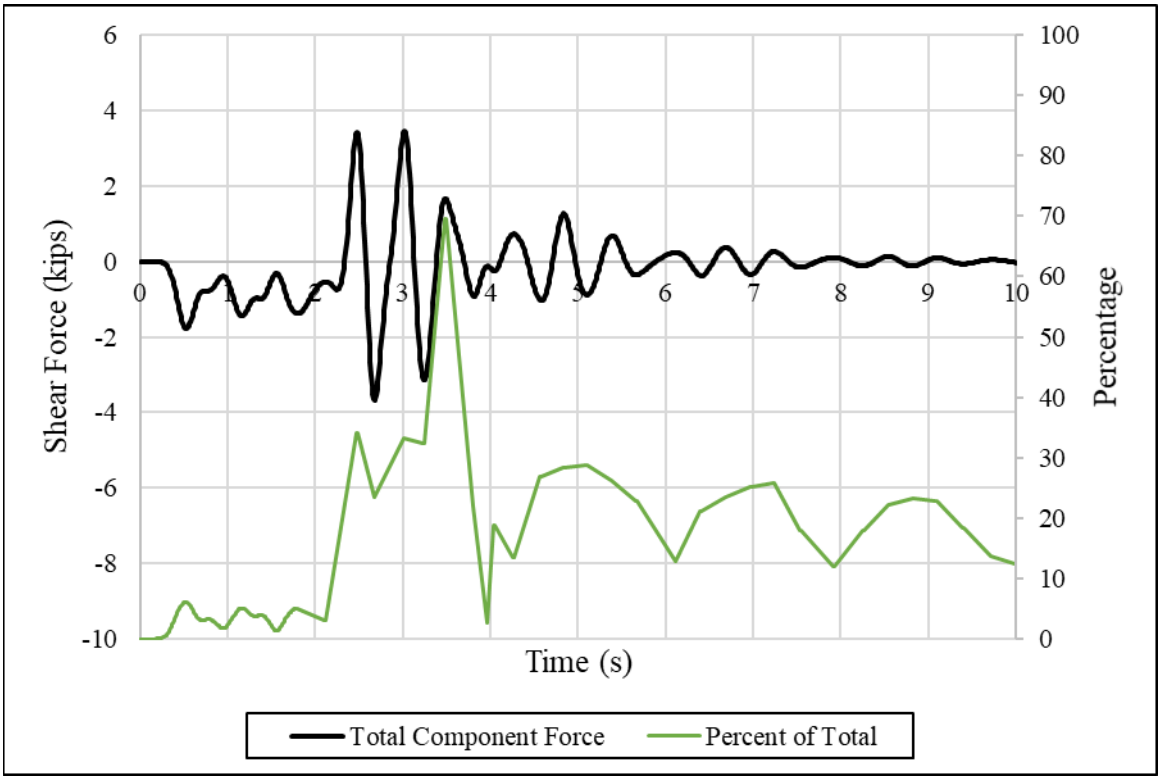

Figure 4-55 – Abutment 1 Horizontal Force due to Braking at Center of Span 5

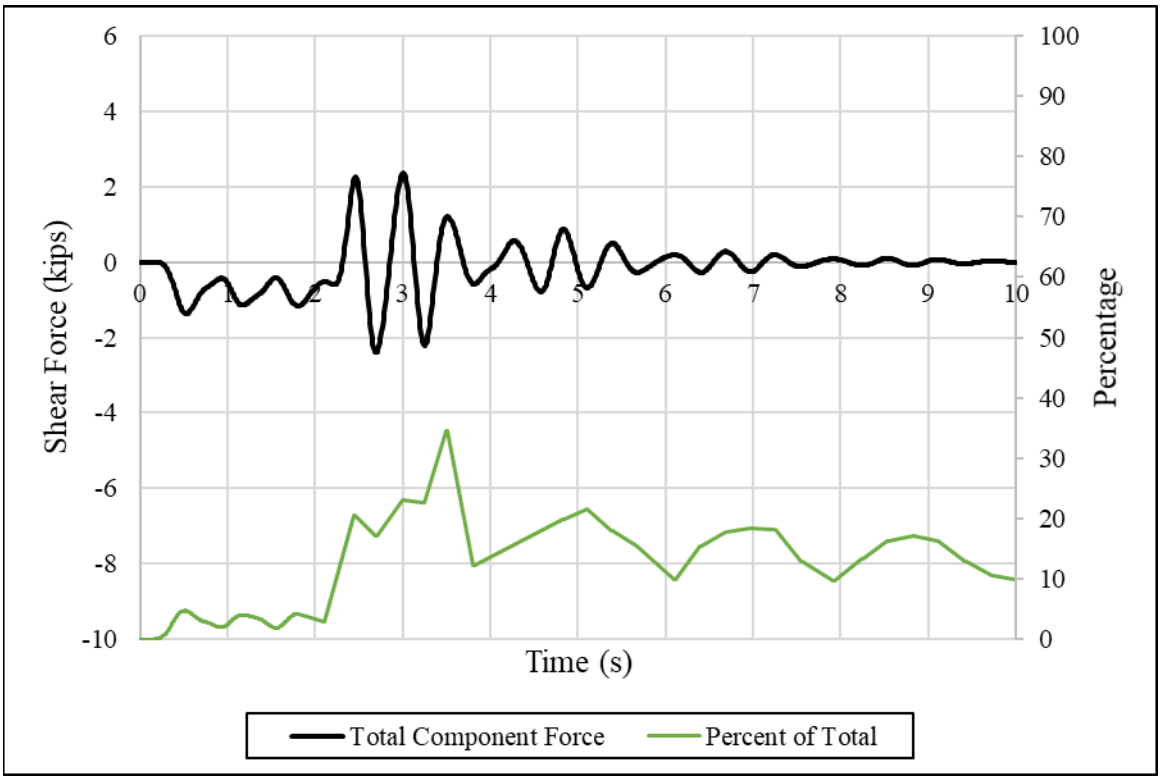

Figure 4-56 – Bent 2 Horizontal Force due to Braking at Center of Span 5

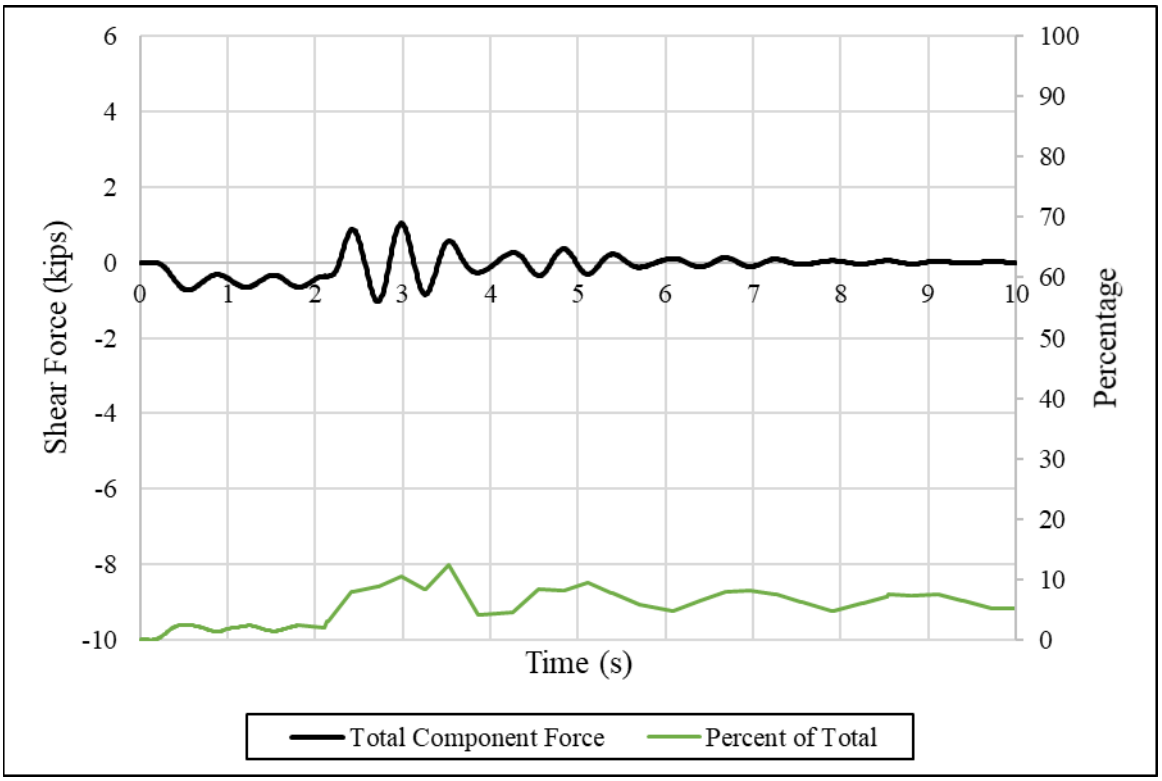

Figure 4-57 – Bent 3 Horizontal Force due to Braking at Center of Span 5

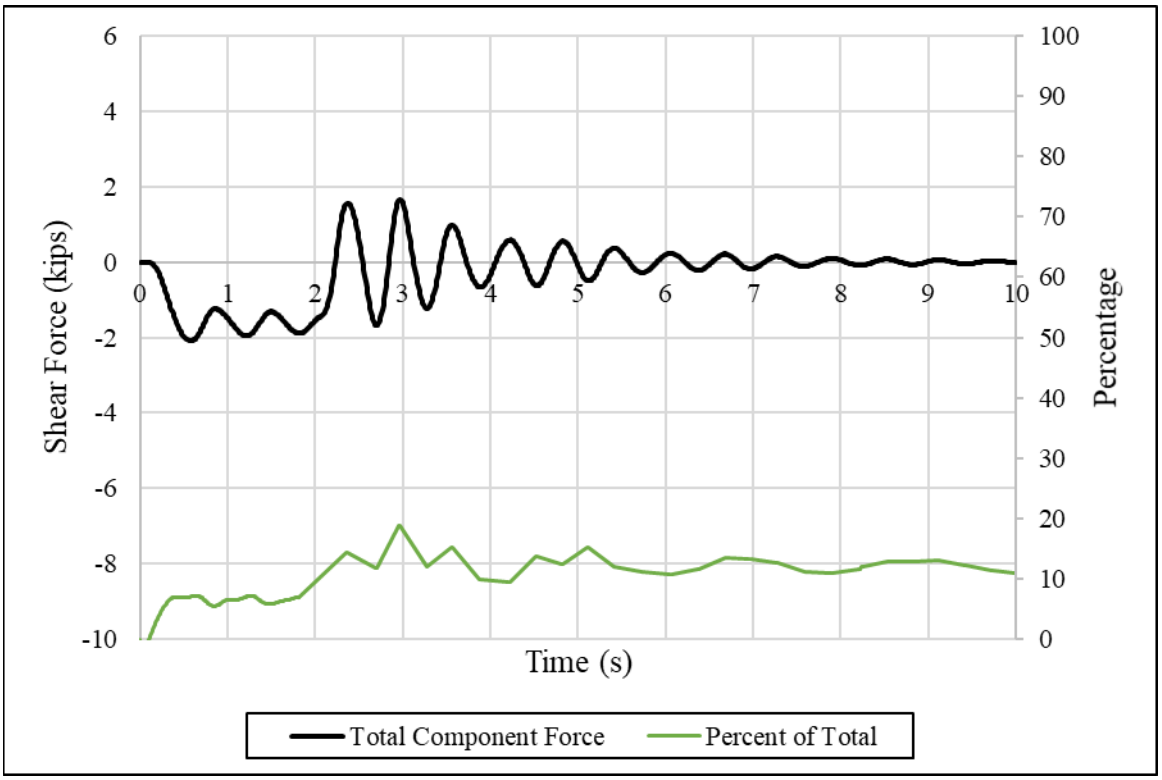

Figure 4-58 – Bent 4 Horizontal Force due to Braking at Center of Span 5

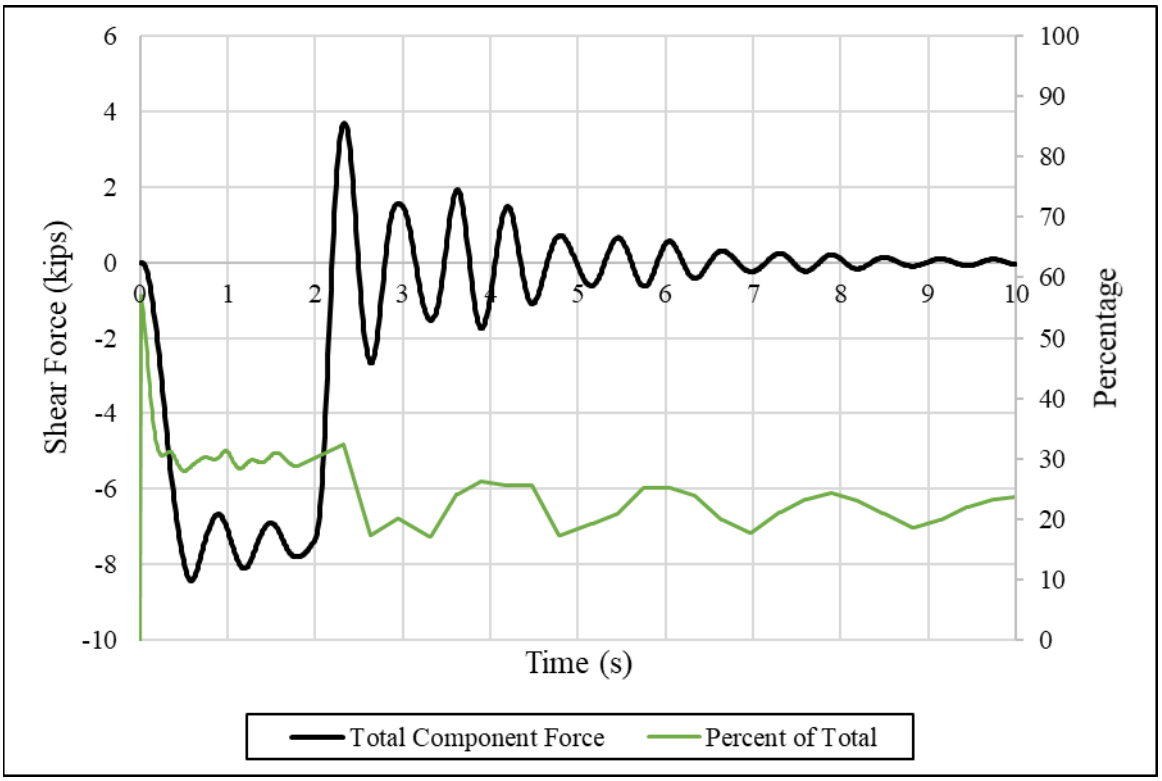

Figure 4-59 – Bent 5 Horizontal Force due to Braking at Center of Span 5

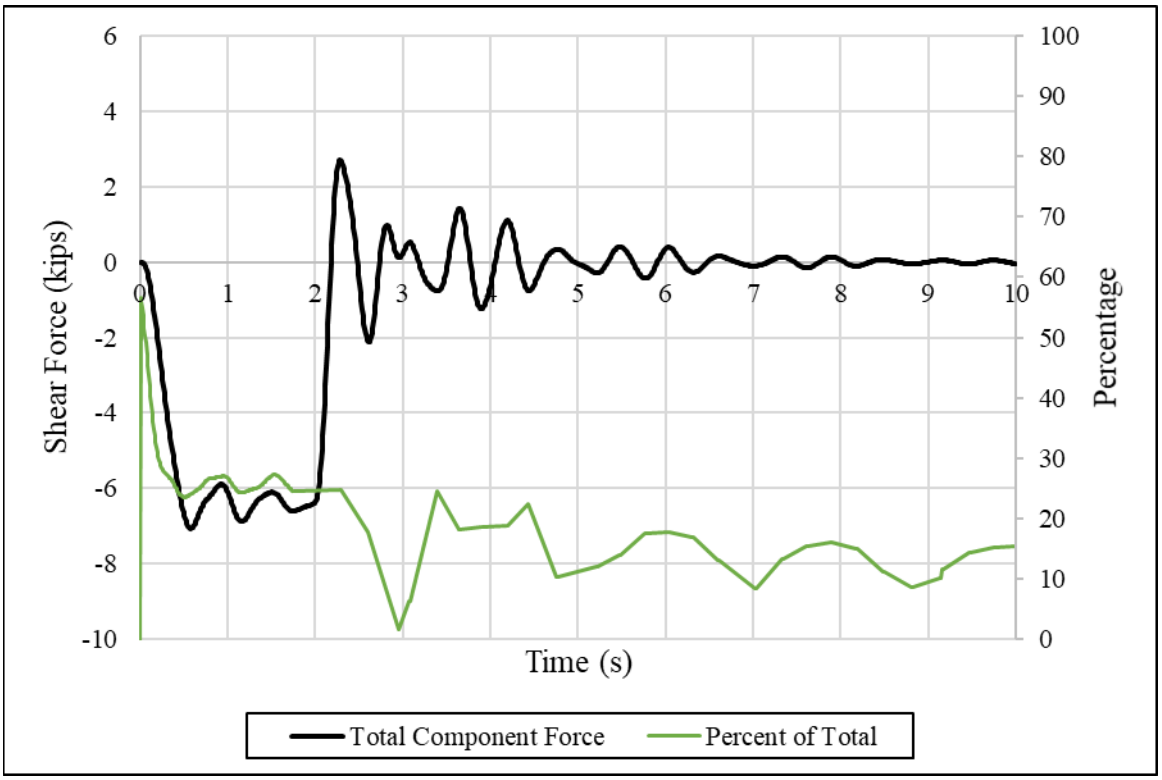

Figure 4-60 – Bent 6 Horizontal Force due to Braking at Center of Span 5

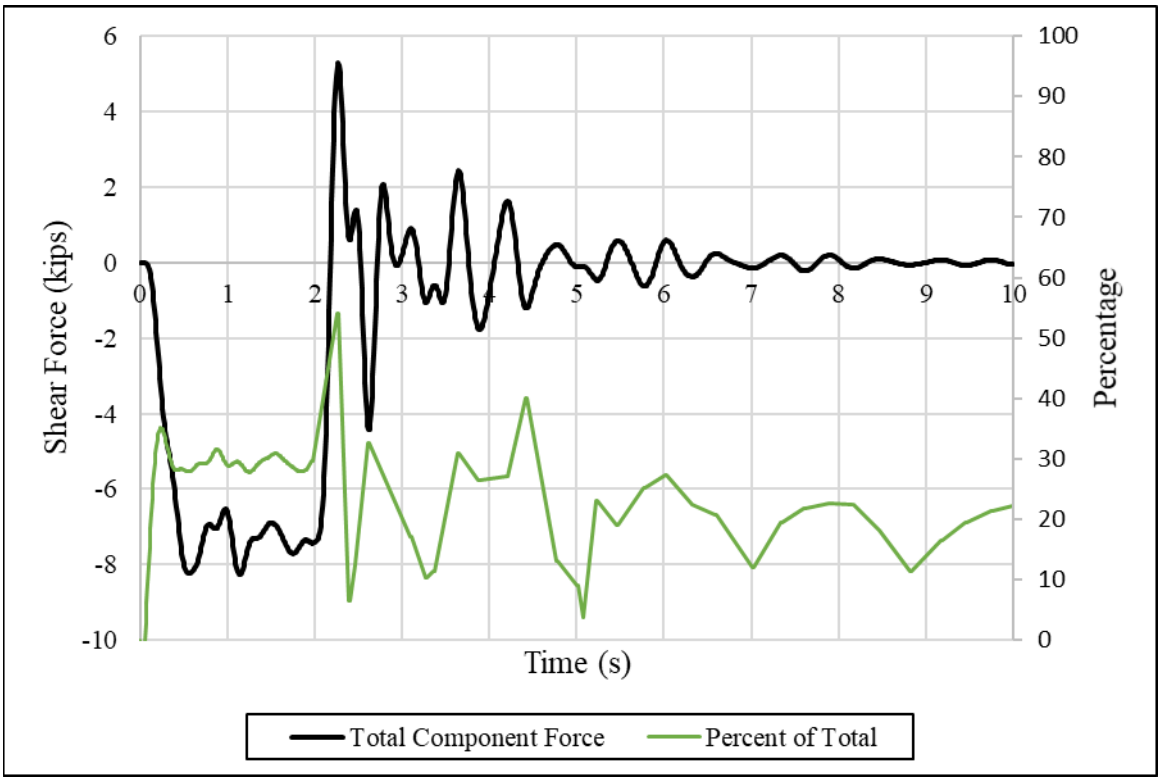

Figure 4-61 – Abutment 7 Horizontal Force due to Braking at Center of Span 5

With span 5 was braked on, the maximum total horizontal shear force that was experienced in the entire substructure was approximately 25 kips. As with the previous two braking tests, one of the abutments experienced the greatest amount of force, for this test it was abutment 7 since the braking occurred further down the bridge. Abutment 7 felt 30 percent of the total force from the entire substructure during the constant deceleration phase and approximately 7.6 kips at the maximum with a jump up to 53 percent of the total overall force during the initial phase of free response. Also, bent 5 experienced a maximum of about 7.5 kips and experienced 30 percent of the total force.

4.3.1.4 Horizontal Substructure Forces Resulting from Braking on Right of Span 2

From the tests conducted on the right side of span 2, the second provided the best data. Figure 4-62 through Figure 4-68 presents the horizontal shear force in each bent or abutment compared to the total horizontal shear force experienced by the entire substructure for this test.

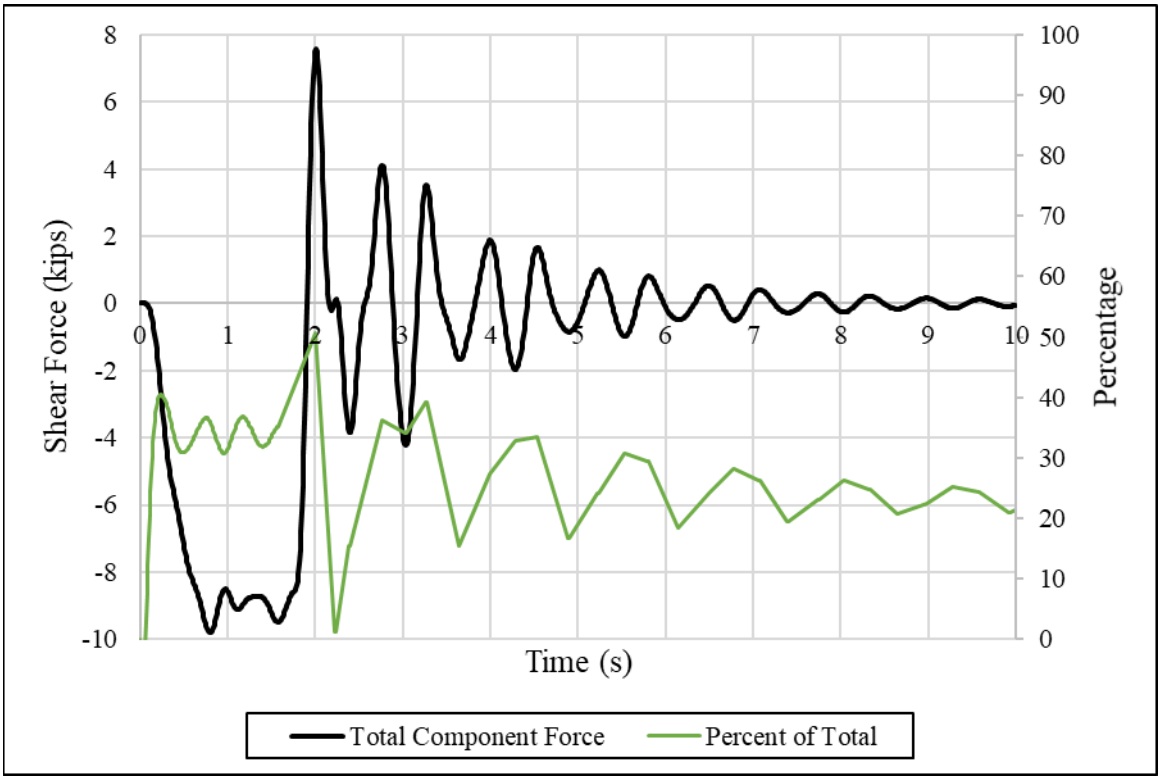

Figure 4-62 – Abutment 1 Horizontal Force due to Braking on Right of Span 2

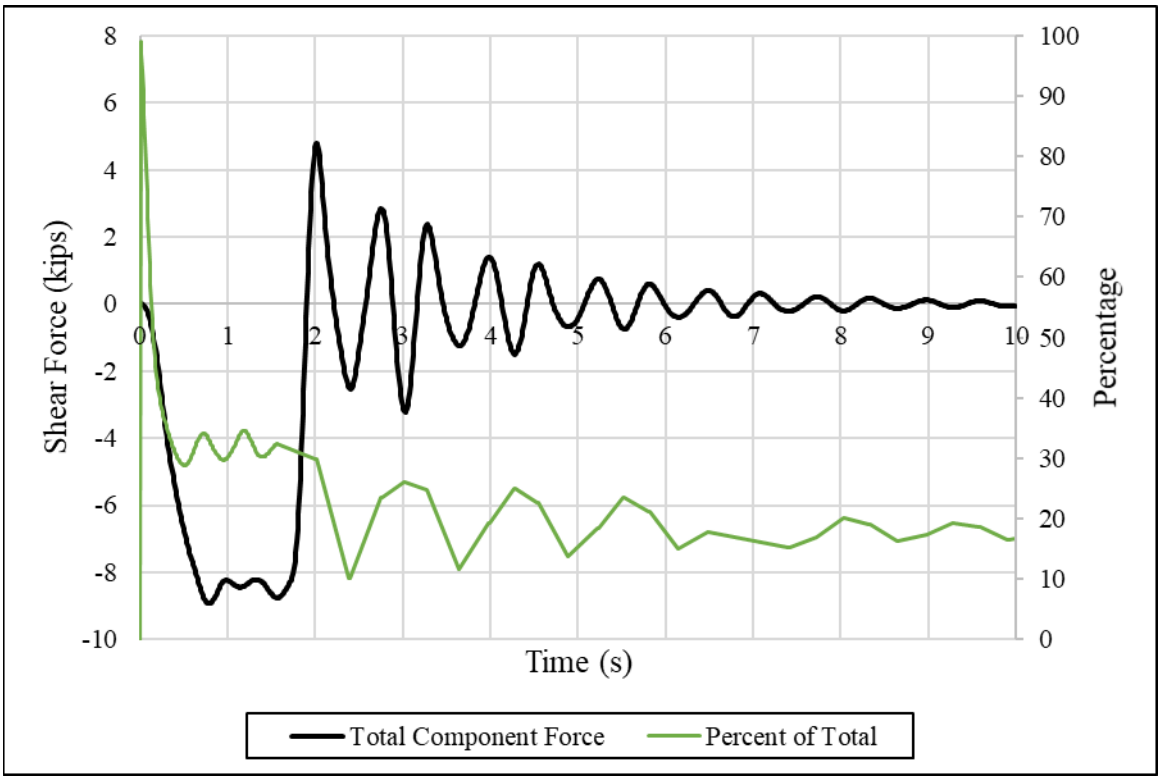

Figure 4-63 – Bent 2 Horizontal Force due to Braking on Right of Span 2

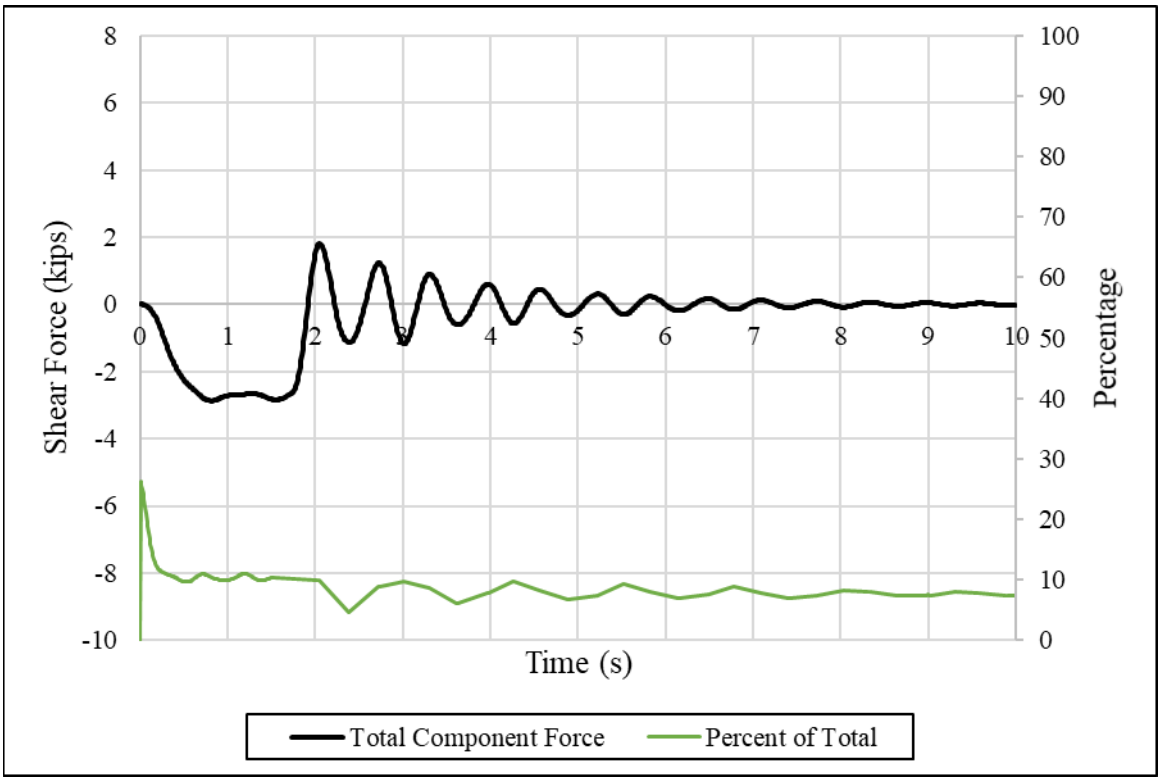

Figure 4-64 – Bent 3 Horizontal Force due to Braking on Right of Span 2

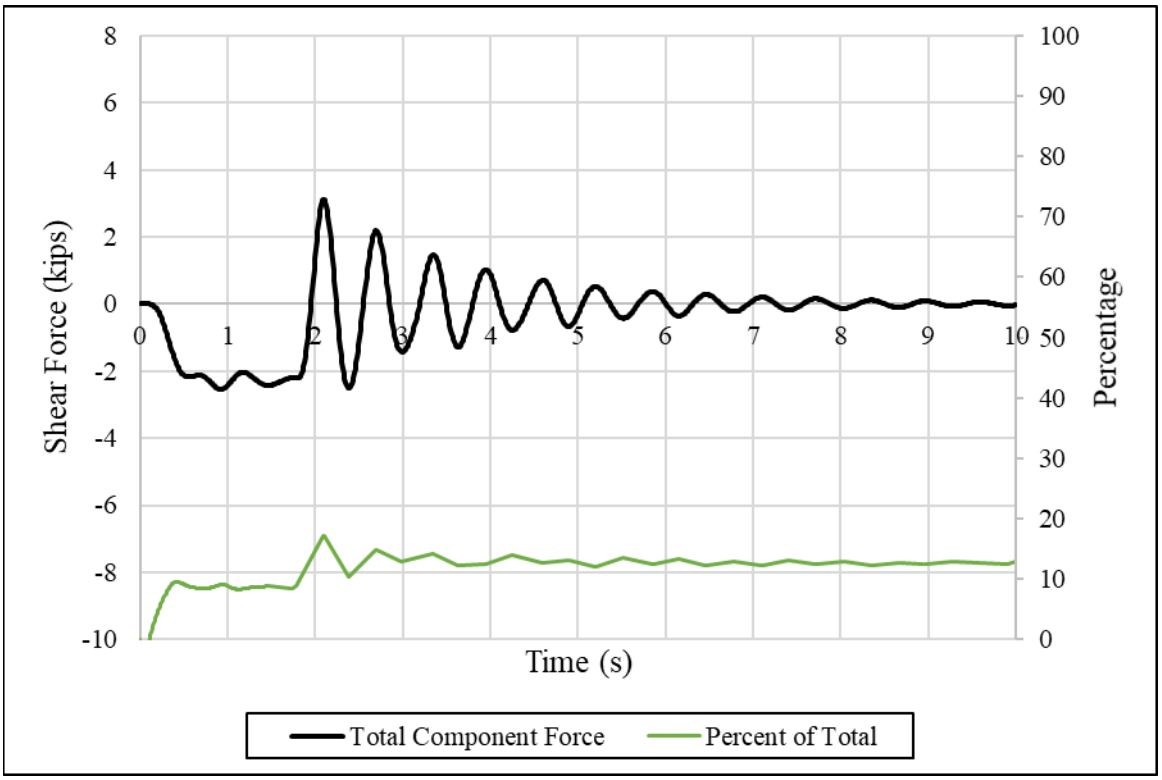

Figure 4-65 – Bent 4 Horizontal Force due to Braking on Right of Span 2

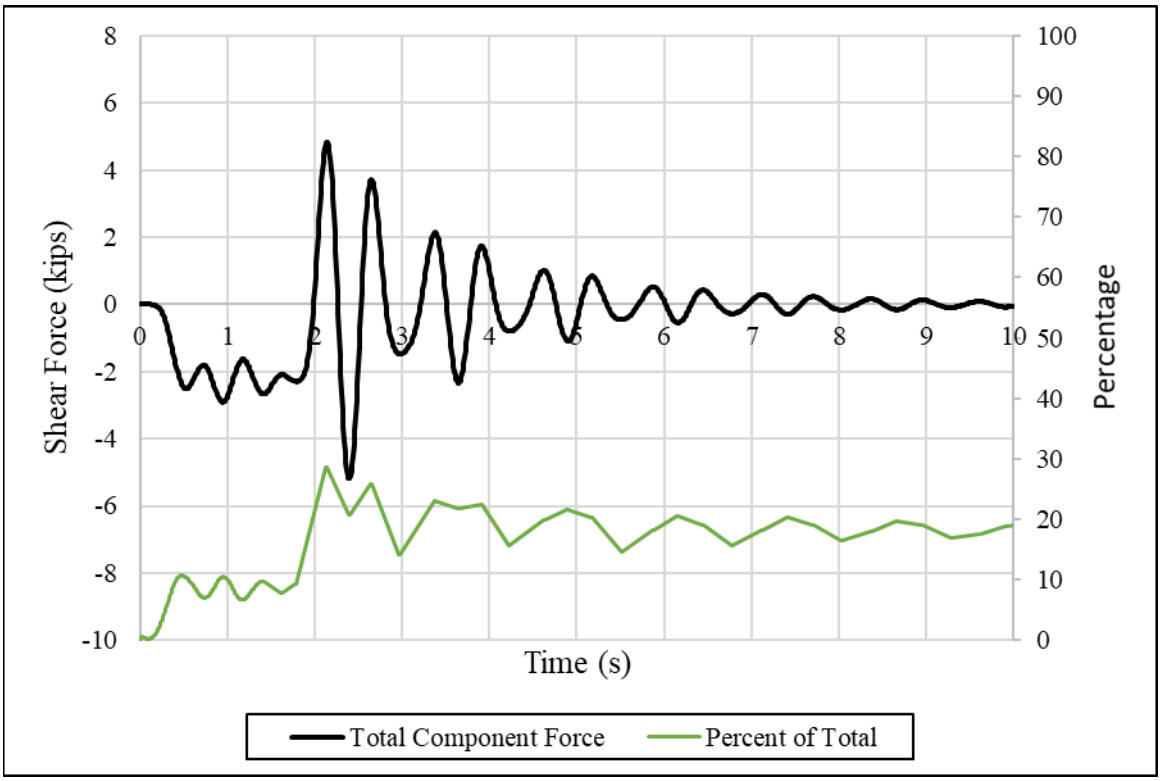

Figure 4-66 – Bent 5 Horizontal Force due to Braking on Right of Span 2

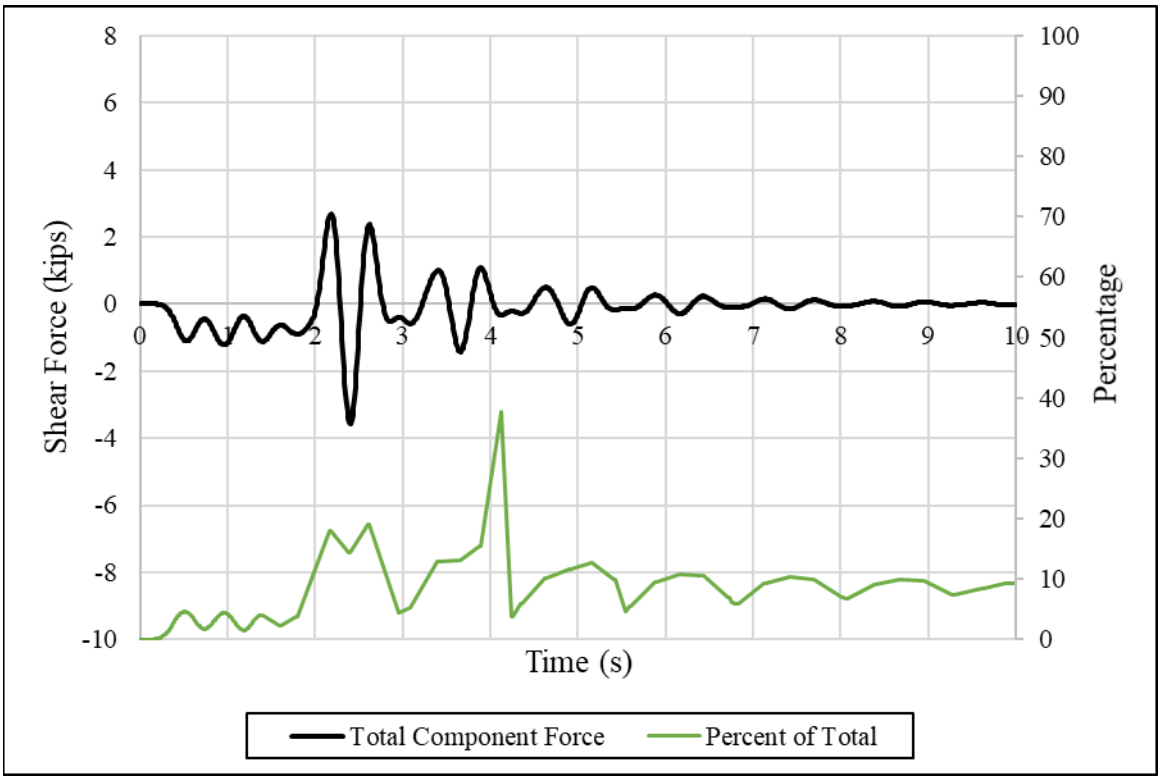

Figure 4-67 – Bent 6 Horizontal Force due to Braking on Right of Span 2

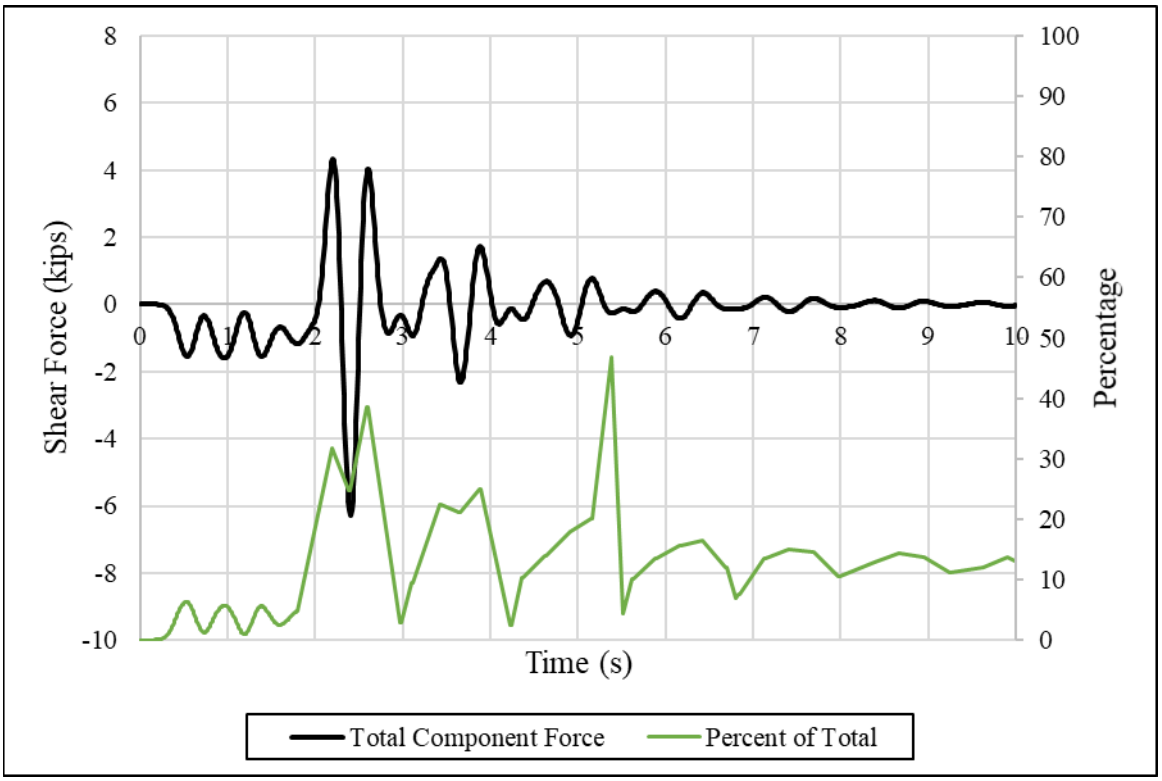

Figure 4-68 – Abutment 7 Horizontal Force due to Braking on Right of Span 2

Just as when span 2 was braked on the center, when braking on the right side abutment 1 and bent 2 experienced the highest percentage of the overall force. Abutment 1 experienced a maximum of 33 percent, 8.9 kips, during braking and bent 2 experienced 31 percent, 8.5 kips, respectively. The maximum total horizontal shear force experienced by the whole substructure during this test was approximately 26 kips.

4.3.1.5 Horizontal Substructure Forces Resulting from Braking on Right of Span 3

From the tests conducted on the right side of span 3, the third provided the best data. Figure 4-69 through Figure 4-75 presents the horizontal shear force in each bent or abutment compared to the total horizontal shear force experienced by the entire substructure for this test.

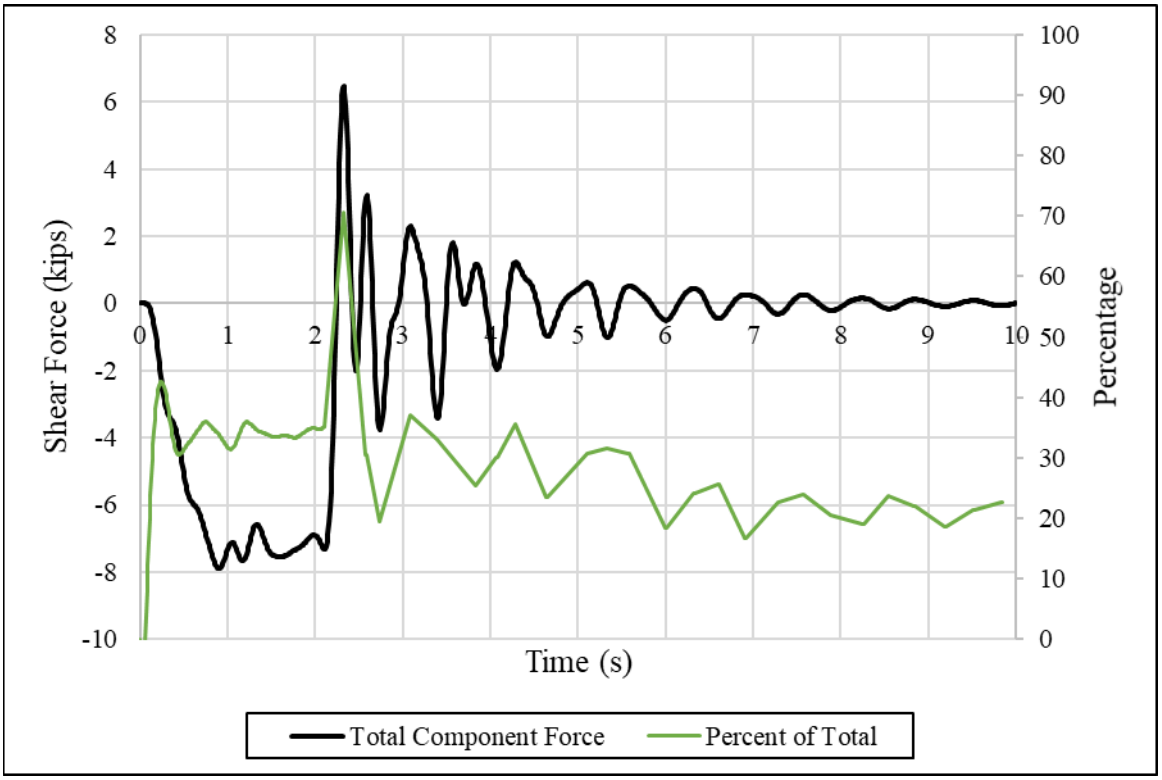

Figure 4-69 – Abutment 1 Horizontal Force due to Braking on Right of Span 3

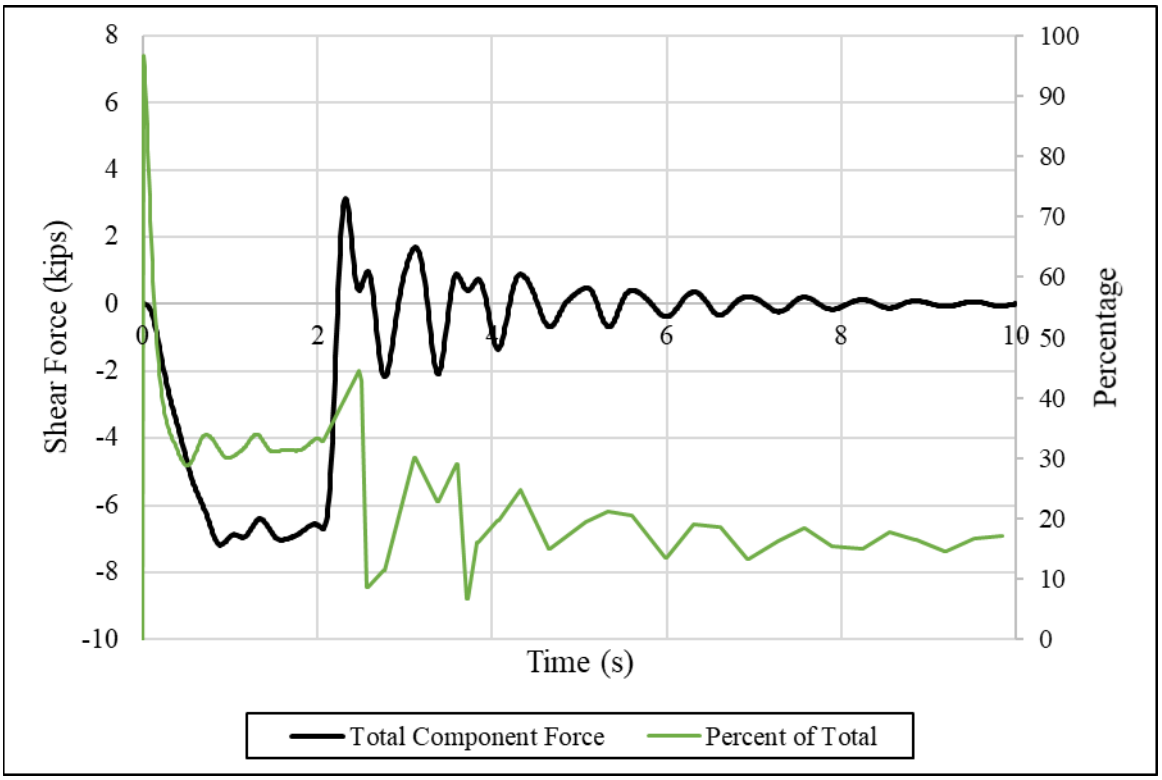

Figure 4-70 – Bent 2 Horizontal Force due to Braking on Right of Span 3

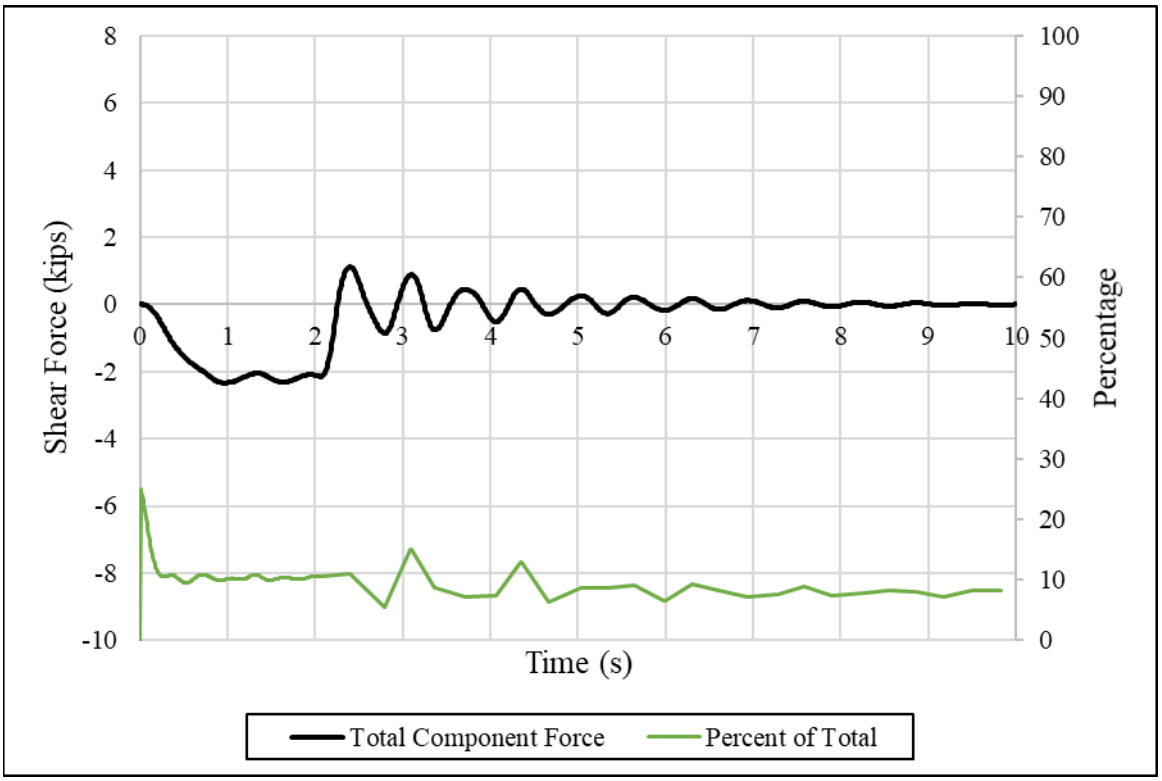

Figure 4-71 – Bent 3 Horizontal Force due to Braking on Right of Span 3

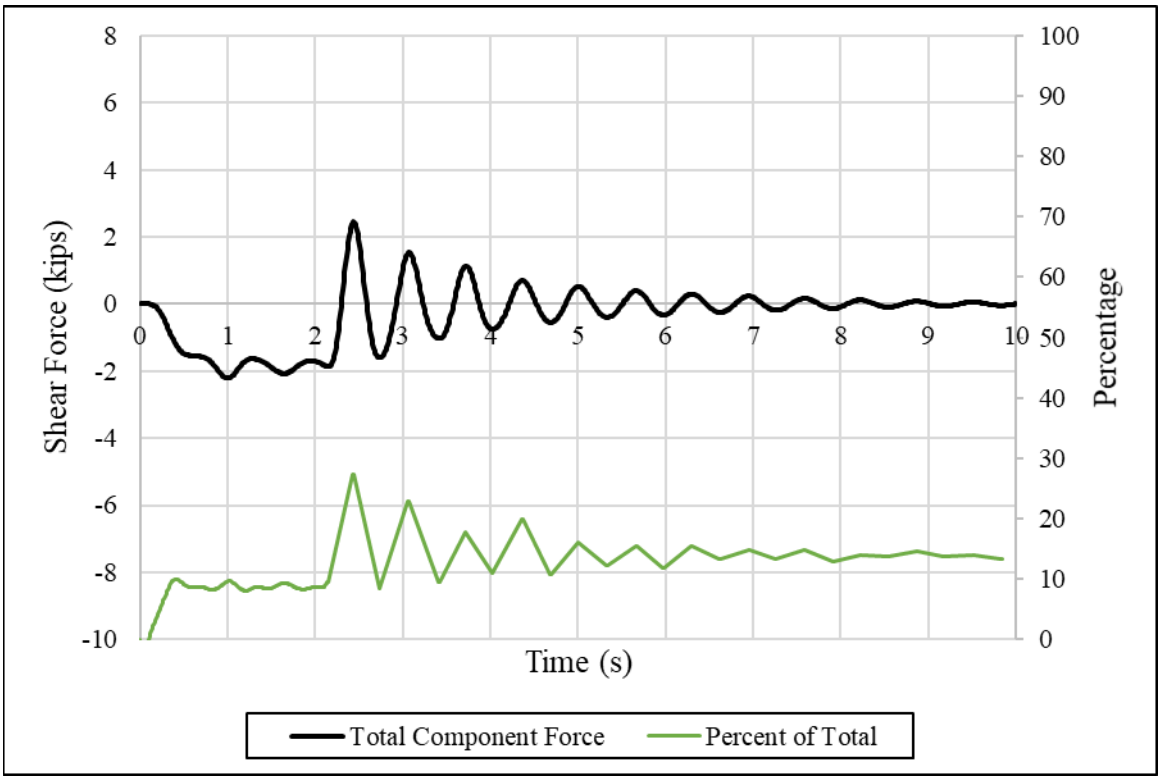

Figure 4-72 – Bent 4 Horizontal Force due to Braking on Right of Span 3

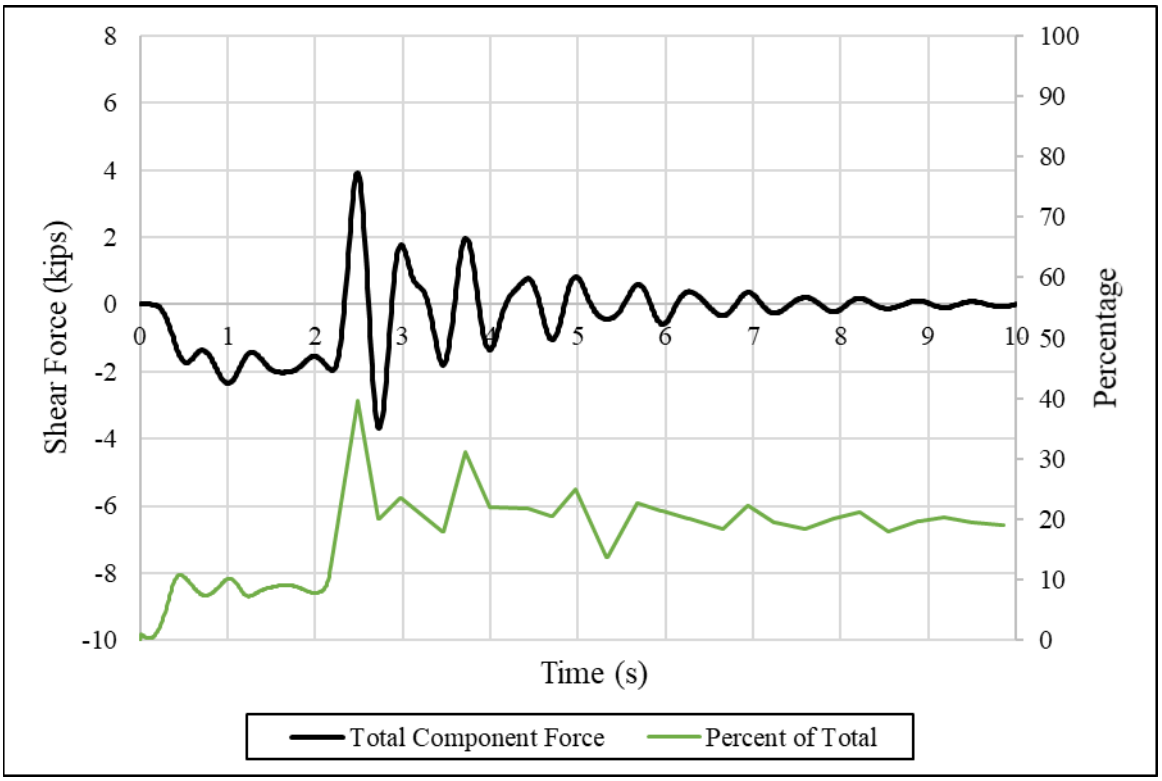

Figure 4-73 – Bent 5 Horizontal Force due to Braking on Right of Span 3

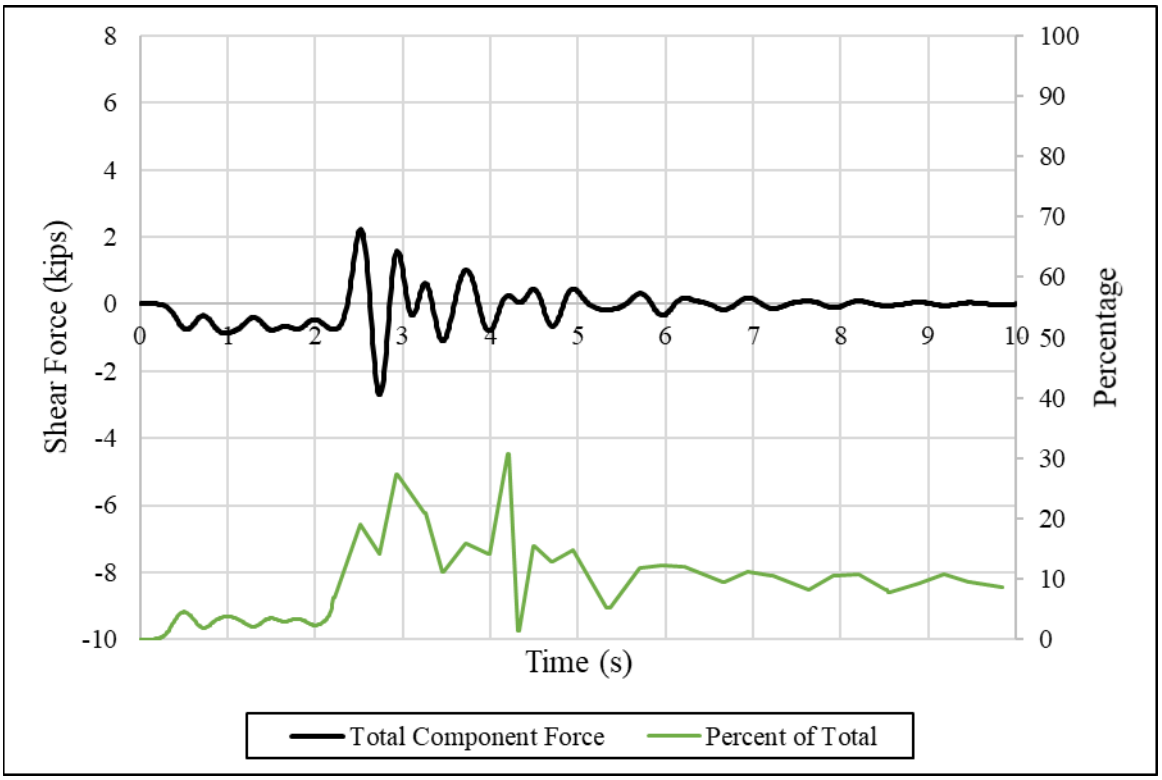

Figure 4-74 – Bent 6 Horizontal Force due to Braking on Right of Span 3

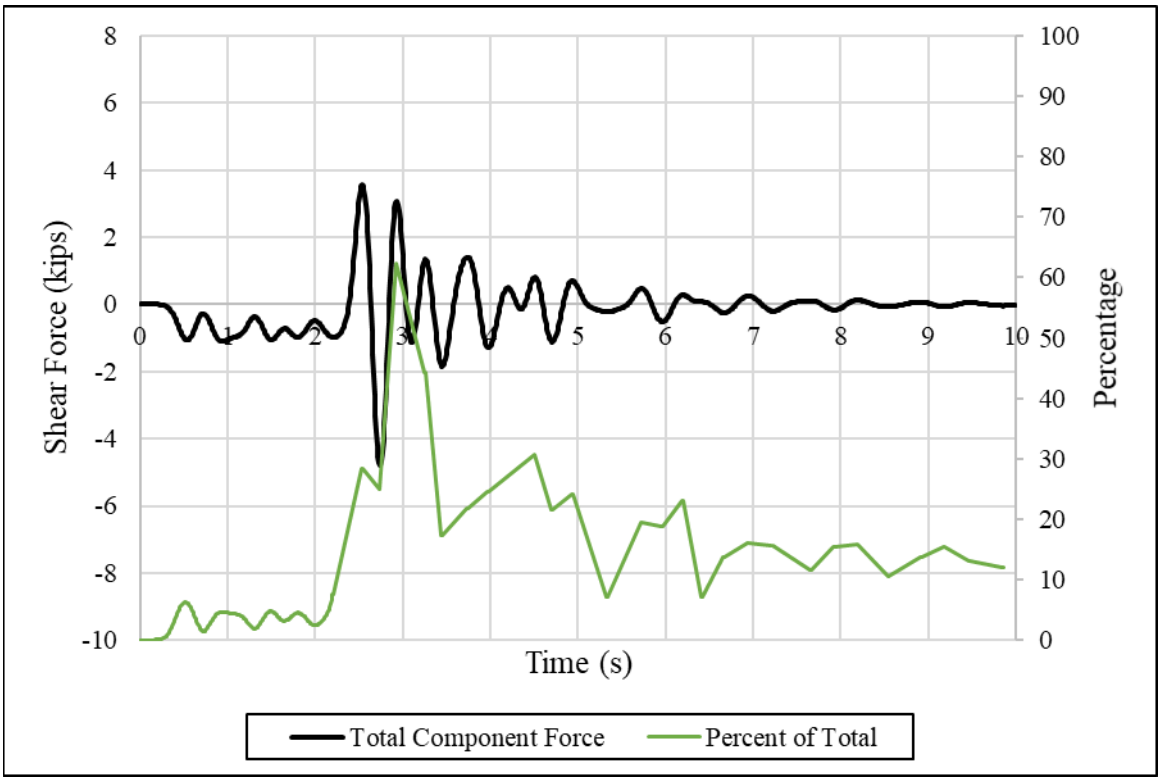

Figure 4-75 – Abutment 7 Horizontal Force due to Braking on Right of Span 3

As with span 2 loaded on the right, when braking on the right side of span 3 abutment 1 and bent 2 experienced the highest percentage of the horizontal shear force. Abutment 1 experienced a maximum of 34 percent and approximately 7.3 kips and bent 2 experienced 31 percent at 6.7 kips, respectively. The maximum total horizontal shear force experienced by the whole substructure was approximately 21 kips.

4.3.1.6 Horizontal Substructure Forces Resulting from Braking on Right of Span 5

From the tests conducted on the right side of span 5, the first provided the best data. Figure 4-76 through Figure 4-82 presents the horizontal shear force in each bent or abutment compared to the total horizontal shear force experienced by the entire substructure for this test.

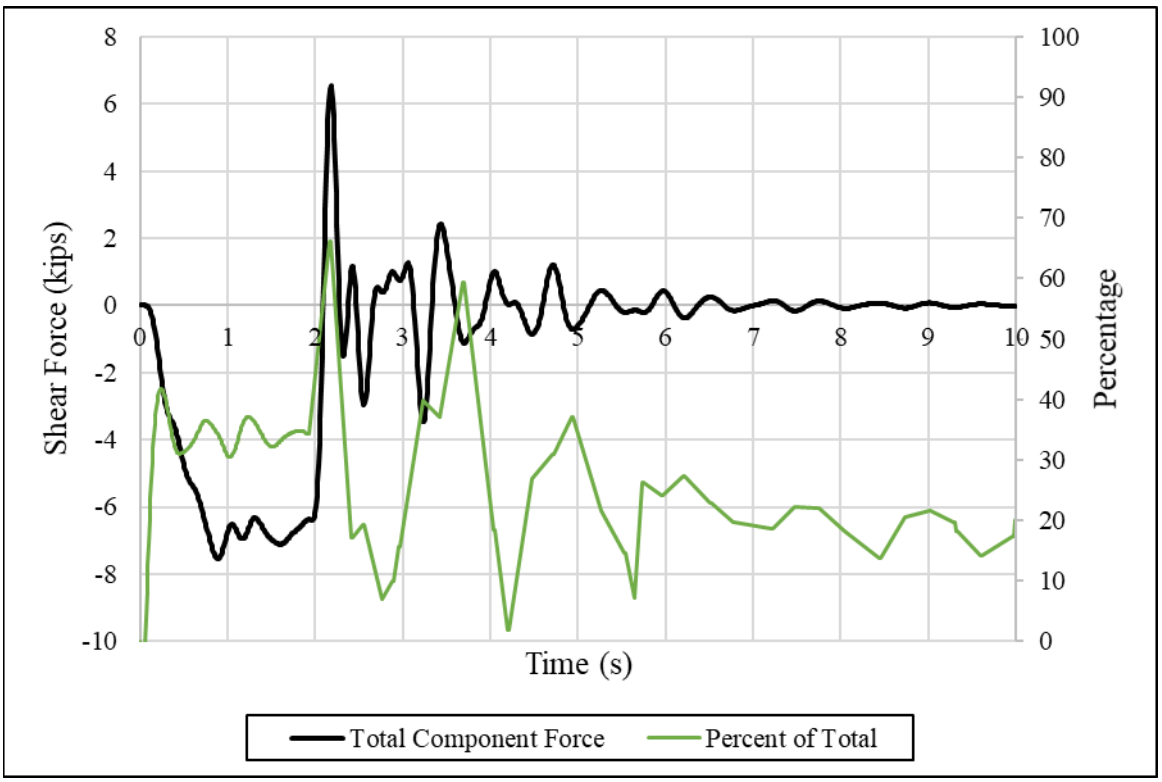

Figure 4-76 – Abutment 1 Horizontal Force due to Braking on Right of Span 5

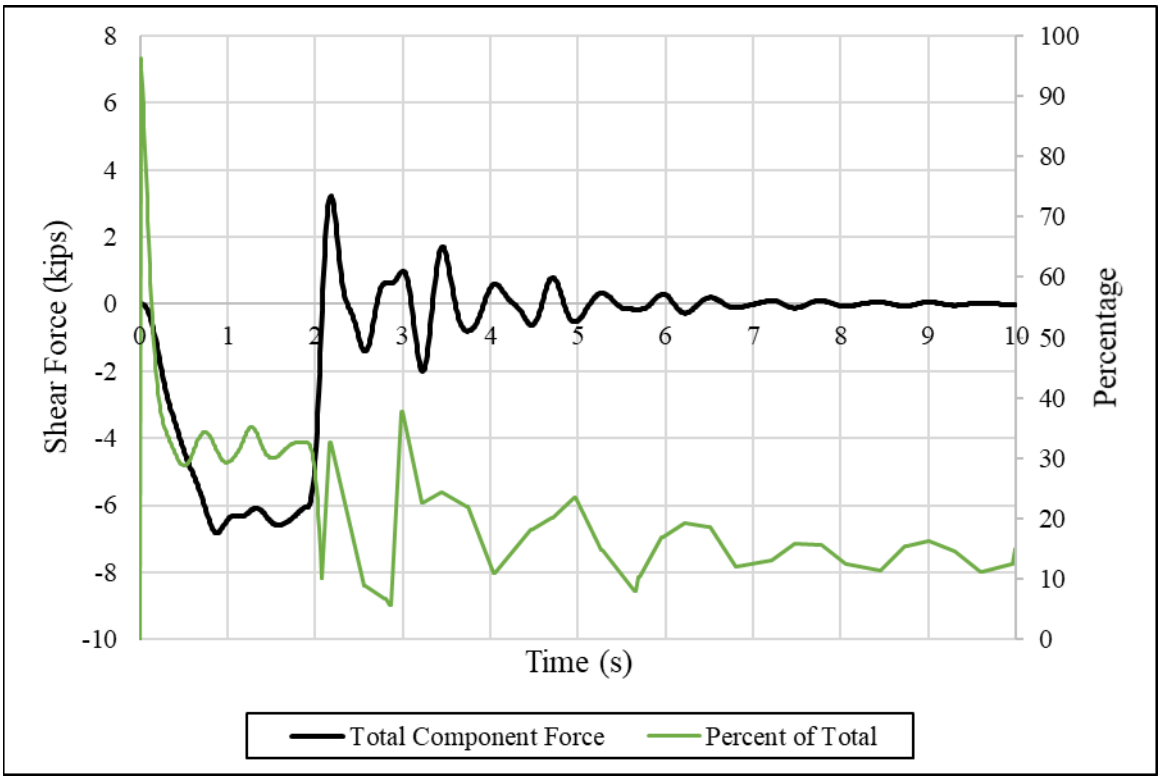

Figure 4-77 – Bent 2 Horizontal Force due to Braking on Right of Span 5

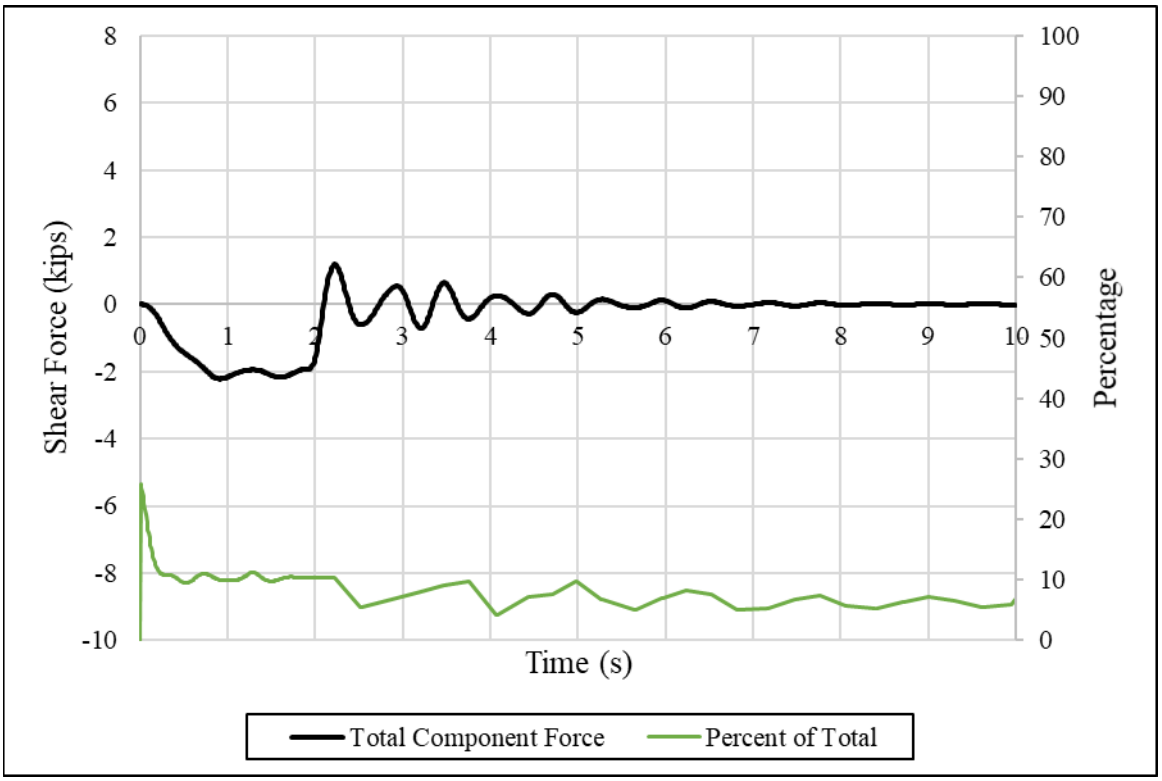

Figure 4-78 – Bent 3 Horizontal Force due to Braking on Right of Span 5

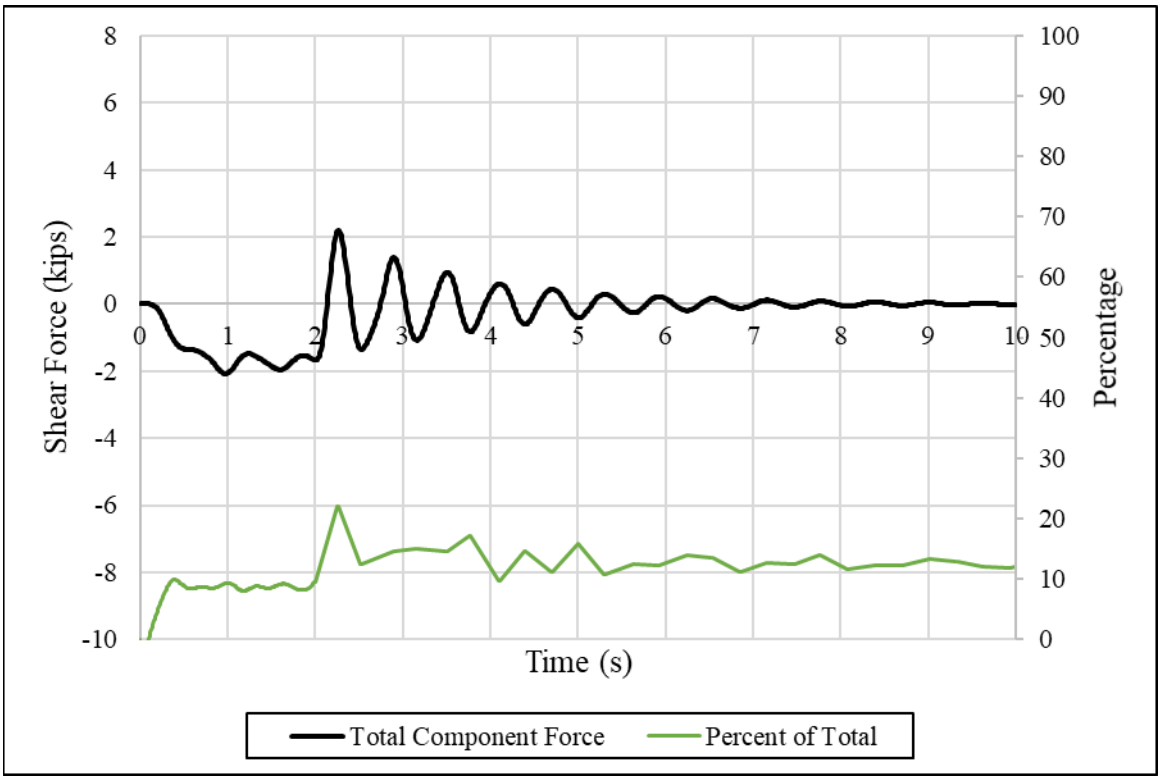

Figure 4-79 – Bent 4 Horizontal Force due to Braking on Right of Span 5

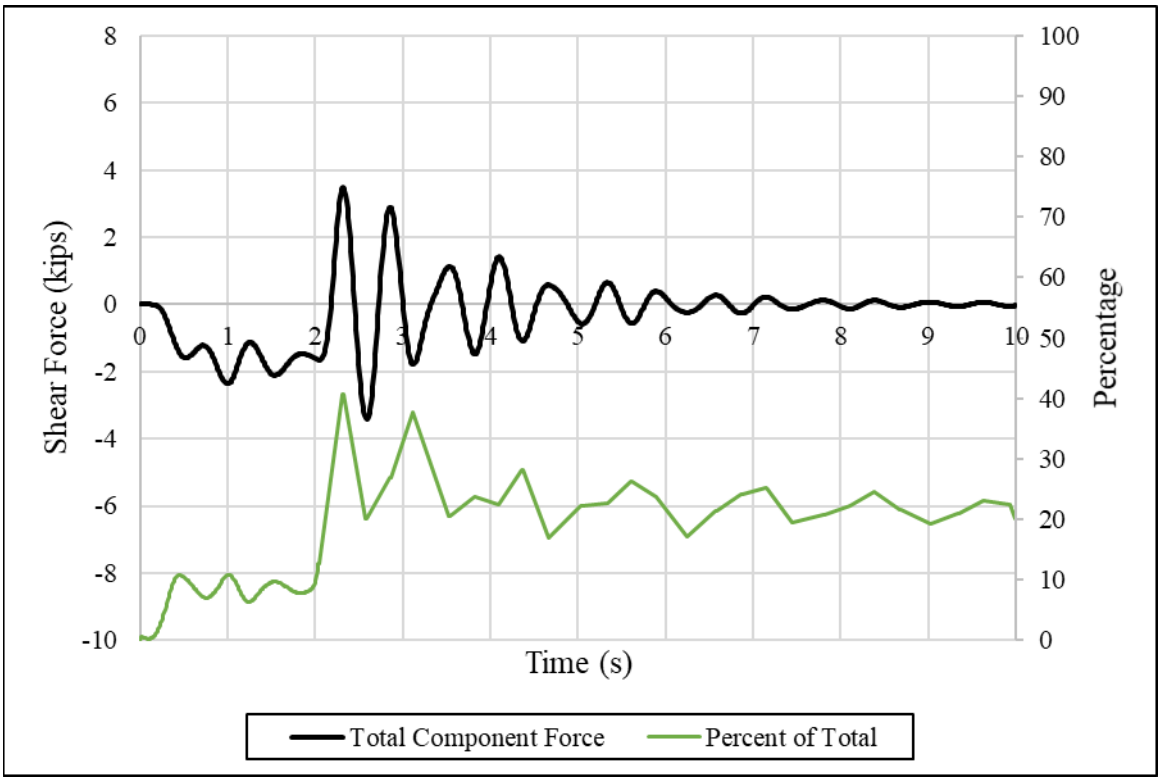

Figure 4-80 – Bent 5 Horizontal Force due to Braking on Right of Span 5

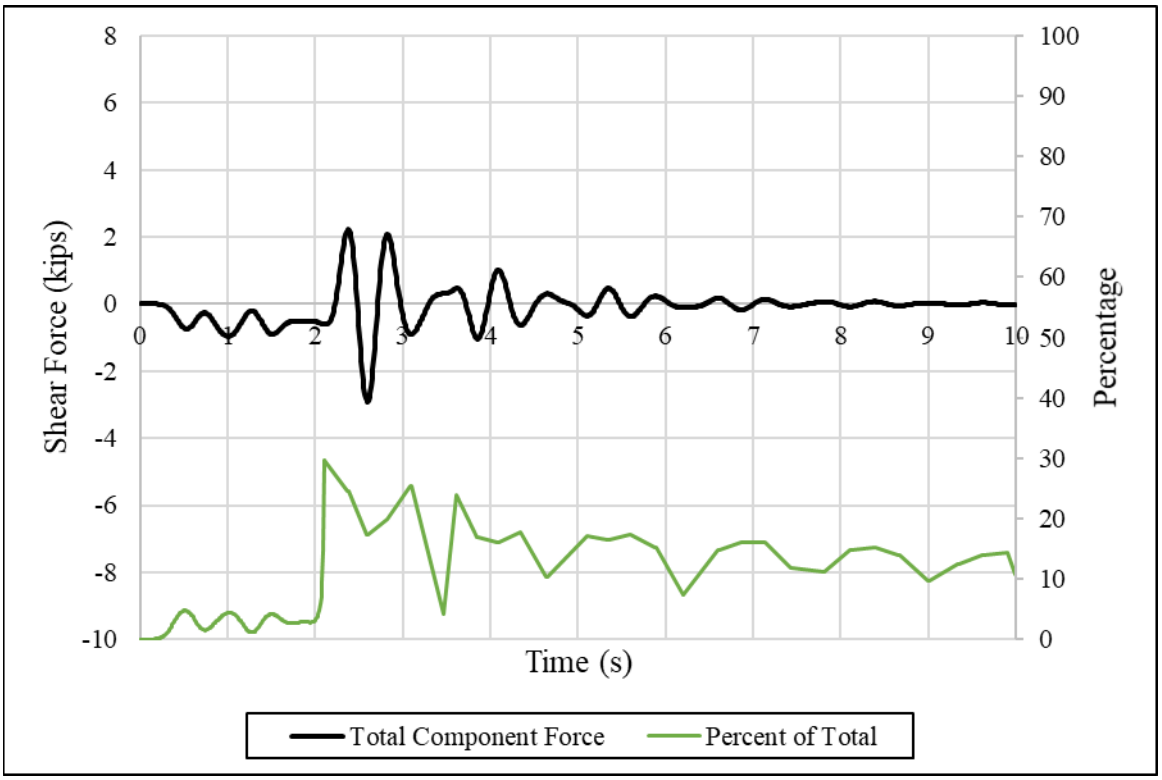

Figure 4-81 – Bent 6 Horizontal Force due to Braking on Right of Span 5

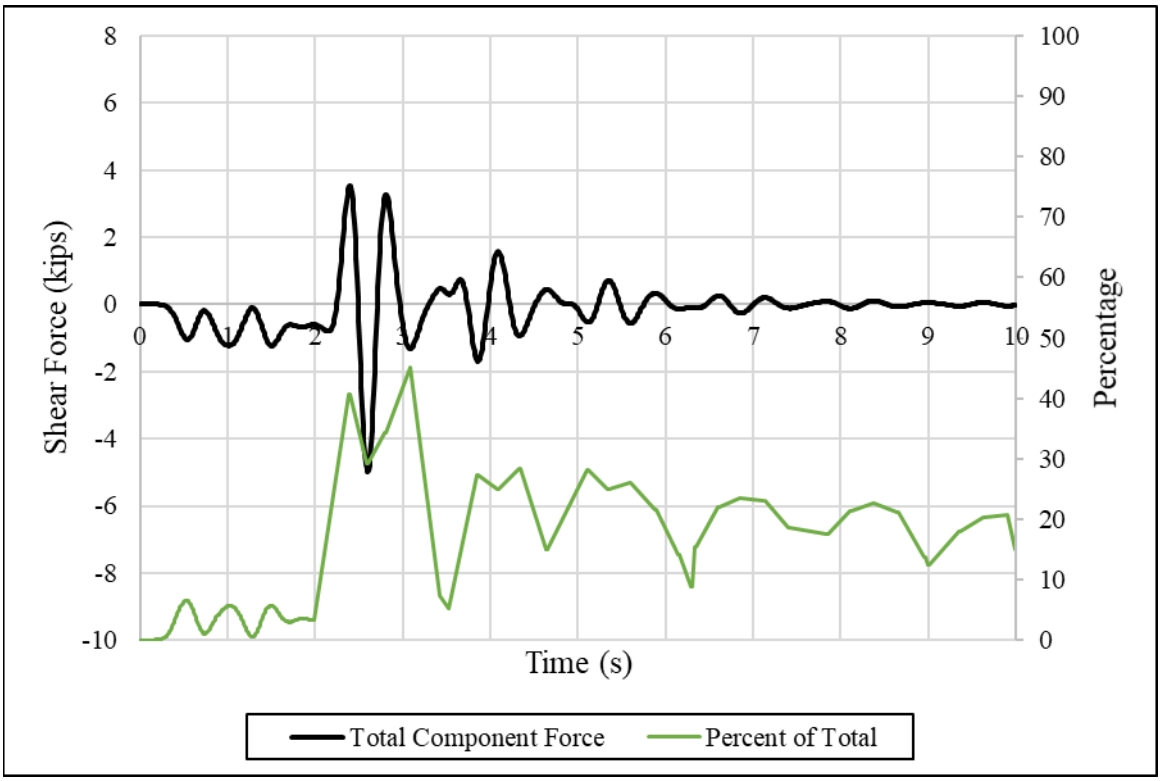

Figure 4-82 – Abutment 7 Horizontal Force due to Braking on Right of Span 5

Again, with span 5 during the right side braking, abutment 1 and bent 2 experienced the highest percentage of the horizontal shear force. Abutment 1 experienced a maximum of 33 percent at approximately 6.8 kips and bent 2 experienced 32 percent at 6.4 kips. The maximum total horizontal shear force experienced by the whole substructure was approximately 20 kips. With this test occurring on the right side and at a smaller maximum deceleration rate compared to the center tests, it is reasonable for the overall magnitudes of the forces to be less and the distribution to be different than when the span was braked on in the center.

4.4 SUMMARY OF RESULTS

To summarize the results of the horizontal shear forces, Table 4-1 contains the approximate maximum horizontal shear force expected in a static loading based off the truck mass and maximum deceleration rate, the maximum total horizontal shear force in the entire substructure from the model, and the maximum horizontal shear force in each bent or abutment. Despite the maximum horizontal shear force for the entire substructure always occurring during braking of the truck, each component did not always experience its maximum horizontal shear force during braking. In several tests, a bent or abutment experienced its maximum horizontal shear force during the free response period of vibration. If this was the case, the component that experienced the greatest force during free response is marked in the table by an asterisk. Even though this occurred, it is of importance to note that the maximum horizontal force was not significantly greater than the amount of horizontal shear force experienced during braking. The shaded cells indicate the substructure components that are directly supporting the loaded span and could be expected to experience the greatest horizontal shear force based on which span was loaded.

Table 4-1 – Maximum Total and Component Horizontal Shear Force for each Dynamic Test

	Maximum Static Horizontal Shear Force (kips)	Maximum Total Horizontal Shear Force in Model (kips)	Abutment 1 (kips)	Bent 2 (kips)	Bent 3 (kips)	Bent 4 (kips)	Bent 5 (kips)	Bent 6 (kips)	Abutment 7 (kips)
Center of Span 2	22.5	22.7	7.9	7.5	2.4	2.5*	4.2*	2.3*	4.0*
Right Side of Span 2	26.0	26.5	8.9	8.5	2.7	3.0*	5.2*	3.6*	6.3*
Center of Span 3	25.3	26.3	6.6*	4.6	3.0	5.1	4.7	2.7*	4.7*
Right Side of Span 3	21.1	21.2	7.3	6.7	2.2	2.4*	3.9*	2.7*	4.7*
Center of Span 5	24.6	25.4	3.7*	2.4*	1.0*	1.7	7.5	6.5	7.6
Right Side of Span 5	20.0	19.7	6.8	6.4	2.0	2.3*	3.4*	2.9*	5.0*

For every test, the maximum total horizontal force in the model was very close to the maximum horizontal force computed statically. There was some oscillation around this maximum value due to the dynamic response of the bridge, but within a few kips of the average that was recorded.

To understand how the forces reported in the model compare to the maximum static horizontal shear force, Table 4-2 was utilized. The table shows how the maximum horizontal shear force in the model was comparable to the static value and it shows how the component maximum shear forces are distributed. Knowing what component under what loading will produce the greatest shear force in that individual component is an invaluable aspect to designers who have to design based off of demand.

Table 4-2 – Percentage of Maximum Total Shear Force Computed Statically to Maximum Shear Force Reported in Model

	Maximum Static Horizontal Shear Force (kips)	Maximum Total Horizontal Shear Force in Model	Abutment 1	Bent 2	Bent 3	Bent 4	Bent 5	Bent 6	Abutment 7
Center of Span 2	22.5	101%	35%	33%	11%	11%	19%	10%	18%
Right Side of Span 2	26.0	102%	34%	33%	10%	12%	20%	14%	24%
Center of Span 3	25.3	104%	26%	18%	12%	20%	19%	11%	19%
Right Side of Span 3	21.1	100%	35%	32%	10%	11%	18%	13%	22%
Center of Span 5	24.6	103%	15%	10%	4%	7%	30%	26%	31%
Right Side of Span 5	20.0	99%	34%	32%	10%	12%	17%	15%	25%

In every case, the magnitude of the total horizontal shear force is directly related to the maximum braking deceleration. If the maximum deceleration was 0.33g, then 33 percent of the truck mass was the magnitude of the maximum total horizontal force in the bents and abutments of the bridge. All of the center tests deceleration rates were comparable to the decelerations rates found to be expected while reviewing the literature discussed in Chapter 2.4. In the Federal Motor Vehicle Safety Standard 121 (NHTSA 2008), the average maximum deceleration rates were 0.39g, 0.36g, and 0.34g for the various truck types. In this study, 0.35g was the average maximum deceleration rate was 0.35g for all the center span braking tests and 0.31g for all the right side braking tests. The implication of this is, if the achievable deceleration rate is ultimately the total maximum horizontal shear force that will be transmitted to the substructure of the bridge, the 25 percent of the truck weight provision in the LRFD Specification could potentially be low. The LRFD Specification is ultimately implying that 0.25g is the achievable effective deceleration rate for design purposes.

When reviewing the effect of off-center braking versus center braking, for spans 3 and 5 at lower total maximum forces, abutment 1 and bent 2 experienced greater forces then when braking occurred in the center of the span. Abutment 1 and bent 2 experienced greater forces on the right side braking then on the center but at a higher total maximum horizontal force. These bents and abutments could be experiencing greater forces as a result of resisting some tendency of the bridge to want to twist as a result of the eccentric load in the plan dimension. Again with

the off-center braking, the maximum deceleration rate is the determining factor in the magnitude of the total maximum horizontal shear force that must be resisted by the bridge.

Based off of these results, if the only force that is of interest is the total maximum horizontal shear force that the all the bents and abutments combined experience, a static analysis of the design truck mass times a reasonable achievable deceleration rate, like the values presented in this chapter, would be a sufficient estimation of the total maximum horizontal shear force. If the horizontal shear force that the individual bents or abutments must resist is the desired value, a dynamic analysis should be performed. Capturing the dynamic forced vibration response and free vibration response is necessary since not every component will experience its maximum horizontal shear force at the same time the entire bridge superstructure does. Additionally, the percentage of the horizontal shear force that a component must resist is variable. Numerous factors such as stiffness, length, number of piles in a bent, and soil-structure interaction will affect the amount of horizontal shear force and as shown in Tables 4-1 and 4-2, the components that are expected to experience the greatest shear force do not always so a more thorough analysis must be completed.

CHAPTER 5: SUMMARY, CONCLUSIONS, AND RECOMMENDATIONS

5.1 SUMMARY

The research conducted in this thesis was undertaken to gain insight into to load path and intensity of the longitudinal braking force in highway bridge substructures, specifically shorter span bridges. With the LRFD Specifications requiring a larger magnitude of force to be designed for than the Standard Specifications, it became necessary to better understand the implications of braking and what magnitude of forces are going to be generated.

To evaluate the braking force, two types of field tests were conducted. First, static pull tests were conducted on each span with the enough force generated to either reach 20 kips of tension in the cable connecting the tow truck and the load truck or the load truck brakes unable to resist the pulling force and the truck beginning to slide. Second, dynamic braking tests were conducted on the center and right side of spans 2, 3 and 5.

From these field tests, the data was processed and an analytical model was created and calibrated to the field data. Measuring the amount of shear force in the bridge bents was not possible to directly measure, therefore, calibrating the displacements and accelerations of the bridge between the field data and model results was crucial to be able to take the forces the model was reporting and rely on the accuracy of the values.

Bent forces from the static and dynamic tests were recorded and analyzed to determine how they compared to code provisions in regards to magnitude. The code does not specially state how the force should be distributed among substructure elements, so the breakdown of total force imparted on the bridge in the longitudinal directions compared to how much of that force each component experienced was analyzed.

The results from these tests are presented in Chapter 4 and individually discussed. The overall observations from this research project and conclusions from the model results are presented in Chapter 5.2. The recommendations made based on this project are given in Chapter 5.3. The recommendations focus on results from the dynamic tests since it is not realistic to have

a static pulling situation on a bridge in service and the purpose of those test were primarily for modeling techniques and calibration purposes.

5.2 RESEARCH OBSERVATIONS AND CONCLUSIONS

From these tests, the maximum deceleration rate of the vehicle, as well as the vehicle weight, are the deciding factors in the amount of longitudinal force imparted into the bridge. The average maximum achievable deceleration rate for braking tests on the center of the span was 0.35g and braking tests conducted on the right side averaged 0.31g. This deceleration rate is ultimately the percentage of the truck mass that potentially must be accounted for. Given the results of these tests, when compared to the LRFD Specification of 25 percent of the truck weight (the controlling provision for short-span bridges), LRFD does not appear to be over conservative.

If designing a bridge with less than 450 ft between expansion joints, 25 percent of the truck weight is the controlling braking force required to design for. This results in 18 kips, given that the design truck axle weight is 72 kips. In every dynamic case in the model, at least 20 kips of longitudinal force was recorded and a maximum of 26 kips was recorded. At 26 kips of force, that is a 44 percent increase in the amount of horizontal shear force the substructure must resist in comparison to the code provision. Furthermore, the weight of the truck used during testing in this research project was 1800 lbs less than the axle weight of the design vehicle so this would lead to an even larger increase in force.

The maximum achievable deceleration rate is not going to increase with increasing speed, rather, it just has to do with the available friction and the capabilities of the braking system of the truck. Higher speed results in longer deceleration time and distance, not higher deceleration rate. Once the maximum deceleration rate is exceeded, the brakes slip or the tires skid, both of which will decrease the force transfer to the deck. Higher deceleration rates might be achievable with advanced braking technology (e.g. computerized, anti-lock systems), but not because the truck is driving faster when the driver hits the brakes.

But, it is important to keep in mind that the likelihood of the worst case scenario happening to cause the worst loading in a bridge is far more unlikely then the structure experiencing lower magnitudes of longitudinal forces on a regular basis.

5.3 RECOMMENDATIONS FOR DESIGNERS USING LRFD SPECIFICATIONS

- Consider up to 35 percent of the axle weight if trying to obtain the worst case horizontal loading for the entire bridge substructure due to vehicular braking.
- Distribute the total force among all substructure elements in accordance with the relative stiffness of the substructure elements. For braking locations near the end of the bridge, this may result in a majority going into the nearest abutment. For braking locations away from the ends of the bridge, the braking force may be more evenly distributed among the bridge bents.
- If able, perform a more rigorous analysis using the steps presented within this thesis to analyze the bridge of interest using a structural analysis software and analyze braking conditions on each span to determine the maximum amount of shear force per substructure component that must be resisted.

5.4 RECOMMENDED TECHNIQUES FOR DETERMINING BRAKING FORCES IN SUBSTRCTURES USING ANALYTICAL TECHNIQUES

From the findings in this project, important modelling decisions that should be considered when designing a model for analysis/design purposes include

- Verification of the actual fixity of the abutments which can result in improved modeling of the abutment behavior,
- Accurate bearing pad stiffness,
- Accurate representation of the entire mass of the bridge,
- Realistic braking deceleration profiles for the span length of the bridge, especially realistic achievable maximum braking deceleration,
- Accuracy of all bridge component geometry,
- Appropriate truck mass depending on LRFD Specification design truck or tandem weights, and
- Appropriate representation of the soil-structure interaction along the length of the piles.

5.5 RECOMMENDATIONS FOR FUTURE RESEARCH

The observations and conclusions presented in Chapters 5.2 and 5.3 should provide conservative advice on the load path and intensity of the braking force. However, further research would be

valuable to confirm these observations and to study the sensitivity of the magnitude of forces in the bridge when changes are made. Topics that could be further investigated are

- Evaluation of how sensitive the bridge is to change in bent stiffness, bent height, bent size, bearing pad stiffness, etc.,
- Evaluation of how the bridge would behave if the ends of the girders were actually fixed as designated in the plans versus how it behaved when the girder fixity was somewhere in between totally fixed and totally free,
- Investigation on how braking force in longer span bridges is distributed and what magnitudes of longitudinal force are expected,
- The effect of off-center braking on different types of substructures, and
- The accuracy of static analysis versus dynamic analysis of the bridge response when focusing on determination of the maximum design force for an individual substructure component.

REFERENCES

AASHTO. 2017. *AASHTO LRFD Bridge Design Specifications: Customary U.S. Units.* 8th. Washington D.C.: American Association of State Highway and Transportation Officials.

AASHTO. 2002. *Standard Specification for Highway Bridges.* 17th. Washington D.C.: American Association of State Highway and Transportation Officials.

ALDOT. 2013. *Bridge over Old Town Creek on County Road 9 (Site #2).* Montgomery, AL.

ALDOT. 2018. *Load Case Drawings.*

ALDOT. 2013. "Standard for Standard Details Drawing No. I-131."

Anderson, J. B. 1997. "A Laterally Loaded Pile Database." Masters Thesis, University of Florida.

Barr, M. D. 2019. "Experimental Determination of Braking Force Distribution in Steel Pile Bent Bridges." Master's Thesis, Auburn University.

Cai, C. S., S. Eddy, and N. Yazdani. 2000. "Effect of Bearing Pads on Precast Prestressed Concrete Bridges." *Journal of Bridge Engineering* (ASCE) 5 (3): 224-232.

Caltrans. 1994. "Memo to Designers 7-1." 1-7.

Chen, W., and L. Duan. 1999. *Bridge Engineering Handbook.* 1st. CRC Press.

Chopra, A. K. 2017. *Dynamics of Structures: Theory and Applications to Earthquake Engineering.* 5th. Hoboken, NJ: Pearson Education, Inc.

Computers and Structures, Inc. 2018. *CSi Knowledge Base.* Accessed February 24, 2019.

CSI. 2010. *CSiBridge 15.2.0.* Berkely, CA: Computers and Structures, Inc. .

CSI. 2012. *SAP2000 Ultimate Version 20.2.0.* Berkley, CA: Computers and Structures, Inc.

Deng, L., F. Wang, and W. He. 2015. "Dynamic Impact Factors for Simply-Supported Bridges Due to Vehicle Braking." *Advances in Structural Engineering* 18: 791-801.

Garrott, W. R., M. Heitz, and B. Bean. 2011. *Experimental Measurement of the Stopping Performance of a Tractor-Semitrailer From Multiple Speeds.* NHTSA.

NHTSA. 2008. *Federal Motor Vehicle Safety Standard 121.* Washington, D.C.: National Highway Traffic Safety Administration.

Panzer, J. L. 2013. "Evaluation of Critical and Essential Concrete Highway Bridges in a Moderate Seismic Hazard." Masters Thesis.

Reese, L. C., and S-T Wang. 1993. *Laterally Loaded Pile Analysis Program for the Microcomputer, Version 2.0. Final Report.* Washington, DC: Federal Highway Administration.

Snare, M. C. 2002. "Dynamics Model for Predicting Maximum and Typical Acceleration Rates of Passenger Vehicles." Master's Thesis, Virginia Polytechnic Institute and State Univeristy, Blacksburg, VA.

Torbic, D. J., D. W. Harwood, K. R. Richard, W. D. Glauz, and L. Elefteriadou. 2003. *NCHRP Report 505: Review of Truck Characteristics as Factors in Roadway Design.* Washington, D.C.: National Cooperative Highway Research Program.

Yazdani, N., S. Eddy, and C. S. Cai. 2000. "Effect of Bearing Pads on Precast Prestressed Concrete Bridges." *Journal of Bridge Engineering* 224-232.

APPENDIX A: FB-MULTIPIER AND SAP2000 SOIL SPRING VERIFICATION

Table A-1 – Soil Layer Definitions Used for All Bents

Soil Layer Table

Soil Set	Soil Layer	Soil Type	Top Layer Elevation (ft)	Bottom Layer Elevation (ft)	Lateral Model	Axial Model	Torsional Model	Tip Model	Unit Weight (Top) (pcf)
1	1	Cohesive	190.00	185.50	Clay (O'Neill)	Driven Pile	Hyperbolic	Driven Pile	120.000
1	2	Cohesionless	185.50	176.00	Sand (Reese)	Driven Pile	Hyperbolic	Driven Pile	120.000
1	3	Cohesive	176.00	152.50	Clay (O'Neill)	Driven Pile	Hyperbolic	Driven Pile	115.000

Table A-2 – Lateral Model Properties Used for All Bents

Lateral Model Table

Soil Set	Soil Layer	Lateral Model	Internal Friction Angle (deg)	Subgrade Modulus (lb/in^3)	Undrained Shear Strength (psf)	Major Principal Strain @50%	Major Principal Strain @100%
1	1	Clay (O'Neill)			635.0000	0.0006	0.0008
1	2	Sand (Reese)	32.0000	260.4000			
1	3	Clay (O'Neill)			5000.0000	0.0100	0.0200

Table A-3 – Axial Model Properties Used for All Bents

Axial Model Table

Soil Set	Soil Layer	Axial Model	Internal Friction Angle (deg)	Shear Modulus (ksi)	Poisson's Ratio	Undrained Shear Strength (psf)	Unconfined Compressive Strength (psf)	Mass Modulus (Em) (ksi)	Modulus Ratio (Em/Ei)	Surface	Split Tensile Strength (psf)	Pile Concrete Unit Weight (pcf)	Slump (in)	Ultimate Unit Skin Friction (psf)
1	1	Driven Pile		3.50	0.30									3000.00
1	2	Driven Pile		3.50	0.30									3000.00
1	3	Driven Pile		3.50	0.30									3000.00

Table A-4 – Torsional Model Properties Used for All Bents

Torsional Model Table

Soil Set	Soil Layer	Torsional Model	Internal Friction Angle (deg)	Undrained Shear Strength (psf)	Shear Modulus (ksi)	Torsional Shear Stress (psf)
1	1	Hyperbolic		635.00	3.50	3000.00
1	2	Hyperbolic	32.00		3.50	3000.00
1	3	Hyperbolic		5000.00	3.50	3000.00

Table A-5 – Tip Model Properties Used for All Bents

Tip Model Table

Soil Set	Soil Layer	Tip Model	Internal Friction Angle (deg)	Shear Modulus (ksi)	Poisson's Ratio	Axial Bearing Failure (kips)
1	3	Driven Pile		3.5000	0.3500	144.0000

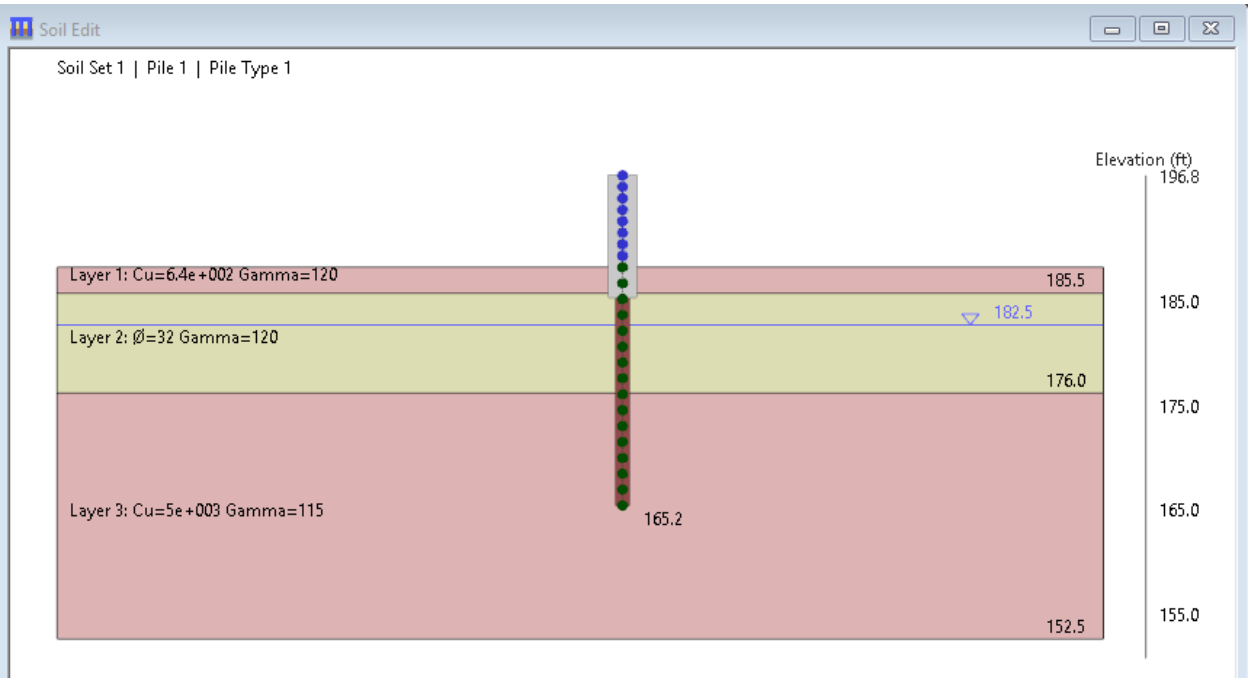

Figure A-1 – Bent 2 Elevation View in FBMP

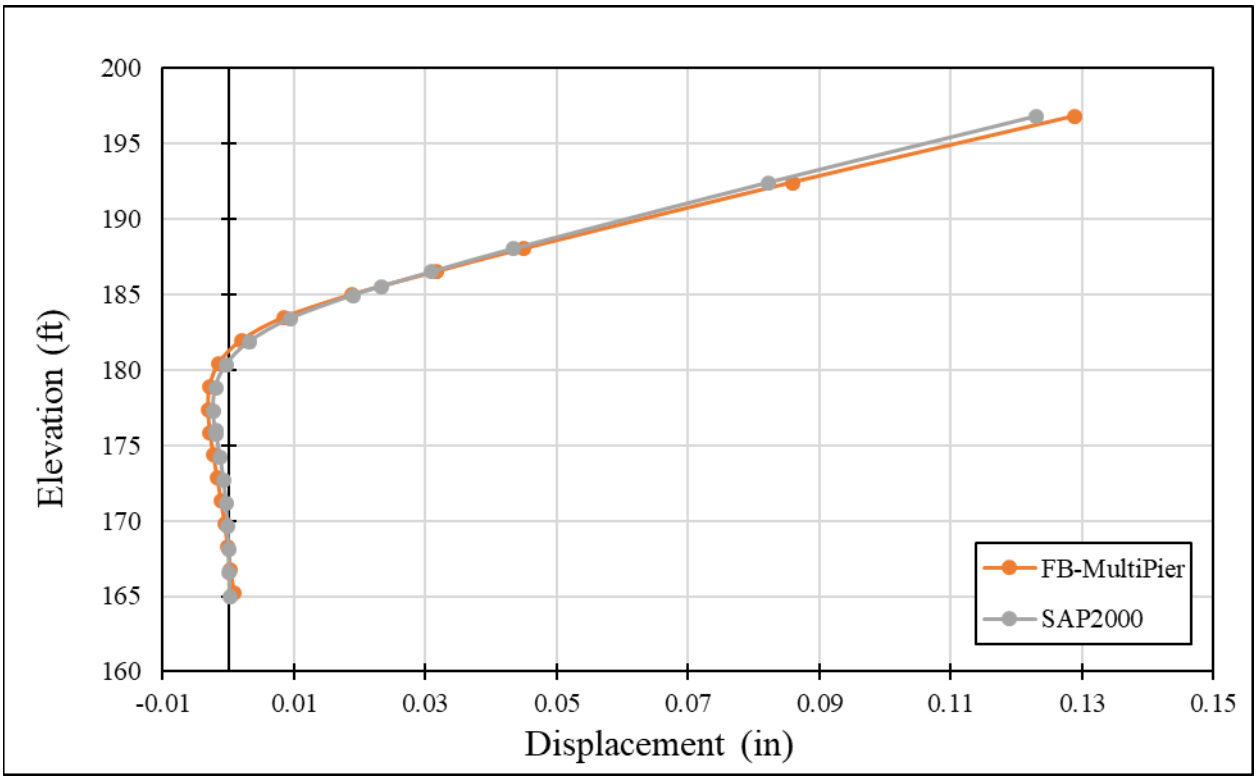

Figure A-2 – Displacement Comparisons for Pile 1 of Bent 2

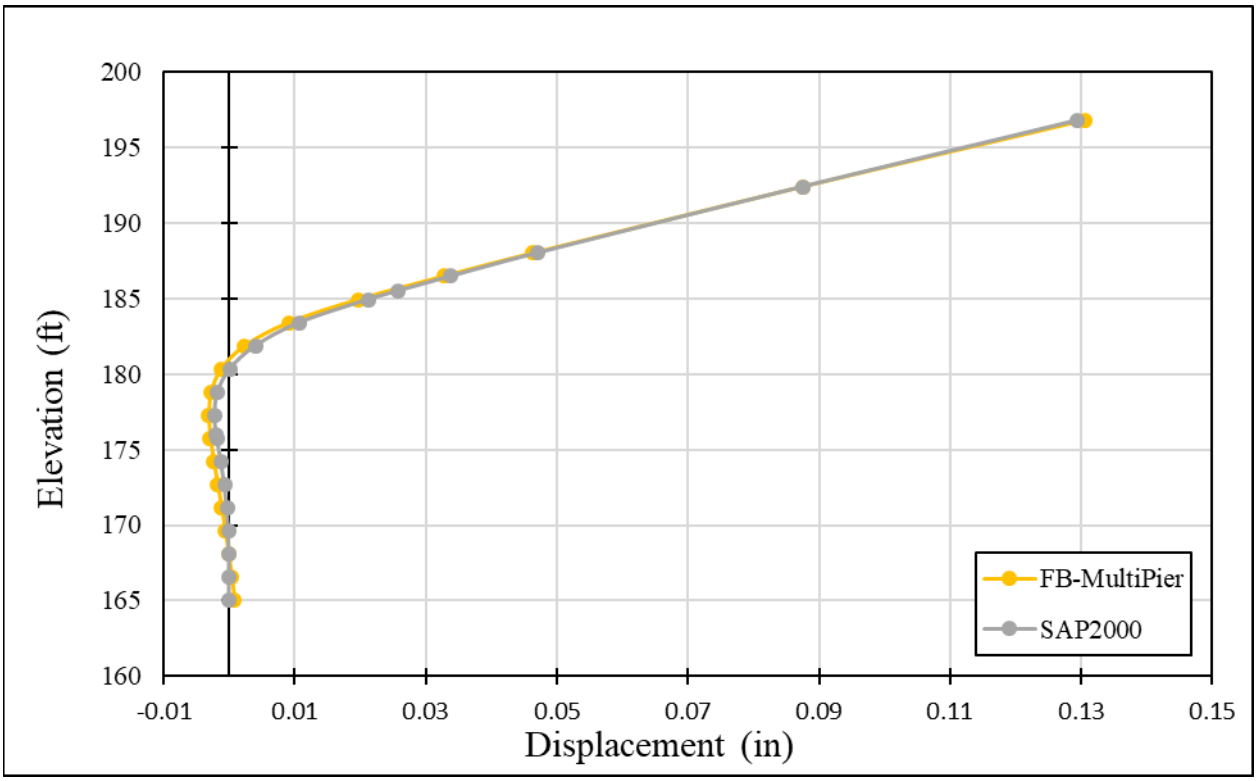

Figure A-3 – Displacement Comparisons for Pile 2 of Bent 2

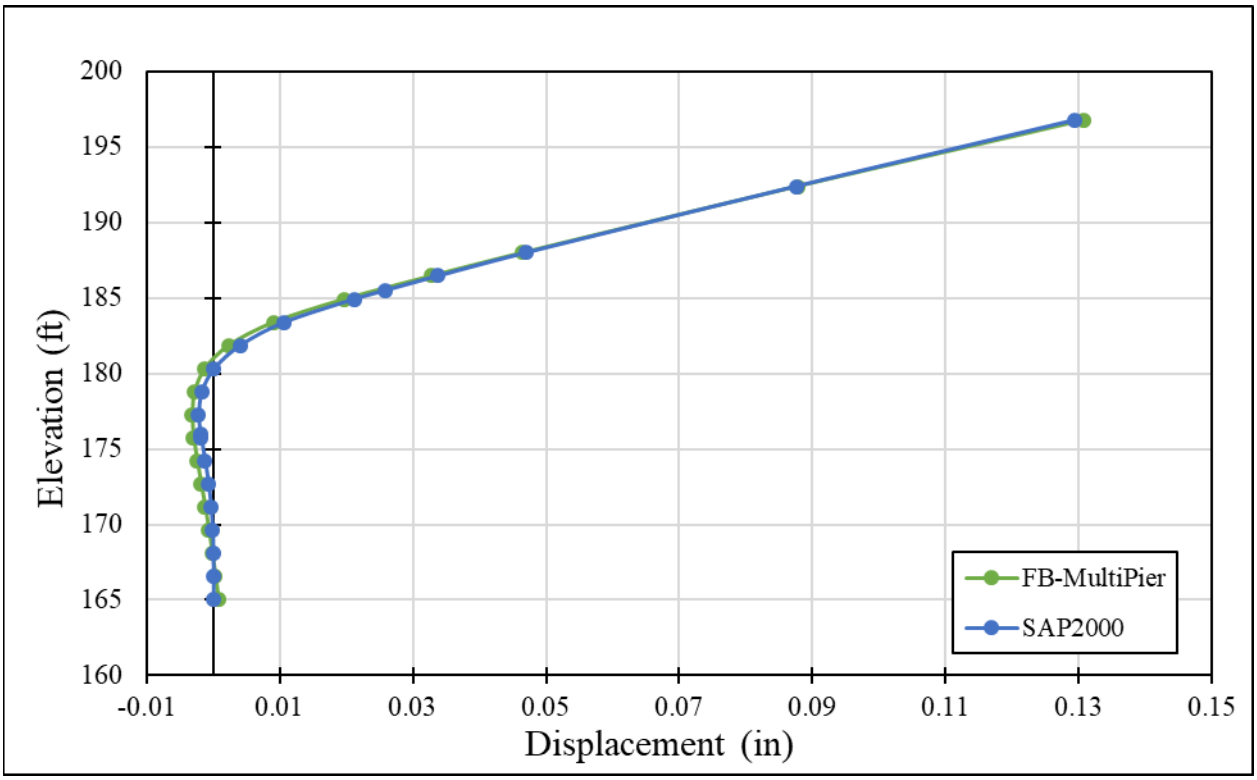

Figure A-4 – Displacement Comparisons for Pile 3 of Bent 2

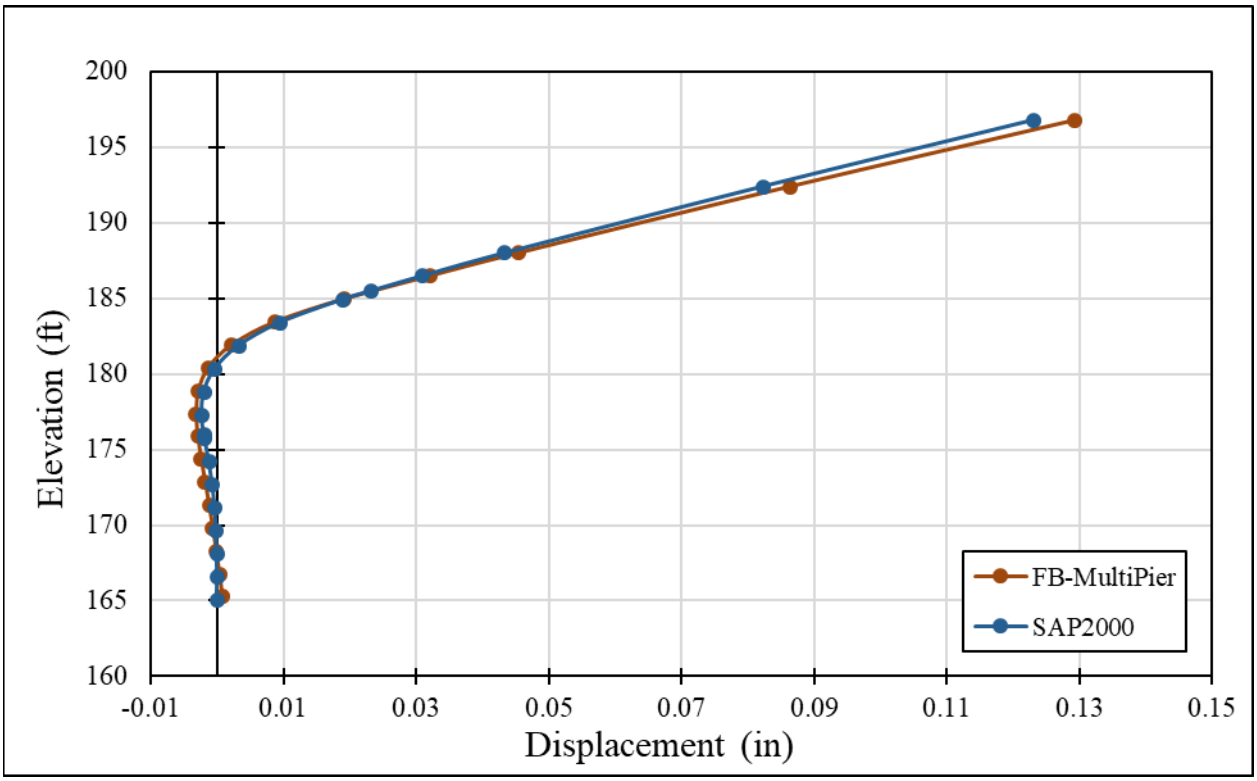

Figure A-5 – Displacement Comparisons for Pile 4 of Bent 2

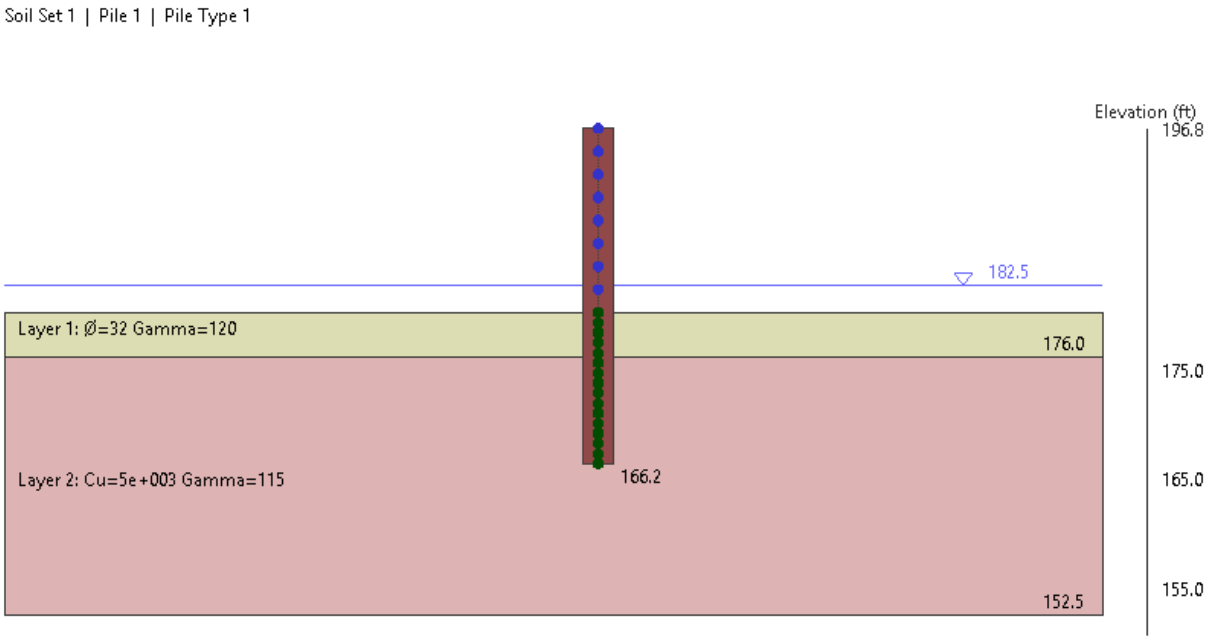

Figure A-6 – Bent 3 Elevation View in FBMP

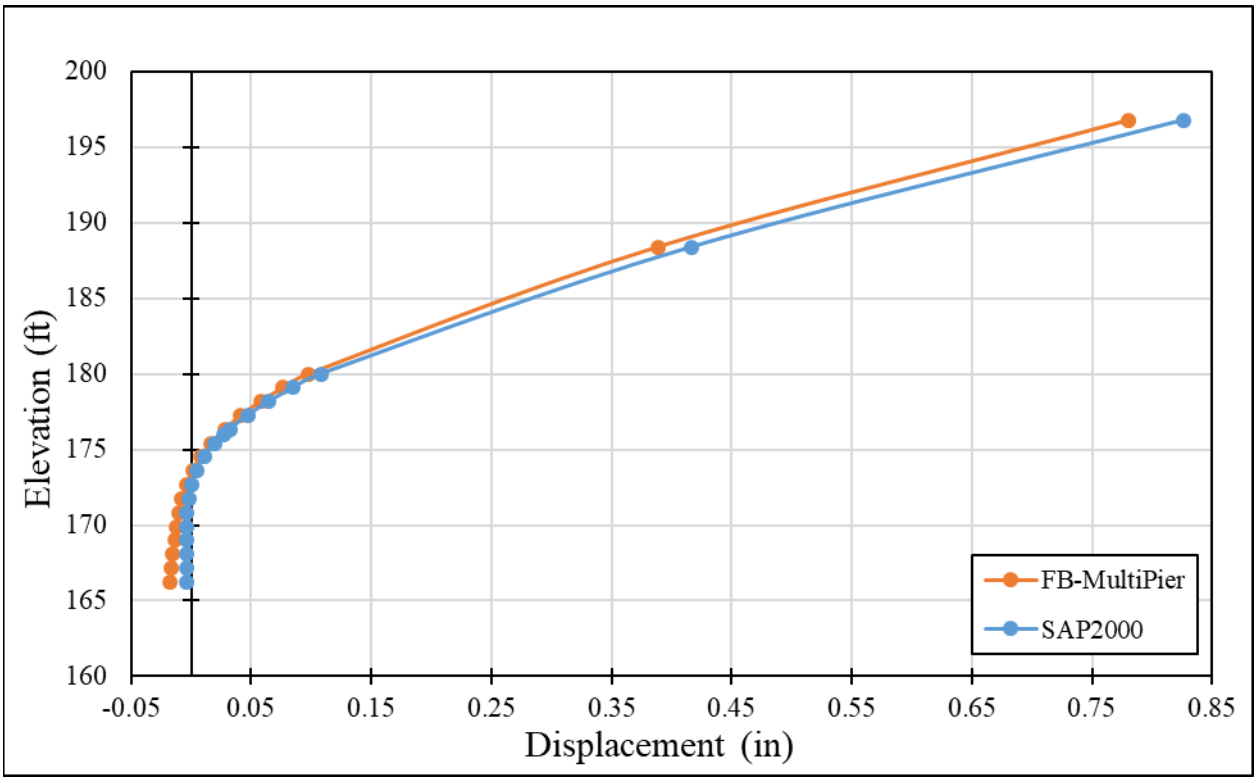

Figure A-7 – Displacement Comparisons for Pile 1 Bent 3

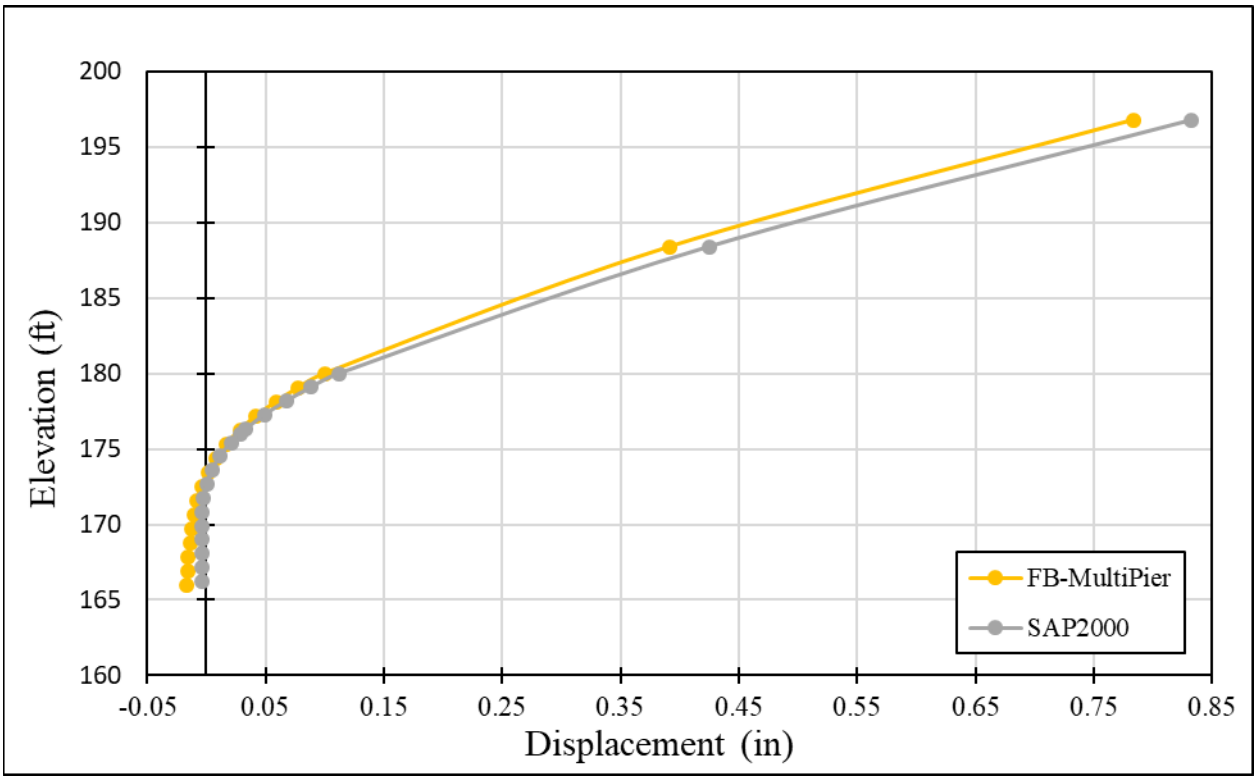

Figure A-8 – Displacement Comparisons for Pile 2 Bent 3

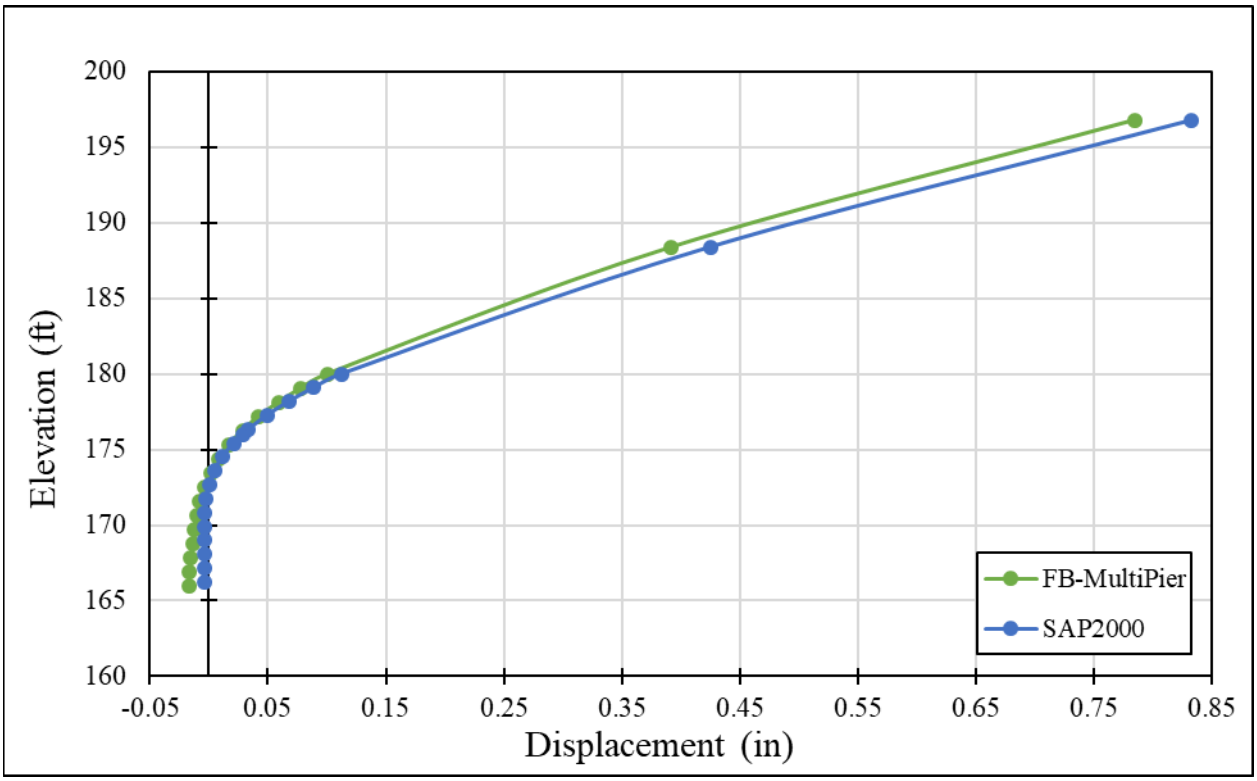

Figure A-9 – Displacement Comparisons for Pile 3 Bent 3

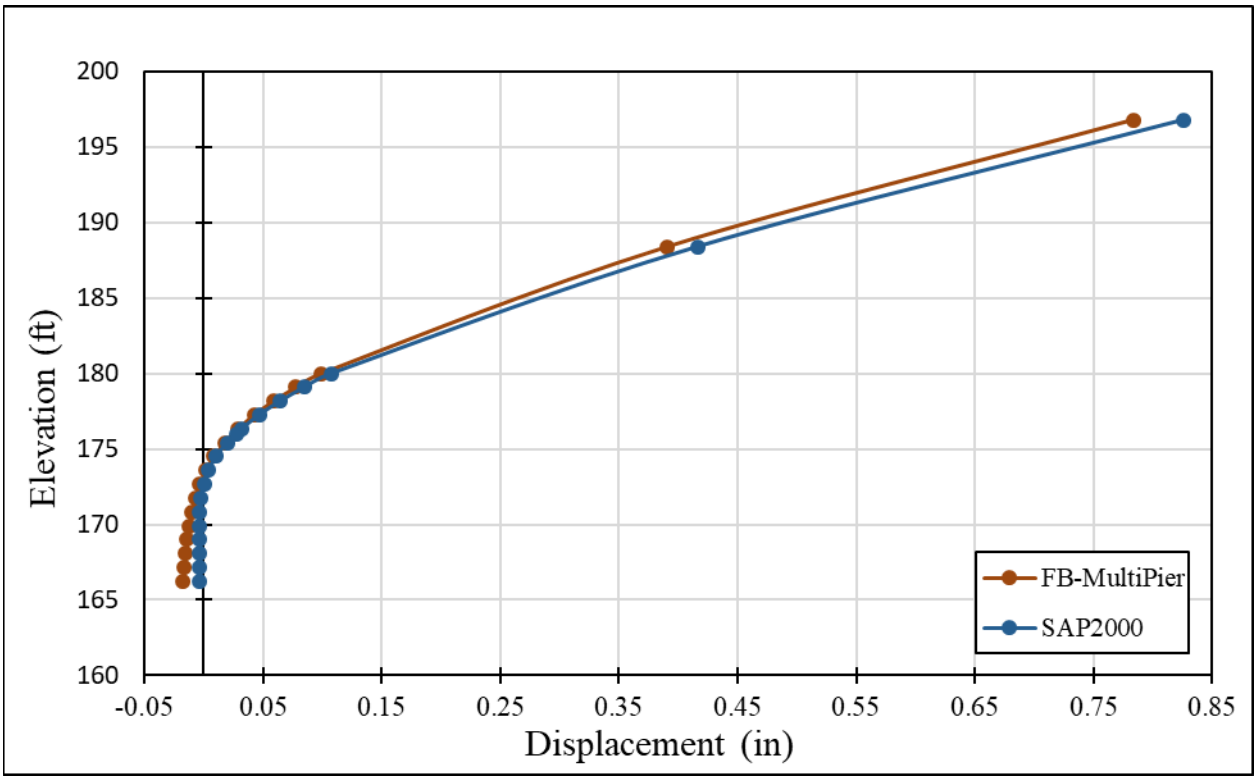

Figure A-10 – Displacement Comparisons for Pile 4 Bent 3

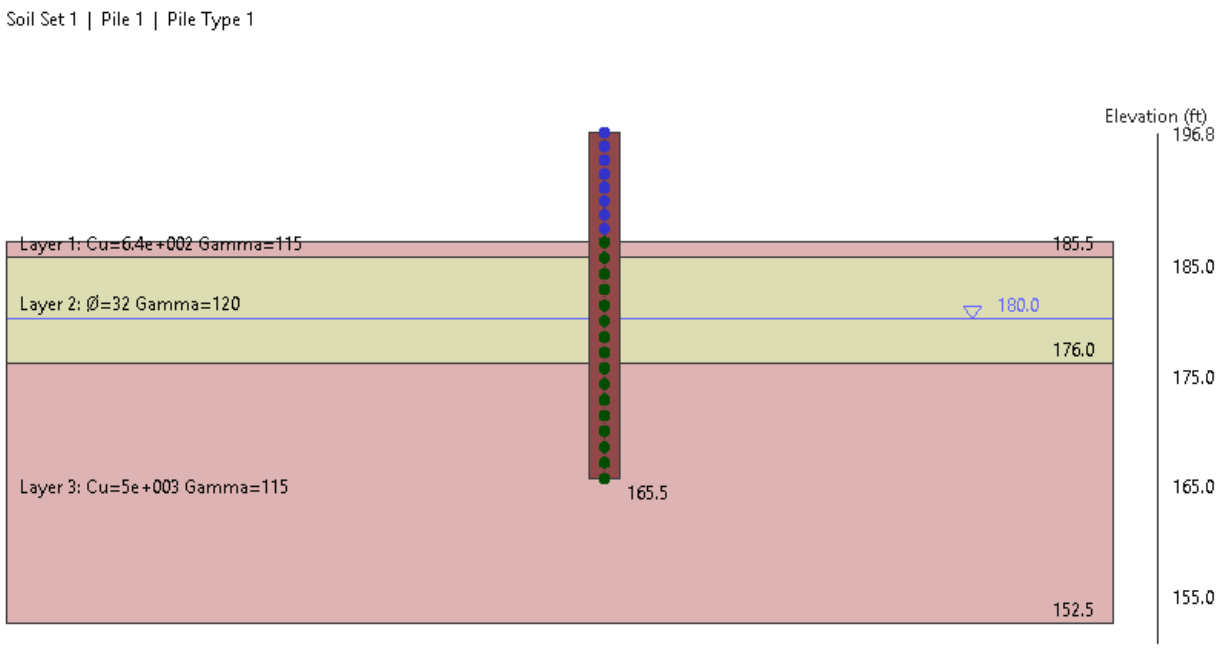

Figure A-11 – Bent 4 Elevation View in FBMP

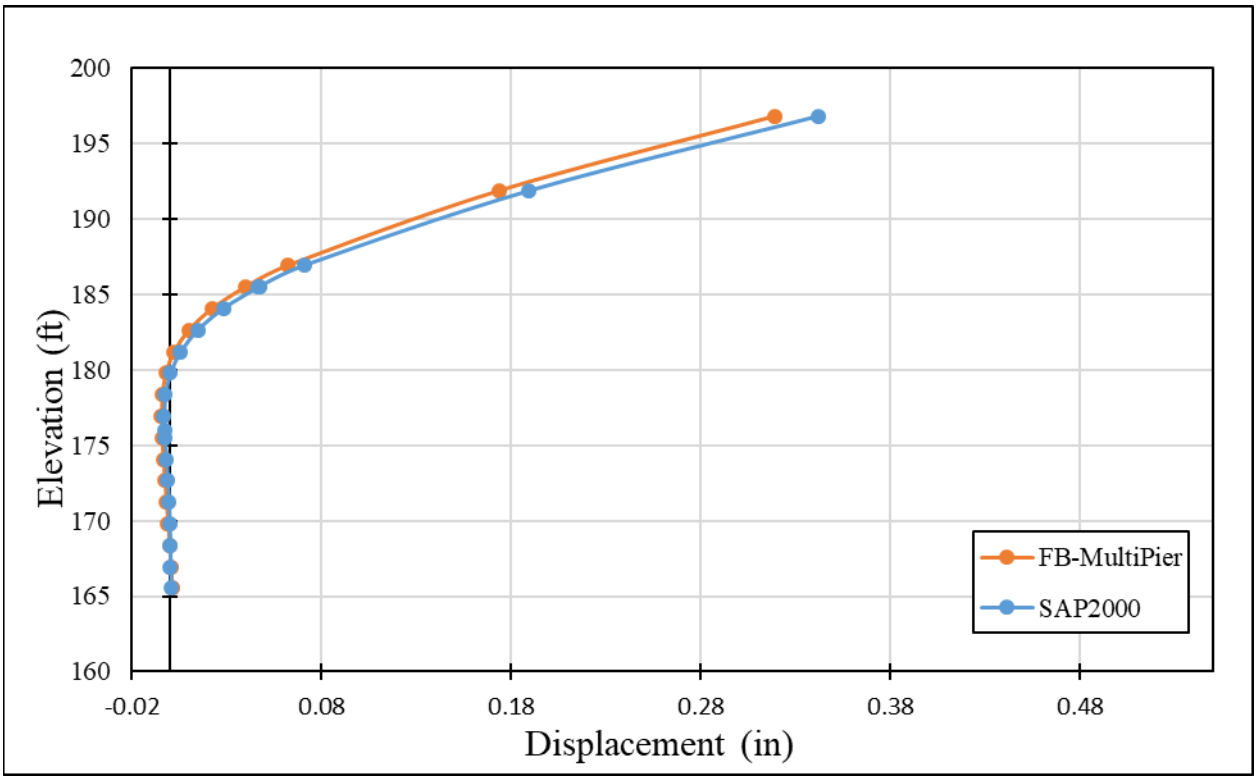

Figure A-12 – Displacement Comparisons for Pile 1 Bent 4

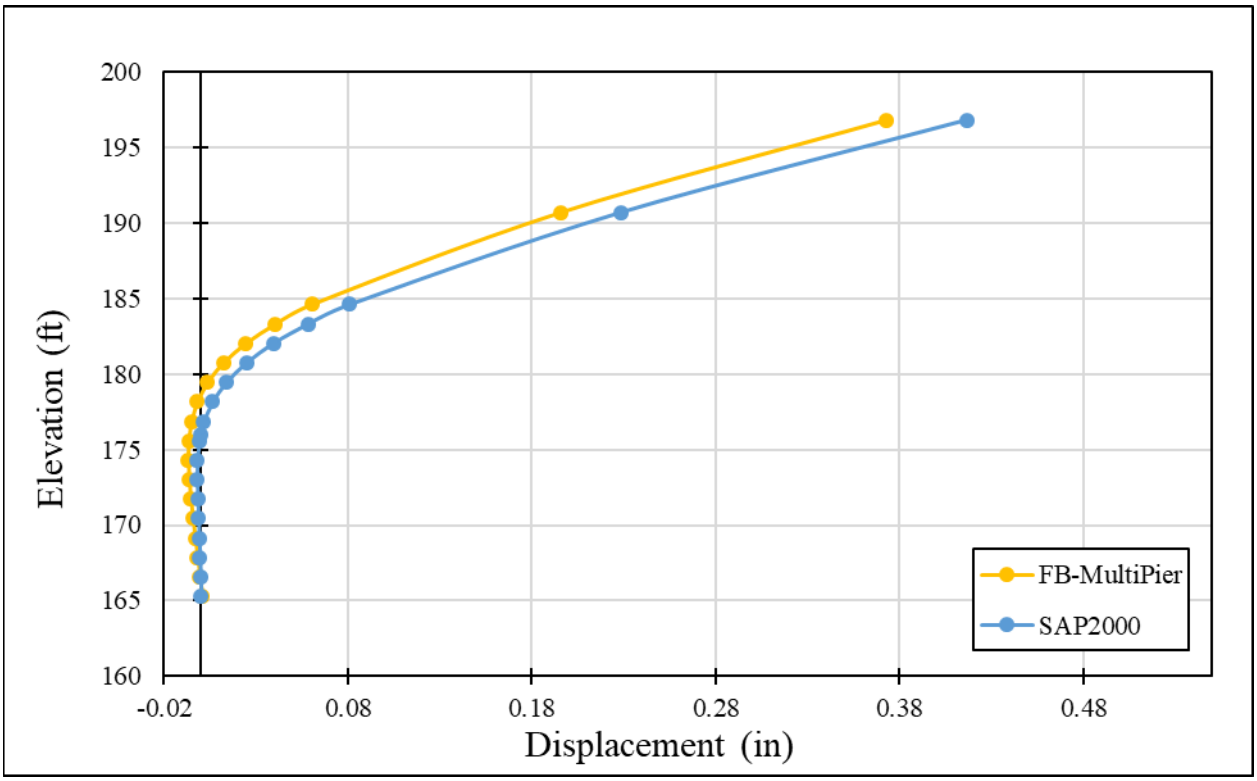

Figure A-13 – Displacement Comparisons for Pile 2 Bent 4

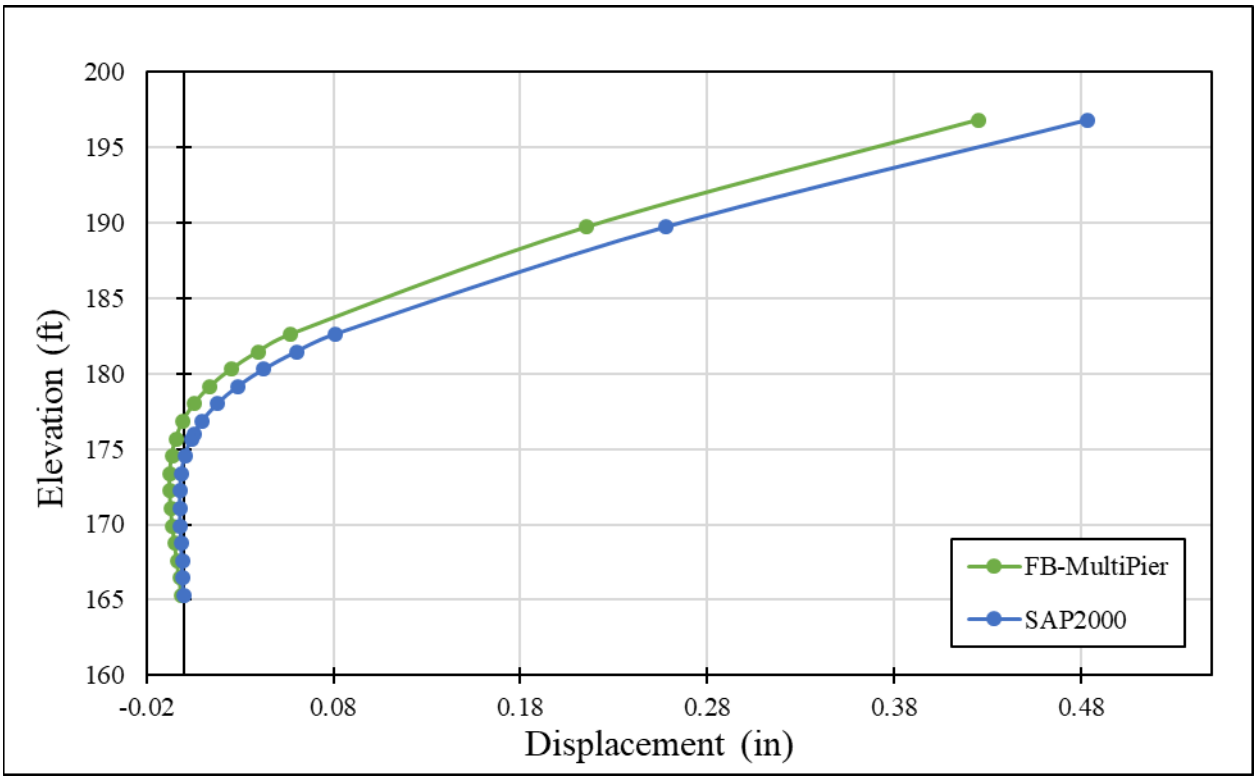

Figure A-14 – Displacement Comparisons for Pile 3 Bent 4

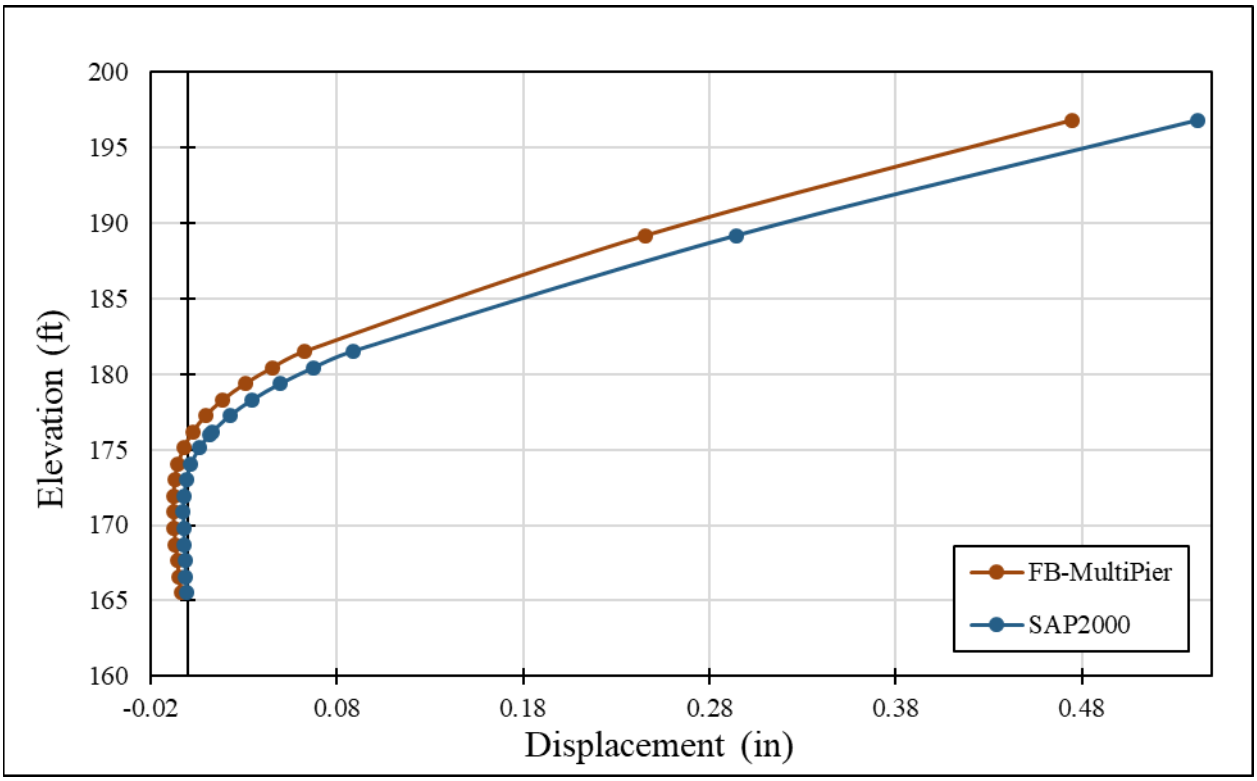

Figure A-15 – Displacement Comparisons for Pile 4 Bent 4

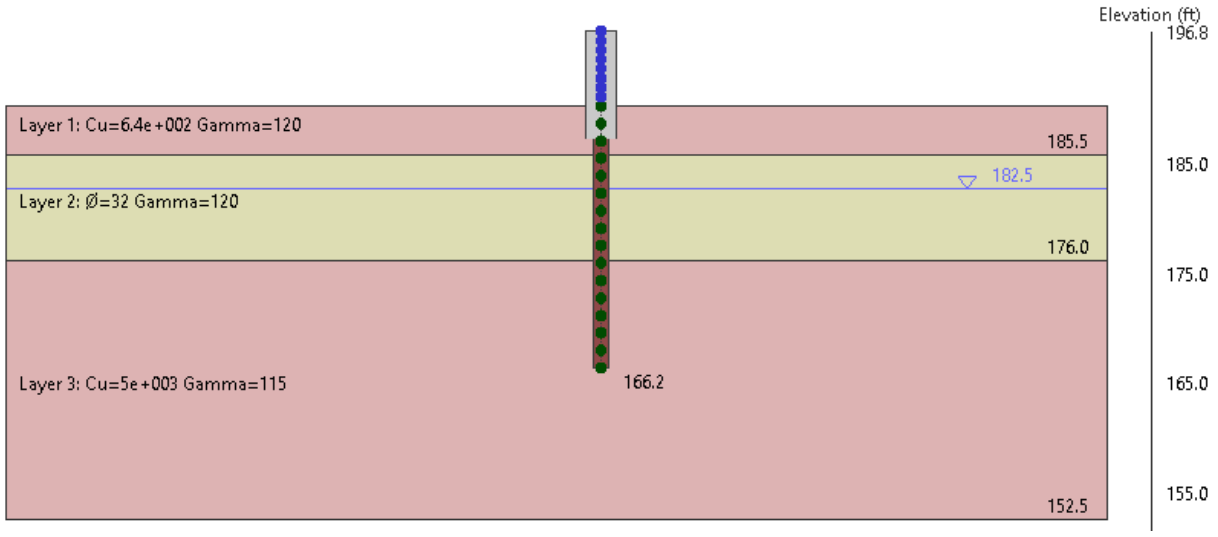

Figure A-16 – Bents 5 and 6 Elevation View in FBMP

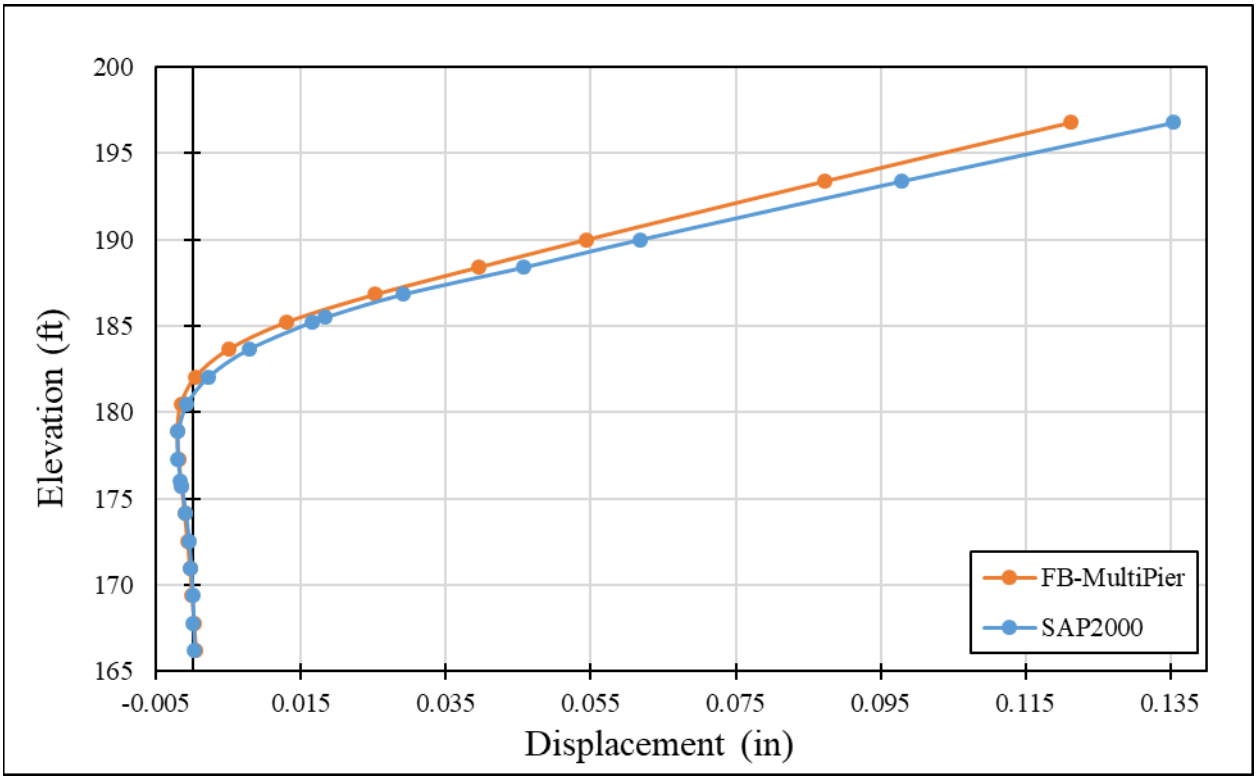

Figure A-17 – Displacement Comparisons for Pile 1 Bent 5&6

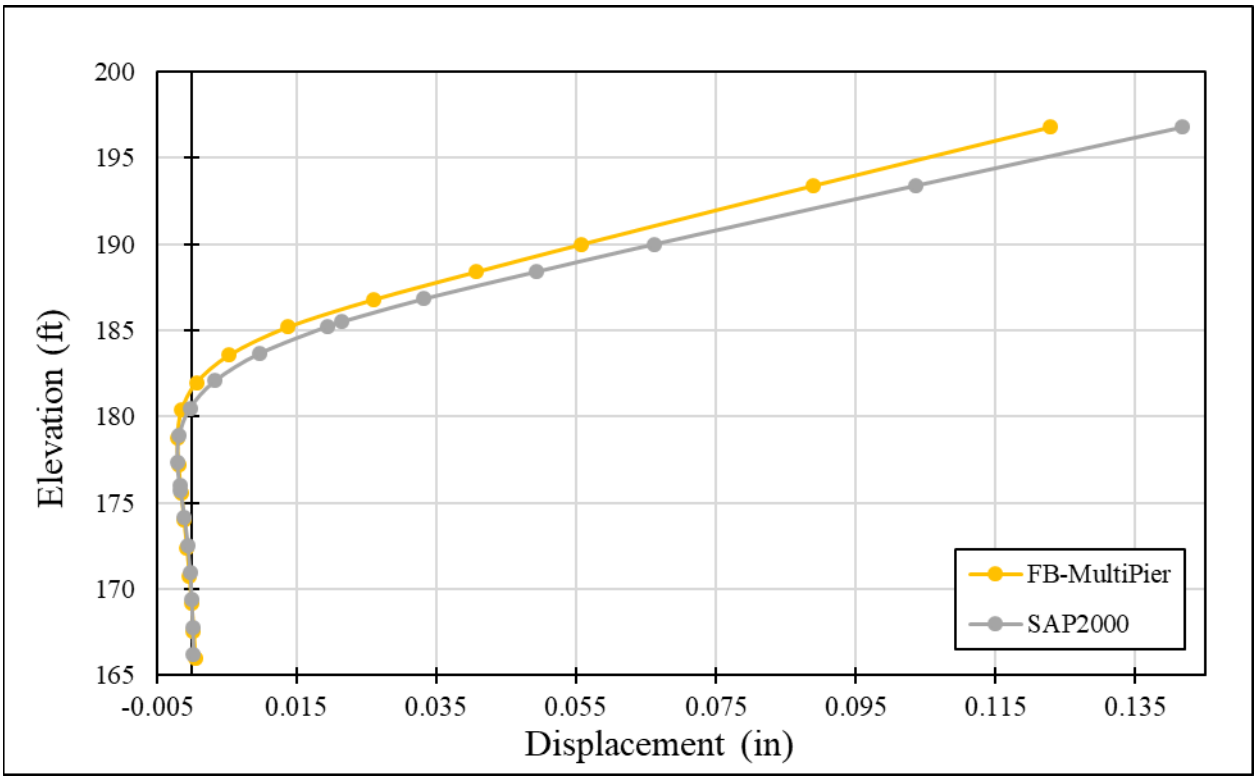

Figure A-18 – Displacement Comparisons for Pile 2 Bent 5&6

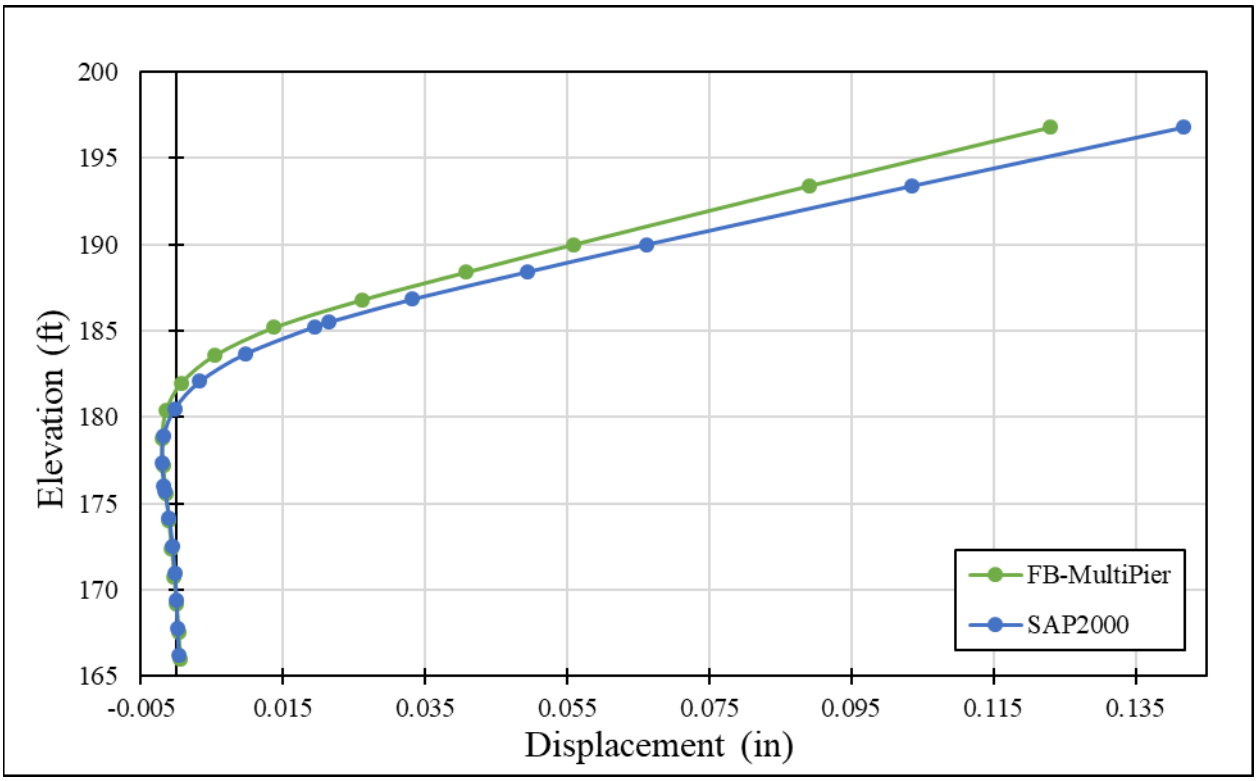

Figure A-19 – Displacement Comparisons for Pile 3 Bent 5&6

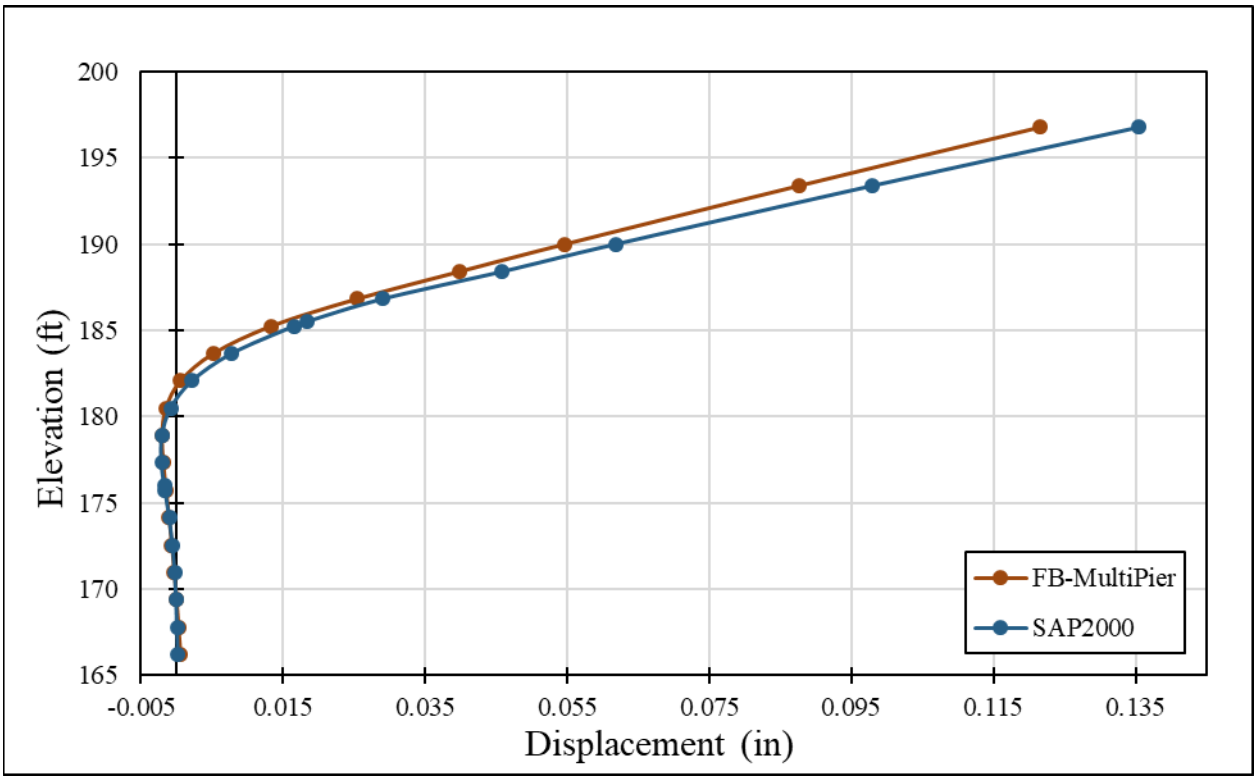

Figure A-20 – Displacement Comparisons for Pile 4 Bent 5&6

APPENDIX B: Static Tests Downsampled Data

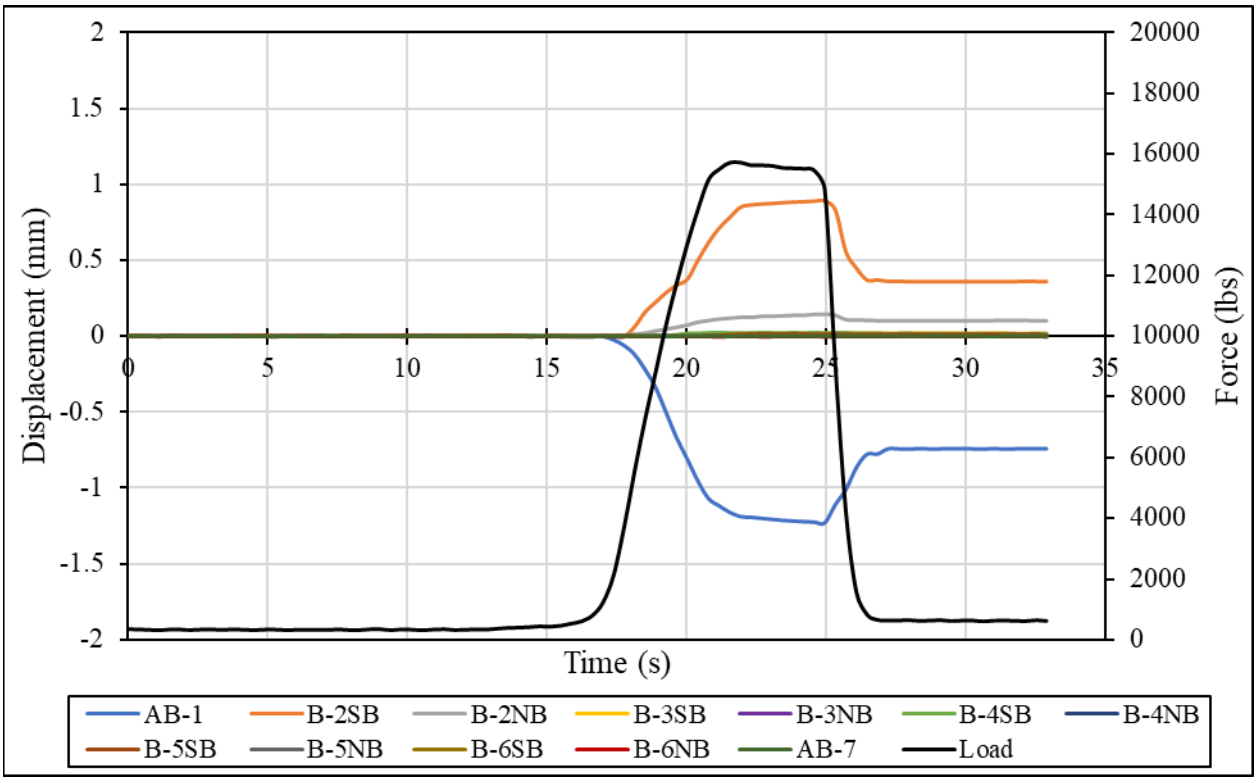

Figure B-1 – Load and Displacement over Time for Span 1 Static Pull Test

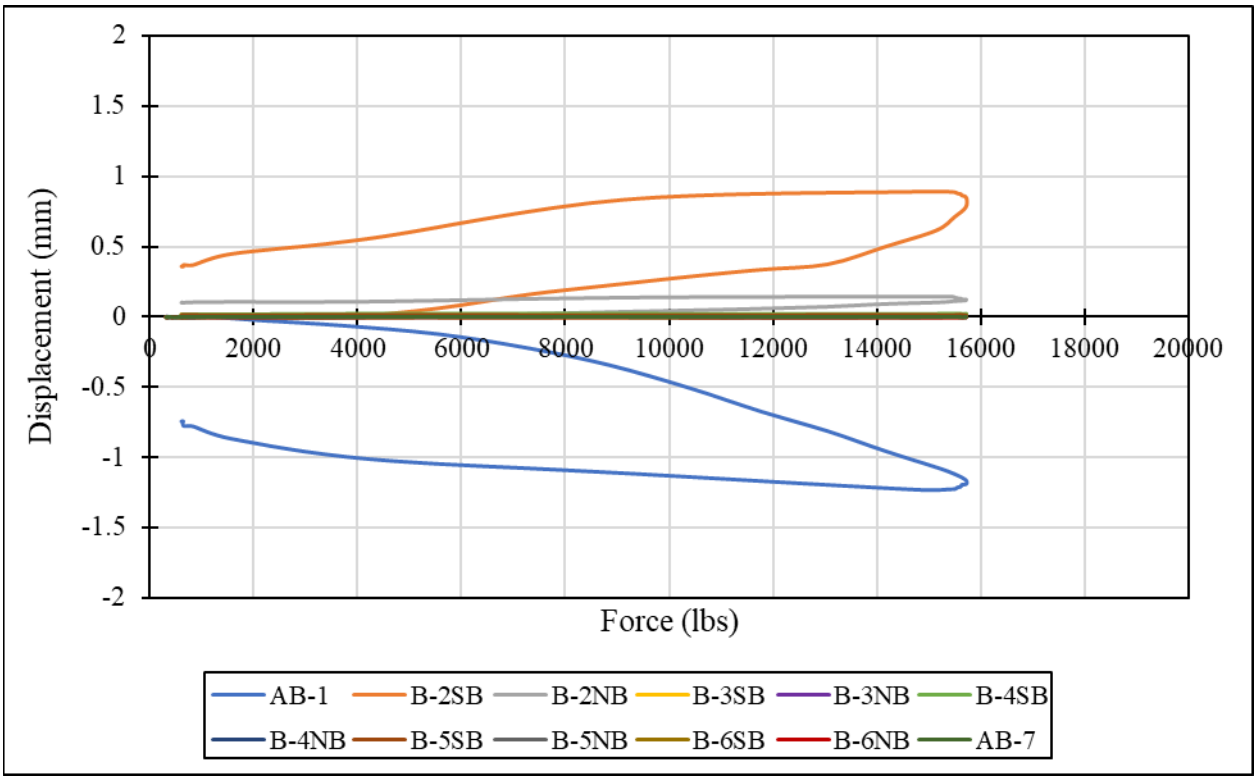

Figure B-2 – Displacement versus Applied Load for Span 1 Static Pull Test

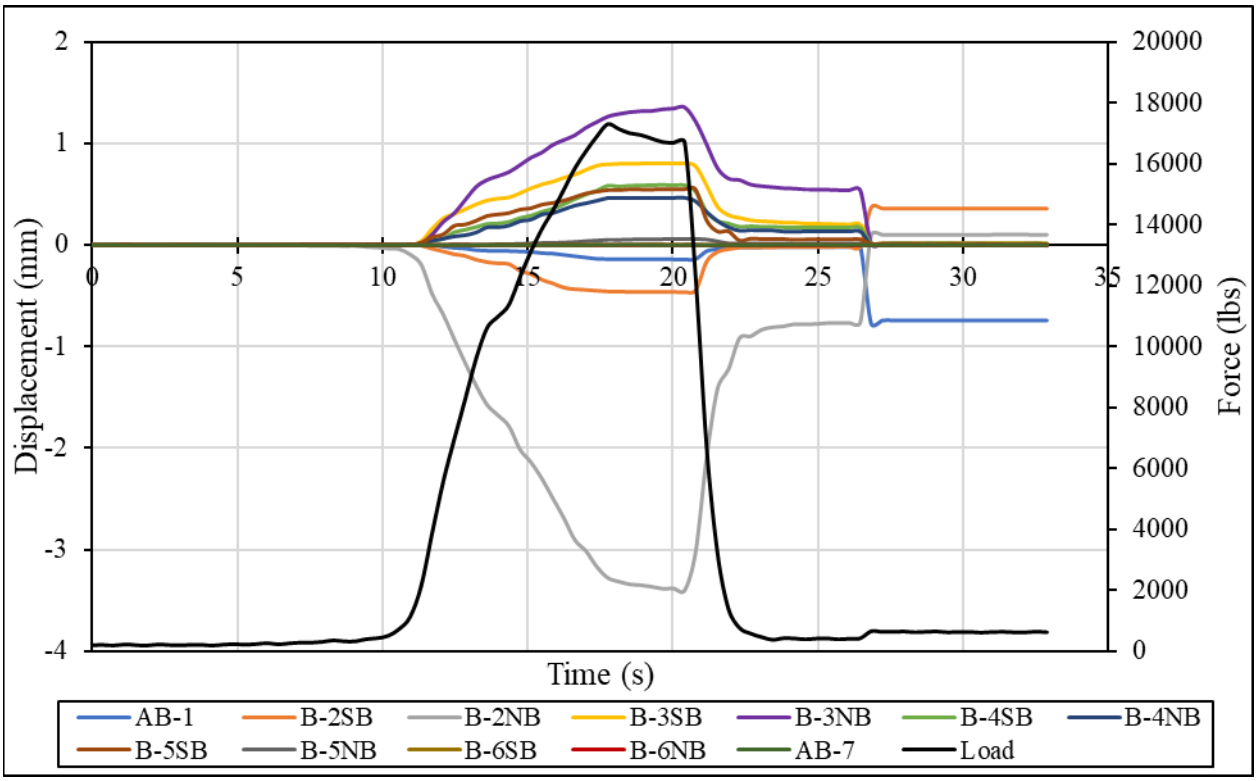

Figure B-3 – Load and Displacement over Time for Span 2 Static Pull Test

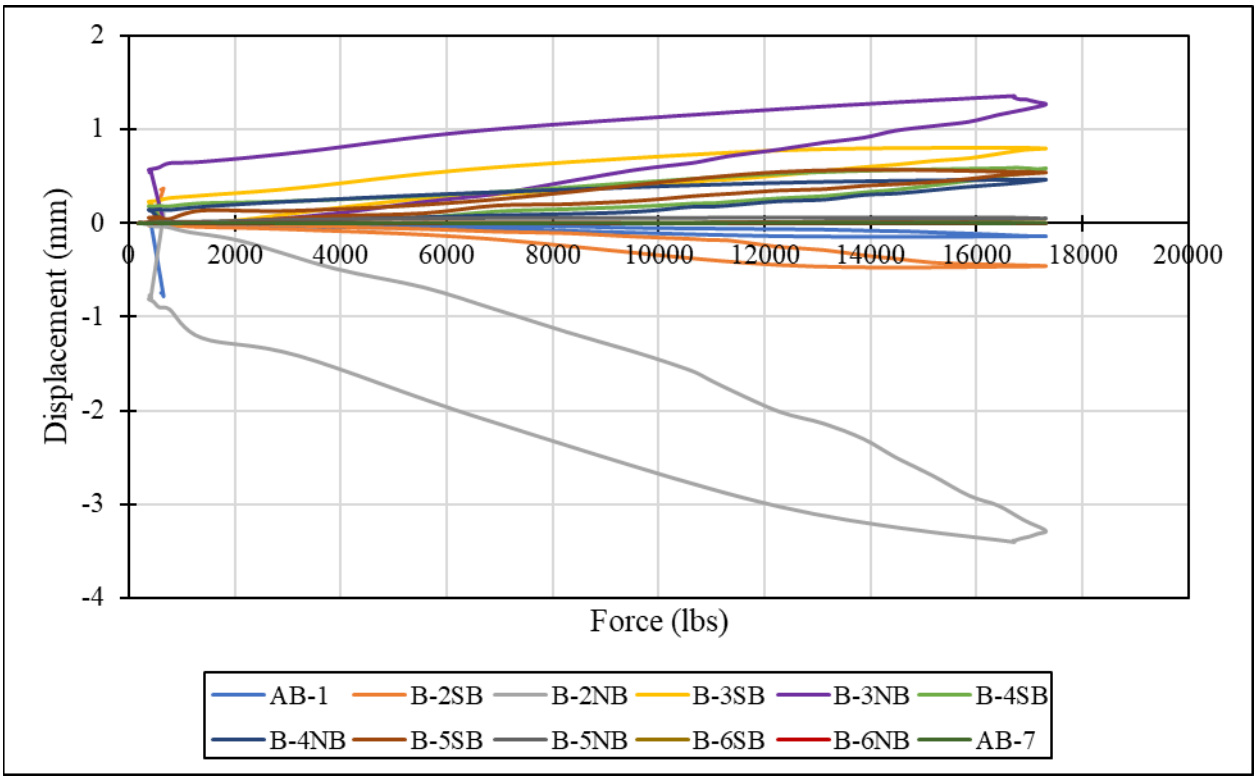

Figure B-4 – Displacement versus Applied Load for Span 2 Static Pull Test

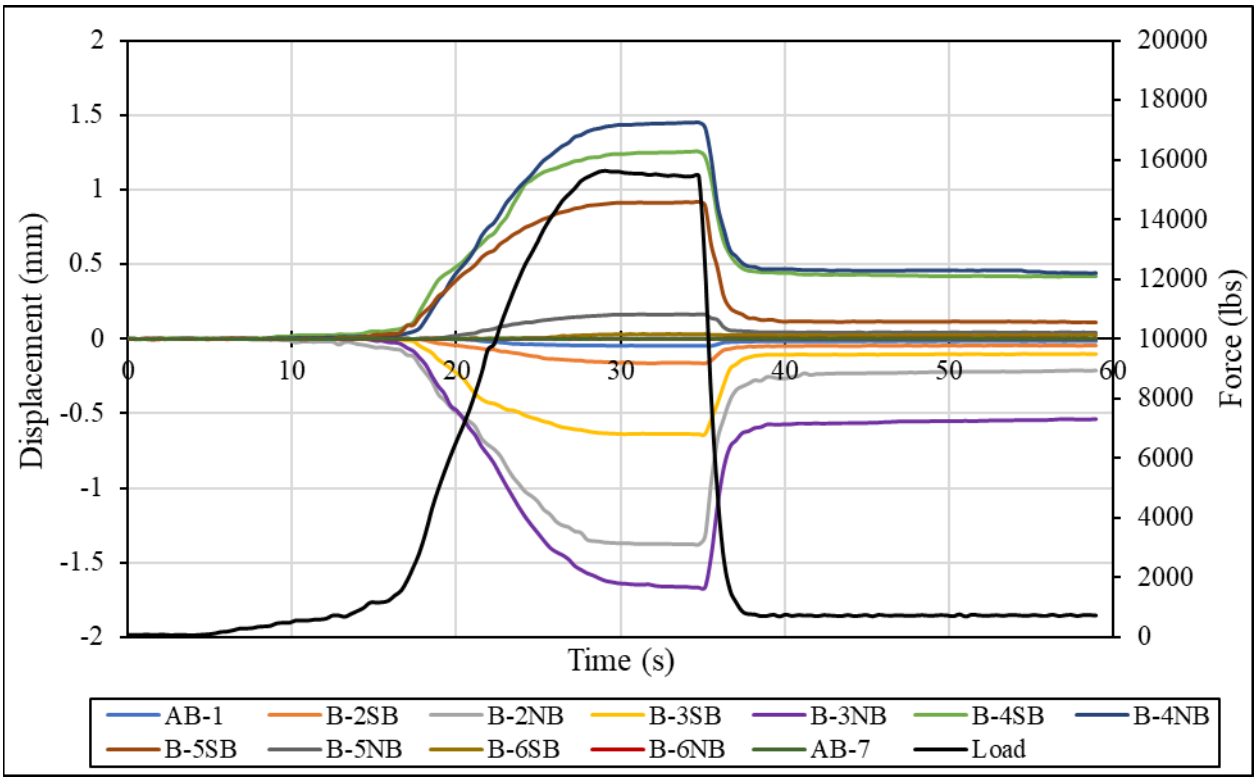

Figure B-5 – Load and Displacement over Time for Span 3 Static Pull Test

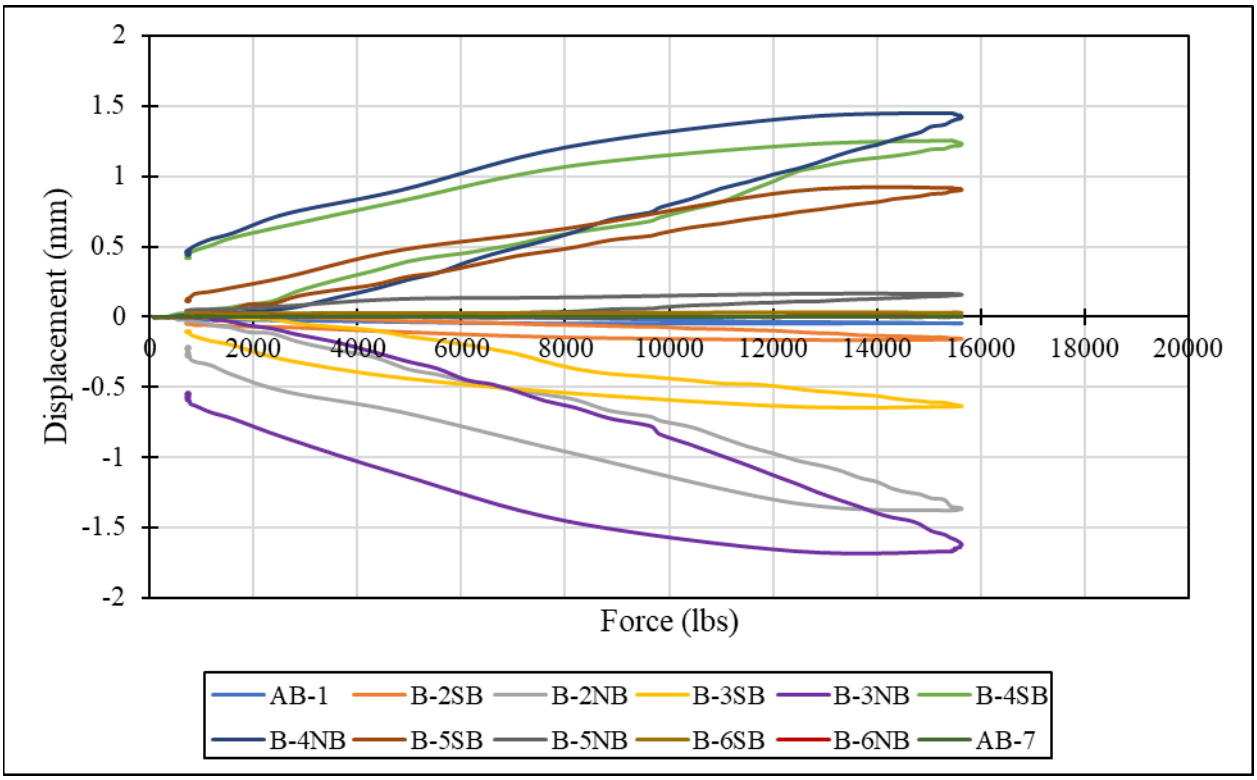

Figure B-6 – Displacement versus Applied Load for Span 3 Static Pull Test

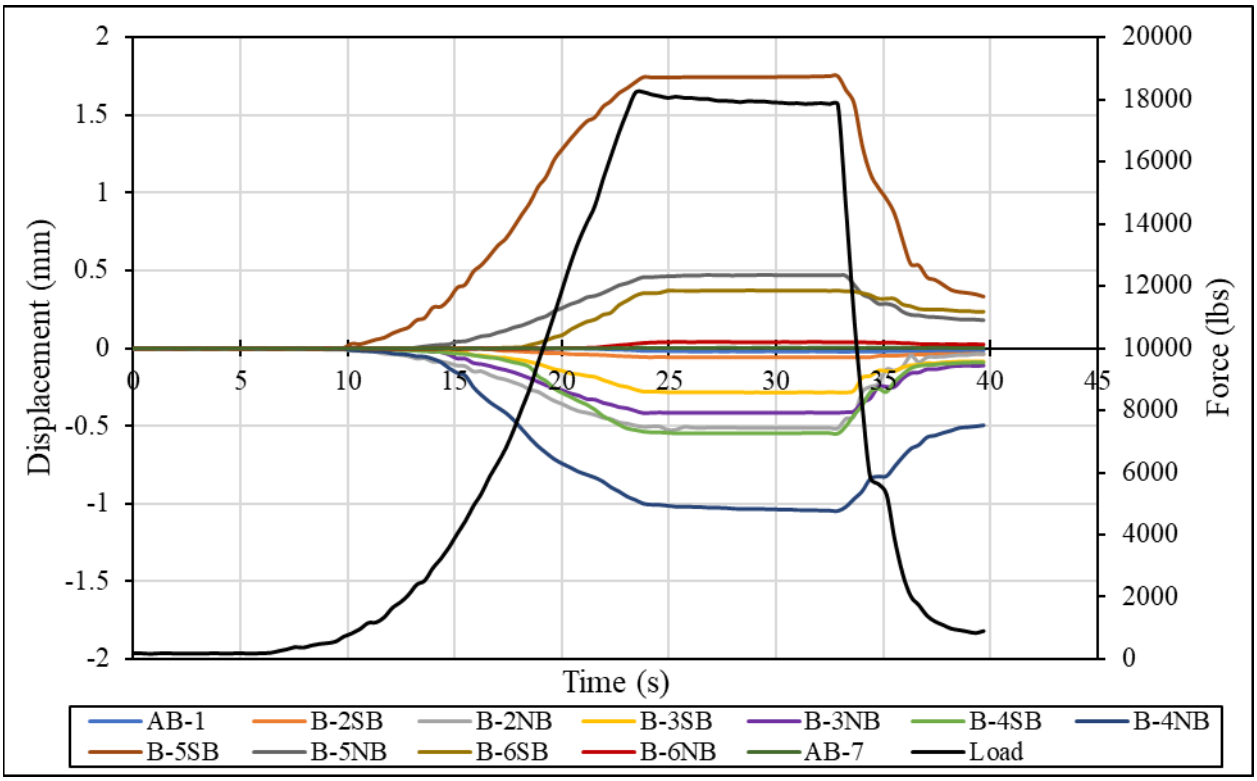

Figure B-7 – Load and Displacement over Time for Span 4 Static Pull Test

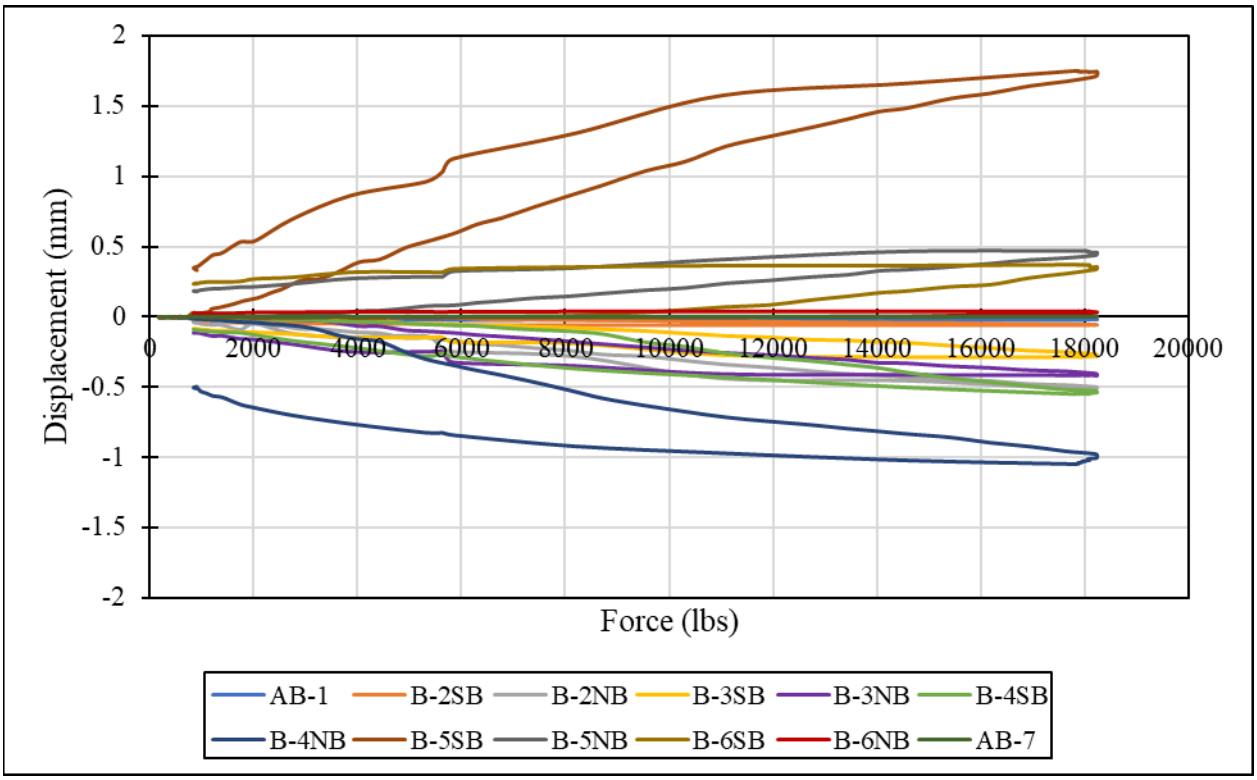

Figure B-8 – Displacement versus Applied Load for Span 4 Static Pull Test

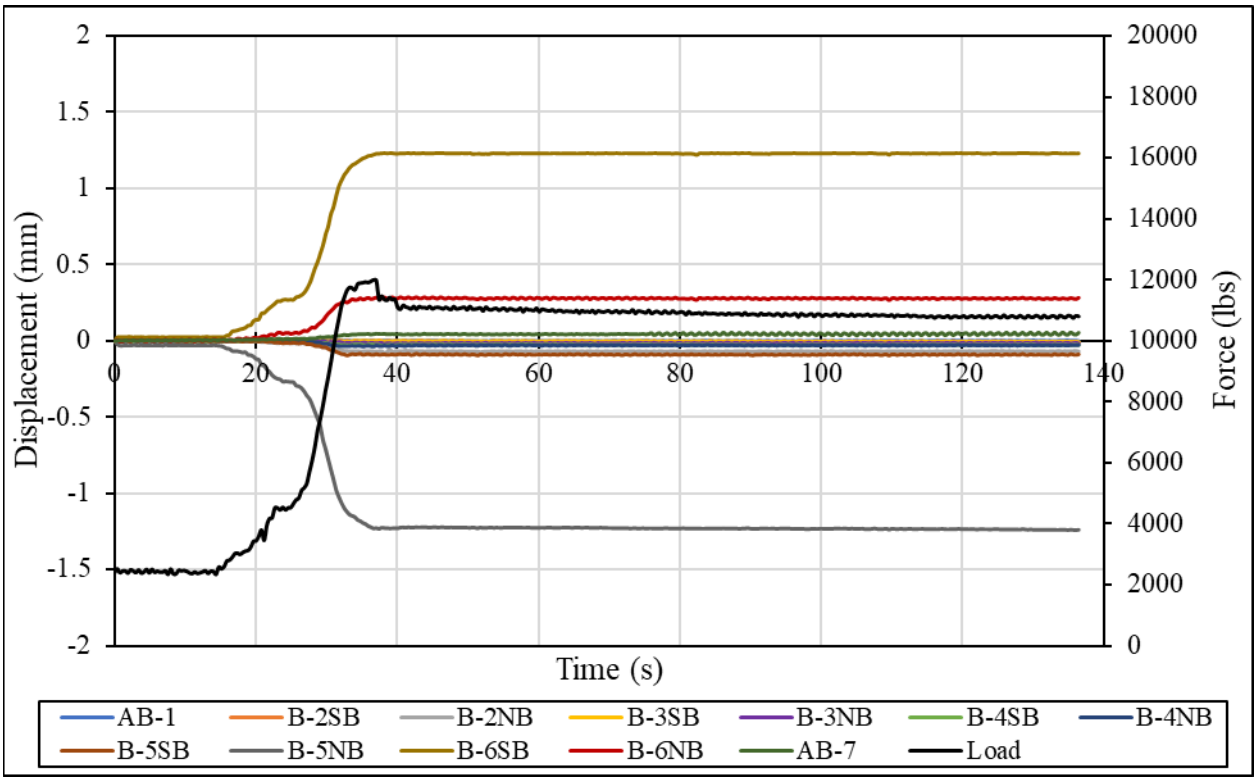

Figure B-9 – Load and Displacement over Time for Span 5 Static Pull Test 1

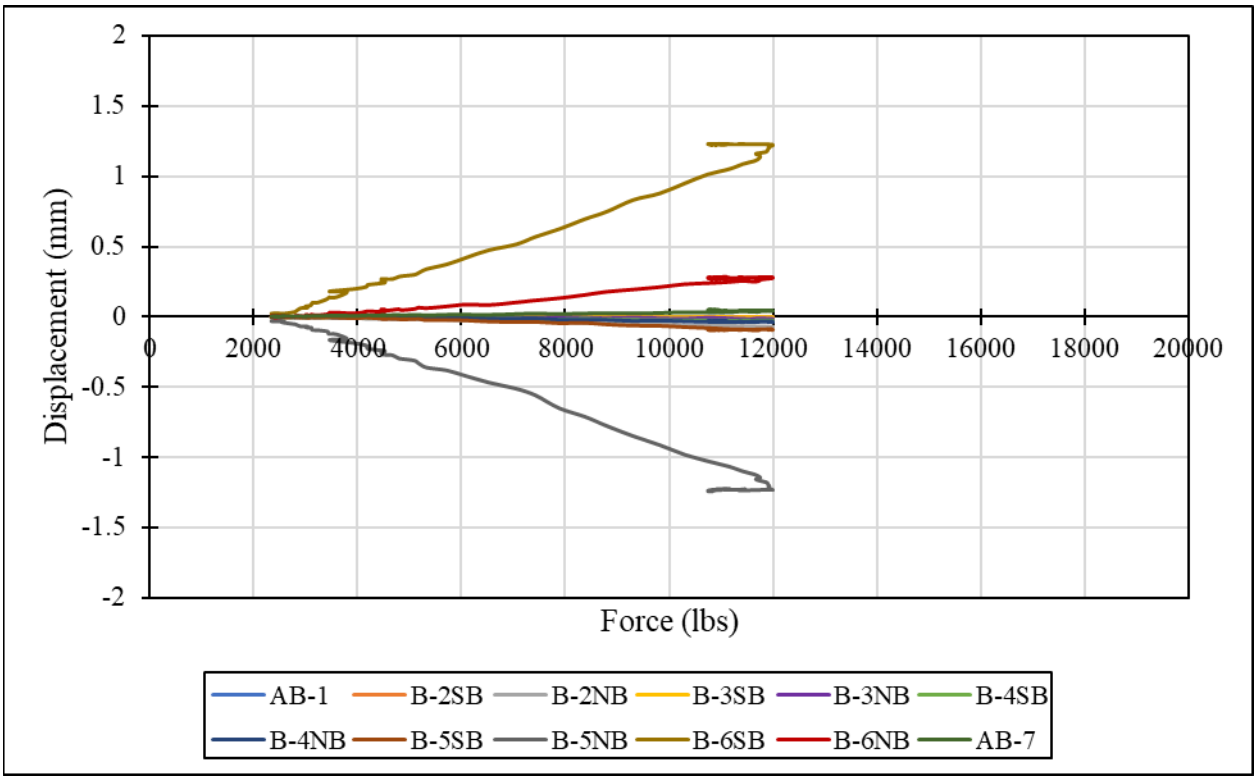

Figure B-10 – Displacement versus Applied Load for Span 5 Static Pull Test 1

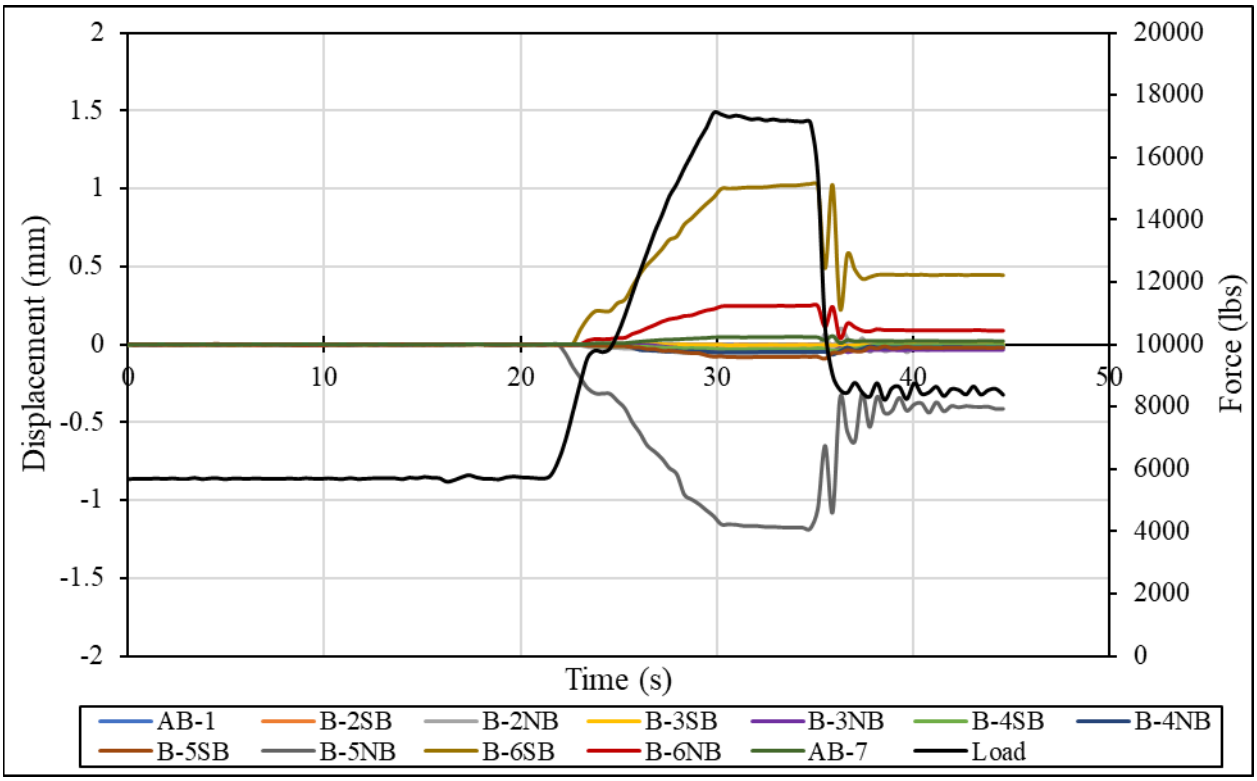

Figure B-11 – Load and Displacement over Time for Span 5 Static Pull Test 2

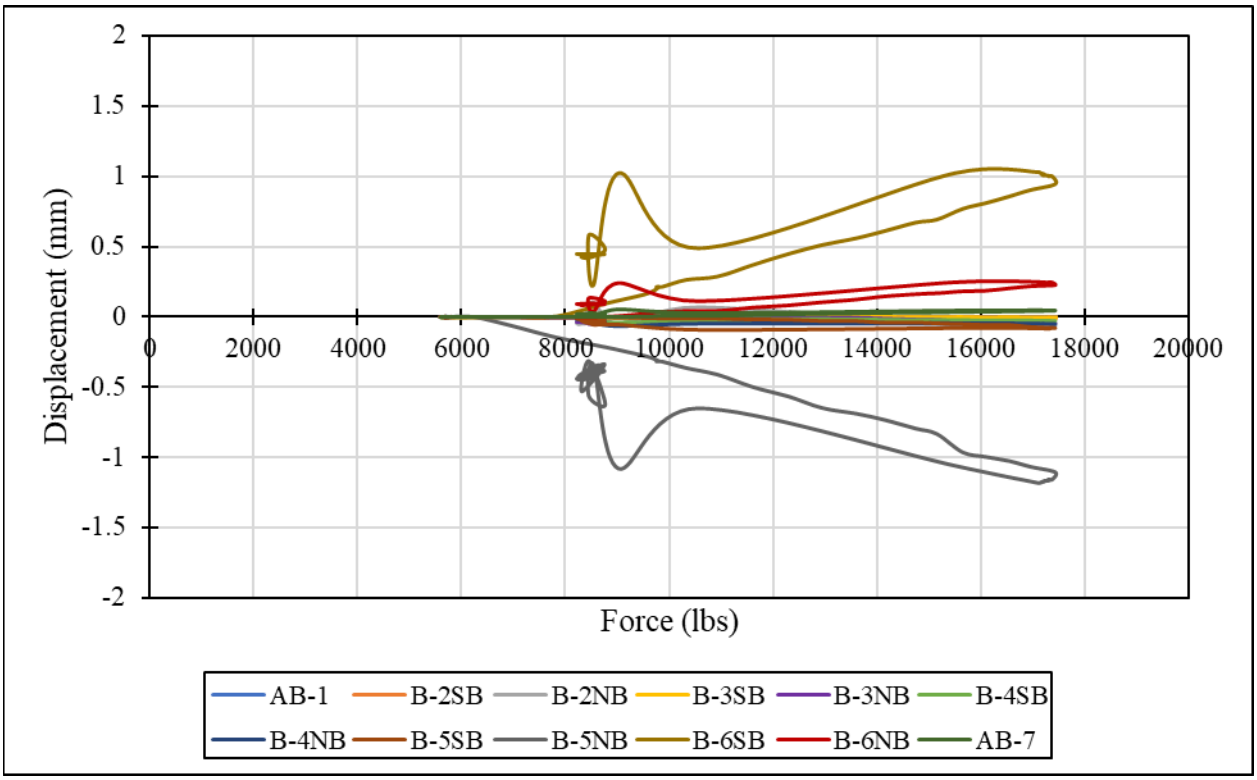

Figure B-12 – Displacement versus Applied Load for Span 5 Static Pull Test 2

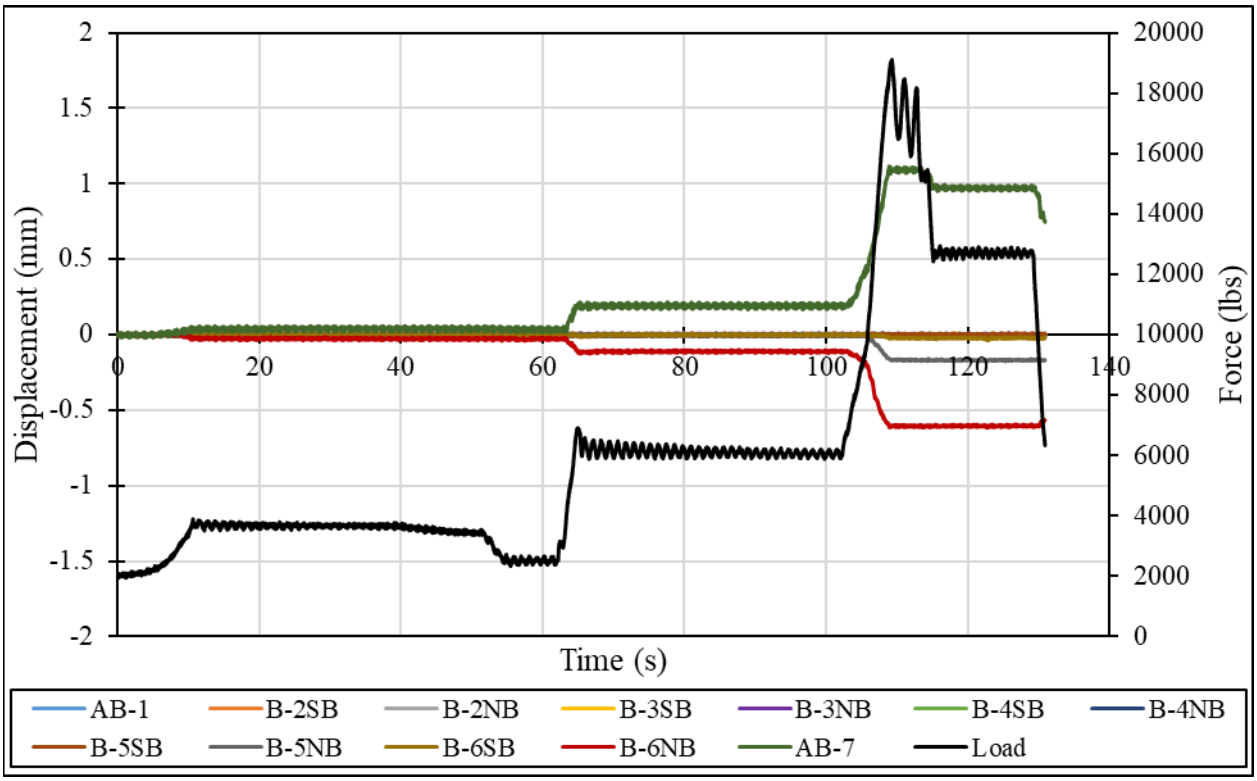

Figure B-13 – Load and Displacement over Time for Span 6 Static Pull Test

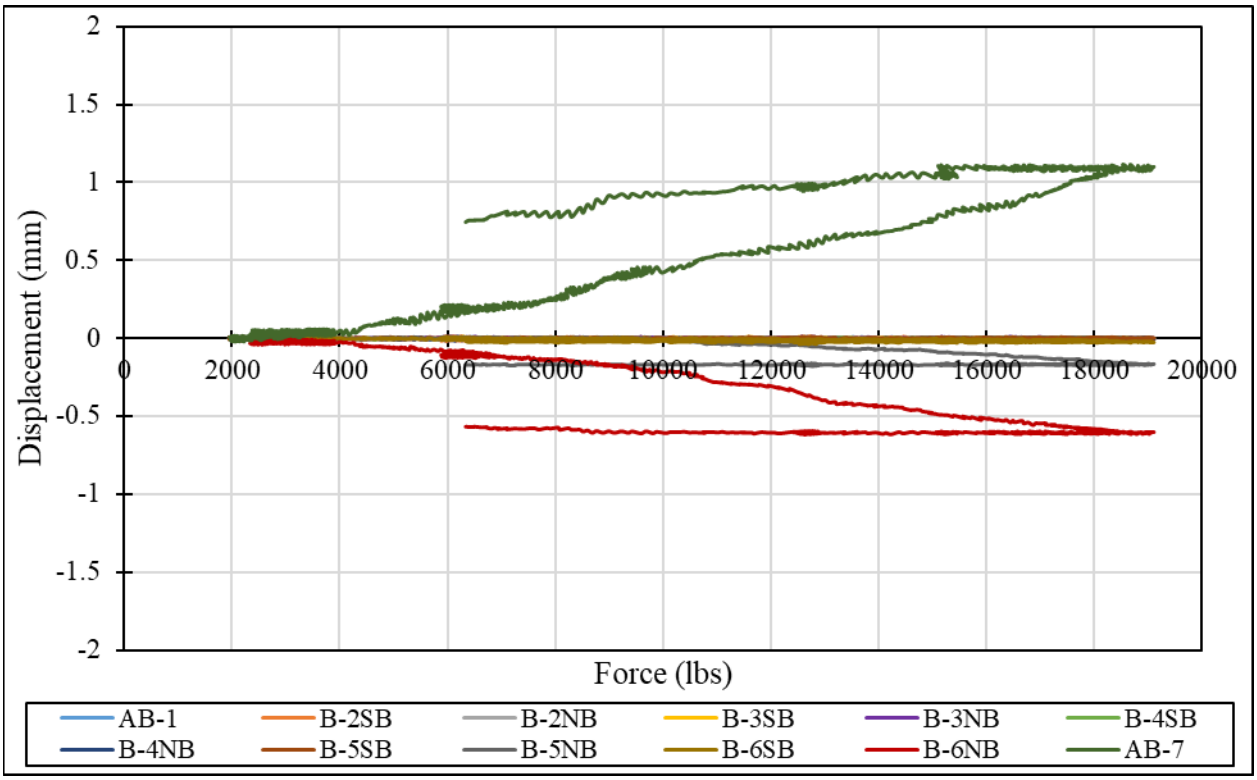

Figure B-14 – Displacement versus Applied Load for Span 6 Static Pull Test

Table B-1 – Field Test Displacement Data for Span 1

At 10400 lbs (ΔF = 10054 lbs) applied to Span 1			
Data From Field Tests			
	Displacement of Girder End Relative to Cap (in)	Displacement Relative to AB1 (in)	
A1	-0.0199	delta_S1	-0.0199
B2S1	0.0113	delta_B2	-0.0086
B2S2	0.0019	delta_S2	-0.0068
B3S2	0.0000	delta_B3	-0.0068
B3S3	0.0001	delta_S3	-0.0067
B4S3	0.0002	delta_B4	-0.0065
B4S4	0.0000	delta_S4	-0.0065
B5S4	0.0000	delta_B5	-0.0066
B5S5	0.0000	delta_S5	-0.0066
B6S5	0.0000	delta_B6	-0.0066
B6S6	0.0000	delta_S6	-0.0067
A7	0.0000	delta_AB7	-0.0067

Table B-2 – Field Test Displacement Data for Span 2

At 10613 lbs (ΔF = 10416 lbs) applied to Span 2			
Data From Field Tests			
	Displacement of Girder End Relative to Cap (in)	Displacement Relative to AB1 (in)	
A1	-0.0022	delta_S1	-0.0022
B2S1	-0.0066	delta_B2	-0.0088
B2S2	-0.0619	delta_S2	-0.0707
B3S2	0.0173	delta_B3	-0.0534
B3S3	0.0253	delta_S3	-0.0281
B4S3	0.0082	delta_B4	-0.0198
B4S4	0.0069	delta_S4	-0.0130
B5S4	0.0113	delta_B5	-0.0016
B5S5	0.0001	delta_S5	-0.0015
B6S5	0.0000	delta_B6	-0.0015
B6S6	0.0000	delta_S6	-0.0015
A7	0.0000	delta_AB7	-0.0015

Table B-3 – Field Test Displacement Data for Span 3

At 9823 lbs (ΔF = 9739 lbs) applied to Span 3			
Data From Field Tests			
	Displacement of Girder End Relative to Cap (in)	Displacement Relative to AB1 (in)	
A1	-0.0007	delta_S1	-0.0007
B2S1	-0.0028	delta_B2	-0.0035
B2S2	-0.0291	delta_S2	-0.0325
B3S2	-0.0170	delta_B3	-0.0496
B3S3	-0.0328	delta_S3	-0.0824
B4S3	0.0279	delta_B4	-0.0545
B4S4	0.0307	delta_S4	-0.0238
B5S4	0.0234	delta_B5	-0.0005
B5S5	0.0027	delta_S5	0.0022
B6S5	0.0001	delta_B6	0.0023
B6S6	0.0000	delta_S6	0.0023
A7	0.0000	delta_AB7	0.0023

Table B-4 – Field Test Displacement Data for Span 4

At 10307 lbs (ΔF = 10117 lbs) applied to Span 4			
Data From Field Tests			
	Displacement of Girder End Relative to Cap (in)	Displacement Relative to AB1 (in)	
A1	-0.0001	delta_S1	-0.0001
B2S1	-0.0012	delta_B2	-0.0013
B2S2	-0.0122	delta_S2	-0.0135
B3S2	-0.0046	delta_B3	-0.0181
B3S3	-0.0094	delta_S3	-0.0274
B4S3	-0.0083	delta_B4	-0.0358
B4S4	-0.0265	delta_S4	-0.0623
B5S4	0.0435	delta_B5	-0.0188
B5S5	0.0081	delta_S5	-0.0106
B6S5	0.0020	delta_B6	-0.0086
B6S6	-0.0001	delta_S6	-0.0087
A7	0.0000	delta_AB7	-0.0087

Table B-5 – Field Test Displacement Data for Span 5 Test 1

At 11998 lbs (ΔF = 9601 lbs) applied to Span 5			
Data From Field Tests			
	Displacement of Girder End Relative to Cap (in)	Displacement Relative to AB1 (in)	
A1	0.0000	delta_S1	0.0000
B2S1	0.0000	delta_B2	0.0000
B2S2	-0.0027	delta_S2	-0.0027
B3S2	-0.0001	delta_B3	-0.0028
B3S3	-0.0005	delta_S3	-0.0033
B4S3	-0.0010	delta_B4	-0.0043
B4S4	-0.0015	delta_S4	-0.0057
B5S4	-0.0036	delta_B5	-0.0093
B5S5	-0.0484	delta_S5	-0.0578
B6S5	0.0481	delta_B6	-0.0097
B6S6	0.0110	delta_S6	0.0013
A7	0.0017	delta_AB7	0.0030

Table B-6 – Field Test Displacement Data for Span 5 Test 2

At 15653 lbs (ΔF = 9977 lbs) applied to Span 5			
Data From Field Tests			
	Displacement of Girder End Relative to Cap (in)	Displacement Relative to AB1 (in)	
A1	0.0000	delta_S1	0.0000
B2S1	-0.0001	delta_B2	-0.0001
B2S2	-0.0022	delta_S2	-0.0023
B3S2	0.0000	delta_B3	-0.0023
B3S3	-0.0012	delta_S3	-0.0035
B4S3	-0.0010	delta_B4	-0.0045
B4S4	-0.0018	delta_S4	-0.0063
B5S4	-0.0020	delta_B5	-0.0083
B5S5	-0.0379	delta_S5	-0.0462
B6S5	0.0303	delta_B6	-0.0159
B6S6	0.0072	delta_S6	-0.0087
A7	0.0014	delta_AB7	-0.0073

Table B-7 – Field Test Displacement Data for Span 6

At 11954 lbs (ΔF = 9973 lbs) applied to Span 6			
Data From Field Tests			
	Displacement of Girder End Relative to Cap (in)	Displacement Relative to AB1 (in)	
A1	0.0000	delta_S1	0.0000
B2S1	-0.0002	delta_B2	-0.0002
B2S2	-0.0002	delta_S2	-0.0004
B3S2	0.0000	delta_B3	-0.0004
B3S3	-0.0003	delta_S3	-0.0007
B4S3	0.0000	delta_B4	-0.0007
B4S4	0.0000	delta_S4	-0.0007
B5S4	0.0001	delta_B5	-0.0007
B5S5	-0.0016	delta_S5	-0.0023
B6S5	-0.0001	delta_B6	-0.0024
B6S6	-0.0119	delta_S6	-0.0143
A7	0.0231	delta_AB7	0.0088

APPENDIX C: Dynamic Tests Downsampled Data

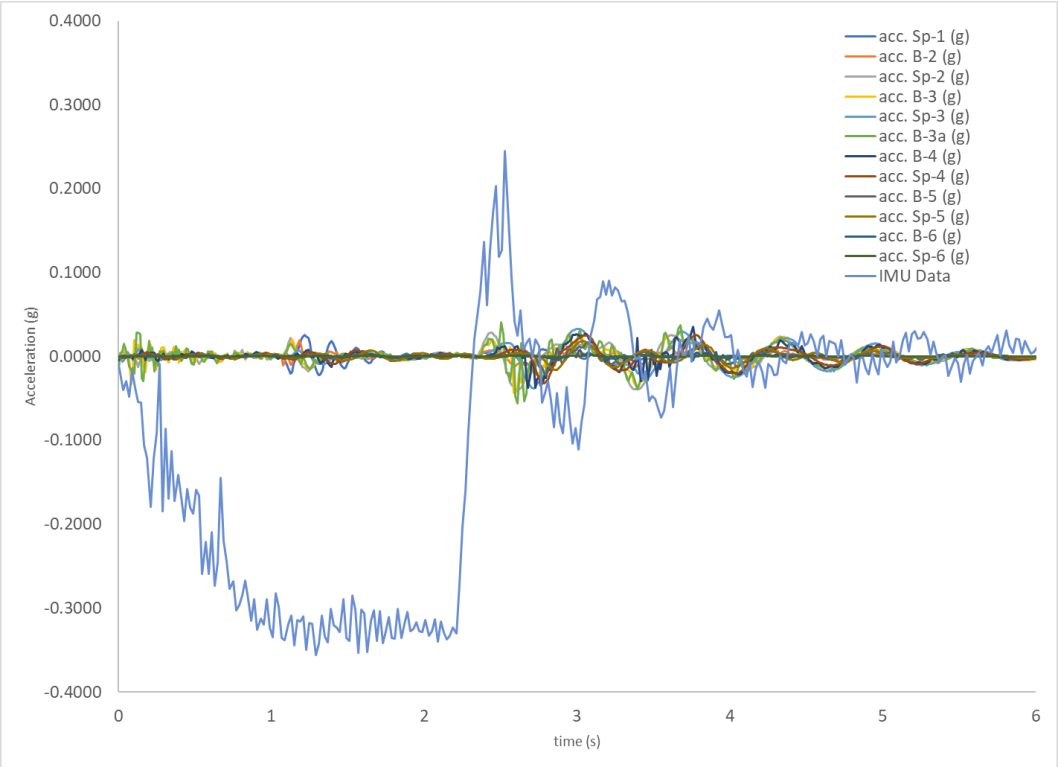

Figure C-1 – DAQ and IMU Data from Center of Span 2 Test 1 (Barr 2019)

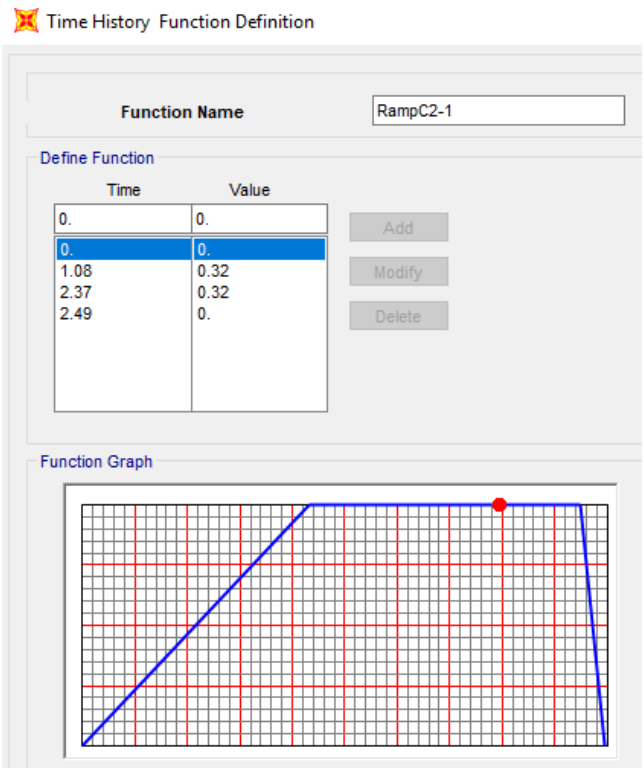

Figure C-2 – SAP2000 Time History Ramp Function from Braking Profile for C2-1

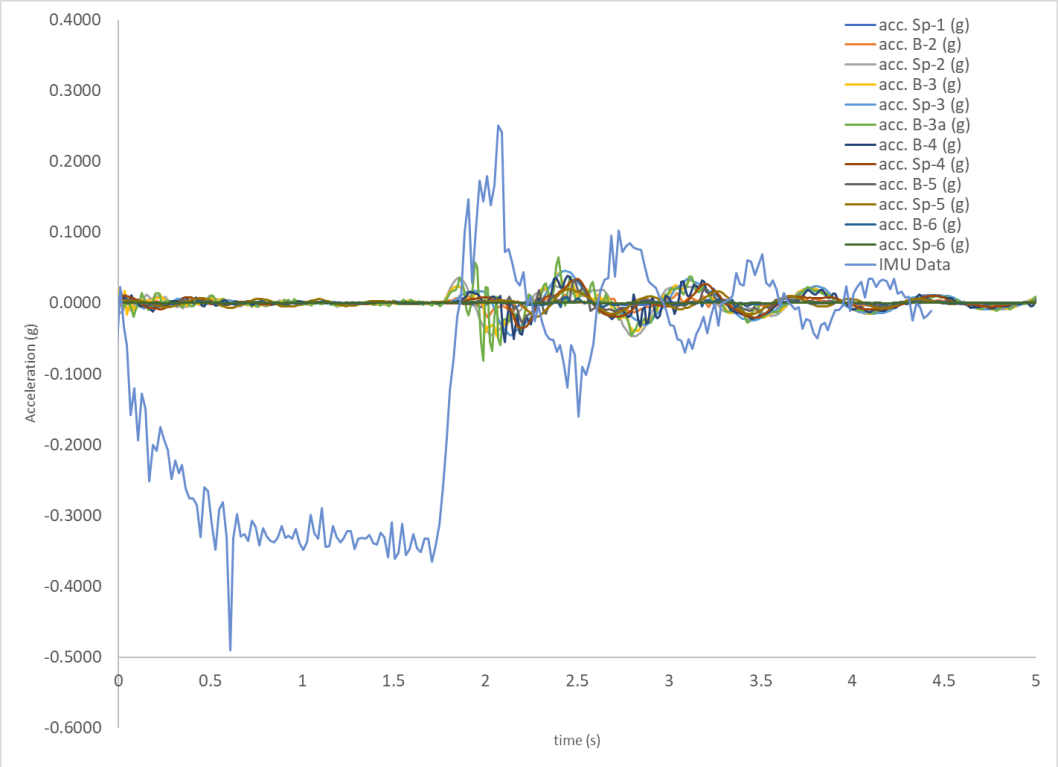

Figure C-3 – DAQ and IMU Data from Center of Span 2 Test 2 (Barr 2019)

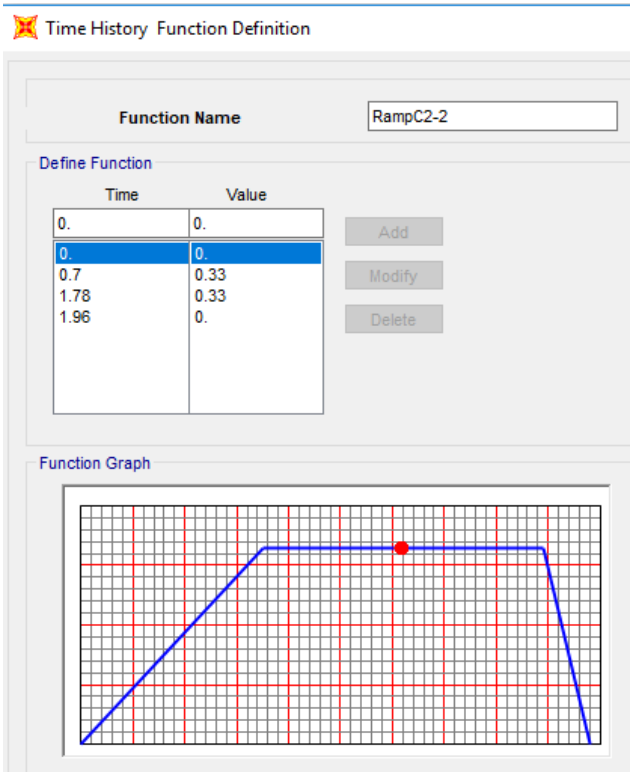

Figure C-4 – SAP2000 Time History Ramp Function from Braking Profile for C2-2

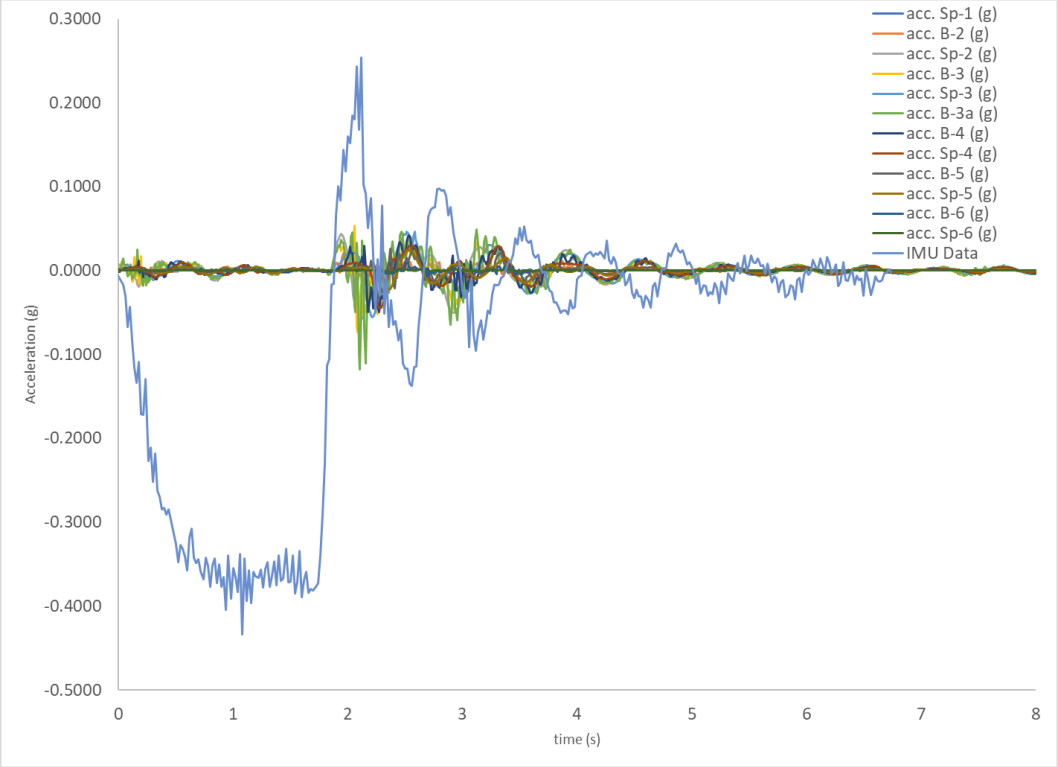

Figure C-5 – DAQ and IMU Data from Center of Span 2 Test 3 (Barr 2019)

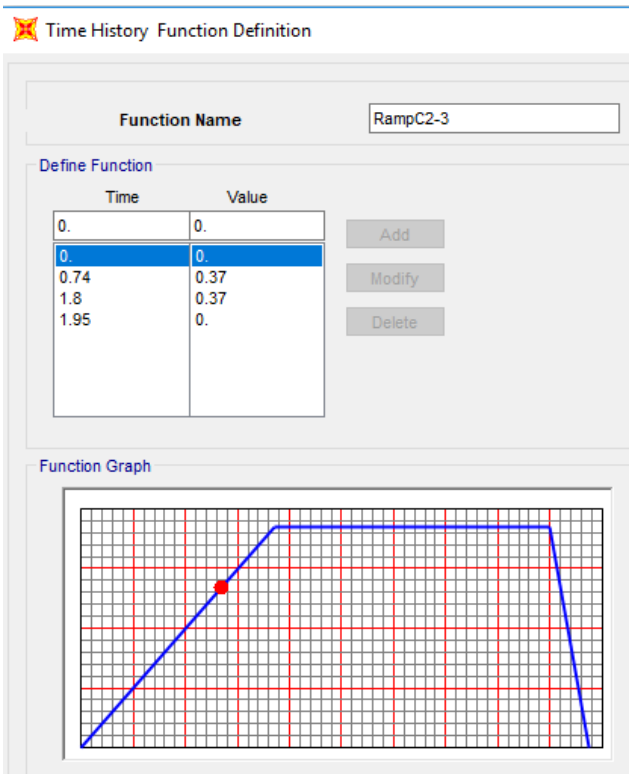

Figure C-6 – SAP2000 Time History Ramp Function from Braking Profile for C2-3

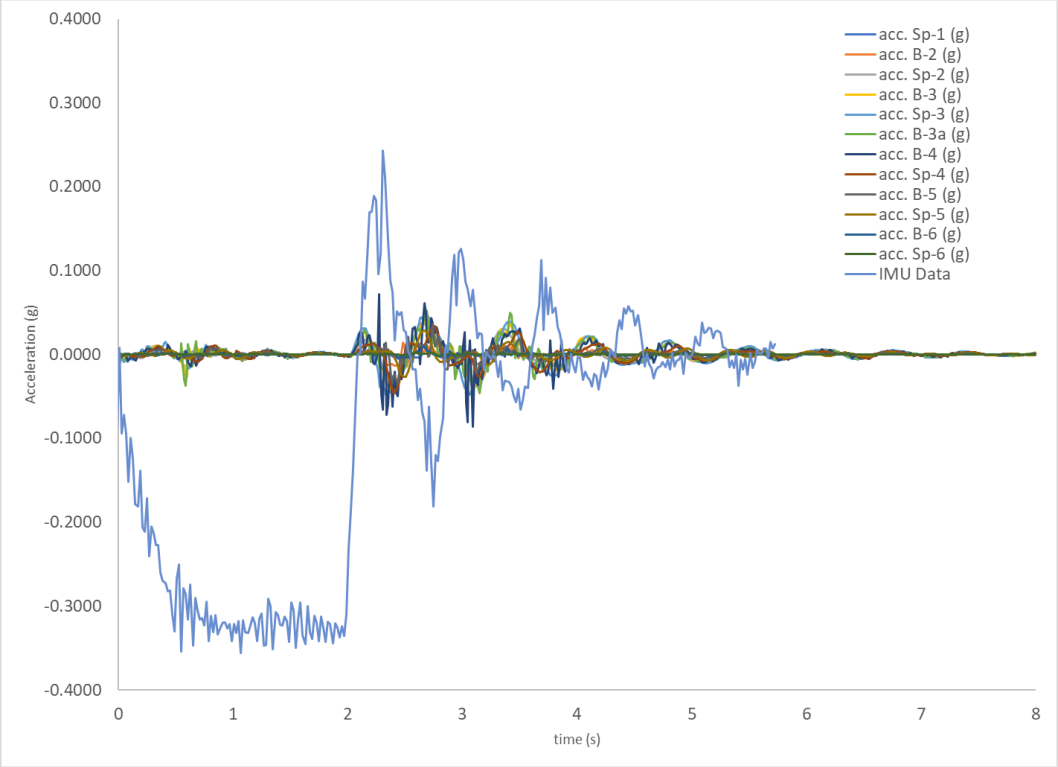

Figure C-7 – DAQ and IMU Data from Center of Span 3 Test 1 (Barr 2019)

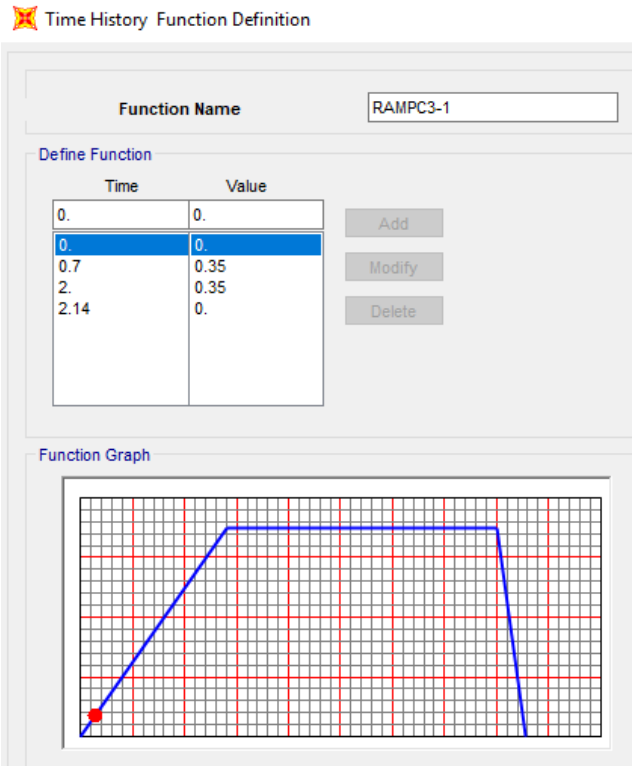

Figure C-8 – SAP2000 Time History Ramp Function from Braking Profile for C3-1

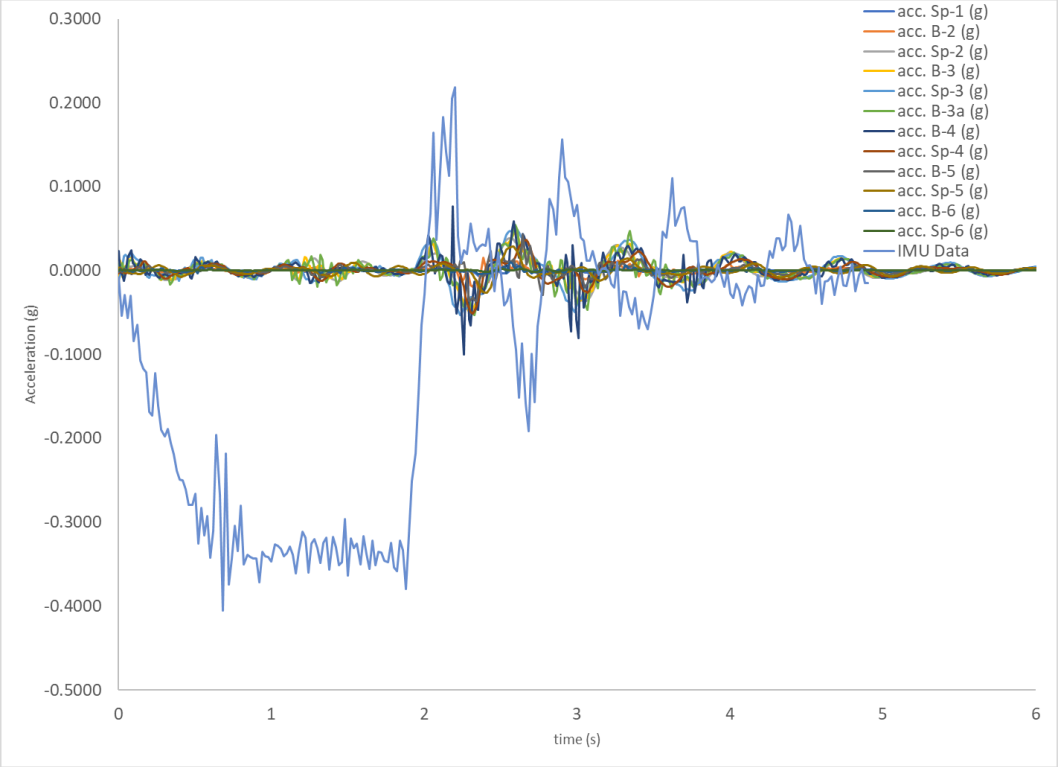

Figure C-9 – DAQ and IMU Data from Center of Span 3 Test 3 (Barr 2019)

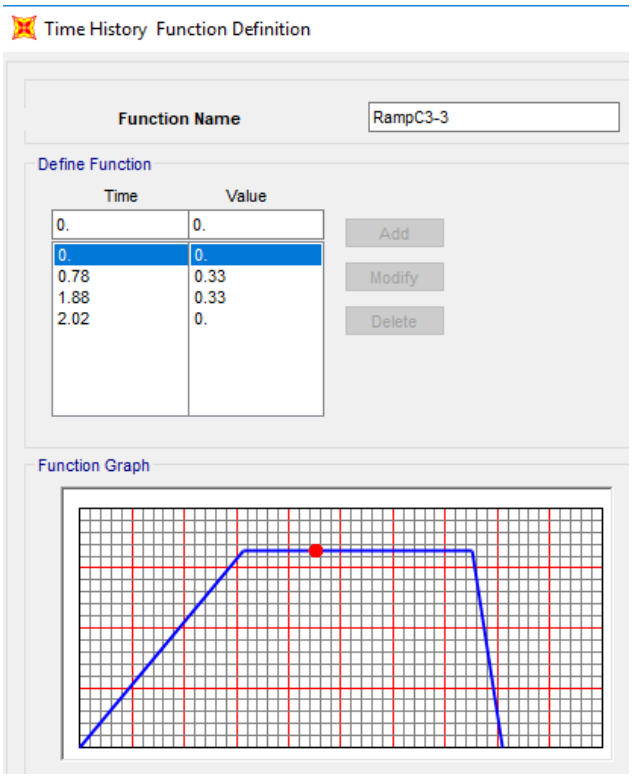

Figure C-10 – SAP2000 Time History Ramp Function from Braking Profile for C3-3

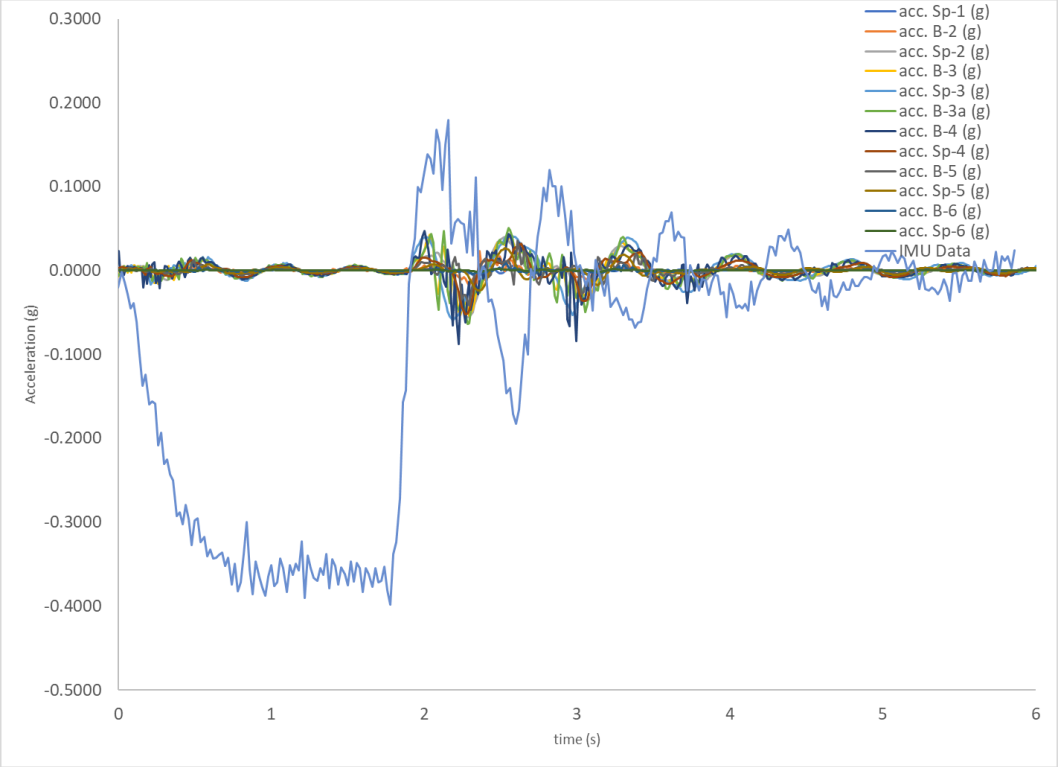

Figure C-11 – DAQ and IMU Data from Center of Span 3 Test 4 (Barr 2019)

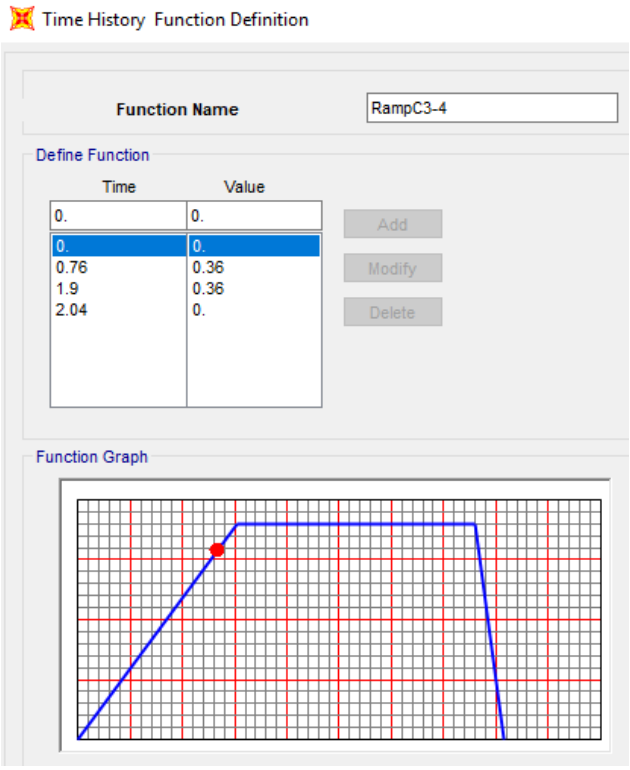

Figure C-12 – SAP2000 Time History Ramp Function from Braking Profile for C3-4

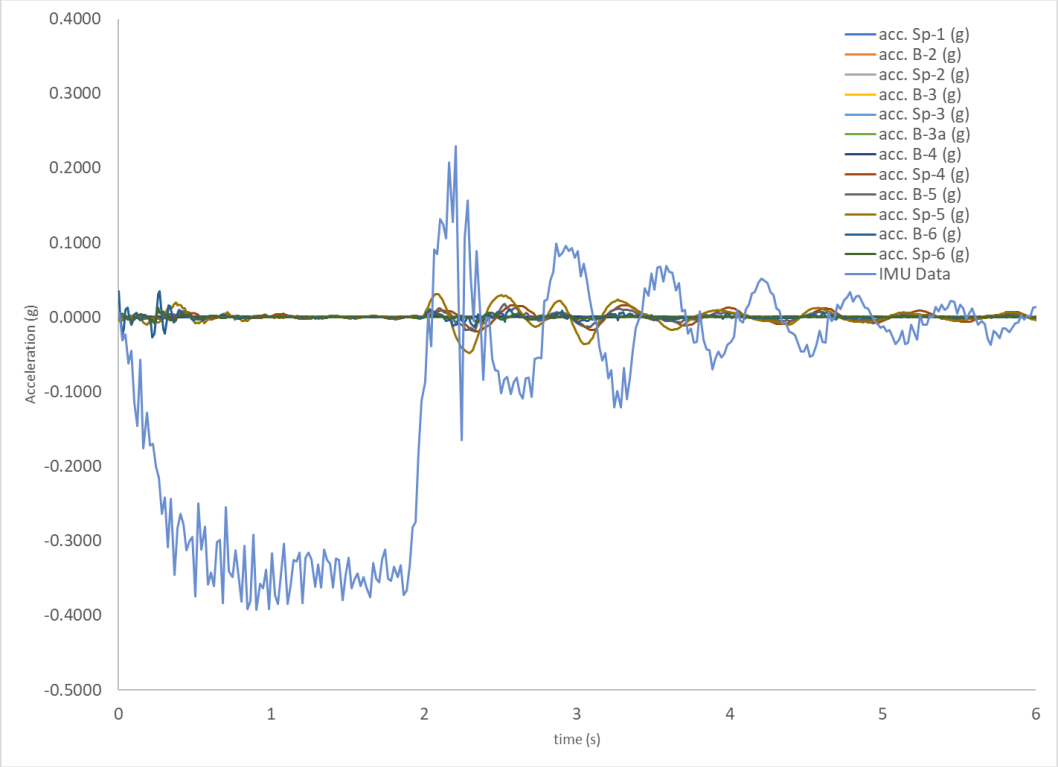

Figure C-13 – DAQ and IMU Data from Center of Span 5 Test 2 (Barr 2019)

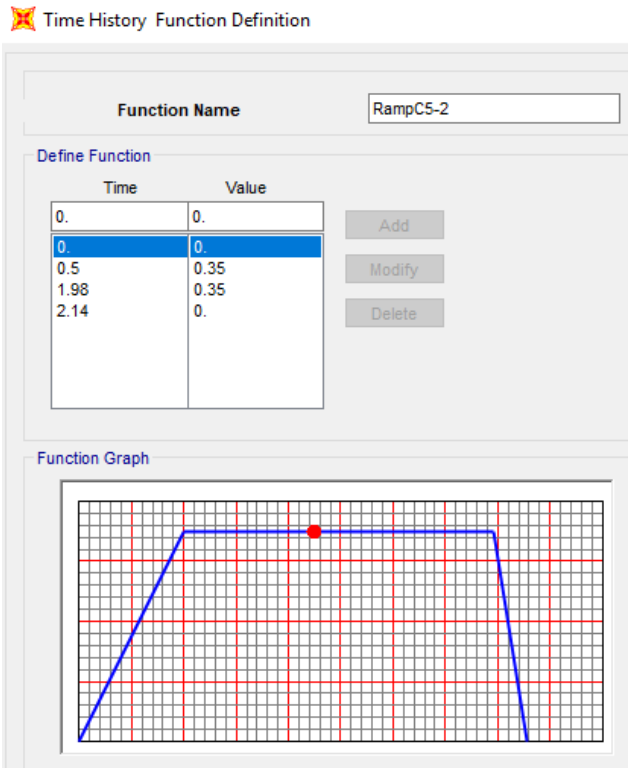

Figure C-14 – SAP2000 Time History Ramp Function from Braking Profile for C5-2

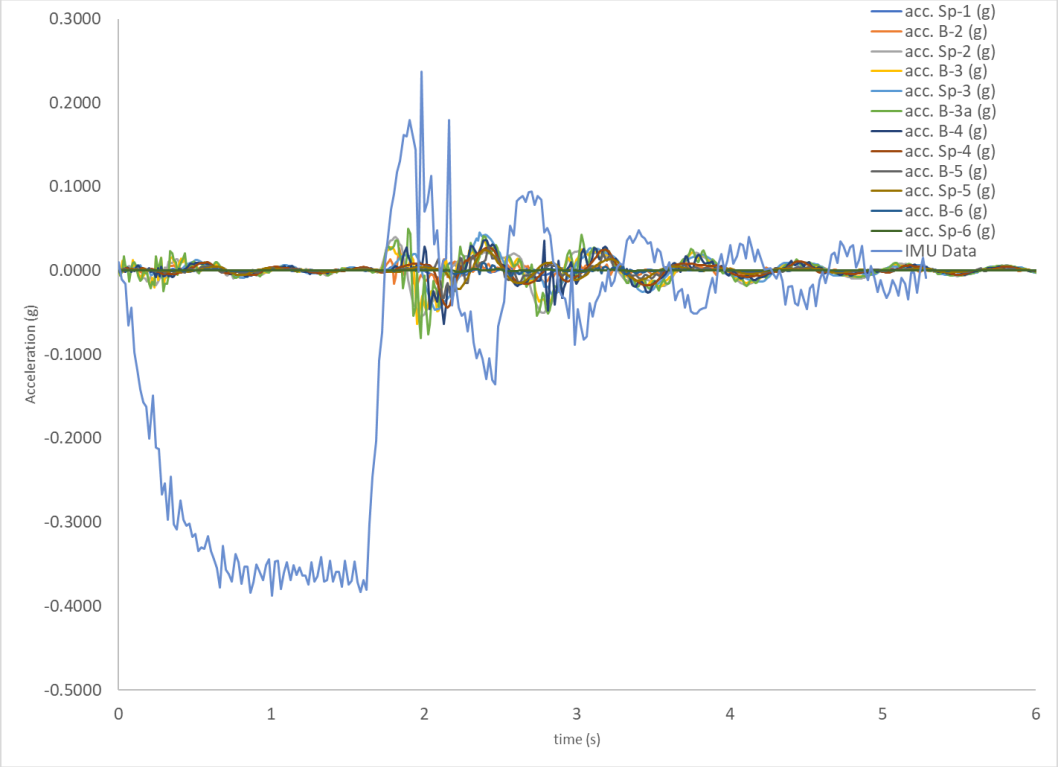

Figure C-15 – DAQ and IMU Data from the Right Side of Span 2 Test 2 (Barr 2019)

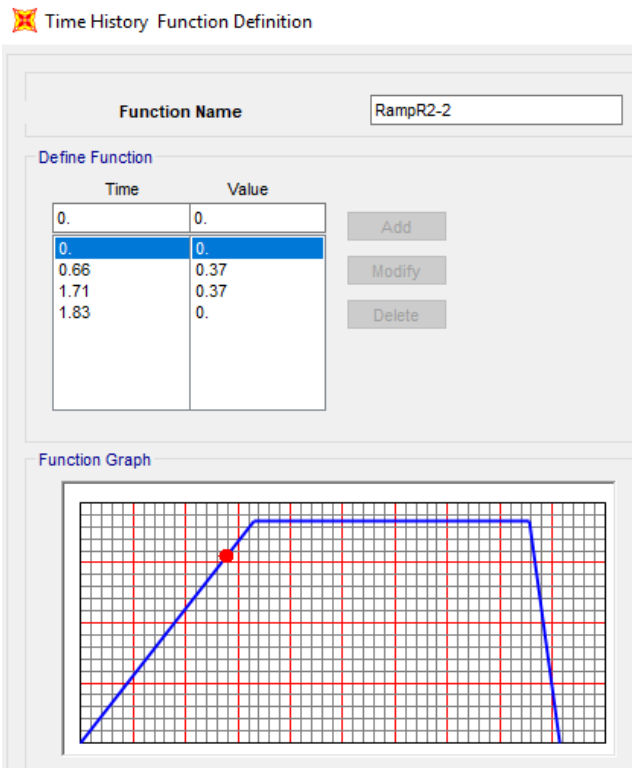

Figure C-16 – SAP2000 Time History Ramp Function from Braking Profile for R2-2

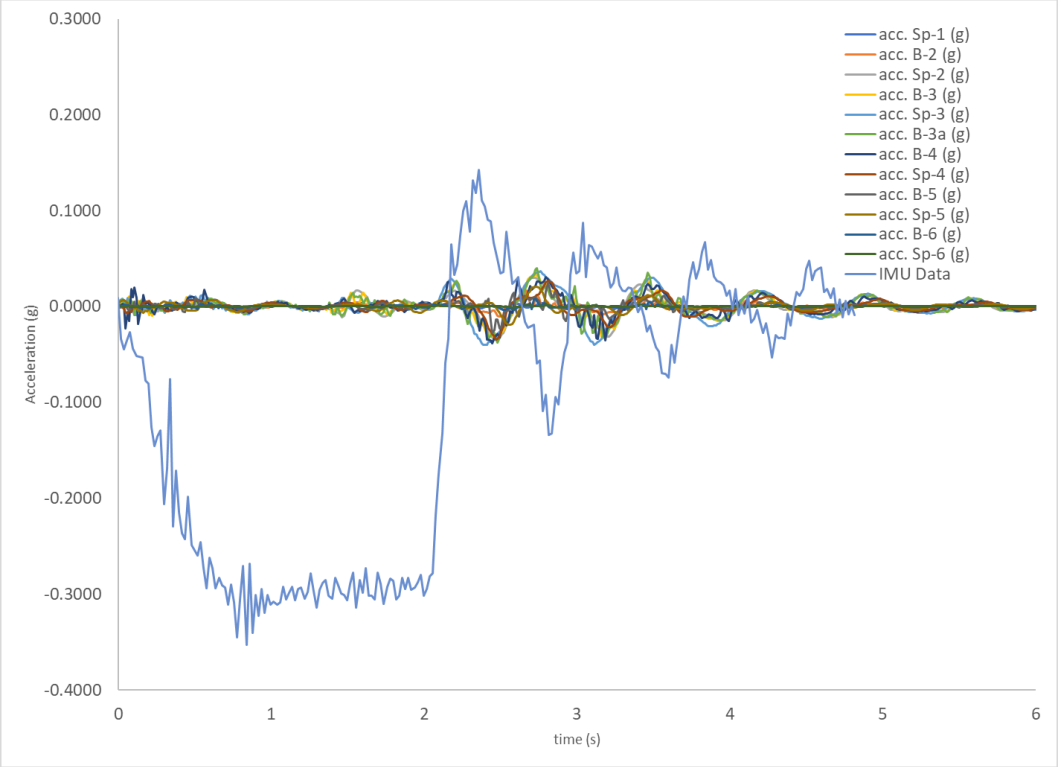

Figure C-17 – DAQ and IMU Data from the Right Side of Span 3 Test 3 (Barr 2019)

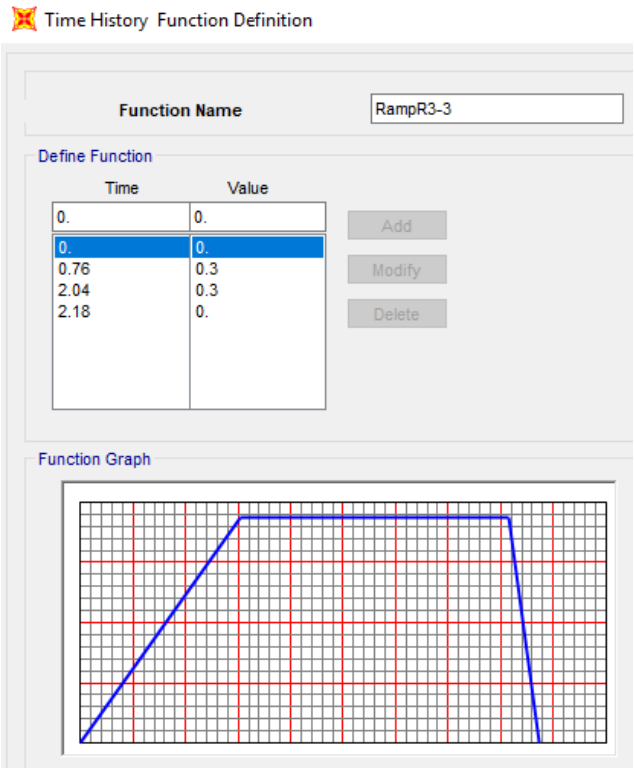

Figure C-18 – SAP2000 Time History Ramp Function from Braking Profile for R3-3

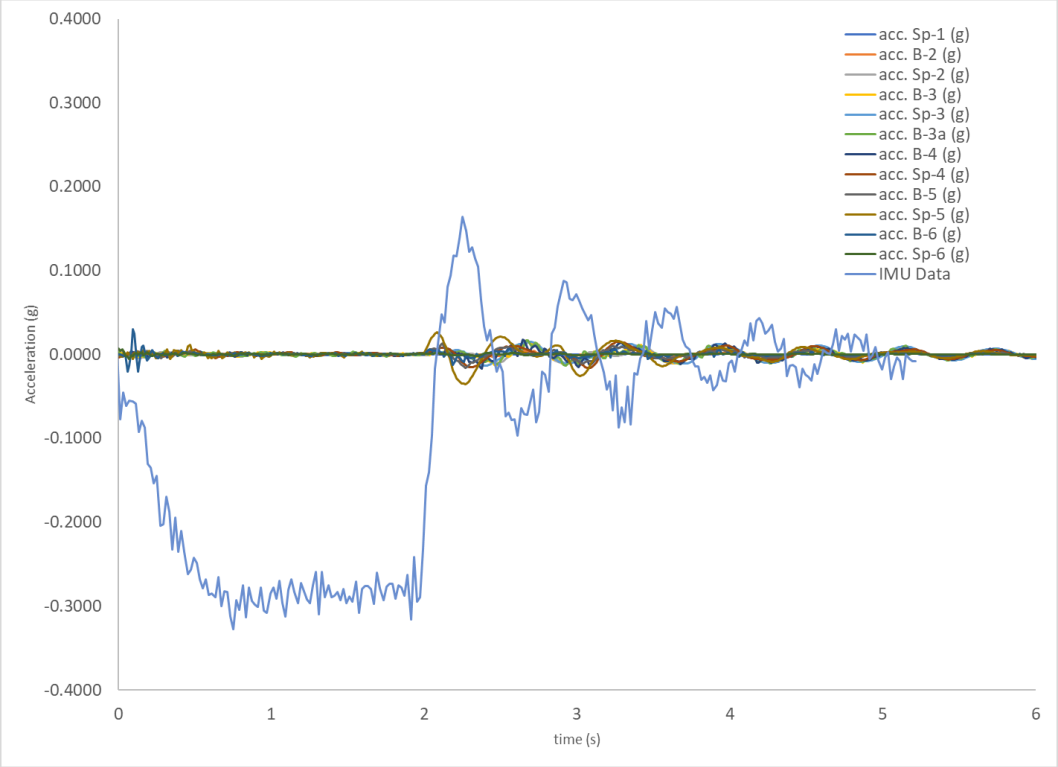

Figure C-19 – DAQ and IMU Data from the Right Side of Span 5 Test 1 (Barr 2019)

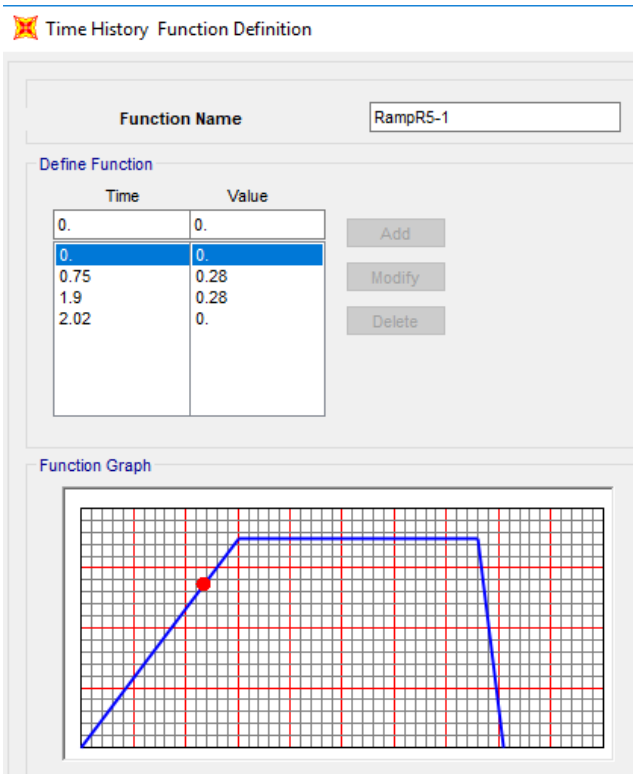

Figure C-20 – SAP2000 Time History Ramp Function from Braking Profile for R5-1

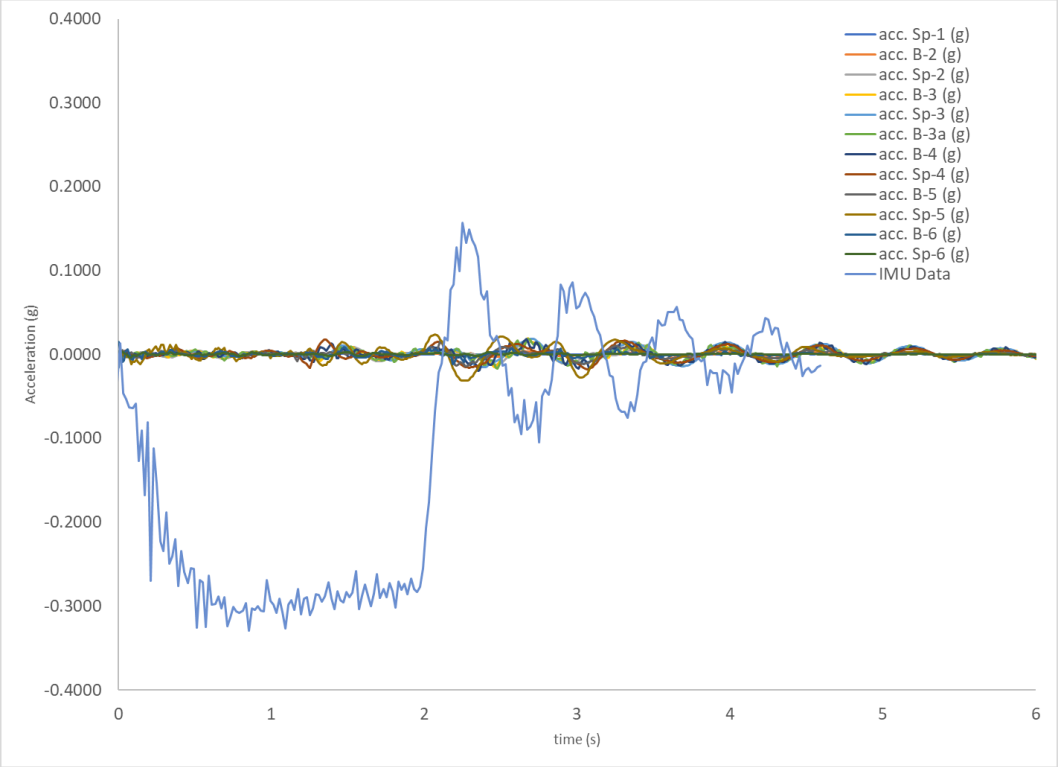

Figure C-21 – DAQ and IMU Data from the Right Side of Span 5 Test 3 (Barr 2019)

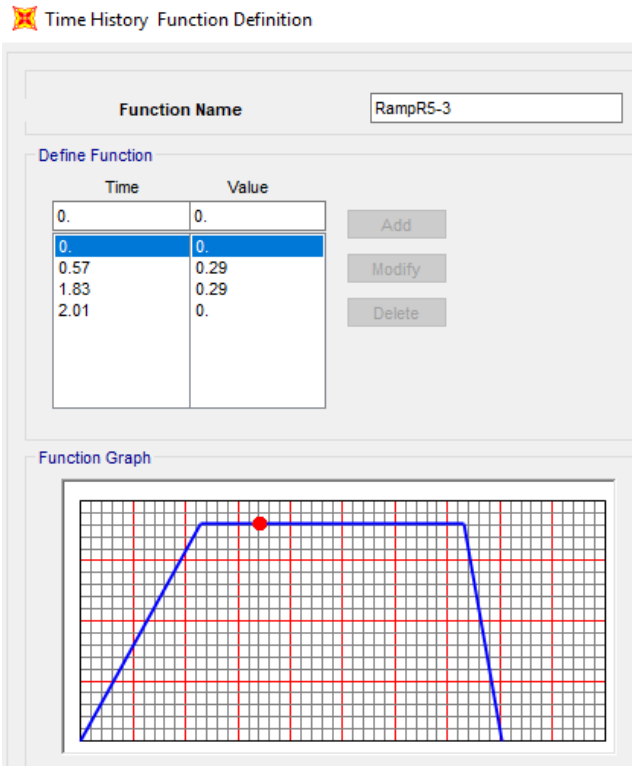

Figure C-22 – SAP2000 Time History Ramp Function from Braking Profile for R5-3